Investigations on Factors Influencing Morphology of Polypyrrole Nanostructures for Enzymatic Biosensing Applications

Ph.D. Thesis

By

PRAMILA

DISCIPLINE OF ELECTRICAL ENGINEERING

INDIAN INSTITUTE OF TECHNOLOGY INDORE

FEBRUARY 2019

Investigations on Factors Influencing Morphology of Polypyrrole Nanostructures for Enzymatic Biosensing Applications

A THESIS

Submitted in partial fulfillment of the
requirements for the award of the degree
of
DOCTOR OF PHILOSOPHY

by

PRAMILA

DISCIPLINE OF ELECTRICAL ENGINEERING
INDIAN INSTITUTE OF TECHNOLOGY INDORE
FEBRUARY 2019

INDIAN INSTITUTE OF TECHNOLOGY INDORE

CANDIDATE'S DECLARATION

I hereby certify that the work which is being presented in the thesis entitled **INVESTIGATIONS ON FACTORS INFLUENCING MORPHOLOGY OF POLYPYRROLE NANOSTRUCTURES FOR ENZYMATIC BIOSENSING APPLICATIONS** in the partial fulfillment of the requirements for the award of the degree of **DOCTOR OF PHILOSOPHY** and submitted in the **DISCIPLINE OF ELECTRICAL ENGINEERING, Indian Institute of Technology Indore**, is an authentic record of my own work carried out during the time period from January 2015 to August 2019 under the supervision of **Dr. Vipul Singh**, Associate Professor, IIT Indore.

The matter presented in this thesis has not been submitted by me for the award of any other degree of this or any other institute.

Signature of the student with date
(PRAMILA)

This is to certify that the above statement made by the candidate is correct to the best of my knowledge.

Signature of the Thesis Supervisor with date
(Dr. Vipul Singh)

PRAMILA has successfully given her Ph.D. oral examination held on August 13, 2019.

Signature of Chairperson (OEB)	Signature of External Examiner	Signature of Thesis Supervisor
Date:	Date:	Date:
Signature of PSPC Member #1	Signature of PSPC Member #2	Signature of Convener, DPGC
Date:	Date:	Date:

Signature of Head of Discipline

Date:

ACKNOWLEDGMENTS

I owe it all to the almighty for blessing me with this opportunity to pursue Ph.D. in a prestigious institute IIT Indore.

I would like to express my sincere gratitude to my thesis supervisor **Dr. Vipul Singh** (Associate Professor, Discipline of Electrical Engineering, IIT Indore) for his continuous guidance, support, patience, motivation and immense knowledge. Being new to the experimental research and field of biosensors his expertise and trust on me were key in achieving the formulated tasks. It has been my privilege and honour to work with him. I have grown as a researcher as well as an individual working with him at IIT Indore. Above all, it was a great learning experience for me.

I express sincere thanks to **Prof. Pradeep Mathur** (Director, IIT Indore), who has been highly encouraging during the entire course of my doctoral work. I also convey sincere thanks to **Prof. Neelesh K. Jain** (Dean of Academic Affairs, IIT Indore) and **Dr. Srivathsan Vasudevan** (DPGC Convener, Discipline of Electrical Engineering, IIT Indore) for their support and motivation during entire course of doctoral work. My sincere thanks and appreciation to the PSPC (Ph.D. Student Progress Committee) members, **Dr. Srivathsan Vasudevan** (Associate Professor, Discipline of Electrical Engineering, IIT Indore) and **Dr. I. A. Palani** (Associate Professor, Discipline of Mechanical Engineering, IIT Indore) for their precise observations and valuable suggestions to improve the quality of my doctoral work. I am highly obliged to **Dr. M. Anbarasu** (Associate Professor, Discipline of Electrical Engineering, IIT Indore) for allowing me to access sputtering facility. Furthermore, I am thankful to **Dr. Parasharam M. Shirage** (Associate Professor, Discipline of MEMS, IIT Indore) for allowing me to access the Electrochemical Impedance Spectroscopy facility.

I extend my gratitude to **UGC - DAE consortium for Scientific Research, Indore** for providing the necessary research facilities. In particular, I would like to thank **Dr. Mukul Gupta** for allowing me to acess the research facilities.

With deep regards, I extend my heartfelt gratitude to **Prof. Pragati Kumar** (Professor, Department of Electrical Engineering, DTU, New Delhi) for his mentorship during my M. Tech (2011-2013) which sowed seeds of research in my life and encouraged me to pursue Ph.D. at IIT Indore.

I express my deepest gratitude to my lovely parents **Shri Phool Chand** and **Smt. Chand Kaur** for encouraging me and making me what I am today. I would further like to thank my family (**Smt. Manju Devi**, **Shri Bajranglal Jakhar, Mr. Vimal Dhaka**), siblings **(Mr. Sandeep Jakhar**, **Mrs. Sushma Jakhar**), and friends (**Mrs. Asha Dhinwa, Mrs. Sangeeta Devra, Dr. Nupur Navlakha, and Ms. Y V Bhuvneshawari**) for always being enthusiast and encouraging.

I am thankful to my colleagues from the **Molecular and Nanoelectronics Research Group (MNRG)**, **Dr. Pragya A. Palod, Dr. Kshitij Bharagava, Dr. Anubha Bilgaiyan, Dr. Ashish Kumar, Dr. Tejendra Dixit, Dr. Mayoorika Shukla, Dr. P. Rajagopalan, Dr. Shalu, Mr. Jitesh Agrawal, Mr. Akash, Ms. Nidhi, and Ms. Tejasvini Lahane** for their company and valuable assistance at various stages of my research work. I would like to especially thank **Dr. Mayoorika Shukla and Dr. P. Rajagopalan** for their continuous motivation and critically reviewing the manuscripts. I would also like to thank **Mr. Nishant Saxena, Mr. Prateek Bhojane** for helping me out during experiments performed in this research work.

Further, I wish to thank **Sophisticated Instruments Center (SIC), IIT Indore** for various experimental and characterization setups used during this research work. Specifically I would like to thank **Mr. Kinny Pandey** and **Mr. Nitin Upadhyaya** for their support.

I acknowledge the **Ministry of Human Resource Development, Govt. of India** for providing the teaching assistantship during my doctoral work.

Finally, I wish to thank all the individuals from the support staff of IIT Indore, whose contributions directly or indirectly contributed to my doctoral work.

Dated: (Pramila)

Dedicated

to

my family

Abstract

Glucose plays an imperative role in human metabolism and any imbalance in blood glucose level leads to diabetes mellitus which is one of the major causes of death and disability in the world. With the drastic increase in the number of diabetic patients around the world and particularly in India, a pressing need has been felt to develop the point of care handheld testing devices which can provide continuous monitoring of glucose level of such patients. Thus, for the diagnosis and effective management of diabetes, the development of a cost-effective, simple, accurate, portable, and rapid sensor for glucose detection is required. For this aim, electrochemical biosensors, especially amperometric have been proved to be successful for the determination of glucose level in human blood. In this regard, Polypyrrole (PPy) nanostructures have been reported to be viable for the development of these devices due to low oxidation potential, high electrical conductivity, environmental stability, biocompatibility, etc. This work aims to achieve improved performance of amperometric glucose biosensor by enhanced material properties. In this work, we have fabricated enzymatic electrochemical biosensor for glucose detection utilizing PPy nanostructures as a support matrix. Different morphologies of PPy with the incorporation of different dopants *viz.* $LiClO_4$ and p-TSA were obtained by a simple, single-step, template-free electrochemical polymerization technique. The work can majorly be divided into three parts: (i) Morphology and charge transfer resistance tuned $LiClO_4$ doped PPy nanofibers network fabricated over Pt (Anode) coated glass substrates; (ii) High electroactive surface area PPy electrode with p-TSA as a dopant was fabricated with the aim of achieving higher enzyme loading (a pre-requisite for improved biosensor response) and (iii) Different immobilization techniques *viz.* physical adsorption and cross-linking were employed and compared. We have systematically studied dopant concentration, type of dopant and enzyme immobilization technique which has influenced the surface area, charge transfer resistance, and enzyme loading and thereby, influencing the performance of glucose biosensor in detail. The best biosensor was developed by crosslinking immobilization of GOx over PPy nanofibers network. The fabricated biosensor device showed a high sensitivity of $\sim$25-30 mA-cm^{-2}-M^{-1} in a linear range of 0.1–2.5 mM with a response time of 30 s. Furthermore,

the biosensor retained 92% of its initial sensitivity after storage of 14 days. The observed results show that PPy nanofibers with improved electrochemical properties can pave way to high performance biosensors.

LIST OF PUBLICATIONS

Peer-reviewed Journals: From Thesis Work

1. **Pramila Jakhar**, Mayoorika Shukla, and Vipul Singh, "Improved performance of electrochemically synthesized Polypyrrole nanofiber array-based amperometric glucose biosensor via crosslinking technique", Journal of Nanoscience and Nanotechnology 19, 7605-7614 (2019). (Impact Factor-1.35).

2. **Pramila Jakhar**, Mayoorika Shukla, and Vipul Singh, "Investigation of Dopant Effect on the Electrochemical Performance of 1-D Polypyrrole Nanofibers Based Glucose Biosensor", Journal of Material Science: Material in Electronics 30, 3563-3573 (2019). (Impact Factor-2.3).

3. **Pramila Jakhar**, Mayoorika Shukla, and Vipul Singh, "Influence of $LiClO_4$ concentration on 1-D Polypyrrole nanofibers for enhanced performance of glucose biosensor", Journal of The Electrochemical Society 165, G80–G89 (2018). (Impact Factor-3.66).

4. **Pramila Jakhar**, Mayoorika Shukla, and Vipul Singh, "Improved Optical and Electrical Properties of Polypyrrole Coated ZnO nanorods Based nanostructured Electrodes for Glucose Biosensing Application". (Manuscript under preparation).

Peer-reviewed Journals: Outside of Thesis Work

1. Mayoorika Shukla, **Pramila**, I. A. Palani and Vipul Singh, "A comparative analysis of ZnO nanorods and nanopencils towards amperometric biosensing applications", Journal of Nanoscience and Nanotechnology 19, 3816-3824 (2019). (Impact Factor-1.35).

2. Mayoorika Shukla, **Pramila**, Jitesh Agrawal, Tejendra Dixit, I. A. Palani and Vipul Singh, "Facile Hydrothermal Synthesis of Mn Doped ZnO Nanopencils for Development of Amperometric Glucose Biosensors", Material Research Express 5, 1-16 (2018). (Impact Factor-1.16).

3. Mayoorika Shukla, **Pramila**, I. A. Palani and Vipul Singh, "Effect of immobilization technique on performance ZnO nanorods based enzymatic electrochemical glucose biosensor", Journal of Physics: Conference Series 924, 012013 (2017).

4. Mayoorika Shukla, **Pramila**, Tejendra Dixit, I. A. Palani and Vipul Singh, "Influence of aspect ratio and surface defect density on hydrothermally grown ZnO nanorods towards amperometric glucose bio sensing applications", Applied Surface Science 422, 798-808 (2017). (Impact factor-4.4).

Conference Proceedings: From Thesis Work

1. **Pramila**, Mayoorika Shukla and Vipul Singh, India-Japan Workshop on Biomolecular Electronics and Organic Nanotechnology for Environment Preservation (IJWBME-2018) NPL, New Delhi (India) December 6–9, 2018.

2. **Pramila**, Mayoorika Shukla and Vipul Singh, DAE-BRNS National Laser Symposium (NLS-27) RRCAT Indore, MP (India) December 3–6, 2018.

3. **Pramila**, Mayoorika Shukla, and Vipul Singh, 19^{th} International Workshop on The Physics of Semiconductor Devices (IWPSD 2017) Delhi (India) December 11-16, 2017.

4. **Pramila**, Mayoorika Shukla, and Vipul Singh, International Conference on Laser Deposition (iCOLD 2017) Chennai (India) November 20-22, 2017.

5. **Pramila**, Mayoorika Shukla and I. A. Palani and Vipul Singh, 3^{rd} NanoSciTech, Chandigarh (India) November 8-10, 2017.

6. **Pramila**, Mayoorika Shukla and Vipul Singh, International Conference on Emerging Trends in Materials and Manufacturing Engineering (IMME 2017) Trichy (India) March 10-12, 2017.

7. **Pramila**, Mayoorika Shukla and Vipul Singh, IUMRS International Conference of Young Researchers (IUMRS-ICYR 2016), Bangalore (India) December 11-15, 2016.

Conference Proceedings: Outside of Thesis Work

1. Mayoorika Shukla, **Pramila**, I. A. Palani and Vipul Singh, 19^{th} International Workshop on The Physics of Semiconductor Devices (IWPSD 2017) Delhi (India) December 11-16, 2017.

2. Mayoorika Shukla, **Pramila**, I. A. Palani and Vipul Singh, 3^{rd} NanoSciTech, Chandigarh (India), November 8-10, 2017.

3. Mayoorika Shukla, **Pramila**, Tejendra Dixit, I. A. Palani and Vipul Singh, 4^{th} International Conference on Nanoscience and Nanotechnology (ICONN-2017) Chennai (India) August 9-11, 2017.

4. Mayoorika Shukla, **Pramila**, Tejendra Dixit, I. A. Palani and Vipul Singh, 12^{th} International Conference on Nano-Molecular Electronics (ICNME 2016) Kobe (Japan) December 14-16, 2016.

5. Mayoorika Shukla, Tejendra Dixit, **Pramila**, I. A. Palani and Vipul Singh, IUMRS International Conference of Young Researchers (IUMRS-ICYR 2016) Bangalore (India) December 11-15, 2016.

Book Chapter

1. **Pramila Jakhar**, Mayoorika Shukla, and Vipul Singh (2019), Electrochemically Synthesized Polypyrrole Nanofibers towards Glucose Biosensing Application, The Physics of Semiconductor Devices, IWPSD 2017, Springer Proceedings in Physics, 215, (pp. 871-874), Springer, Cham, ISBN 978-3-319-97604-4.

TABLE OF CONTENTS

LIST OF FIGURES

LIST OF TABLES

LIST OF NOMENCLATURE & ACRONYMS

NOMENCLATURE

λ	Wavelength [nm]
v	Scan rate at which the potential was swept
θ	Angle of incidence between the incident ray and scattering planes [degree/radian]
A_{eff}	Effective surface area of the electrode
c	Speed of light in vacuum
C_0	Concentration of $K_3Fe[CN]_6$ and $K_4Fe[CN]_6$ in solution
D	Diffusion coefficient
e	Electronic charge
h	Planck's constant
k	Shape factor
K_m	Michaelis-Menten constant
m_0	Electron rest mass
V	Accelerating voltage
v	Order of refraction
V_0	Initial reaction rate
V_{max}	Maximum value of initial reaction rate

ACRONYMS

$[Fe(CN)_6]^{3-/4-}$	Potassium ferricyanide/ferrocyanide

AAO	Anodic Aluminum Oxide
AC	Alternating Current
Ar	Argon
BSA	Bovine serum albumin
CCD	Charge coupled device
CNT	Carbon Nanotubes
CPs	Conducting Polymers
Cr	Chromium
CV	Cyclic Voltammetry
DBSA	Dodecylbenzenesulfonic acid
DI	De-ionised
DLE	Deep Level Emission
DNA	Deoxyribonucleic acid
EIS	Electrochemical Impedance Spectroscopy
$FeCl_3$	Iron(III) Chloride
FESEM	Field Emisson Scaning Electron Microscope
FRA	Frequency Response Analyzer
FTIR	Fourier Transform infrared spectroscopy
GOx	Glucose Oxidase
HRTEM	High Resolution Transmisssion Electron Spectroscopy
IDF	International diabeteties Federation
IPA	Iso-propyl alcohol
ITO	Indium Tin oxide
KBr	Pottasium Bromide
KCl	Pottasium Chloride
KNO_3	Potassium Nitrate

$LiClO_4$	Lithium perchlorate
LOD	Limit of Detection
$MeSA$	Methanesulfonic acid
Na_2HPO_4	Sodium Phosphate Dibasic
NaH_2PO_4	Sodium Phosphate Monobasic
NBE	Near Band Edge Emission
$p-TSA$	p-Toluenesulfonic acid
PBS	Phosphate-buffered saline
PL	Photoluminescence
PNN	Polypyrrole Nanofibers Network
$POCT$	Point of Care Testing
PPy	Polypyrrole
Py	Pyrrole
Q_1&Q_2	Constant Phase Element
SDS	Sodium Dodecyl Sulfate
SnO_2	Tin dioxide
TEM	Transmisssion Electron Spectroscopy
TiO_2	Titanium Oxide
UV	Ultra violet
XRD	Xray Diffraction
ZnO	Zinc Oxide

Chapter 1

Introduction

The advancement in the field of nanotechnology has opened new exhilarating opportunities in biosensing devices. It has affected almost all aspects of biosensing devices in medical diagnostics, pharmaceutical, agricultural, food, beverages, environmental, and many other biotechnological industries. The incredible progress has been made in biosensor applications since the development of oxygen electrode by Lyon and Clark in 1962 [1, 2]. The astounding success of biosensors in biomedical field has been the driving factor for the accelerated research in this area. Integration of nanostructured materials for biosensor fabrication has been reported to be viable for high sensitivity, versatility, stability, and selectivity of biosensing devices. These nanostructured materials have been employed as a support matrix for enzyme immobilization, enzyme stabilizers, or surface modifiers for biosensing device application. Among the other sensing platforms, glucose biosensors are of special clinical and industrial significance [3–5]. The estimation of the glucose level is significant in biological and clinical samples, as well as in food processing and fermentation, chemical samples. Glucose plays an imperative role in human metabolism and any imbalance in blood glucose level leads to diabetes mellitus which is one of the major causes of death and disability in the world. With this drastic increase in the number of patients suffering from diabetes around the world and particularly in India, a pressing need has been felt to develop the point of care handheld testing devices which can provide continuous monitoring of glucose level of such patients. Thus, for the diagnosis and effective management of diabetes, the development and fabrication of a cost-effective, simple, accurate,

portable, and rapid sensor for glucose detection is required [6]. In this regard, electrochemical biosensors have been reported to be successful for the determination of glucose level in human blood [7]. This work mainly focuses on the growth of different Polypyrrole (PPy) nanostructures by the simple, amicable and cost-effective template-free method; to be used as a support matrix for immobilization of enzymes for the development of amperometric glucose biosensors.

1.1 Biosensor

Biosensors are user-friendly Point of care testing (POCT) devices facilitating the qualitative and quantitative measurement of several analyte molecules [8]. Some of the commercially available biosensors in medical diagnosis have been shown in Fig. 1.1. Biosensors are the analytical devices which consist of a bio-recognition layer (biosensing elements) in close contact with a transducer to convert the biological reaction into measurable and quantifiable signal for real-time monitoring. The schematic of biosensor has been shown in Fig. 1.2 which presents the main

Fig. 1.1: **Commercially available biosensors in medical diagnosis.**

components of a biosensor:

1. **Bio-recognition layer:** These are the biomolecules such as Enzymes, Antibodies, Whole cell, Probe DNA etc. specific towards selective determination of analyte molecules as Glucose, Cholesterol, Antigen, Target DNA, Tricglycerides etc. [9]. Based on the biomolecule utilized for detection of analyte, biosensors can be categorized as Enzymatic, Immuno and Aptasensors corresponding to enzymes, antibody and probe DNA respectively.

2. **Transducer:** The transducer carries the support matrix which provides a solid support for immobilization of biomolecules (Enzymes, Antibodies, Probe DNA etc.) so that enzyme do not get leached out of the matrix. The bio-recognition layer is attached to the transducer which converts the biological reaction between the immobilized biomolecule and analyte into electrical signal. This electrical signal is sent to the signal processing and display unit [10]. Based on the biological reaction different transduction methods can be divided as electrochemical, optical, calorimetric, piezo-electric, mass-sensitive etc.

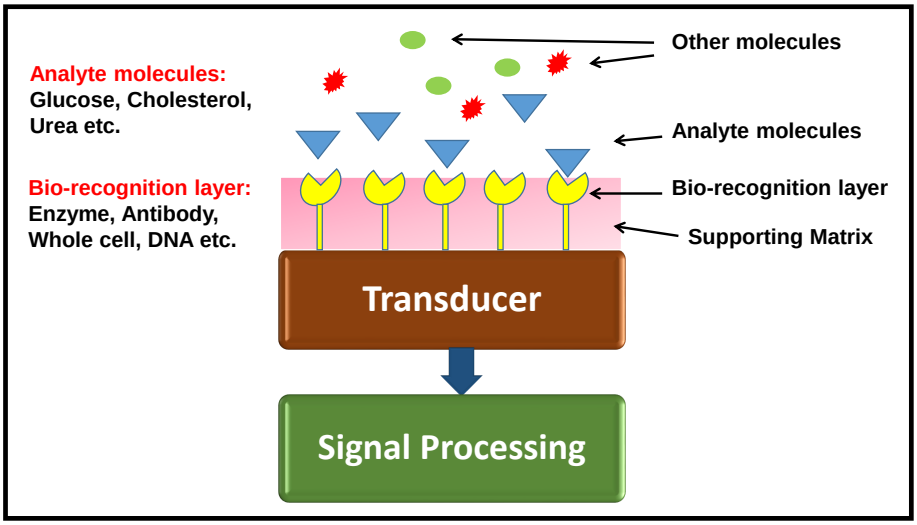

Fig. 1.2: **Schematic of biosensor.**

Figure of Merits of Biosensor:

Some of the typical features of a biosensor are as follows:

1. **Sensitivity:** Sensitivity is defined as the ability of a device to generate as large a response as possible, on interacting even with small amount of analyte. A sensor is said to be sensitive, if a small change in the analyte concentration causes a large change in the response. Within the linear range of response, the sensitivity is defined as the ratio of change in output to change in input. The sensitivity of a biosensor depends on (a) sensitivity of the detection system and (b) distribution of the functional biological molecules near the sensor surface.

2. **Linear Range:** The linear range of a biosensor is defined as the range of analyte concentration upto which the biosensor response changes linearly with

the analyte concentration.

3. **Response Time:** The Response time of biosensor is the time required by a biosensor to generate the response as a result of biorecognition event. It is a collective time taken by the interaction event and transduction of the generated response through the transducer which is measured as time taken to reach 90% of the steady state value. Response time of an ideal biosensor should be minimum in order to have a real time quick diagnosis.

4. **Selectivity:** Selectivity is defined as the ability of a sensor to detect one specific species even in the presence of a number of other chemical species or interferents. High selectivity enables a biosensor to inhibit the interfering species from contributing and thereby affecting the accuracy in the measurements of the analyte.

5. **Stability:** Stability of a biosensor is defined as the duration of time till a biosensor (under the specified storage conditions) remains suitable for analyte assay. It is the extent to which a device retains (within specified limits) the same properties and characteristics throughout its period of storage and use that it possessed at the time of fabrication. This feature takes into account the time dependent degradation in the performance of a device. Long shelf life is one of the essential features for a commercial reliable biosensor [11].

1.2 Glucose: Analyte under study

The detection of glucose has been widely accepted in every field ranging from agricultural, food, and biomedical applications. Glucose, metabolic fuel molecule plays an imperative role in human metabolism [12]. Any imbalance in blood glucose concentration can cause chronic disease like diabetes mellitus which has been found to be a leading cause of death and disability in the world. The hidden danger of diabetes mostly lie in the undiagnostic disease. Due to either lack of realization or ignorance of the symptoms of diabetes, it is left untreated, and thus raises the risk of various diseases like kidney failure, heart disease, blindness or even death [6]. From the last few decades, there has been tremendous increase in diabetic patients. These patients require continuous monitoring of blood glucose concen-

tration to provide a guide by monitoring day to day blood glucose level. Thus there is a high demand to provide hand-held Point of Care Testing (POCT) device which can provide continuous monitoring of blood glucose level. Electrochemical glucose biosensors have been proved to be viable for continuous monitoring of glucose level of patients suffering from diabetes [13]. Additionally, the detection of glucose is also important in fermentation, food and beverage industries.

1.2.1 Diabetes Mellitus

Diabetes mellitus is one of the most commonly occurring diseases worldwide. It is one of the leading causes of death and disability in the world. The increasingly unhealthy diets and lethargic lifestyles have been reported to be the major reasons for unnoticed higher rates of obesity and diabetes [14]. According to International Diabetes Federation (IDF) 2017, 425 million people in the world were reported to be suffering from diabetes and this number is anticipated to increase upto 629 million (48% increase) in 2045 as shown in Fig. 1.3. The number of deaths due to the diabetes has been reported to be 4 million. The total expenditure per year on diabetes related healthcare was estimated to be around USD 727 billion. Moreover, India has reached at the second largest capital of diabetic patients after China. These statistics indicate that diabetes is a global issue with epidemic concerns but also reduces productivity and economic growth. With this drastic increase in number of diabetic patients and increased mortality rate, research in the field of diagnosis, treatment and continuous monitoring of diabetes is of extreme relevance [15]. This metabolic disorder results from insulin deficiency in the body and causes either higher blood-glucose levels (hyperglycaemia), or reduced glucose concentrations (hypoglycaemia) than the normal blood glucose concentration (4.4-6.6 mM). Insulin is produced by pancreas and helps in transporting the glucose through blood to the body cells. The cells utilizes this glucose as the energy. The increased glucose in bloodstream or hyperglycemia causes diabetes. The undiagonosed hyperglycemia leads to many health complications such as cardio-vascular disoder, nephropathy (kidney disease in diabetes), glaucoma (diabetic eye disease), neuropathy (nerve damage) and diabetic foot etc. [16]. Therefore a diabetic patient is required to continuously monitor the blood glucose concentration for timely diagnosis of diabetes. It has been broadly divided into three types as shown in Fig.

1.4.

1. **Type 1:** The insulin hormone is produced by the beta cells of pancreas. In Type 1 diabetes, body's immune system attacks the insulin-producing beta cells of the pancreas gland. As a result, the body produces no or very less insulin which creates insulin deficiency in the body. The causes of this disorder are not fully understood but some of the reasons such as genetic susceptibility, toxins viral infection, or some dietary factors have been implicated. Type 1 diabetes occurs generally in children and adolescents. These patients require daily insulin injections to maintain the glucose level in proper range. People having type 1 diabetes can live a healthy life by taking daily insulin treatment, regular blood glucose monitoring and maintaining a healthy diet and lifestyle.

2. **Type 2:** Type 2 diabetes is the most commonly found diabetic condition. In this case, the body either produces insufficient amount of insulin or body cells are unable to respond to it (insulin resistance occurs) and thus glucose remains circulating in blood [17]. In this condition, body cells are unable to utilize the glucose. It is generally found in older adults but now increasingly found in children and younger adults. People with type 2 diabetes usually do not need insulin. But they can manage their condition through a healthy diet and increased physical activity.

3. **Gestational:** The higher glucose level during pregnancy has been defined as gestational diabetes mellitus. This can arise in any duration of pregnancy (usually during the second and third trimesters of pregnancy) and resolves after pregnancy. The blood glucose levels during pregnancy can be controlled by gentle exercise, a healthy diet, continuous blood glucose monitoring, and by taking insulin or oral medication.

Thus, the diagnosis, treatment, and regular monitoring are crucial for management of all forms of diabetes.

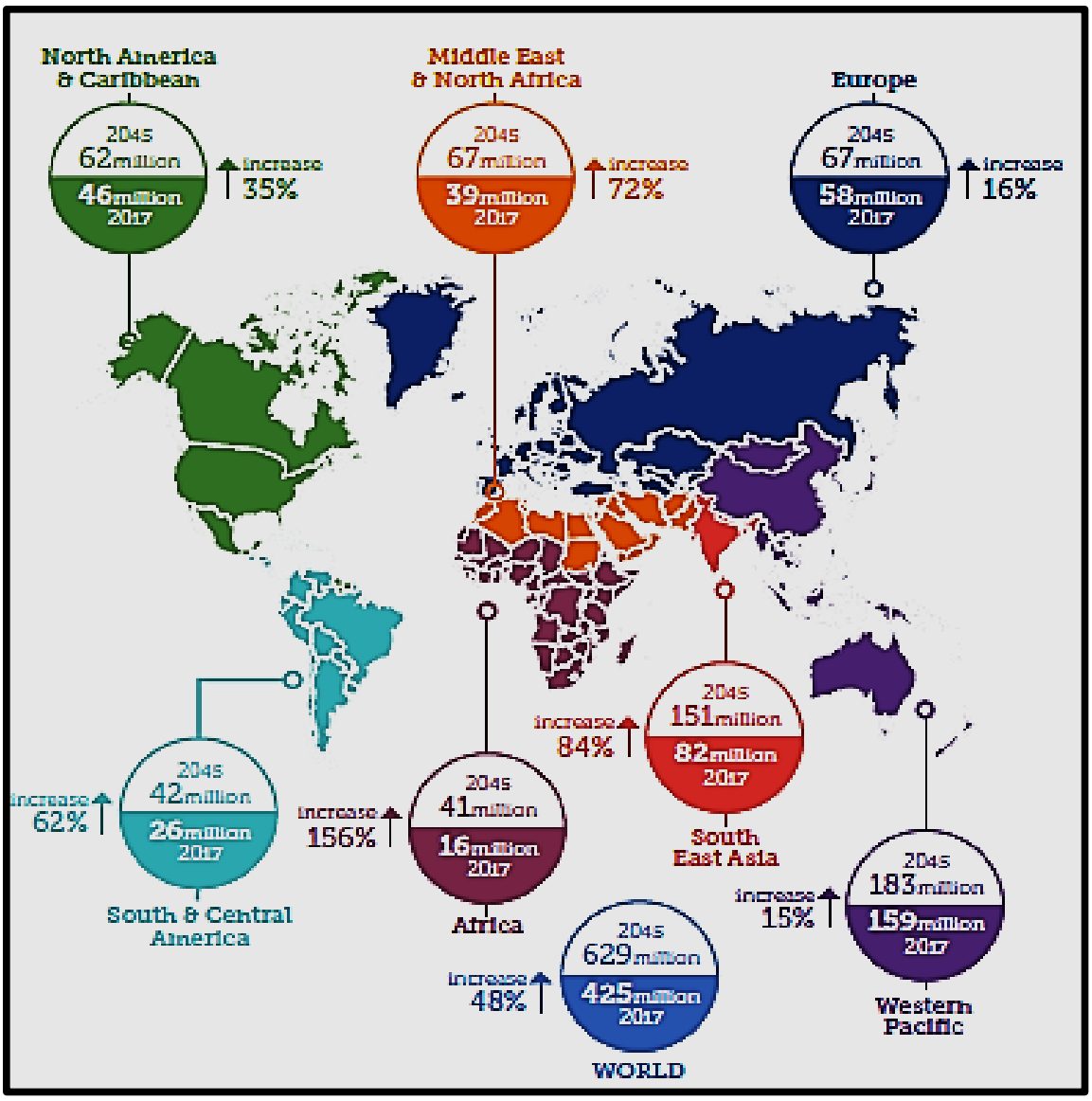

Fig. 1.3: **Global status of diabetes according to International Diabetes Federation (IDF) Report 2017. Image taken from [15].**

1.3 Enzymes: Bio-recognition layer

The performance of biosensor highly depends on the catalytic activity of enzyme towards the analyte detection. The support matrix is utilized for the attachment of enzymes. Enzymes are biocatalyst which speed up the biochemical reactions in living beings under the mild conditions. There are approximately 40,000 enzymes in human cells. They are very specific to their substrates and play the essential role in several functions such as in digesting food, respiration, nerve and muscle functioning, information storage etc. [19]. In this work, we have used Glucose oxidase (GOx) enzyme, a most widely used biomolecule for selective detection of glucose.

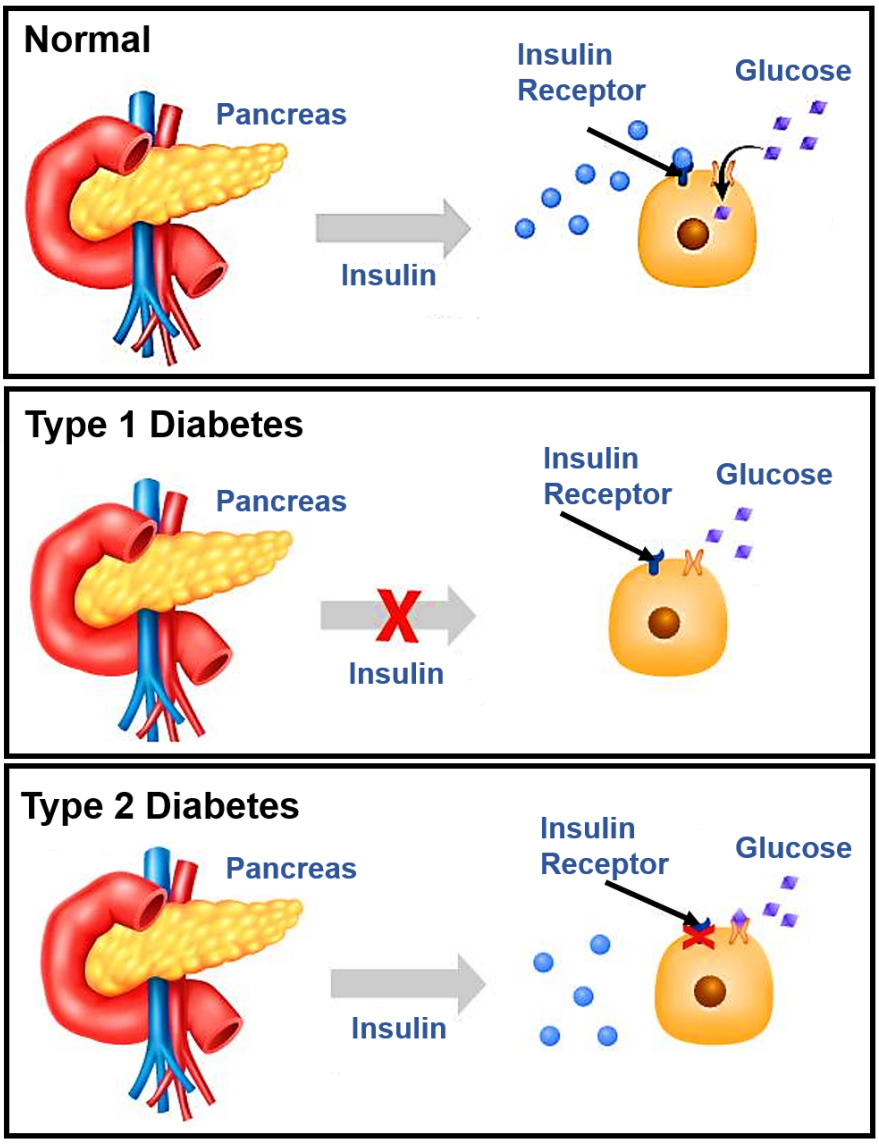

Fig. 1.4: **Schematic illustration of functioning of insulin in healthy and diabetic patients (type 1 and type 2 diabetes). Image taken from [18].**

The detailed explanation and working principle of GOx has been explained in section 1.7.

Glucose Oxidase: Glucose oxidase (GOx) is a flavoenzyme with flavin adenine dinucleotide (FAD) as redox active group. It consists of two subunits having MW of 80 kDa each [20]. It is one of the most widely explored enzymes due to its high catalytic activity and stability. It catalyzes the glucose into gluconolactone, while the enzyme GOx itself is reduced from GOx(FAD) to GOx($FADH_2$). Structurally, it is a rigid glycoprotein with a molecular weight of 152000–186000 Da, with two identical polypeptide chains, each having a FAD redox center. It can operate in a wide pH range from 4 to 7 [21]. However, as the FAD moiety is deeply buried inside the protective protein shell as shown in Fig. 1.5, well-defined direct electro-

chemical behavior of GOx is challenging.

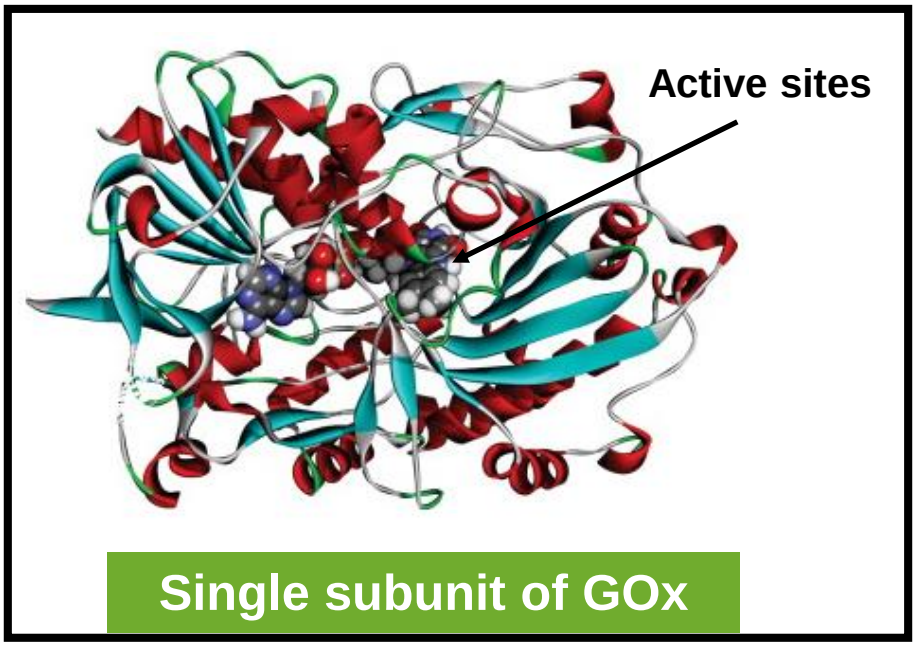

Fig. 1.5: **A single subunit of GOx with active site. Image taken from [21].**

1.3.1 Enzyme structure

Enzymes are three dimensional, complex, large molecules. These are proteins which consist of a number of amino acids joined by peptide bonds. The amino acid has two functional groups i.e. amine (-NH_2) and carboxylic acid (-COOH) that is why called amino acid. The protein formation take place when several amino group are connected by peptide bond. The peptide bond is a covalent bond between C of carboxylic acid group of one amino acid and N of amino group of another amino acid as shown in Fig 1.6. The sequence of amino acids (also called “residue") connected by peptide bonds leads to the formation of polypeptide chain [22]. Thus, enzymes are proteins of complex structures and their protein structure can be classified at four levels as shown in Fig. 1.7.

A detailed discussion of protein structure has been presented as follows:

1. **Primary structure:** The primary structure of protein is a linear sequence of amino acids as shown in Fig. 1.7. This protein structure is an important characteristic to define the three dimensional structure and retained catalytic activity of enzyme.

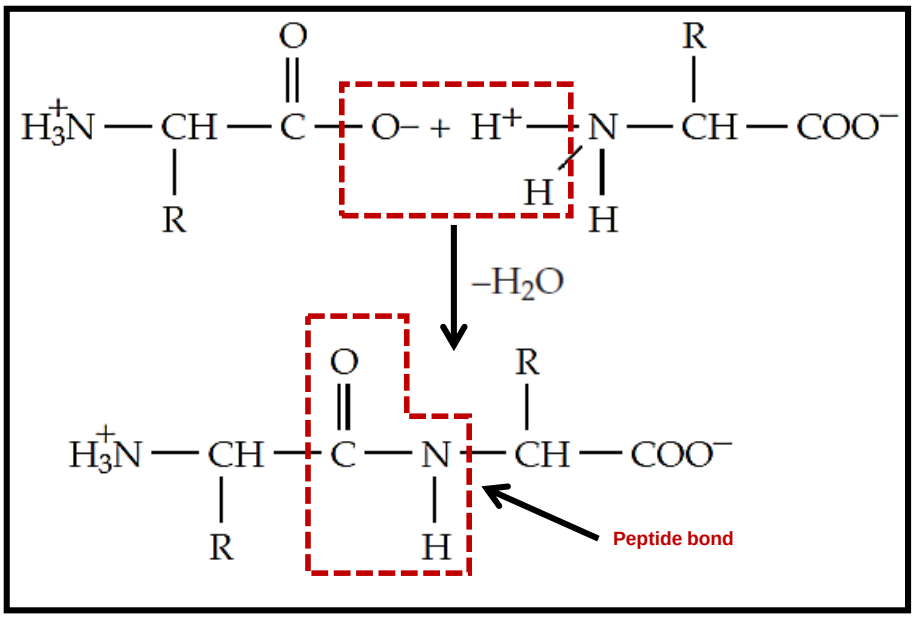

Fig. 1.6: **Peptide bond formation between amino acids.**

2. **Secondary structure:** The secondary structure of protein form when the linear sequence of polypeptide chain folds due to hydrogen bonding and forms three dimensional shape. The linear polypeptide chain can fold in the form of helix and sheets and are classified as α-helix and β-sheets. The α-helix structure folds in the helical form and it is formed due to hydrogen bonding between the oxygen of carboxylic acid and the hydrogen of N-H group. The linkage of the residues happens between the four residues ahead of the one. Thus forms the helical structure. It defines the three dimensional conformational changes in the protein structure. The β-sheets are made when the hydrogen bond forms between the two or more polypeptide strands. Based on the two strands ending, it can be parallel or anti-parallel. In parallel β-sheets structure, both the polypeptide strands have same amino to carbonyl direction while in antiparallel β-sheets, both the strands endings are opposite. In addition to these structures, β-turns have also been present at the end of β-sheets due to 180 degree turn in polypeptide chain which has been stabilized by hydrogen bonding.

3. **Tertiary structure:** The tertiary structure is formed by folding of secondary structures due to electrostatic interactions between oppositely charged species. It is folded into local conformation resulting in protein sub-units. There can be infinite types of protein structures in tertiary form. The most

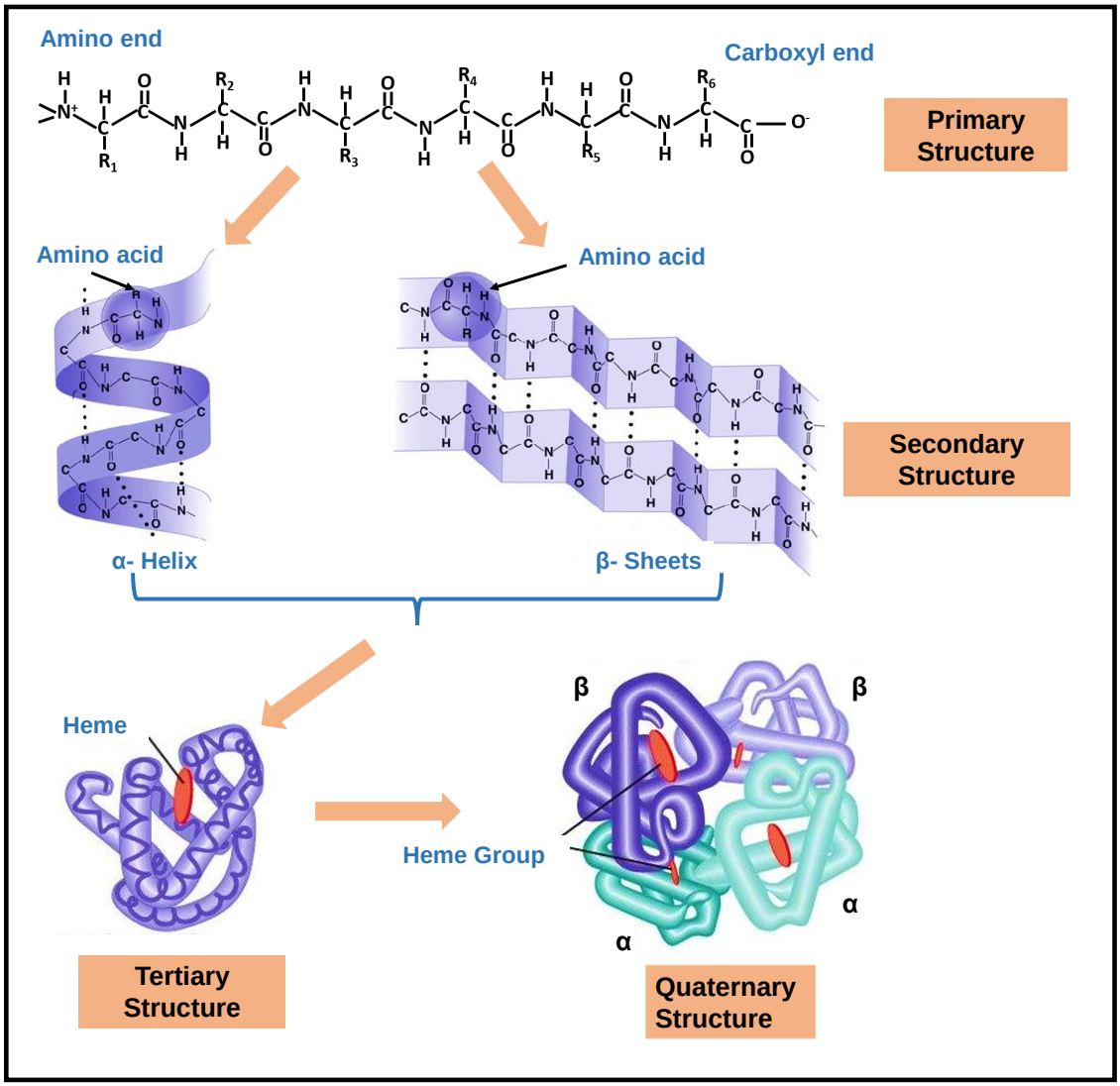

Fig. 1.7: **Levels of Protein structure. Image taken from [23].**

common structures are α-helical proteins and anti-parallel structures depending on the fundamental secondary structure involved.

4. **Quaternary structure:** Many of the tertiary structures (protein subunits) fold to form the quaternary structure. These subunits can be identical or non-identical which forms a more complex structure of protein [23].

1.3.2 Enzyme kinetics

The enzyme kinetics have been defined as the rate of enzyme catalyzed reactions. A schematic representaion of enzyme kinetics has been presented in Fig. 1.8. When the Enzyme (E) is added to the Substrate (S), it binds with the specific substrate via the active site and makes enzyme-substrate (ES) complex [24]. The enzyme-

substrate complex finally produces the product (P) when the reaction is complete. This phenomena has been explained by the Michaelis-Menten model for a simple

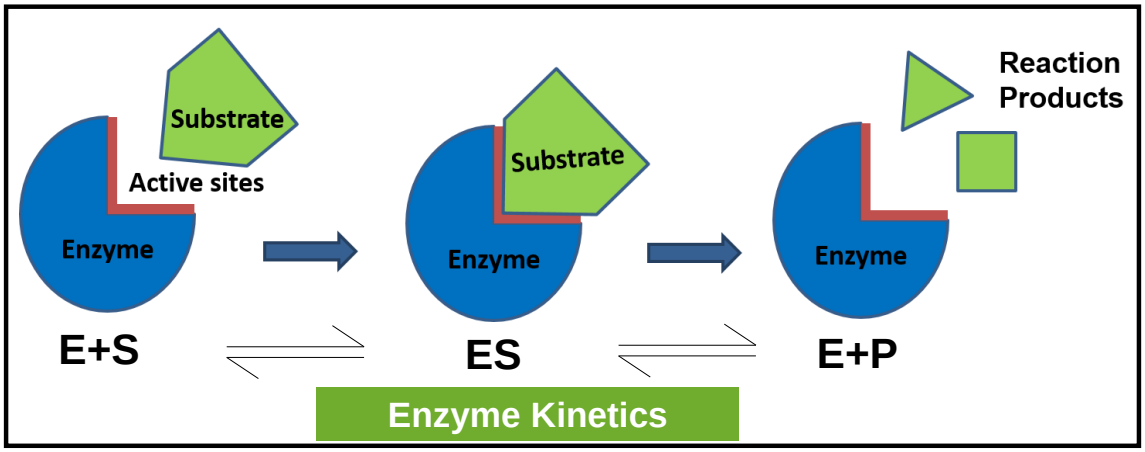

Fig. 1.8: **Schematic illustration of enzyme substrate reaction. Image taken from [25].**

enzymatic reaction as given below:

$$E + S \underset{k_{-1}}{\overset{k_1}{\rightleftharpoons}} ES \xrightarrow{k_2} E + P \tag{1.1}$$

Where, E is enzyme, S is substrate, P is product of the reaction, k_1, k_{-1}, and k_2 defines the reaction rate constants. The formation of intermediate constant is reversible for most of the enzymes. In this reaction, the enzyme has not been consumed as clear from equation 1.1. When a reaction consists of intermediate steps then the overall reaction rate is determined by the step which has the highest activation energy and characterized as "rate-limiting step". Figure 1.9 has shown the progress of chemical reactions without and with enzyme. As depicted in Fig. 1.9 that with the help of enzyme the progress of enzyme catalyzed reactions reduces the activation energy which enhances the rate of a biochemical reaction. In 1913 Leonor Michaelis and Maud Menten derived the rate equation using steady state approximation to understand the enzyme kinetics. Which has described that the enzymatic reaction quickly reaches a steady state i.e. the concentration of ES remains constant. The other important consideration was that the amount of enzyme (E_0) in the system is constant and equal to sum of free enzyme (E) in the system and enzymes used up in the enzyme-substrate (ES) complex. According to the steady state approximation: Rate of formation of ES = Rate of consumption of ES

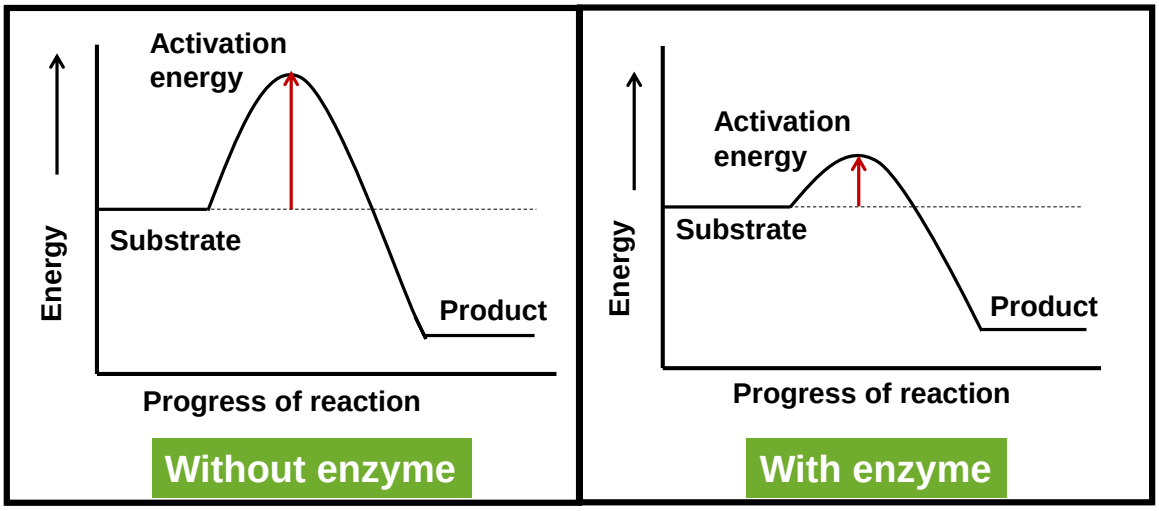

Fig. 1.9: **Enzyme facilitated reduction in activation energy (EA).**

$$k_1[E][S] = k_2[ES] + k_{-1}[ES] \tag{1.2}$$

Total amount of enzyme:

$$[E_0] = [E] + [ES] \tag{1.3}$$

Using equation 1.3 and 1.2 we get,

$$k_1[E_0][S] - k_1[ES][S] = k_2[ES] + k_{-1}[ES] \tag{1.4}$$

$$=> [ES] = \frac{k_1 E_0[S]}{k_1[S] + k_2 + k_{-1}} \tag{1.5}$$

Finally, according to reaction 1.1 rate of formation of P is,

$$k_2[ES] = \frac{k_1 E_0[S]}{(\frac{k_{-1}+k_2}{k_1}) + [S]} \tag{1.6}$$

Thus the relation between initial reaction rate and substrate concentration is given as follows:

$$V_0 = \frac{V_{max}[S]}{K_m + [S]} \tag{1.7}$$

Where, V_0 is initial reaction rate, V_{max} is maximum value of V_0 and K_m is Michaelis-Menten constant.

According to this equation, the reaction rate and substrate concentration are defined by hyperbolic relation known as Michaelis-Menten equation. It is evident from equation (1.7) that for lower substrate concentration, the reaction rate is di-

rectly proportional to the substrate concentration following the first order kinetics as shown in Fig 1.10. When the substrate concentration is higher, the reaction rate becomes independent of substrate concentration which shows that all the active sites of enzymes have been occupied by substrate molecules and define the zero order kinetics or saturation kinetics. The value of K_m is the half of the maximum reaction rate V_{max}. To define the enzyme kinetics, K_m and V_{max} are two important parameters where K_m defines the enzyme affinity towards the substrate which shows how rapidly enzyme binds to the substrate and reaches V_{max}. K_m represents a special characteristic of enzyme towards the substrate and its value should be as low as possible [26]. Although, it is challenging to calculate the value

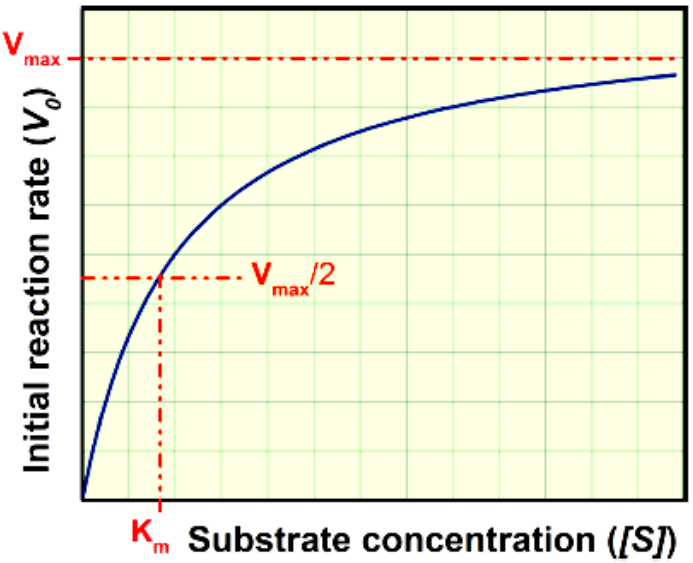

Fig. 1.10: **The effect of substrate concentration on the initial reaction rate of an enzyme catalyzed single substrate reaction.**

of K_m from equation (1.7), therefore various methods such as Hanes–Woolf plot, Eadie–Hofstee diagram, and Lineweaver–Burk plot etc. have been suggested to evaluate K_m value by linear transformation of equation (1.7). Mostly, Lineweaver Burk transformation has been accepted to calculate these values. In this method, the reciprocal of Mechaelis- Menten equation is taken as shown in equation (1.8) and a plot between $1/V_0$ and $1/[S]$ gives a straight line. The slope, y-axis intercept and x-axis intercept of the straight line gives the value of K_m/V_{max}, $1/V_{max}$ and $-1/K_m$ respectively as depicted in Fig. 1.11. Additionally, other transformations of Michaelis-Menten equation have also been presented for estimation, such as Hanes

equation (Equation 1.9) and Eadie-Hofstee equation (Equation 1.10).

$$\frac{1}{V_0} = \frac{K_m}{V_{max}}\frac{1}{[S]} + \frac{1}{V_{max}} \tag{1.8}$$

$$\frac{S}{V_0} = \frac{[S]}{V_{max}} + \frac{K_m}{V_{max}} \tag{1.9}$$

$$\frac{V_0}{[S]} = \frac{V_{max}}{K_m} - \frac{V_0}{K_m} \tag{1.10}$$

All these methods were prone to errors since unrealistic assumptions were made about the distribution of experimental errors. The Lineweaver Burk linear trans-

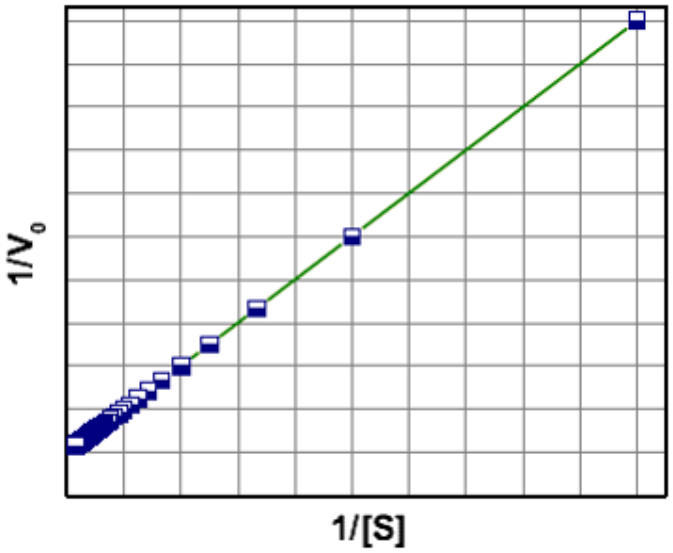

Fig. 1.11: **Lineweaver Burk plot.**

formation leads to the unequal distribution of data points resulting in cluttering of the data points near the origin for high substrate concentration as shown in Fig. 1.11 which causes the erroneous results. Similar problems occur with other linear transformations as well. Thus, a simple graphical method, direct linear plot had been proposed by Eisenthal and Bowden. This method does not require any mathematical calculations since all the observations are represented by a straight line in K_m-V_{max} space [27] as shown in Fig 1.12. The Michaelis Menten equation was converted in the form of equation (1.11), i.e. a straight line equation in K_m-V_{max} space with intercepts at –[S] and V_0 respectively.

$$\frac{V_{max}}{V_0} - \frac{K_m}{[S]} = 1 \tag{1.11}$$

For all observations ([S], V_0) straight lines were drawn in K_m-V_{max} space according to equation (1.11). These straight lines intersect at a common point which gives the values of K_m and V_{max}. A unique intersection point is difficult to obtain because of observational errors. Therefore, median of all the intersection points gives the best-suited value of K_m.

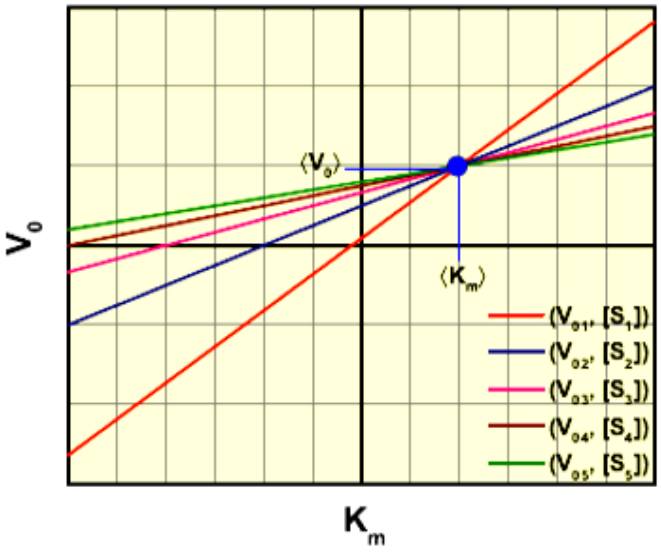

Fig. 1.12: **Direct linear plot.**

1.4 Enzyme Immobilization

Enzyme immobilization i.e. attachment of enzymes to electrode surface so that enzymes do not get denature and leach out of the support matrix. Enzyme immobilization plays an important role in fabrication and performance of biosensors which defines the storage stability, selectivity, and reproducibility of the biosensor. The catalytic activity of the enzyme is very much dependent on the microenvironment (pH, temperature, etc.). After the immobilization the enzymes should retain their structure, their function, their catalytic activity and should be tightly bonded to the surface of the electrode so that it should not desorb from the electrode during the use. The retained catalytic activity and stability of enzymes defines the long-term usability of the biosensor [28]. Thus the mode of enzyme immobilization is very critical for development of biosensors with high sensitivity and stability. There have been reported various successful enzyme immobilization strategies, broadly classified into four categories *viz.* physical adsorption, cross-linking,

covalent binding, and co-entrapment as shown in Fig. 1.13. Each immobilization technique has its own merits and demerits. The selection of suitable strategy depends on the enzyme structure, support matrix, and transduction method i.e. mode of detection. For practical applications, the required stability, sensitivity, reproducibility, complexity of immobilization, and cost of the biosensor are some of the important parameters which define the appropriate choice of enzyme immobilization method. One of the most important aspect during immobilization is the availability of the active site of the enzyme to the substrate. The different immobilization techniques are as follows:

1. **Physical Adsorption:**

   This is the simplest immobilization method where the enzymes are directly attached to the support matrix via weak bonds such as Van der Waal's forces, electrostatic interaction or hydrophobic interaction as shown in Fig. 1.13. In this method either the enzyme solution is dropped over the supporting electrode surface or the electrode is dipped into the enzyme solution. The adsorption process takes place at interface of the solid support matrix and enzyme due to electrostatic interactions between the polycationic matrix of the polymer and the negatively charged enzyme (enzyme has a net negative charge, at a pH higher than its isoelectric point). The adsorbed enzyme electrode is required to store for a period of time and finally the electrode is washed into the buffer solution to remove the unadhered enzyme molecules. In this case, the enzymes loosely bind to the electrode surface and can easily leach out from the support matrix due to weak forces involved. Thus, very less amount of enzyme gets adsorbed onto the supporting electrode. Additionally, no chemical change takes place when enzymes are physically adsorbed leading to the retained catalytic activity of enzymes.

2. **Covalent Binding:**

   Immobilization by covalent binding requires the modification of support matrix surface by a functional group for attachment of enzymes. In this method, covalent bond forms between the functional group of the enzyme and the functional group of the modified supporting electrode surface. Due to the strong interaction between enzyme and the support matrix, this method re-

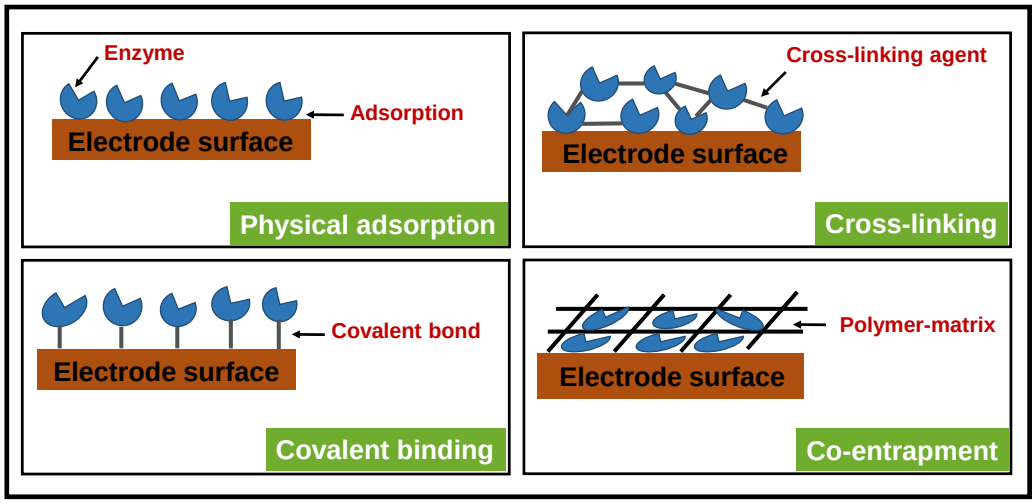

Fig. 1.13: **Schematic of enzyme immobilization techniques. Image taken from [29].**

duces the probability of leakage of immobilized enzymes from the matrix. However, the enzyme activity loss owing to the chemical changes is one of the major disadvantage of this method.

3. **Cross-linking:**

   In this approach, enzymes are immobilized via a bi- or multi-functional agents or crosslinking agents such as glutaraldehyde, glyoxal, or hexamethaylenediamine. The enzymes are crosslinked with each other via covalent bond formation along with the covalent bond formation with the support matrix. This process is performed either in the presence of functionally inert stabilizer such as Bovine Serum Albumin (BSA) or cross-linked with each other. The immobilization of the enzymes utilizing a crosslinking agent has been considered an attractive method due to its simplicity and strong chemical bond formation between the enzymes which can facilitate higher enzyme loading. However, this method is prone to the chemical changes in the enzyme structure which can lead to the enzyme activity loss.

4. **Co-entrapment:**

   This method has been utilized for three-dimensional matrices such as an electropolymerized film, a silica gel, or a carbon paste. Immobilization via this process requires enzymes to be mixed with the monomer solution and they gets attached to the polymer matrix during the polymerization via electrostatic binding. In this method no chemical change take place in enzyme caus-

ing the retained activity of enzymes. However, this method requires a large amount of enzyme for efficient enzyme loading over the support matrix and is also very sensitive to pH of the monomer solution. One of the major drawbacks of this method is that during polymerization the enzymes get buried deep within the polymer matrix causing a reduced response time of the fabricated biosensor due to the delayed interaction between enzyme and substrate molecule.

1.5 Support Matrix for Enzyme Immobilization

The choice of support matrix for enzyme immobilization is one of the most critical aspects as it directly affects the enzyme activity, orientation, enzyme loading which influence the biosensor performance. Thus, immobilization of enzyme molecules without harming the activity and specificity is of fundamental importance for the fabrication of biosensor. Considering all the factors, the support matrix should have the following characteristics:

1. The support matrix should be biocompatible i.e. non-toxic.
2. It should be cost-effective and eco-friendly.
3. It should facilitate higher surface area so that higher enzyme loading can be obtained.
4. It should expose the active site of the enzyme after the immobilization process.
5. It should have high electro-activity and should be stable in environmental conditions.

1.5.1 Conducting Polymer Nanostructures: As support matrix

Conducting polymers are carbon based materials which have alternate single and double bond along the polymer chains. The alternate single and double bond are responsible for the conduction in these materials [30]. They can be synthesized by chemical, physical, and electrochemical methods. Amongst all, electrochemical polymerization is the simplest technique for synthesis of CPs. The conductivity of

these materials can be easily tuned via doping and dedoping process based on the electrochemical synthesis condition [31]. Additionally, CPs are compatible with biological molecules and thus can be used to entrap the enzymes at the electrode surfaces. Thus, having all the required properties, CPs have been proved to be a suitable support matrix for the enzyme immobilization. In this regard, various CPs *viz.* Poly(3,4-ethylene dioxythiophene), Polythiophene, Polyaniline, Polypyrrole, etc. have been employed a support matrix for fabrication of high sensitivity and high selectivity glucose biosensor. Nanostructured materials exhibit narrow

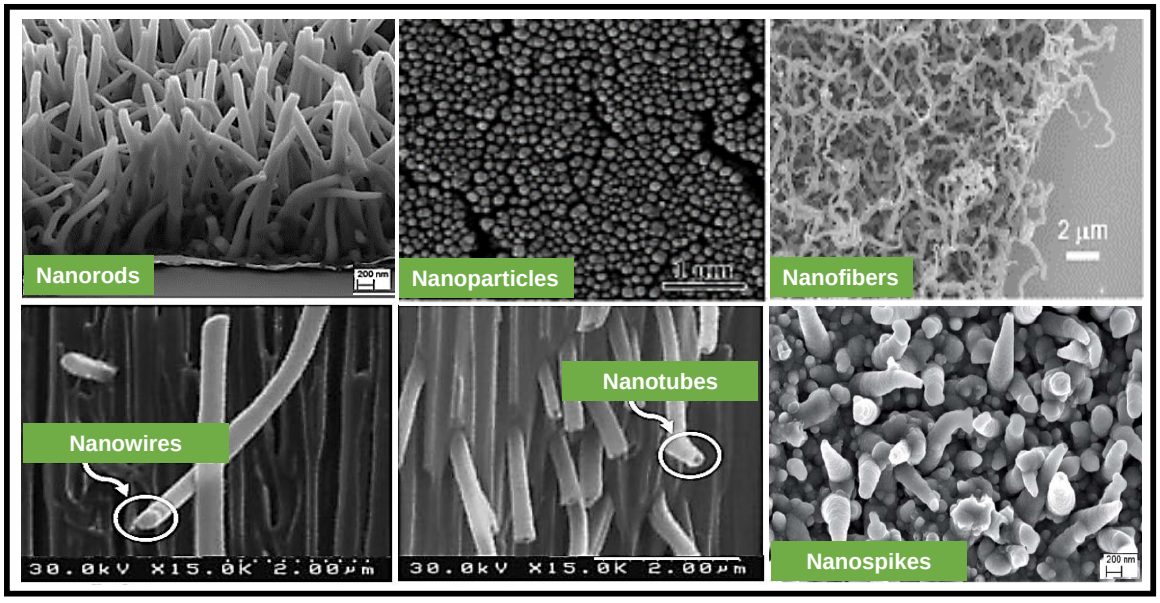

Fig. 1.14: **FESEM images of different nanostructures. Image taken from [32–34].**

dimensions and high surface to volume ratio which are advantageous for the development of biosensing devices at nanoscale. The higher surface area of support matrices offers the enhanced interaction between the material and the biomolecules which majorly increases the enzyme loading and improve the sensitivity of biosensor. Additionally, the nanoscale dimensions improve catalytic activity. In this regard, nanostructures of CPs have been attractive due to their unique chemical, biochemical, and improved electronic properties as compared to the bulk counterpart. Some of the well-reported CPs nanostructures have been shown in Fig. 1.14. 1-D CPs nanostructures *viz.* nanowire, nanotubes, nanofibers, etc. have received great interest due to their higher surface area, electrical conductivity, and biocompatibility.

1.5.2 Polypyrrole

Among the so far explored various CPs, Polypyrrole (PPy) is one of the most extensively utilized CP for biosensor fabrication due to its easy synthesis, high electrical conductivity, thermal stability, extraordinary redox behavior, and biocompatibility [32]. PPy is an organic polymer, synthesized by polymerization of Pyrrole (Py) monomer. Py is a heterocyclic aromatic compound having five membered ring with the chemical formula C_4H_5N. Figure 1.15 has shown the aromatic ring model of Py monomer. Polypyrrole can be synthesized easily via chemical or electro-

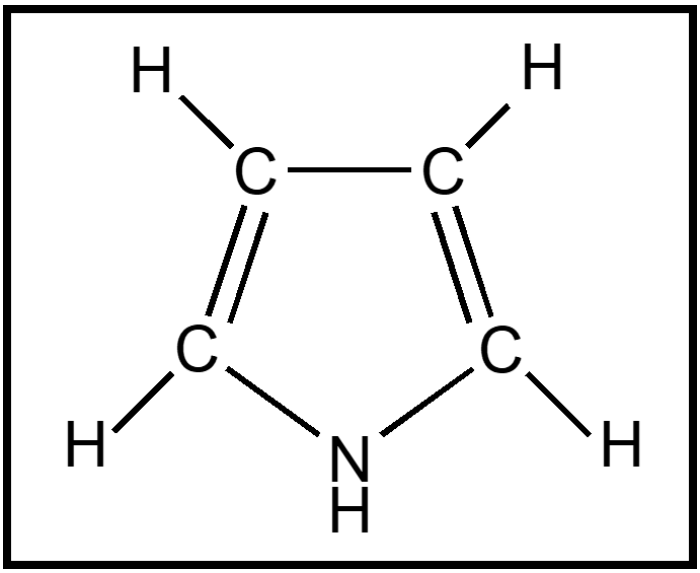

Fig. 1.15: **Heterocyclic aromatic structure of Py monomer. Image taken from [35].**

chemical methods in various organic as well as in aqueous media due to its good solubility. It has low oxidation potential which makes it convenient to synthesize via electrochemical method under mild conditions such as low oxidation potential, neutral pH of electrolyte solution, etc. The most developed PPy nanostructures are nanotubes, nanowires, nanofibers, etc. which have found potential applications in solid electrolytic capacitors, energy storage devices, gas sensor, electrochemical batteries, biosensor, microactuators, electrochromic windows and displays.

Synthesis of Polypyrrole- Electropolymerization method

CPs can be synthesized by chemical or electrochemical polymerization method. Among these, electropolymerization is the simplest and one step deposition method which facilitates the growth of CPs directly onto the electrode surface.

However, in case of chemical polymerization, it requires an oxidative species and produces the powdery form of CPs which further needs to be deposited onto the electrode surface for biosensor application [36]. Additionally, electropolymerization provides the reproducible CP coatings over the electrode surfaces. The thickness of these materials can be easily controlled by varying electrochemical synthesis conditions [34].

1.6 Transduction Methods

In a biosensor, the transducer is attached to the bio-recognition layer. The transducer converts the bio-recognition event i.e. interaction between biomolecule and analyte into a measurable electrical signal proportional to biomolecule and analyte interaction. Based on the biological reactions (interaction between analyte and biomolecules) which can be either physical, chemical, or biological changes, the transduction methods have been classified as follows:

1. **Optical:**
   The optical transduction method utilizes the changes in the optical properties such as absorption, fluorescence, chemiluminescence, refractive index, etc. upon interaction of the analyte and biomolecules. When the analyte molecule interacts with biomolecules it results in change in refractive index. The change in refractive index causes a variation in propagation constant of incident wave. The variation of absorption is measured. Moreover, chemical reactions result in luminescence causing in the emission of light at the end of reaction which has been detected [37]. This method requires complex systems and additional instrumentation and has low quantitative accuracy.

2. **Calorimetric (Thermometric):**
   In this method, the biological reactions are associated with either the generation or absorption of heat. The change in the temperature between the substrate and product due to interaction between substrate and biomolecules is determined by using temperature sensors such as thermistors. The amount of heat generated is proportional to the amount of reactant and product consumed. In this type of method, it is difficult to maintain the constant temperature of substrate.

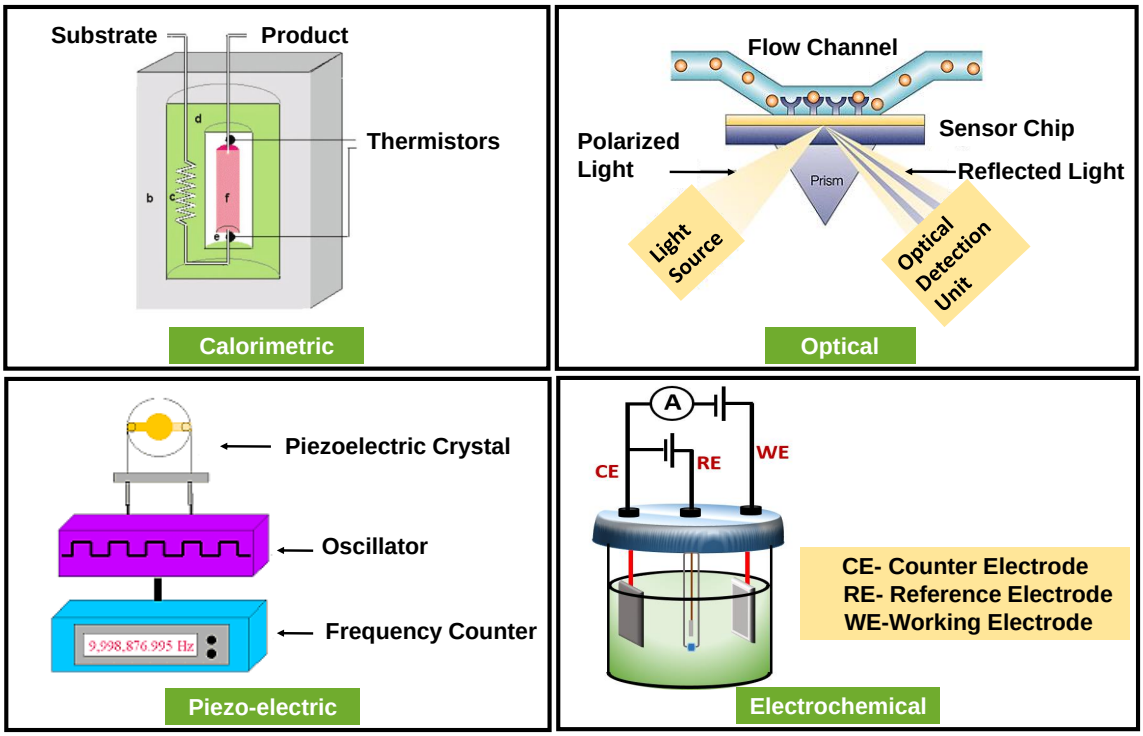

Fig. 1.16: **Transduction methods.**

3. **Piezo-electric:**

   The piezo-electric transduction method involves the attachment of biomolecule to a piezoelectric material which generates a potential when mechanical stress is developed. The piezo-electric crystals vibrate at a characteristics frequency called resonance frequency. This resonance frequency changes with the adsorption of analyte molecules on the piezo-electric crystal surface. This shift in the resonance frequency can be related to the mass of analyte [38]. The main drawbacks of this type of transduction methods are lack of sensitivity and specificity.

4. **Electrochemical:**

   This is one of the simplest transduction methods. The electrochemical transduction methods are based on the measurement of electrical signal due to the redox chemical reaction between analyte and biomolecules which are very specific for the analyte molecule detection. In this method, the bio-recognition layer is in direct spatial contact with the transducer surface. According to the type of the measured electrical signal in electrochemical reaction, it can be classified into four types as amperometric (measurement of current as a function of time), potentiometric (measurement of potential as

a function of time), impedometric (conductivity detection with electrical frequency variation), and conductometric (based on conductivity of electrolyte solution) transduction methods. Among these methods, the amperometric and impedometric measurements can be performed by using three electrode cell while the other two can be performed by the two electrode cell system. The electrochemical transduction method has many advantages such as simplicity, high sensitivity, response time, low cost, high specificity, and simple instrumentation [39, 40]. Therefore, in this work, electrochemical transduction process has been used for the detection of bio-recognition event.

1.7 Principle of Enzymatic Electrochemical Detection

In principle, amperometric electrochemical transduction method has been widely explored and attracted substantial interest for detection of glucose due to its simplicity and high sensitivity. In enzymatic glucose biosensors, Glucose oxidase (GOx), a model enzyme has been immobilized over the support matrix which makes the surface specific towards the glucose. It has Flavin Adenine dinucleotide (FAD) as active center which should be exposed to the glucose solution for the catalysis. Further, the GOx immobilized electrode has been utilized as a working electrode for the detection of glucose by amperometric transduction method. Equation (1.12-1.14) presents the basic principle of operation of amperometric glucose biosensor:

$$C_6H_{12}O_6 + GOx(FAD) + H_2O \longrightarrow C_6H_{12}O_7 + GOx(FADH_2) \tag{1.12}$$

$$GOx(FADH_2) + M \longrightarrow GOx(FAD) + M_{red} \tag{1.13}$$

$$M_{red} \xrightarrow{V} +2e^- + M_{ox} \tag{1.14}$$

The immobilized GOx catalyzes the oxidation of glucose ($C_6H_{12}O_6$) into gluconic acid ($C_6H_{12}O_7$) and the enzyme gets reduced itself in this reaction. Further, the reduced GOx($FADH_2$) oxidizes by a mediator or electron acceptor which is represented as M_{ox} in equation 1.13. The regeneration of GOx(FAD) in the presence of a mediator is very important for the reaction, otherwise the reaction will cease once the enzymes are consumed. Additionally, in the reaction with the regeneration of

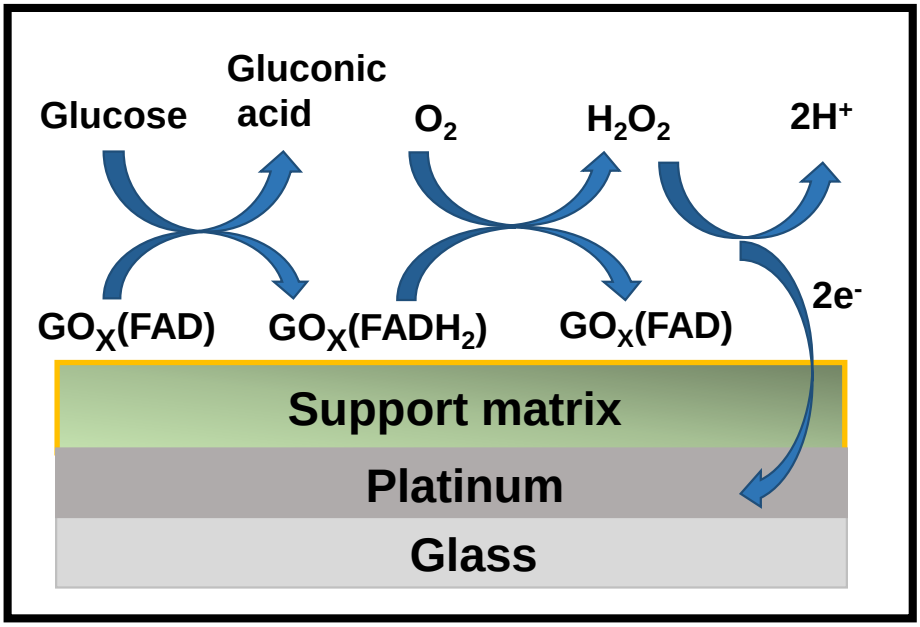

***Fig. 1.17:* Schematic of amperometric enzymatic detection of glucose.**

GOx(FAD), M_{red} produces as a by-product. This by-product can again be oxidized with the application of sufficient potential to the electrode which results in ions and electrons. Thus, the generated electrons produce a current proportional to the glucose concentration [4, 5]. Figure 1.17 shows the schematic of amperometric detection of glucose where the physiological oxygen act as the mediator. With the continuous evolution in technology since the development of glucose biosensors, they have been classified in three generations [20] (shown in Fig. 1.18) based on the nature of "M" which are as follows:

1. **First generation:**

   In first-generation glucose biosensor physiological O_2 has been utilized as "M_{ox}" to re-generate GOx(FAD) and detection of glucose is performed by monitoring either the consumption of O_2 or generation of H_2O_2. In this type of detection, the O_2 concentration plays an important role since the normal O_2 concentration in the physiological fluids is one order less than that of glucose which creates "oxygen deficit" condition. Thus, the upper limit of linear range and sensitivity of first generation biosensors' are majorly influenced by this problem. To overcome this situation diffusion biocathode is used [41]. Moreover, the measurement of H_2O_2 has to be performed at a high potential at which other electroactive species, such as ascorbic acid and uric acid can be oxidized resulting in erroneous results. The interference of these species

can be reduced either by decreasing the required H_2O_2 oxidation potential or by using permselective film.

2. **Second generation:**

   The limitations in first generation glucose biosensors were tried to reduce by replacing the O_2 with artificial mediators for regeneration of GOx(FAD). The mediator is either directly attached to the enzyme or it is present in the solution and were able to transfer the electrons between the FAD center and the electrode surface by the following scheme:

$$C_6H_{12}O_6 + GOx(FAD) + H_2O \longrightarrow C_6H_{12}O_7 + GOx(FADH_2) \tag{1.15}$$

$$GOx(FADH_2) + M_{ox} \longrightarrow GOx(FAD) + M_{red} \tag{1.16}$$

$$M_{red} \xrightarrow{V} +2e^- + M_{ox} \tag{1.17}$$

   where M_{ox} and M_{red} are the oxidized and reduced forms of the mediator. The catalytic process as represented in equation (1.15-1.17), takes place in three steps. Firstly, the transfer of electrons from glucose to GOx(FAD) reducing it to GOx($FADH_2$), then a reduced mediator is formed instead of hydrogen peroxide and finally with the application of potential to the electrode, M_{red} reoxidizes to M_{ox} at the electrode, generating the current proportional to glucose concentration. Some of the widely utilized artificial electron mediators are ferricyanide, ferrocene derivatives, quinone compounds, or conducting organic salts (particularly tetrathiafulvalene tetracyanoquinodimethane, TTF-TCNQ) etc. The measurements become independent of oxygen partial pressure by using these electron mediators and the detection can be performed at lower potentials which eliminates the interference effect of coexisting electroactive species. The major drawback of these sensors is the competition between the mediator and physiological oxygen for oxidation of the reduced GOx, which results in the accumulation of hydrogen peroxide near the electrode surface leading to reduced bioactivity of enzyme and biosensor response.

3. **Third generation:**

   Third generation biosensor involves the direct electron transfer between en-

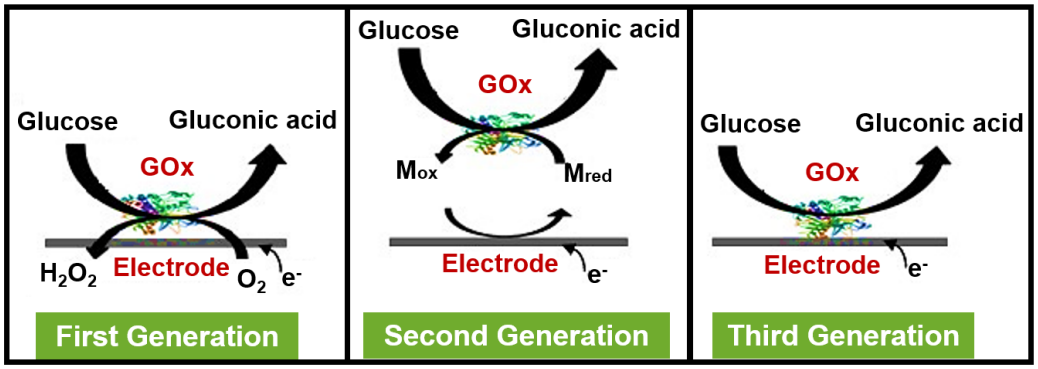

Fig. 1.18: **Three generations of enzymatic amperometric glucose biosensor. Image taken from [41].**

zyme and electrode without any mediator. The detection can be performed by using the three dimensional network of organic conducting polymer which is attached to GOx resulting in high and faster response current. Additionally, due to the direct attachment of GOx, the detection can be performed at lower electrode potential which improves the selectivity of the biosensor. The direct electron transfer between enzyme active site and electrode surface depends on the distance between the two and the long electron-tunneling distance were made to realize the direct electrochemistry of enzymes. In this regard, electrical wiring of redox enzymes with electrodes is an effective method. Though, the complex procedure inhibits its wide use in practice. Although well-defined voltammetric peaks of direct electrochemistry of GOx have been defined in various studies, the detection of glucose based on the direct electron transfer of GOx, need mediators to catalyze the oxidation of glucose. In addition to this, the direct electron transfer between the deeply buried redox active center of the enzyme and the electrode surface involves the conformational change of the enzyme, which can cause the enzymatic activity loss. Therefore, the third generation amperometric glucose biosensors have a long way to go in this respect.

At present, mostly first and second generation glucose biosensor have been developed successfully. The unique properties of nanostructures are being utilized to improve the figure of merits of glucose biosensor where, number of glucose biosensors based on different nanostructured materials like polypyrrole, carbon nanotubes (CNTs), metal nanoparticles, etc. have been developed.

1.8 Review of Past Work

The extensive research efforts towards the development of efficient and high-quality glucose biosensor with high sensitivity, selectivity, response time, linear range with low cost have increased continuously. In this regard, numerous variations in the fabrication of biosensors such as appropriate support matrix, growth techniques, and immobilization techniques have been explored. The field of enzymatic biosensors utilizing conducting polymers as support matrix has been explored exhaustively. These materials have unique physical, chemical and electrical properties in nano-regime which leads to high sensitivity and fast response. Different 1-D nanostructures of Polypyrrole (PPy) such as nanofibers, nanotubes, nanorods, and nanowires have received great attention as a possible alternative for support matrix towards the biosensor fabrication [2, 42–44]. Nanostructures of PPy can be easily synthesized by electrochemical polymerization which is a straightforward, simple, cost-effective, and reliable approach. Electro-synthesis of the polymer can be performed using two approaches: Template-based [7, 45–47] and Template free method [32, 34, 48–50]. The template-based method first utilized by Martin et al. [51] in the year 1995, has received considerable attention over the years due to its controllability and widespread applications. Some of the Porous materials such as anodic aluminum oxide (AAO), Zeolite channels, particle track-etched membranes, etc. have been utilized as hard templates. Additionally, the soft templates such as micelles, surfactants, liquid crystals, etc. have been utilized [52]. The growth of nanotube or nanowire arrays along the porous walls of the Anodisc^{TM} is highly dependent on the experimental conditions such as monomer and supporting electrolyte concentrations, applied potential or current density, polymerization duration etc. Xiao et al. [53] studied the growth of various conducting polymers using porous alumina templates and concluded that low monomer concentration and high polymerization potential is required for growth of polymer nanotubes. Ekanayake et al. [54] have fabricated PPy nanotubes based glucose biosensor and the sensitivity of the biosensor was 4.45 mA-cm^{-2}-M^{-1} with a response time of 8 s and a linear range from 0.5 to 16 mM. PA Palod et al. [55] have synthesized PPy nanotubes using AAO as the template and studied the effect of immobilization techniques on the performance of glucose biosensor. They

reported the sensitivity of fabricated biosensor as 18.6 mA-cm^{-2}-M^{-1} in a linear range of 0.25-25 mM by using physical adsorption of GOx over PPy nanotube. With crosslinking, the sensitivity was around 72 mA-cm^{-2}-M^{-1} [56]. G. Xu et al. [57] have fabricated PPy nanowires in AAO template for glucose biosensor and reported the sensitivity as 9.97 mA-cm^{-2}-M^{-1} in a linear range of 0.1 mM to 8 mM. Many other reports in the literature have mentioned the application of templates for biosensor fabrication. The electropolymerization using templates requires multiple complicated steps which make it tedious, complex, time-consuming and expensive. Additionally, the templates necessitate careful handling during and after fabrication. Further, removing the hard templates of diameters less than 100 nm after polymerization may often affect the structure, alignment, and properties of the polymer nanostructures which increases the complexity and overall cost of the biosensor fabrication [52]. The growth of nanostructures without using any template is attractive as well as a challenging field of research. In this respect, a template-free method for fabrication of nanostructured conducting polymer with controlled size and morphologies was developed for utilization as a support matrix in the biosensing device applications. The electrospinning technique which has been primarily used for the synthesis of various CPs nanofibrous networks is relatively easier and compatible for large area fabrication. However, it requires the application of a very high potential to the polymer solution. It also suffers from the use of additives which alter the properties of the nanofibers fabricated using conducting polymers. Thus, another interesting template-free fabrication method for the development of the nanofibrous network has gained attention due to its low cost, large scale fabrication, easy synthesis process, etc. Zang et al. [32] have synthesized super hydrophilic 1-D PPy nanofibers network and explained the favorable experimental conditions for the formation of the same. Liao et al. [48] also fabricated vertically aligned PPy nanofibers on the titanium surface, with the length of 500 nm and explained the effect of polymerization time on nanofibers length. Fakhry et al. [34] fabricated different morphology of PPy from nanowires to nanofiber network. Palod et al. [52] synthesized PPy nanofibers based glucose biosensor using physical adsorption of GOx. The sensitivity of the as-fabricated biosensor was reported to be 1.9 mA-cm^{-2}-M^{-1}. Additionally, the nanocomposites of PPy with carbon nanotubes, metal nanoparticles, graphene oxide have also been

reported a suitable candidate for glucose biosensor fabrication. B. K. Shrestha et al. [58] have synthesized Polypyrrole doped well dispersed functionalized carbon nanotubes and reported excellent electrocatalytic activity of the hybrid electrode for the same. T. C. Gokoglan et al. [42] fabricated a paper-based glucose biosensor utilizing graphene oxide and gold nanoparticles with PPy and reported the improved sensitivity of 7.357 mA-cm^{-2}-M^{-1}. G. Xu et. al. [45] demonstrated the modification of PPy with gold nanoparticles and demonstrated a sensitivity of 34.7 mA-cm^{-2}-M^{-1}. Raicopol et al. [59] utilized PPy-carbon nanotube (CNT) composite with GOx immobilization using entrapment. The fabricated biosensor exhibited a sensitivity of about 6 mA-cm^{-2}-M^{-1} with a linear range of operation from 0.002 to 6 mM. M. Z. Cetin et al. [60] also developed PPy nanofibers via electrospinning technique and utilized the PPy nanofibers for biosensor which has shown high sensitivity of 68.95 mA-cm^{-2}-M^{-1} in a linear range of 0.01-.4 mM biosensor. Though the PPy nanofibers were synthesized by electrospinning technique which is costlier as compared to the template-free method. The major objective of these studies was to obtain the high surface area nanostructures to improve enzyme loading thereby influencing biosensor figure of merits. Thus, synthesis of nanostructures with improved physical properties via low cost, amicable synthesis technique using simple instrumentation are desirable for biosensor device applications.

1.9 Objective of Present Work

The main objective of the present work is to investigate different factors influencing the morphology of PPy nanostructures synthesized via a simple, straightforward and cost-effective template-free electropolymerization method for enzymatic biosensor applications. Primarily, the high surface to volume ratio and electrochemical properties of PPy nanostructures have been explored to elucidate its effect on the glucose biosensor figure of merits. The morphology of PPy was varied by means of dopant concentration variation and the type of dopant which has been found to play the important role in higher surface area and reduced charge transfer rate thereby influencing the biosensor performance. The highlights of this work have been summarized as follows:

1. Effect of different dopants on the morphological variations of PPy with the

incorporation of DBSA, MeSA, pTSA, and $LiClO_4$ during electropolymerization process and optimization of growth conditions towards the improved performance of glucose biosensor by varying the concentration of $LiClO_4$.

2. The influence of two different dopants *viz.* $LiClO_4$ and pTSA on the glucose biosensor performance.

3. The fabrication of electrochemically synthesized Polypyrrole nanofiber array-based amperometric glucose biosensor with improved performance via crosslinking immobilization as compared to physical adsorption technique.

4. To study the effect of nanocomposite of PPy with ZnO on electrochemical properties of ZnO electrodes.

1.10 Organization of the Thesis

Chapter 1 describes a brief introduction of biosensors and electrochemical enzymatic detection. The discussion about diabetes, glucose as an analyte molecule, the importance of enzymes as chosen biomolecules, and PPy as a support matrix for enzyme immobilization has also been presented. The chapter also introduces enzymatic electrochemical detection which is one of the simplest approaches for analyte detection. The main objectives of research work for glucose detection in this thesis with a brief review of past work has also been discussed.
Chapter 2 presents a detailed discussion of experimental techniques and the characterization tools used for the research work.
Chapter 3 demonstrates the template-free electrochemical method for the fabrication of PPy nanostructures with the incorporation of DBSA, MeSA, pTSA, and $LiClO_4$ as dopants. Further, the influence of different dopants on the morphology of PPy nanostructures has been discussed followed by the study of $LiClO_4$ concentration variation on the performance of glucose biosensor.
Chapter 4 illustrates the systematic study of different dopant *viz.* p-TSA and $LiClO_4$ on the morphology and electrical properties of PPy nanostructures. The main purpose was to develop high surface area nanostructures with improved electrochemical properties for improving the figure of merits of glucose biosensor.

Chapter 5 describes the influence of different immobilization techniques for improvement in biosensor performance towards glucose detection. The two immobilization techniques such as physical adsorption and crosslinking immobilization were utilized with the aim to increase enzyme loading which in turn is prerequisite for improvement in biosensor figure of merits.

Chapter 6 demonstrates a preliminary investigation of a nanocomposite electrode of electropolymerized PPy over ZnO nanorods. The electrochemical properties on modification of ZnO with PPy have been discussed.

Chapter 7 summarizes and concludes the work with the future scope of the research work discussed in this thesis.

Chapter 2

Materials, Experimental and Characterization Techniques

This chapter includes the description of materials, experimental work carried out, and the characterization techniques utilized for the presented research work. The discussion starts with the introduction of materials followed by the fabrication method of the biosensor. Further, it includes the description of characterization techniques and their working principles utilized at different fabrication steps of the biosensor.

2.1 Materials

Pyrrole monomer (C_4H_5N), Sodium phosphate dibasic (Na_2HPO_4), Sodium phosphate monobasic (NaH_2PO_4), Dodecylbenzene sulfonic acid (DBSA), para-Toluene sulfonic acid (p-TSA), Methane sulfonic acid (MeSA), Lithium perchlorate ($LiClO_4$), Potassium ferricyanide/ferrocyanide $[Fe(CN)_6]^{3-/4-}$, Potassium Chloride (KCl), Potassium bromide (KBr), D-(+)-glucose, L-ascorbic acid, Uric acid, and Glucose oxidase (GOx) from Aspergillus niger (E. C. 1.1.3.4) were obtained from Sigma-Aldrich. All the chemicals were of analytical grade. Microscopic glass slides utilized for sample preparation were purchased from ABDOS Labtech private limited (India). Deionized water (DI) of 18 MΩ resistivity was used for the preparation of all aqueous solutions. 0.1 M Phosphate buffer solution (PBS) with pH 6.8 was prepared using NaH_2PO_4 and Na_2HPO_4.

2.2 Fabrication of Electrodes

In this work, the biosensor was fabricated using mainly three steps as follows:

1. Pt deposition over a cleaned glass substrate by the sputtering technique.
2. Electropolymerization of Polypyrrole over Pt-coated glass substrate.
3. Enzyme immobilization over electropolymerized PPy.

2.2.1 Pt deposition

Cleaning of Glass substrate

The glass slides typically 3 x1 inches and about 1 mm thick were used as the substrate. It is the most commonly used substrate for making samples because of its flatness, rigidity and its transparency in the spectral range of interest, i.e. ultraviolet, visible and near-infrared. The substrate of size 1 cm^2 was used for the sample preparation. The cleaning of substrate surface is an important step for good quality deposition, adhesion, growth of nanostructures and device performance. These substrates were cleaned to remove inorganic and organic impurities from their surfaces. The cleaning was performed in an ultrasonic bath of detergent in water and rinsed with deionized water. Followed by the sequential cleaning in ultrasonic baths of distilled water, acetone, and isopropanol for 10 min each. The high-frequency ultrasonic waves help to remove the settled dust particles from the substrate during the ultrasonic process. The cleaned substrates were then dried and placed in a desiccator.

Sputter deposition of Pt

The schematic of DC sputtering is shown in Fig. 2.1. The deposition of material by sputtering is allowed by creating a plasma between the electrodes in an ultra-high vacuum chamber. The system comprises of a pair of parallel metal electrodes, where target of the metal to be deposited act as the cathode. It is connected to the negative terminal of a DC power supply. The substrate onto which the deposition is to be performed is grounded and is placed facing the cathode. The system was

evacuated using a two-stage rotary pump and diffusion pump assembly. A working inert gas, typically argon (Ar) is introduced into the deposition chamber in a controlled manner using a mass flow controller (MFC) after evacuation of chamber. With the application of bias to electrodes, the intrinsic electrons and Argon ions are accelerated and further neutral Argon atoms are ionized with the influence of electrons and ions. The created plasma is easily visible as it shines blue/violet in case of an Argon plasma (control by eye) since impact processes transfer energy to the atoms (excited states/electrons) which relax radiatively. Electrons and Argon ions are further accelerated to the corresponding electrodes. The material to be deposited is fixed at the negative electrode (target) because the attack of Argon ions ablates material which accelerates towards the substrate attached at the positive electrode.

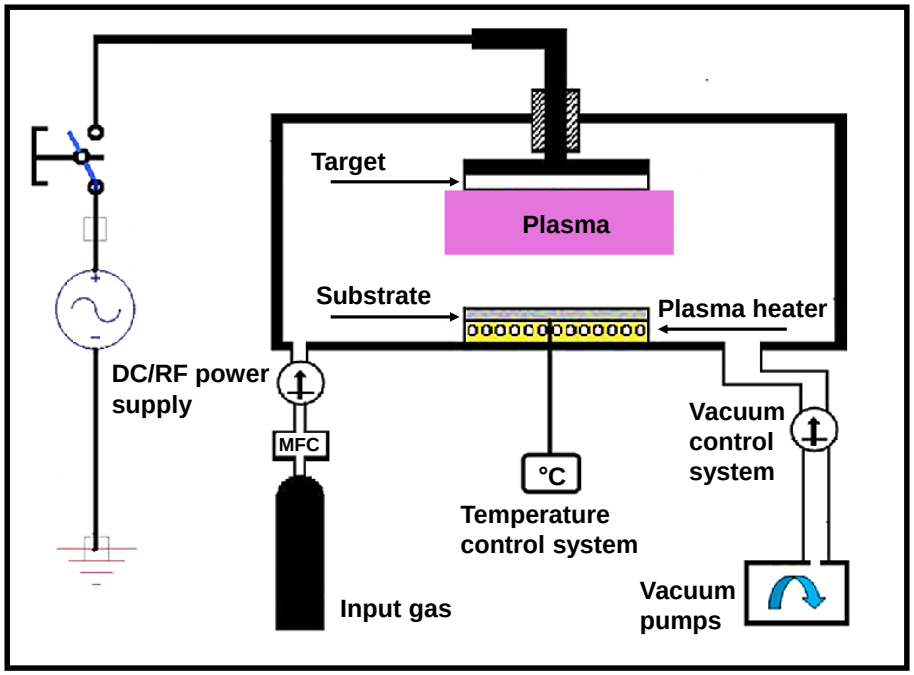

***Fig. 2.1:* Schematic of sputtering system. Image adapted from [61].**

In sputtering, the deposition of the material is very homogeneous (better covering of edges) due to the scattering with the plasma. The substrates were placed on the surface of a 2" diameter substrate holder and its distance with the target was maintained at 5.0 cm. After achieving the desired value of chamber pressure, the dc power of 50 W was applied to the target for generating the self-sustained plasma in the deposition chamber to start the film deposition. The deposition was performed at a base pressure of 1×10^{-6} mbar. A 50 nm thick layer of Pt was sputtered over

the cleaned samples with a 5 nm intermediate layer of Cr between glass and Pt. Cr layer was incorporated to improve the adhesion of Pt over glass [42]. Samples were rotated at a speed of 10 revolutions per minute (rpm) to ensure uniform deposition of Pt over the substrate.

2.2.2 Distillation of monomer

Distillation is one of the most commonly employed techniques for purifying liquids and separating mixtures of liquids into their individual components. It is a process of transformation of liquid phase to the vapour phase, then condensation back to the liquid phase with the collection of this liquid in a separate container. The basic principle of distillation is based on the difference in boiling points of the constituents of the mixture. At a particular temperature, some molecules of a liquid possess enough kinetic energy to escape into the vapor phase called evaporation and some of the molecules in the vapor phase return to the liquid called condensation. An equilibrium is set up, with molecules going back and forth between liquid and vapor phases. At higher temperatures, more molecules possess enough kinetic energy to escape, which results in a greater number of molecules in the vapor phase. When the vapor pressure of the liquid equals the applied pressure (for an apparatus that is open to the atmosphere the applied pressure equals atmospheric pressure), the liquid starts boiling. Thus, the boiling point of a liquid is the temperature at which its vapor pressure equals atmospheric pressure. Since at any given temperature, the vapor pressure of the lower-boiling compound will be greater than the vapor pressure of the higher-boiling compound. Thus, the vapor above the liquid will be richer in the lower-boiling compound, compared to the relative amounts in the liquid phase. Hence, distillation is a suitable technique for the purification of compounds (elements) having large differences in their boiling points.

Pyrrole is a colorless volatile liquid which darkens readily in air. Its boiling point is 130 °C and is usually purified by distillation immediately before use. The schematic shown in Fig. 2.2 presents the experimental setup for the distillation process. The flask containing the impure liquid (monomer + impurities) is heated up to the desired temperature (boiling temperature) using heating mantle. The vapours of monomer (having a lower boiling point than impurities) rise in column

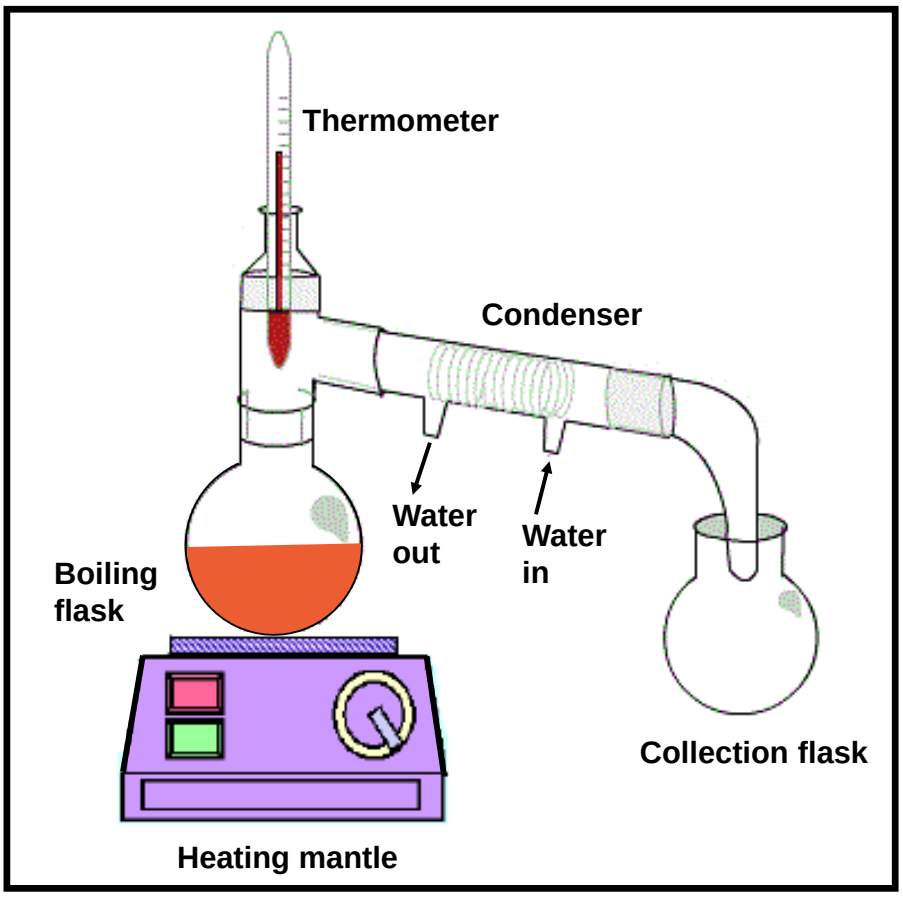

Fig. 2.2: **Distillation set-up for purification of Pyrrole monomer.**

of flask. As the vapours enter the condenser, due to the cool water running in the outer tube of the condenser, they are converted into the liquid. The purified monomer is collected in a separate flask (condensate receiver).

2.2.3 Electrochemical experiments

All electrochemical experiments: enzyme activity assay, electropolymerization of PPy, electrochemical impedance spectroscopy, cyclic voltammetry, and current measurements were carried out by using electrochemical workstation PG-STAT302N. The electrochemical setup has been shown in Fig. 2.3. The schematic shows a three electrode electrochemical cell consisting of an electrolyte solution.

The three electrodes dipped in the electrolyte solution are known as working electrode, reference electrode, and counter electrode. For the electrochemical experiments, Platinum foil and Ag/AgCl (3 M KCl) were used as the counter and reference electrodes respectively. The Platinum foil was cleaned by the electrochemical CV method before each electrochemical experiment. The Pt foil as work-

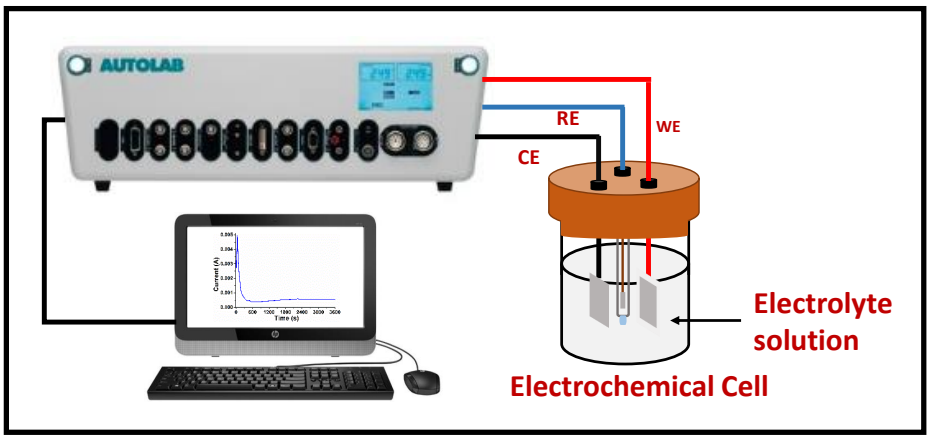

Fig. 2.3: **Schematic of electrochemical set-up.**

ing electrode was scanned in a potential range from -0.2 to 1.5 V at 100 mV/s until the voltammogram was settled with well-defined peaks corresponding to hydrogen and oxygen absorption and desorption. Lastly, it was washed thoroughly in DI water and dried.

Electropolymerization of Polypyrrole over Pt-coated glass substrate

The electrochemical deposition of PPy over Pt-coated glass substrate was performed in the three electrode electrochemical cell setup. For the deposition, firstly, the electrolyte solution of distilled Py monomer was prepared and the three electrodes Glass/Cr:Pt, Ag/AgCl, and Pt foil employed as working, reference, and counter electrodes respectively were immersed into it. The deposition of PPy was performed by applying a potential to the working electrode (Glass/Cr:Pt).

2.2.4 Enzyme immobilization and quantification

The enzyme was immobilized over the as-prepared PPy electrode surfaces by physical adsorption and crosslinking immobilization techniques as described below:

Physical adsorption

Firstly, the GOx solution of 10 mg/mL was prepared in 0.1 M PBS (pH-6.8). In physical adsorption method, the aliquots of prepared GOx solution was dropped over the as-fabricated PPy electrode surface and kept overnight in the incubator at 4 °C temperature for proper adsorption of enzyme. In this method, the enzymes

bind with the PPy electrode surface via electrostatic interaction between the two.

Crosslinking immobilization

The attachment of GOx to water-insoluble carriers (*viz.* CPs) via glutaraldehyde is one of the simplest and most gentle coupling methods in enzyme immobilization techniques [29]. The glutaraldehyde with chemical formula OHC-CH_2-CH_2-CH_2-CHO act as the cross-linker. The crosslinking agent forms the covalent bond at the two ends: (i) one with the terminal functional groups of the enzyme (not required for catalytic activity) and (ii) the other with reactive groups on the solid surface of the insoluble matrix which helps in binding the enzyme to the support matrix. The amino group as the functional groups available in the enzymes play an important role in the binding reactions [62]. To avoid the extensive modification in the structure of enzyme (as a higher concentration of cross-linking agent may result in a distortion of the enzyme structure, thereby affecting the enzyme activity), the lysine-rich protein viz. BSA as a stabilizer has been proposed by the researchers. Thus, in the crosslinking immobilization process, a mixture of BSA and glutaraldehyde was prepared and dropped over the PPy electrode. After drying the electrode at room temperature, GOx solution was drop cast over it and kept in an incubator at 4°C temperature for proper immobilization of GOx.

Enzyme quantification

The amount of enzyme loaded over PPy electrode surfaces was determined by fluorescence emission spectra, recorded using Fluoromax-4p spectro-fluorometer from Horiba Jobin Yvon (Model: FM-100). Some of the molecules emit light in electronically excited states known as Luminescence which can be majorly divided into two categories: phosphorescence and fluorescence. Phosphorescence is the emission of light from triplet excited states, in which the electron in the excited orbital has the same spin orientation as the ground state electron. Transitions to the ground state are forbidden and the emission rates are slow (10^3 to 1 per second). However, Fluorescence occurs from excited singlet states. The electron in the excited orbital is paired (by opposite spin) to the electron in the ground state and thus the process returning to the ground state is spin allowed. This occurs rapidly by the emission of a photon at emission rates of typically 10^8 s^{-1}. The emission spectrum

acquired on excitation denotes fluorescence spectral data. A fluorescence emission spectrum is a plot of the fluorescence intensity versus wavelength. An emission spectrum is the wavelength distribution of emission measured at a single constant excitation wavelength. A schematic of a spectro-fluorometer setup has been shown in Fig. 2.4.

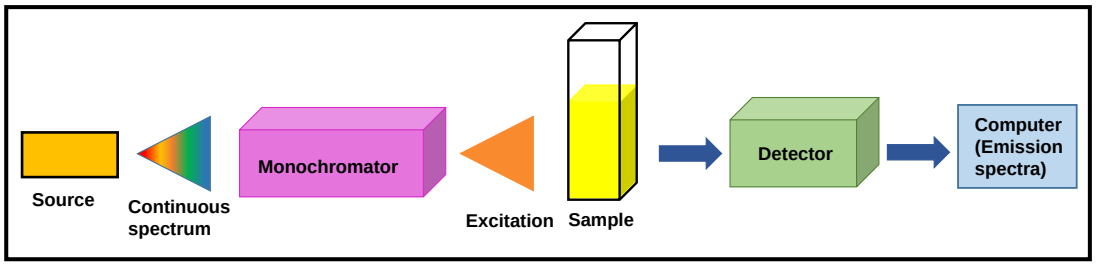

***Fig. 2.4:* Schematic of Flourescence spectroscopy set-up.**

The xenon lamp is used as the excitation source of light. The required excitation wavelength is selected by the monochromator. The light with the desired wavelength from monochromator interacts with the sample solution and spectrum of the emitted light is analyzed by the detector which after signal processing is displayed on the computer. Each GOx molecule consists of an aromatic residue called tryptophan, which contributes an intrinsic fluorescence in GOx. Therefore, when the solution having GOx molecule is excited at 280 nm, it contributes to fluorescence emission at 330 nm. The intensity of fluorescence emission at 330 nm is directly related to GOx concentration in the solution. Thus, the optical characteristic of GOx molecule has been utilized to evaluate the amount of enzyme loaded over the PPy support matrix. The instruments used in the fabrication of the biosensor electrode has been shown in Fig. 2.5. All experiments were performed in a generally clean environment and extra care has been taken to avoid the dust particles and impurities that can contaminate the samples.

2.2.5 Enzyme structural characterization by FTIR spectroscopy

Almost every compound (organic or inorganic) having covalent bonds, absorbs various frequencies in infrared (IR) region, which extends from 2.5 to 25 µm wavelength range or from 4000 to 400 cm^{-1} wavenumber range. When the molecules absorb IR radiation, they are excited to higher energy state. The simplest IR active modes of vibrational motion in a molecule are the stretching and bending modes.

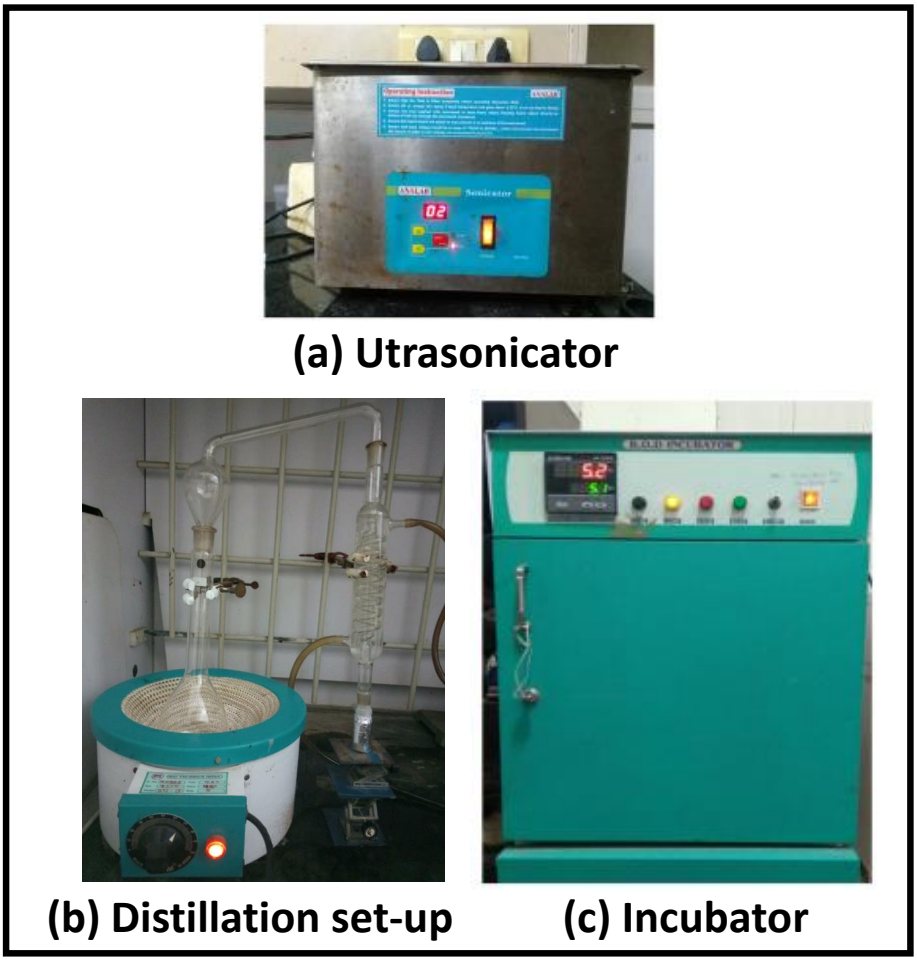

Fig. 2.5: **Instruments used for fabrication of biosensor (a) Ultrasonicator (b) Distillation set-up (c) Incubator.**

Typically, asymmetric stretching vibrations occur at higher frequency than symmetric stretching vibrations and stretching vibrations occur at higher frequencies than bending vibrations. Absorption is a quantized process. A molecule absorbs only selected frequencies. The absorption corresponds to a change in the energy on the order of 8 to 40 kJ/mole. Since every type of bond has a different natural frequency of vibration and two identical bonds in two different compounds are in different environments; therefore no two molecules of the different structure have exactly the same IR absorption pattern. Thus, the IR spectrum is a fingerprint of the molecule. The schematic of a typical FTIR instrument set up has been shown in Fig. 2.6. A source which produces a broad spectrum of IR energy passes through an aperture. The aperture controls the amount of energy falling on the sample. An interferometer consists of two mirrors (stationary and movable) and a beam splitter. The incoming IR beam splits into two by beam splitter. One beam falls at fixed

mirror getting reflected back from it while another one reflects off a movable mirror (very short distance movement i.e. a few millimeters). Thus resulting in two beams which are interfering with each other. This will result in a sequence of maxima and minima due to constructive and destructive phases respectively. The beam which is coming out of interferometer falls on the sample resulting in IR absorption. The detector records the IR spectrum which has not been absorbed by the sample. The detector of IR spectrometer produces a plot of intensity versus time. Later Fourier transform of the recorded spectrum is obtained to convert the interferogram from the time domain to the frequency domain.

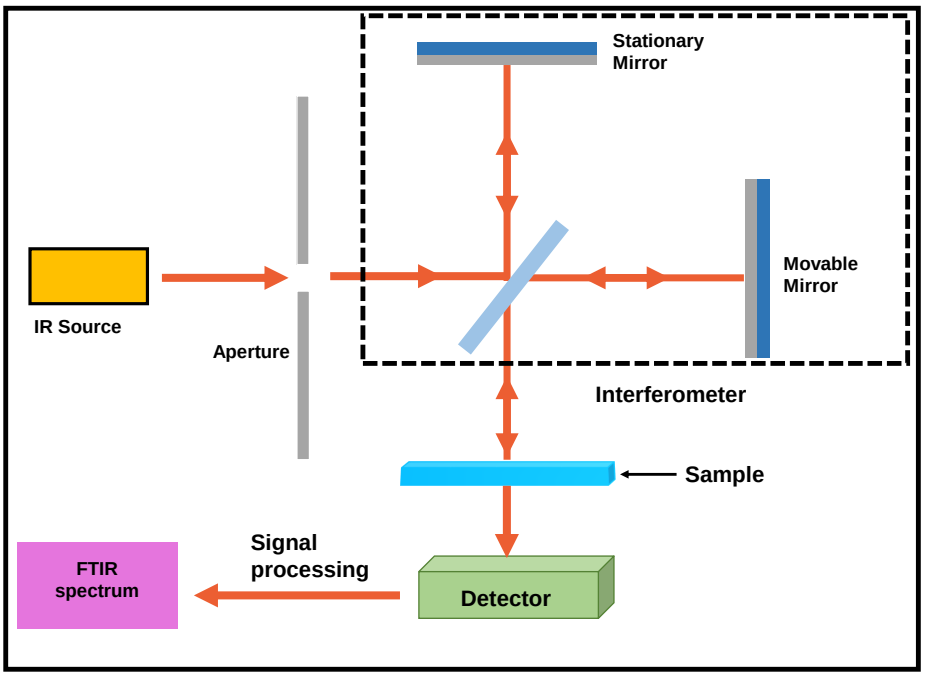

Fig. 2.6: **Schematic of FTIR spectroscopy set-up.**

For measurement, first of all, the spectrum of background consisting of IR active atmospheric gases, carbon dioxide, water vapors, etc. is obtained. Subsequently, the sample is placed in the beam path which results in a spectrum containing absorption bands for the compound as well as the background. Subtraction of background spectrum from that of the sample and background (both) yields the spectrum of the sample.

2.3 Characterization Techniques

2.3.1 Field Emission Scanning Electron Microscopy (FESEM)

FESEM is a non-contact, non-destructive technique for imaging surface topography. The FESEM employs a focused beam of high-energy electrons with significant amounts of kinetic energy, and this energy is dissipated as a range of signals on interaction with the surface of specimens. The signals that obtained from the electron-sample interactions reveal information about the sample's surface topography and composition.

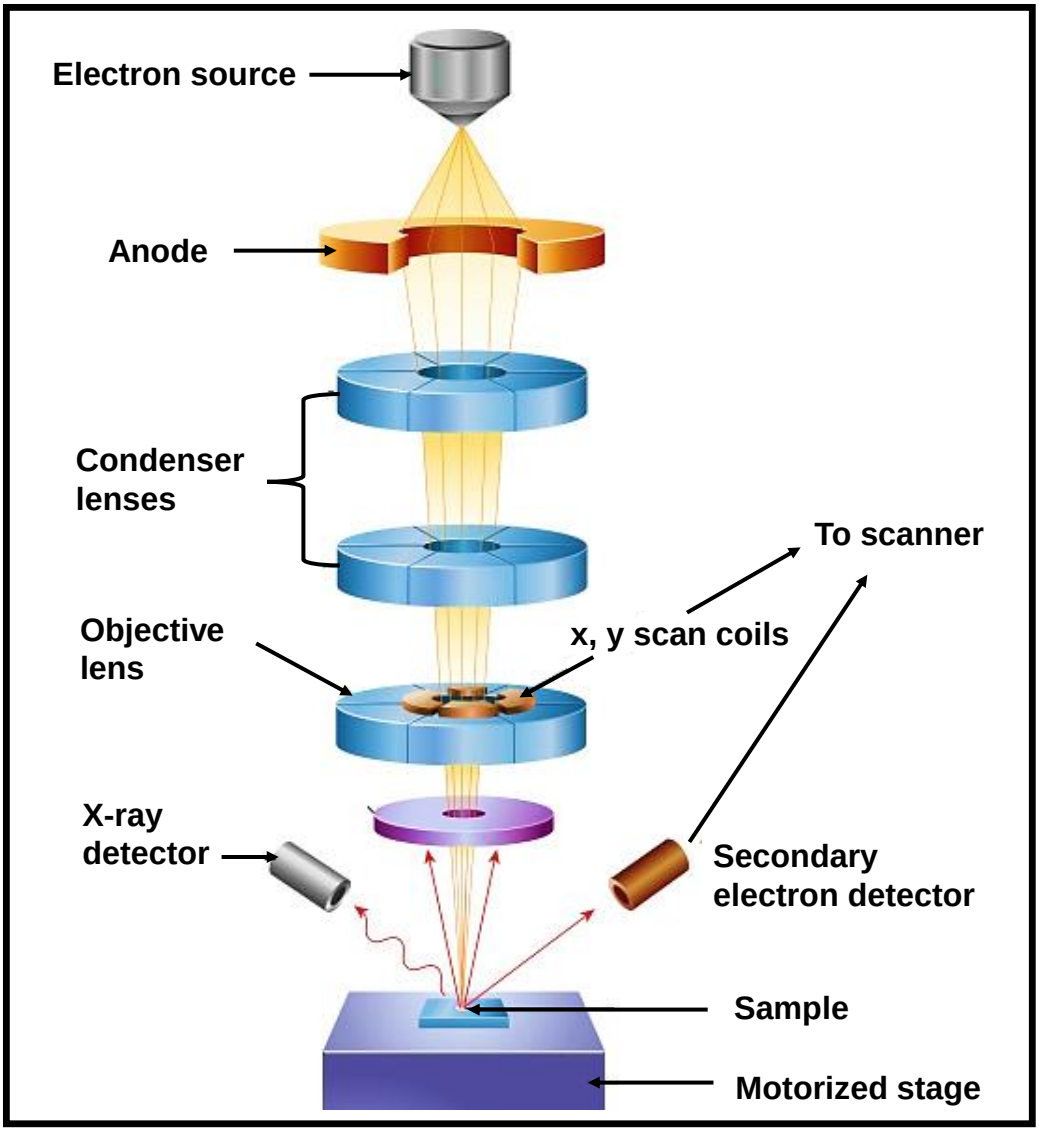

Fig. 2.7: **Schematic of FESEM [63].**

The illumination system of FESEM consists of an electron source (field emission gun), which is maintained at a negative potential with respect to wehnelt cylinder.

The emitted electron beam, which typically has an energy ranging from a few hundred eV to 30 KeV, is passed through a magnetic lens system. The magnetic lens system consists of two condenser lenses for maintaining the spot size and the intensity of the electron beam, respectively, as shown in Fig. 2.7. This is achieved by varying the current in these lenses. These condenser lenses collimate the electron beam to a very fine spot of 1-5 nm. Thereafter, the beam passes through a pair of scanning coils in the objective lens system. The objective lens focuses the electron probe onto the specimen so that the final probe diameter lies between 2 and 10 nm. The objective aperture limits the angular spread of the electrons. The focused beam is scanned in a two-dimensional raster fashion over a selected area of the sample surface. When the incident electron beam interacts with the sample, the electrons lose their energy by repeated scattering and absorption within a pear shaped volume of the specimen known as the interaction volume, which extends from less than 100 nm to around 5 nm deep into the surface. The size of the interaction volume depends on the beam accelerating voltage and the atomic number and the density of the specimen. This interaction leads to emission of secondary electrons (SEs), backscattered electrons (BSEs), auger electrons, X-rays, etc. In case of SEM, the interaction products most frequently used for the generation of images are (i) SEs and (ii) BSEs. SEs are generated by inelastic scattering of the primary electrons on the atomic core or on the electrons of the atomic shell of the sample material and generally escape from the sample at a depth of around 5 to 50 nm. SEs are low energy electrons that escape from the specimen with kinetic energies below about 50 eV. Alternatively, they may be primary electrons which have lost nearly all their energy through scattering and have reached the surface. SEs are extremely abundant and the SE yield (the number emitted per primary electron), is dependent on the accelerating voltage and can even exceed 1. For this reason, SEs are extensively used for imaging in SEM. All electrons with energies higher than 50 eV are known as BSEs. They are generated by elastic scattering in a much deeper range of the interaction volume and carry depth information. The BSEs originate from Rutherford backscattering from the nucleus; therefore BSE yield strongly depends on the atomic number (Z) of the material. Hence, BSE imaging can be used to differentiate phases of differing average atomic numbers.

2.3.2 Transmission Electron Microscopy (TEM)

The morphology of PPy was studied by TEM from JEOL JEM-2000 EX microscope at an accelerating voltage of 200 kV. The TEM operates on the same basic principles as the light microscope but uses electrons instead of light. The resolution of any microscope is limited by the wavelength of the light/object used for imaging. Since in TEM, electrons are used for imaging any object, hence owing to the small de Broglie wavelength of electrons, TEMs are capable of imaging at a significantly (about 1000 times) higher resolution than a light microscope. Hence it is possible to investigate different materials down to near atomic levels. A typical ray diagram presented in Fig. 2.8 shows the working of a TEM system.

1. **Illumination system:** It consists of:

   (i) Electron gun: Here the electrons produced by the filament (Tungsten or LaB6) either through thermionic emission or field emission are accelerated to the energy to be used in the microscope. The electron wavelength λ is given by equation (2.1):

   $$\lambda = \frac{h}{\sqrt{2m_0eV \times (1 + \frac{eV}{2m_0c^2})}} \tag{2.1}$$

   Where, h is Planck's constant, m_0 is the electron rest mass, e is electronic charge, V is accelerating voltage and c is speed of light in vacuum.

   (ii) Magnetic/condenser lenses: Interaction of these electrons with magnetic field governs the operation of TEM lenses. A spatially varying magnetic field is required for focussing parallel rays at some constant focal length, which is referred to as magnetic lens. The majority of electron lenses for TEM utilize electromagnetic coils to generate a convex lens. Two magnetic lenses, C_1 and C_2 are placed after the electron gun. These lenses are adjusted to illuminate the sample with a nearly parallel beam (convergence angle 10^{-4} rad).

2. **The sample:** The sample is placed after magnetic lenses. It should be thin enough to transmit sufficient electrons so that the intensity falling on the screen / photographic plate may give an interpretable image in a reasonable time.

3. **Imaging system:** Imaging system consists of:

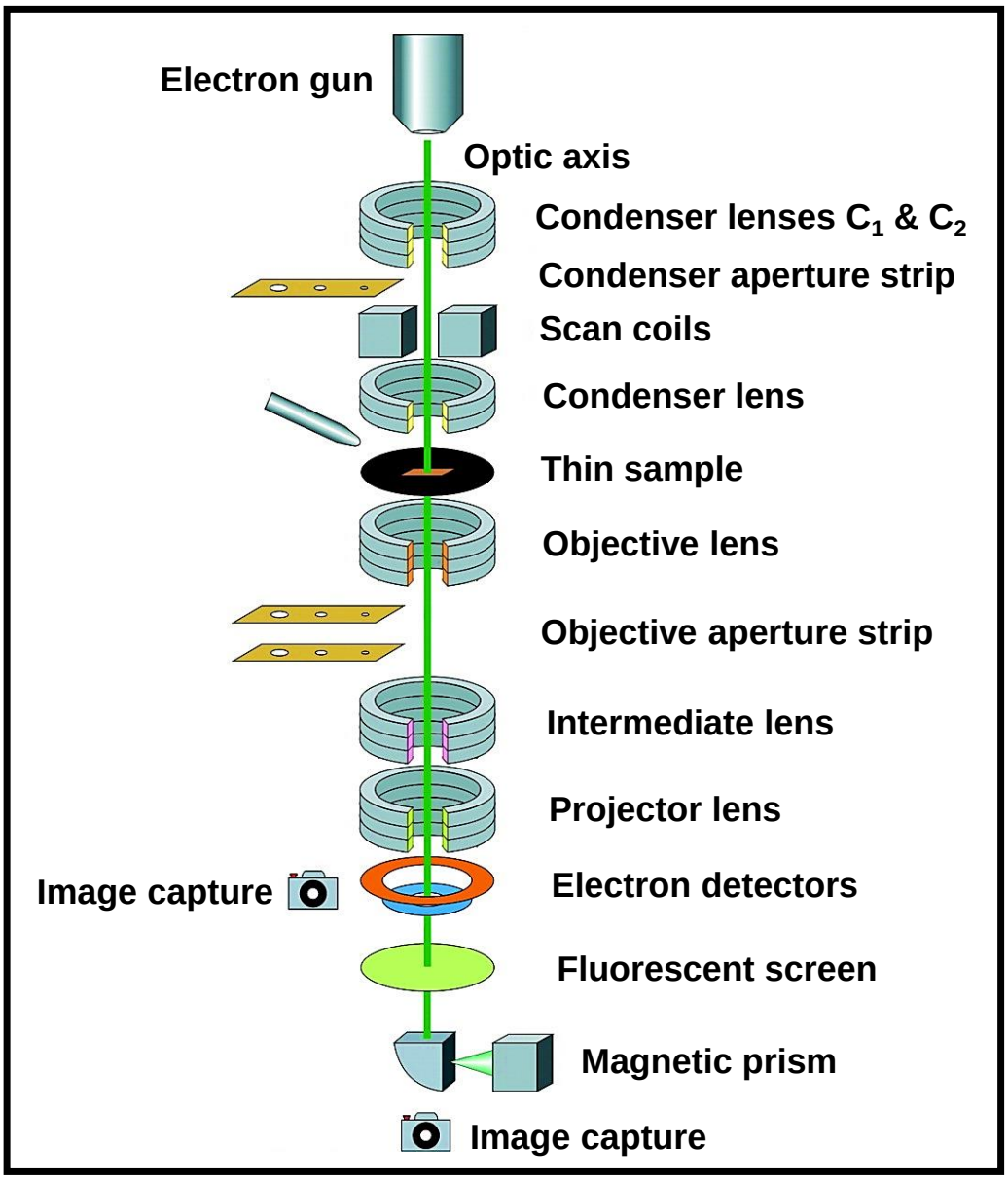

Fig. 2.8: **Schematic of TEM imaging.**

(i) Objective lens: The electrons emerging from the exit surface of the specimen are incident on the objective lens, which disperses them to create a diffraction pattern in the back focal plane and recombines them to form an image in the image plane.

(ii) Objective aperture: An aperture is inserted into a lens to limit the collection angle of the lens. On passing through the aperture, electrons farther than a fixed distance from the optic axis are stopped. Thus, objective aperture allows controlling the resolution of the image formed by the lens.

4. **Magnification system:**

(i) 1st Intermediate lens: For projecting image onto the screen, strength of this

lens is adjusted such that it selects the image plane of the objective lens as its object.

(ii) 2^{nd} Intermediate lens: Image obtained by 1st intermediate lens is magnified using 2^{nd} intermediate lens.

(iii) Projector lens: Projector lens further magnifies the image.

(iv) Screen: The final magnified image is obtained on a fluorescent screen or recorded on a CCD (charge coupled device) camera.

The morphology of PPy was studied by TEM from JEOL JEM-2000 EX microscope at an accelerating voltage of 200 kV.

2.3.3 X-ray diffraction measurements

X-ray diffraction (XRD) is a qualitative technique used to determine the crystallographic structures of solids, including lattice constants, orientation of single crystals, stresses, defects, and the chemical composition. It is reliable, simple and non-destructive in nature. The incident X-ray beam diffract into many specific directions from the atoms of the crystal by which we can determine the crystal structure. The wavelength of incident electromagnetic radiation onto the substrate is of only a few angstroms (ranging between 0.7 - 2 Å). In this technique, a monochromatic

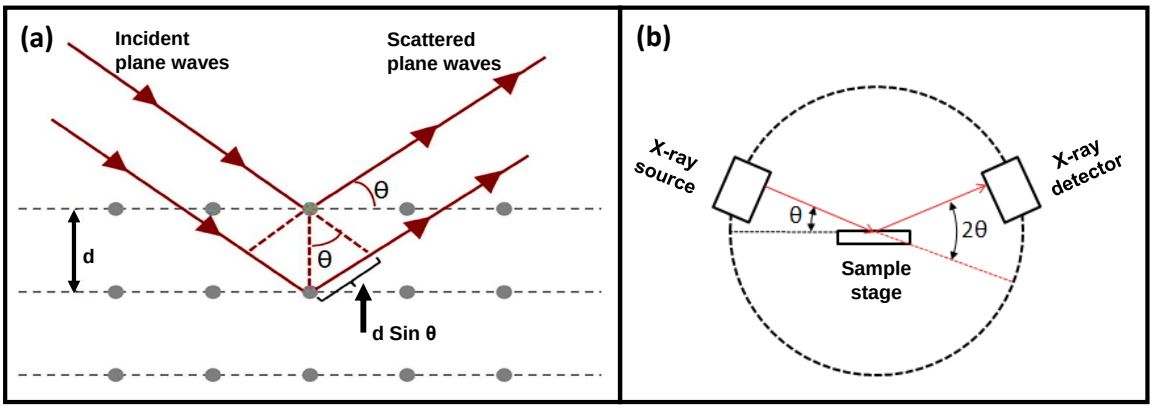

Fig. 2.9: **Schematic of (a) Bragg's law and (b) XRD set-up. [64]**

X-ray beam is incident onto the sample and a detector is placed at the opposite angle of incidence. By changing the angle of incidence and measuring the reflected intensity results in angles of peak reflection intensity that are used to form the diffraction pattern. Diffraction phenomenon only occurs when the distance traveled by the rays reflected from successive planes differ by a whole number n of

wavelengths. Bragg's law for an electromagnetic wave incident on lattice states is defined as:

$$n \times \lambda = 2 \times d \times sin(\theta) \tag{2.2}$$

Where, n is the order of refraction, λ is the wavelength of the incident X-rays, d is the spacing between atomic planes in the crystalline phase and Θ is the angle of incidence between the incident ray and scattering planes as shown in Fig. 2.9 (a). The planes vary in orientation from material to material each with its unique d-spacing. The XRD pattern is obtained by plotting the resultant diffracted peaks intensities vs angular positions. The relative intensity of diffraction peaks depends on the type and arrangement of the atoms in the crystals. By analyzing the diffraction pattern, one can have insights into the phase composition and crystal structure of the studied materials [65]. The crystalline structure and phase information was analyzed by powder XRD (RigakuS-mart LabSystem) with Cu Kα radiation operating at 40 kV and 40 mA, using Cu Kα radiation (λ = 1.5418 Å) in the 2Θ range from 20° to 80° at a scanning rate of 2°/min. Figure 2.9 (b) shows schematic of typical XRD set up.

2.3.4 Raman spectroscopy

Raman spectroscopy is a spectroscopic technique used to determine vibrational, rotational and other low frequency modes in a system. It is based on inelastic scattering or Raman scattering of monochromatic light, usually from a laser in the visible, near infrared or near ultraviolet range. The experimental set-up of Raman Spectroscopy is shown in Fig. 2.10. The laser light interacts with molecular vibrations, phonons or other excitations in the system, resulting in the energy of the laser photons being shifted up or down. The shift in energy provides information about the vibrational modes in the system [66]. In this experiment, a sample is illuminated with a laser beam. Electromagnetic radiation from the illuminated spot is collected by a lens and sent through a monochromator. Elastic scattered radiation at the wavelength corresponding to the laser line (Rayleigh scattering) is altered out, while the rest of the collected light is dispersed onto a detector by either a notch filter or a bandpass filter. Spontaneous Raman scattering is characteristically very weak and as a result, the main difficulty of Raman spectroscopy is separat-

ing the weak in-elastically scattered light from the intense Rayleigh scattered laser light.

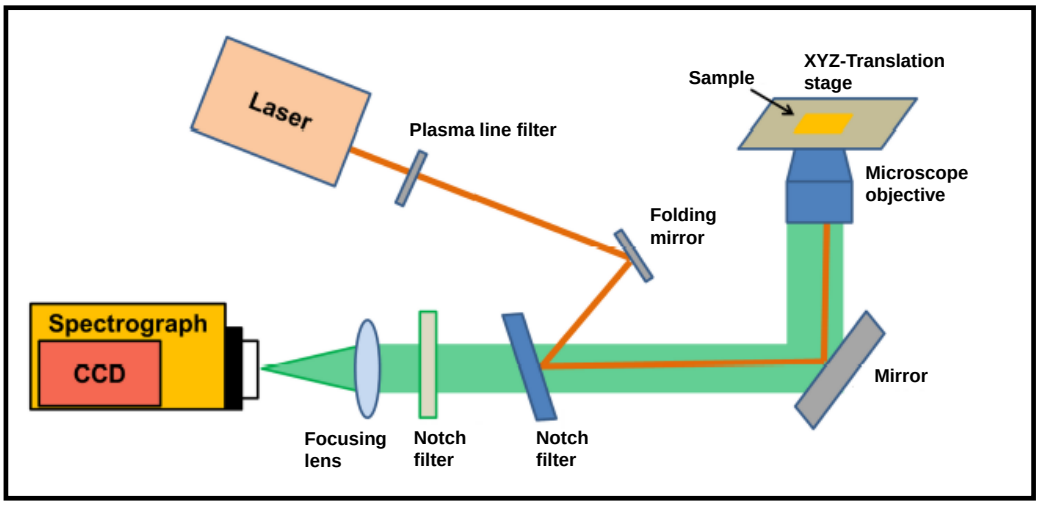

Fig. 2.10: **Schematic of Raman spectroscopy set-up.**

2.3.5 Photoluminescence spectroscopy

When a semiconductor material is excited with photons of energy greater than that of the bandgap of the material, the electrons get excited from the valence band into the conduction band. Laser is the primary source of achieving this in Photoluminescence (PL). Electrons in an excited state always seek to return to their lowest energy state; in this case, the ground state is at the top of the valence band. In semiconductors with a direct bandgap and few mid gap energy states, a favourable outcome is the production of a photon, where the energy of the photon corresponds to the bandgap of the semiconductor, however energy may also be lost through phonons (vibrations) in the lattice. In a perfect semiconductor, consisting of an infinitely homogenous and isotropic lattice, every emitted photon would exhibit the same characteristic energy and the PL. PL of a semiconductor is largely dependent on the temperature due to the thermal expansion/contraction of the lattice and changes in the electron-phonon interaction. To investigate the optical characteristics of the samples, PL measurements were performed using a Dongwoo PL system at an excitation wavelength of 325 nm at room temperature. The schematic of PL measurement system is shown in Fig. 2.11. The output of a laser light source (325 nm) is passed through the excitation slit and sample is placed in the path of the monochromatic light with an angle close to 45°. While placing the sample, it

is important not to send the reflected excitation light directly to the emission slit [67]. When the sample is optically excited, it emits light in all directions at various wavelengths depending on its band gap and defect states. A small portion of the emitted light passes through the emission slit and then it is filtered by the monochromator. Typically, the remaining optical signal has a very low intensity; hence a PMT (Photomultiplier tube) detector is used to measure such low intensities. To get the spectral distribution of the emitted light, the emission monochromator scans the desired wavelength spectrum and the light intensity measured by the detector is recorded [68].

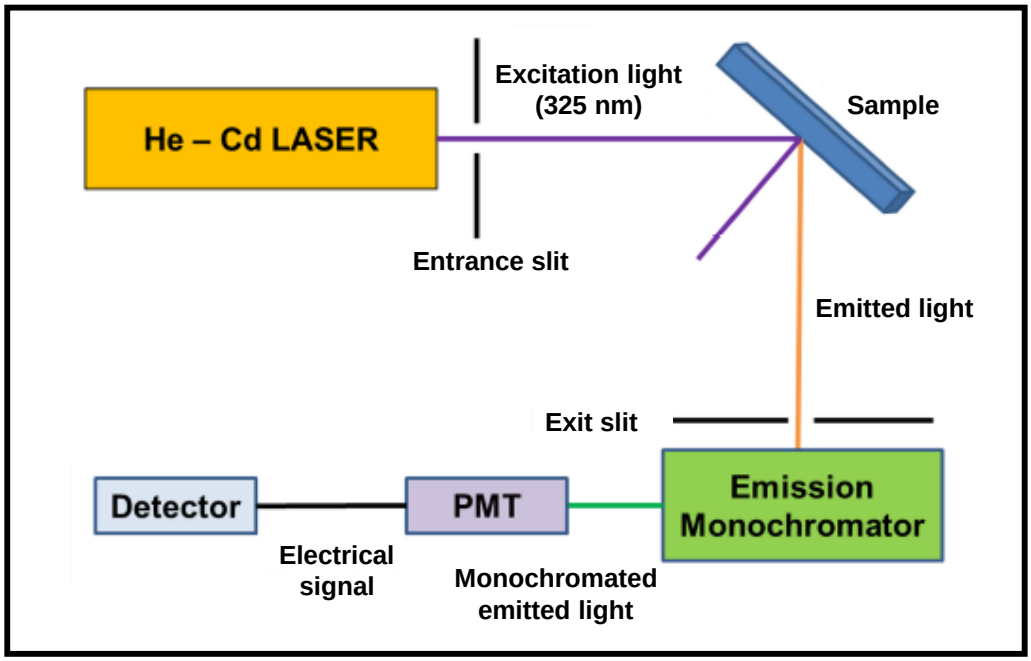

Fig. 2.11: **Schematic of Photoluminescence spectroscopy set-up.**

2.3.6 Electrochemical characterizations

All the electrochemical characterizations of PPy electrodes have been performed by electrochemical workstation (Autolab PGSTAT302N) from Metrohm. The three electrode electrochemical cell set-up has been shown in Fig. 2.12 (a) where Glass/Cr:Pt/PPy nanostructures or Glass/Cr:Pt/PPy nanostructures/GOx, Ag/AgCl (3M KCl) and Pt foil are used as working, reference and counter electrodes respectively. In this work electrochemical impedance spectroscopy was performed to analyze the charge transfer resistance at the electrode-electrolyte interface, cyclic voltammetry study was carried out to estimate the electroactive surface

area, and chronoamperometry to study the biosensor response.

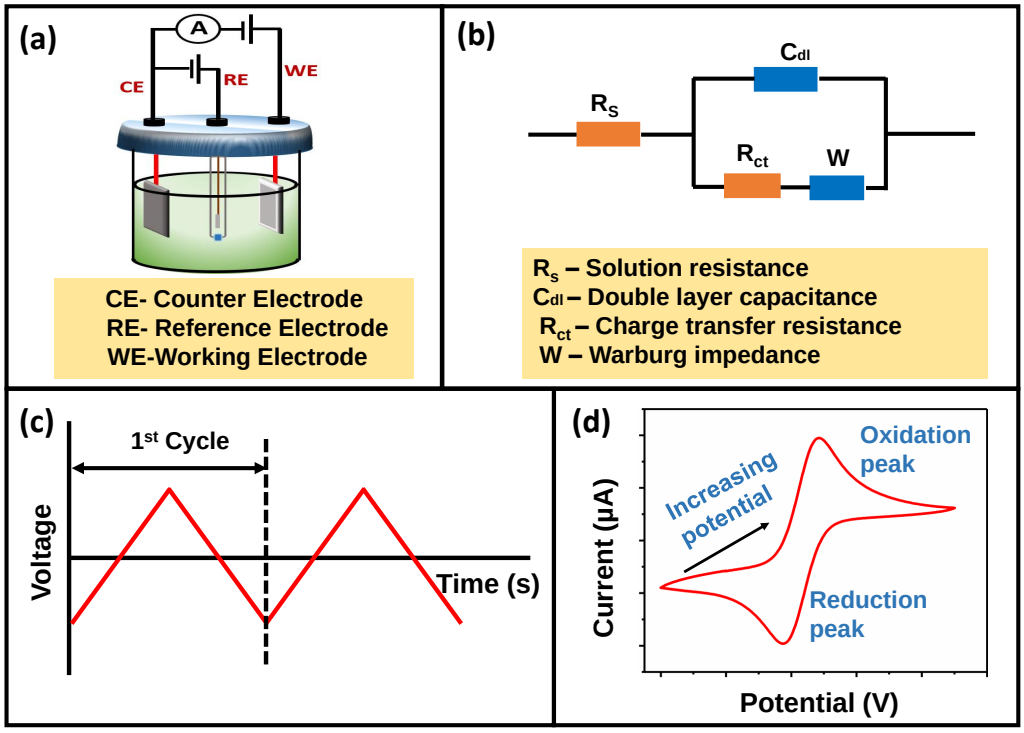

Fig. 2.12: **Schematic of (a) Three electrode electrochemical cell set-up and Randle's circuit (c) Ramp input voltage for Cyclic voltammetry (d) Cyclic voltammogram.**

Electrochemical impedance spectroscopy (EIS)

The electrochemical impedance spectroscopy has been widely used to study the charge transport properties at electrode-electrolyte interface. It is a powerful tool for characterization of electrical properties of materials and their interfaces. In this technique ionic conduction is more dominant than electronic [69]. The analysis is performed by applying a small Alternating Current (AC) voltage to the system and the response is taken as a function of frequency. This technique is executed using a potentiostat and Frequency Response Analyzer (FRA). The input AC voltage is kept low (but it should be sufficient to obtain a response) to make the system pseudo linear since electrochemical systems are not intrinsically linear [70]. The frequency range which is swept is usually large and extends from MHz to few mHz. From this applied potential V(ω, t) and obtained I(ω, t), Z(ω, t) is calculated which gives the imaginary and real part on complex plane to obtain Nyquist plot. Here, ω is frequency and t is time. Although frequency dependence is not explicitly evident in Nyquist plot, the representation is more compact. Here, to

study PPy nanostructures which form solid/liquid interface Voigt element model is used. A typical electrochemical system can be represented by Randle's circuit as shown in Fig. 2.12 (b) where solution resistance (R_s) is connected in series with a parallel combination of double layer capacitance (C_{dl}) and charge transfer resistance R_{ct}. Usually this representation is used for an electrochemical system where an electrode is immersed in an electrolyte solution with dissolved ionic species. A typical nyquist plot corresponding to Randle's circuit consists of a semicircle with diameter equal to R_{ct}. Moreover, a diffusional element Warburg (W) in series with R_{ct}. It shows the impedance of semi-infinite Nernst diffusion to/from electrolyte as represented in equation (Eq. 2.3):

$$Z_w(\omega,t) = \frac{W}{\sqrt{\omega}} \tag{2.3}$$

Cyclic voltammetry (CV)

CV is a powerful technique to investigate the oxidation and reduction processes of the molecular species. It is an important tool to study the electron transfer-initiated chemical reactions such as catalysis. In this method, a linear sweep voltage in a potential limit i.e. a triangular waveform is applied to the working electrode which is scanned cyclically at a scan rate. The CV is taken in unstirred electrolyte solution. The CV scan is a plot of current verses potential and demonstrate the potential at which the oxidation or reduction process happens [71]. The schematic illustration of a cyclic voltammogram have been shown in Fig. 12 (c). In this process, as the potential is swept in the forward and reverse direction and reaches higher than the formal potential of the species, current flows through the electrode and leads to the oxidation or reduction peaks corresponding to the species as shown in Fig. 12 (d). The peak current value corresponding to the oxidation potential (potential applied in the positive direction) is the anodic peak and the peak at reduction potential (potential in negative direction) is referred to as cathodic peak current. The two peaks are separated by a potential which defines the diffusional process of the species to and from the electrode. This peak separation voltage signifies the reversibility of the species whether it is stable in the reduced form or can be oxidized again. The electrochemical reversibility denotes the electron transfer kinetics between the electrode and the analyte [72]. Here, in this work to study the

electro catalytic behavior and charge transfer kinetics of PPy nanostructured and PPy/GOx electrodes, CV was carried out in an unstirred electrolyte solution.

Characterization of biosensor electrodes

The chronoamperometric response of the fabricated biosensor was carried out in a stirred electrolyte solution. The detection of glucose was performed by applying a constant potential to the biosensor electrode. When an oxidation potential is applied to the working electrode Glass/Cr:Pt/PPy nanostructures/GOx, due to the enzyme catalyzed reactions, the electrons are generated leading to current rise which gives the measure of the glucose concentration. The characterized biosensor responses were analyzed and all the figure of merits of the biosensor such as sensitivity, linear range of operation, response time, selectivity, shelf life were determined.

Chapter 3

Template-free Method for the Fabrication of Polypyrrole Nanostructures Based Biosensor

In this chapter, we have discussed a template-free single-step fabrication of Polypyrrole (PPy) nanostructures with the incorporation of different dopants *viz.* DBSA, MeSA, p-TSA, and $LiClO_4$. Further, the Polypyrrole nanofibers network (PNN) (without using electrospinning) with different concentrations of $LiClO_4$ was fabricated and utilized as a support matrix for enzyme immobilization. The properties of PNN play an important role in biosensor fabrication. Thus, the effect of $LiClO_4$ concentration on glucose biosensor performance has been demonstrated in this work. The modification in morphology and reduction in charge transfer resistance of PNNs by varying $LiClO_4$ concentration were found to play a significant role in the improved figure of merits of the biosensor. Among all the types of as-fabricated PNN electrodes (prepared by using different concentrations of $LiClO_4$ *viz.* 1, 10, 50, and 70 mM), the best response was obtained corresponding to highest $LiClO_4$ concentration. The enzyme loading and charge transfer resistance were drastically improved by approximately three folds owing to the higher surface area and improved conductivity of PNN electrodes thereby resulting in ten-fold increment in sensitivity. The as-prepared biosensor showed the highest sensitivity of 4.34 mA-cm^{-2}-M^{-1} and a linear range of 0.1 - 4.6 mM with good stability and high selectivity for glucose detection.

3.1 Introduction

Glucose plays an important role in human metabolism and any imbalance in blood glucose level leads to diabetes mellitus which is one of the major causes of death and disability in the world [6, 55]. With the increase in the number of patients suffering from diabetes around the world and particularly in India, a pressing need has been felt to develop the point of care handheld testing devices which can provide continuous monitoring of glucose level of such patients. In this context, research efforts in the field of enzymatic glucose biosensors have accelerated since the development of enzymatic electrodes for enzymatic glucose biosensors have widely been accepted as a possible candidate for development of sensing devices mainly owing to the fact that enzymes are highly specific towards analyte [29, 73]. In such sensors, enzymes are immobilized on a biocompatible support matrix using different immobilization techniques i.e. physical adsorption, crosslinking, coentrapment and covalent binding. It has already been shown that performance of enzymatic biosensors is highly dependent on immobilization technique and can be improved by using more efficient strategies of immobilization. The prerequisites of an ideal support matrix for the immobilization of enzymes are the high surface area along with a biocompatible environment so that enzymes do not get denatured or leach out of the matrix [56]. In this respect, nanostructured conducting polymers, having semiconducting properties [74, 75] were found to be appropriate candidates because of its larger surface area and biocompatibility. The field of enzymatic biosensors utilizing conducting polymers as support matrix has been explored exhaustively. Specifically, 1-D nanostructures of Polypyrrole (PPy) such as nanofibers, nanotubes, nanorods, and nanowires have received great attention as a possible alternative for support matrix due to their higher surface area, electrical conductivity, and biocompatibility [2, 42, 43]. Nanostructures of PPy have been reportedly synthesized via chemical [76], electrospinning [77] and electrochemical method [52]. Among these methods, electrochemical polymerization is relatively straightforward, simple, cost-effective and reliable approach which facilitates the growth of polymer directly onto the electrode surface. Moreover, the electrical conductivity of nanostructured PPy films can be easily tuned by doping and de-doping process during electro-synthesis [78]. In this method, on the ap-

plication of a potential to the electrode, due to the oxidation of Pyrrole monomer into radical cations, the film begins to grow on the surface of the electrode. As the polymerization progresses, the anions present in the electrolyte solution incorporates with the positively charged PPy via electrostatic force. Various different size dopants *viz.* potassium nitrate (KNO_3), sodium dodecyl sulfate (SDS), para-Toluene sulfonic acid (p-TSA), lithium perchlorate ($LiClO_4$), etc. have been utilized for the formation of PPy nanostructures. The incorporation of different size anions during polymerization influences both the morphology and conductivity of PPy nanostructures [78, 79]. Based on the type of electrode surface used, electrosynthesis of the polymer can be performed using two approaches: Template-based [7, 45–47, 55, 56] and Template-free method [32, 34, 48–50]. For template-based approach, either a soft or hard template is required to achieve anisotropic growth of nanostructures on a confined path defined by the template. Porous materials such as zeolite channels, particle track-etched membranes, anodic aluminum oxide (AAO), Titanium dioxide (TiO_2) etc. have been employed as hard templates [46, 55]. Some of the soft templates used are surfactants such as liquid crystals, micelles etc. Template-assisted electropolymerization involves multiple complicated steps which make it tedious, complex, time-consuming and expensive. Moreover, the templates require careful handling during and after fabrication. Further, removing the hard templates of diameters less than 100 nm after polymerization may often affect the structure, alignment, and properties of the polymer nanostructures which increases the complexity and overall cost of the biosensor fabrication [55]. The electrospinning technique which has been primarily used for the synthesis of nanofibrous networks is relatively easier and compatible for large area fabrication. However, it also suffers from the use of additives which alter the semiconducting properties of the nanofibers fabricated using conducting polymers. Therefore, development of a template-free method for fabrication of nanostructured conducting polymer is highly desirable for utilization as a support matrix in the biosensing device applications. Synthesis of these nanostructures with different morphology and controlled dimensions via electrochemical route is dependent on various growth parameters such as applied potential, polymerization time, dopant and monomer concentration etc., which influence the growth kinetics and the final structure of the polymer [32, 34, 48, 78, 80]. In addition to the morphological variations, the electri-

cal conductivity of the PPy film can be tailored with the help of dopant concentration variation, during electropolymerization. Recently template-free fabrication of nanofibrous network of PPy has gained interest [32, 34, 48–50, 80]. Zang et al. [32] have synthesized super hydrophilic 1-D PPy nanofibers network and explained the favorable experimental conditions for the formation of the same. Liao et al. [48] also fabricated vertically aligned PPy nanofibers on the titanium surface, with the length of 500 nm and explained the effect of polymerization time on nanofibers length. Fakhry et al. [34] fabricated different morphology of PPy from nanowires to nanofiber network. Laith Al-Mashat et al. [49], Xia et al. [50], and Palod et al. [52] have demonstrated the application of grown PPy nanofibers in hydrogen gas sensing, fuel cells, and enzymatic biosensors respectively. Here in this work, we have discussed the influence of dopant ($LiClO_4$) concentration on the performance of PNN based glucose biosensors. The $LiClO_4$ doped PNNs have been synthesized via a simple, cost-effective, single step, template-free electrochemical polymerization method. The experimental conditions *viz.* potential, Py monomer concentration, and $LiClO_4$ concentration have been optimized for the growth of nanofibers. Further, $LiClO_4$ concentration has been varied with the aim to improve PNN film conductivity. The as-synthesized $LiClO_4$ doped PNN was utilized as a support matrix for enzyme immobilization. Moreover, glucose biosensing response of fabricated biosensor was analyzed and the influence of $LiClO_4$ concentration on glucose biosensor performance has been discussed.

3.2 Experimental Details

3.2.1 Elucidation of different dopants influencing the morphology of electropolymerized Polypyrrole

A schematic representation of fabrication steps of biosensor has been shown in Fig. 3.1. Initially, glass substrates (1cm x 1cm) were cleaned by ultrasonication in acetone, isopropanol, and DI water. Further, 50 nm platinum (Pt) with an intermediate 5 nm chromium layer (to improve the adhesion of Pt on glass) was deposited over the cleaned glass substrates using dc magnetron sputtering at a base pressure of $1x10^{-6}$ mbar. Working pressure was maintained at 3 mTorr during deposition. The continuous flow of Ar gas was maintained at 10 sccm during

deposition of Pt. Further, Polypyrrole was deposited over a Pt-coated glass substrate using electropolymerization method. The electrochemical deposition of PPy was executed using electrochemical workstation (Autolab PGSTAT302N) having three-electrode cell configuration as shown in Fig. 3.1. Different parameters *viz.* types of dopant and concentration were investigated to influence the morphology of Polypyrrole nanostructures for biosensor fabrication. In the preliminary stage of the work, we have employed different dopants to study the morphological variations of PPy with different dopants. The different dopants were utilized with the aim to achieve high aspect ratio PPy nanostructures, which is a prerequisite for higher enzyme loading in enzymatic glucose biosensors. Here, we have prepared PPy nanostructures doped with DBSA, MeSA, p-TSA, and $LiClO_4$ which can provide a high electroactive and bio-compatible microenvironment for the enzymes. The incorporation of different size anions during polymerization influences both the morphology and conductivity of PPy nanostructures. The electrochemical deposition of PPy was executed using electrochemical workstation (Autolab PGSTAT302N) having three-electrode cell configuration as shown in Fig. 3.1. The

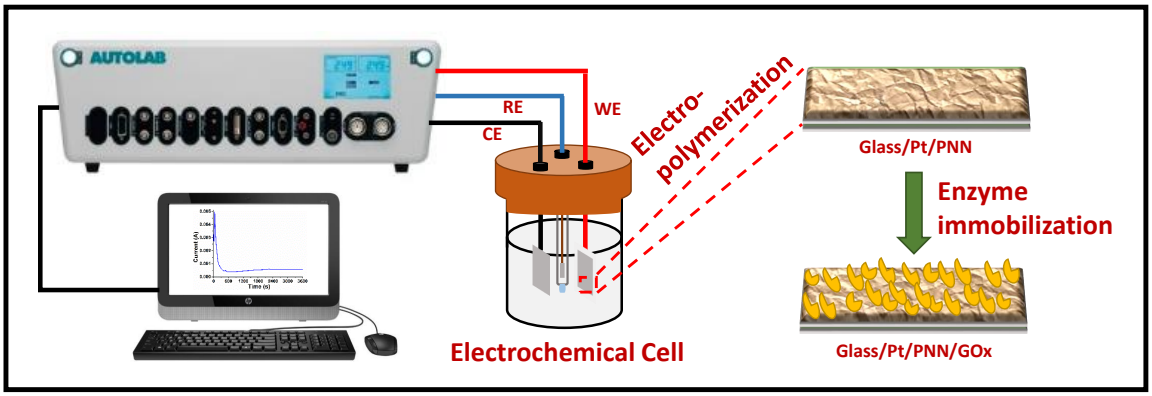

***Fig. 3.1:* Schematic of biosensor fabrication.**

Pyrrole (Py) monomer was distilled at 130 °C before the electropolymerization process. The electrolyte solution of 0.1 M Py and 70 mM concentration of one of the investigated dopants *viz.* DBSA, MeSA, p-TSA, and $LiClO_4$ in 0.1 M PBS (pH 6.8) were prepared for the PPy deposition. The cell consisted of an electrolyte solution where platinum coated glass substrate, platinum foil, and Ag/AgCl electrode have been utilized as working, counter, and reference electrode respectively. The measured values of pH were found to be ∼2.5-3 for 70 mM concentration of DBSA, MeSA, and p-TSA. However, the pH value for $LiClO_4$ was ∼6.8. A constant poten-

tial of 0.85 V was applied to the working electrode for 3600 s to obtain PPy nanostructures over a Pt-coated glass substrate. The electrodes prepared using DBSA, MeSA, p-TSA, and $LiClO_4$ as dopants were named PPy-DBSA, PPy-MeSA, PPy-pTSA, and PPy-$LiClO_4$ respectively. The morphology of as-fabricated electrodes was determined using Field Emission Scanning Electron Microscopy (FESEM, Carl Zeiss SUPRA55).

3.2.2 Fabrication of biosensor electrode: $LiClO_4$ as dopant for fabrication of PNN electrode

To obtain the morphological variations of PPy electrode, $LiClO_4$ concentration was varied from 1-70 mM. Pyrrole (Py) was distilled at 130 °C and electrolyte solution of 0.1 M Py, 1-70 mM $LiClO_4$ in 0.1 M PBS with pH 6.8 was prepared. The three electrode electrochemical cell was utilized for electropolymerization where Pt-coated glass substrate, Ag/AgCl electrode, and Pt foil was used as working, reference, and counter electrode respectively. Electrodeposition of Polypyrrole nanofibers network (PNN) was carried out potentiostatically at 0.85 V for 3600 s with four different (1, 10, 50, and 70 mM) $LiClO_4$ concentrations. Corresponding to 1, 10, 50, and 70 mM $LiClO_4$ concentration, the as-prepared electrodes were named as PNN-1, PNN-10, PNN-50 and PNN-70 respectively. Finally, Glucose oxidase (GOx) was immobilized over the Glass/Cr-Pt/PNN electrode for biosensor characterization as shown in Fig. 3.1.

3.2.3 Enzyme activity assay

The enzymes are very sensitive to their environmental conditions such as temperature, pH, etc. which can alter the activity of enzymes. The specific activity (SA) of enzymes is defined as micro-moles of substrate molecules converted into product per minute by 1 mg enzyme [81]. In conventional colorimetric assays, H_2O_2 (by-product of glucose oxidation) needs to be coupled with dye molecules such as o-dianisidine in the presence of a second enzyme such as horseradish peroxidase (HRP) responsible for absorption in the visible region for activity assay. The change in the absorption determines the enzyme activity. The sensitivity of these chemicals reagents and the use of second enzyme may often lead to unpredictable

results. Hence, in the present work, electrochemical assay has been chosen to determine the specific activity of GOx. The H_2O_2 concentration is directly related with

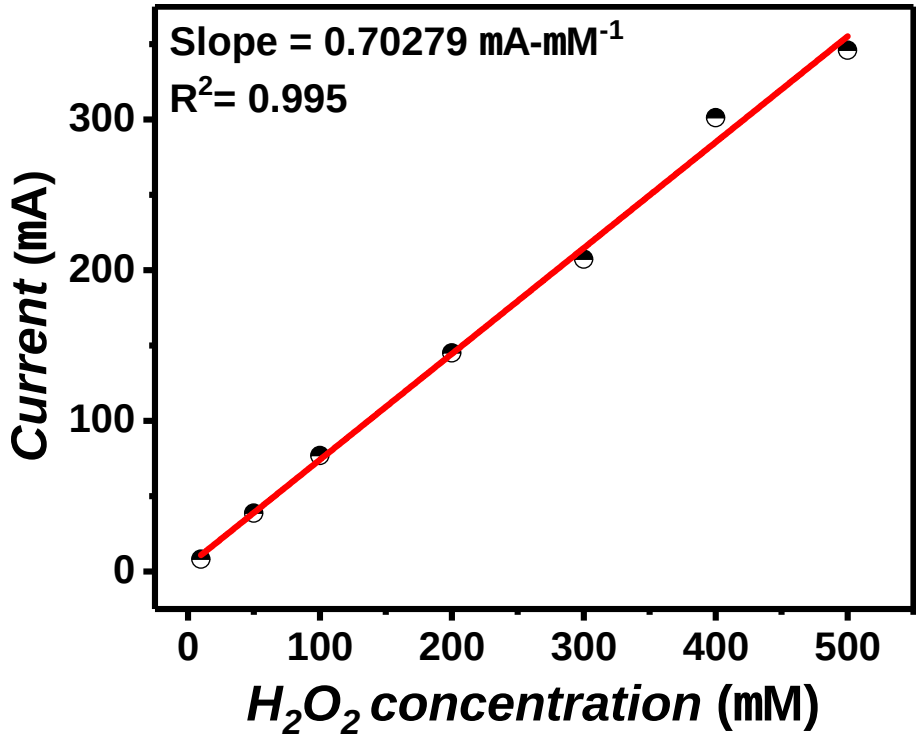

Fig. 3.2: **H_2O_2 calibration curve.**

the glucose concentration. Thus, for known concentration of H_2O_2 varying from 10-500 µM, steady state current values were recorded at an applied potential of 0.7 V to the working electrode in three electrode electrochemical cell. The Pt coil, Pt foil, and Ag/AgCl were used as working, counter, and reference electrodes respectively in a continuously stirred 0.1 M PBS (pH-6.8). The H_2O_2 calibration plot was obtained by taking the steady state values of current corresponding to H_2O_2 concentrations as shown in Fig. 3.2. A linear calibration plot with the slope $\partial I/\partial[H_2O_2]$ equal to 0.702 µA-µM^{-1} was obtained which implies that the rate of change of current is directly related with the H_2O_2 concentration. The activity assay (shown in Fig 3.3) was performed by injecting GOx in continuously stirred 50 mM PBS (pH-6.8) (20 mL) mixed with different concentrations of glucose. The 20 µL of GOx (200 µg) from GOx stock solution (10 mg/mL GOx in PBS) was injected into the solution and instantaneous current rise was observed relating to the enzyme catalysed reactions. This experiment was repeated for glucose concentrations varying form 500 μM-100 mM and the maximum rise in the current was observed for 50 mM glucose concentration [82].

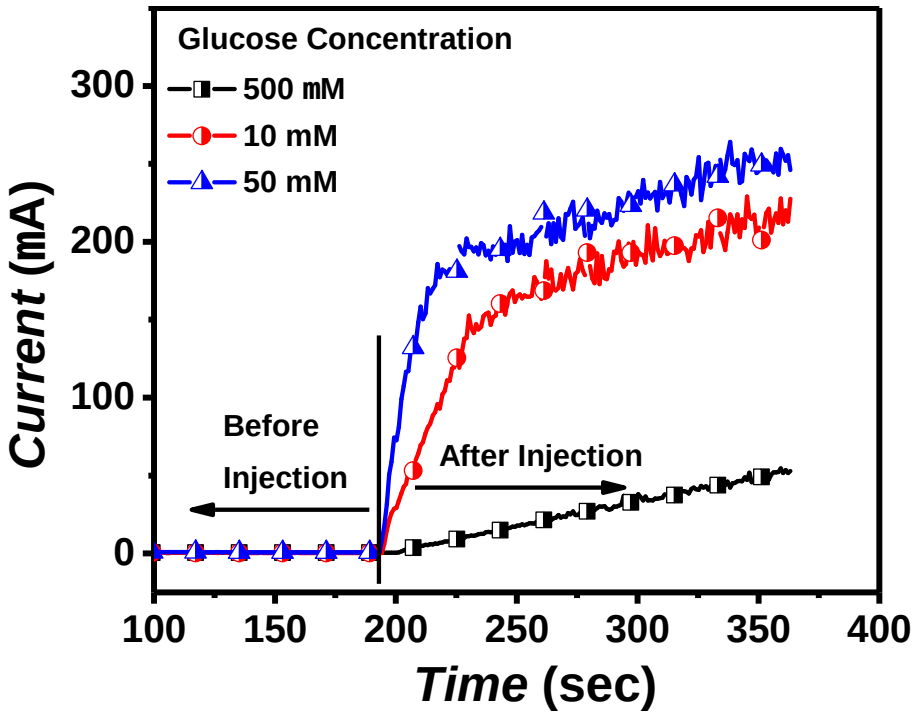

Fig. 3.3: **The assay curve for different glucose concentrations.**

The glucose assay curve has been shown in Fig. 3.3 which has exhibited highest slope i.e. $\partial I/\partial t_{max}$ = 14.06 μA-s^{-1} for 50 mM which correspond to the maximum reaction rate. No further increase in the current was observed with increase in the glucose concentration which has indicated that all the active sites of enzymes have been occupied by the glucose. The specific activity of enzyme was calculated by using the equation as follows:

$$SA = \frac{(\partial I/\partial t)_{max}}{(\partial I/\partial H_2O_2)}\left(\frac{5\times 60}{50}\right) \tag{3.1}$$

where, the multiplication factor $\frac{5\times 60}{50}$ in equation 3.1 was utilized to get the desired unit of the SA i.e. 5 to convert 200 µg into 1 mg, 60 to convert sec into min, and 1/50 to convert molar concentration of H_2O_2 into number of H_2O_2 molecules in 20 mL PBS. The calculated value of SA was estimated to be 120 U/mg (1U = 1 µmole of substrate converted per minute). The obtained SA value was well within the range of specified value by manufacturer which has confirmed the usable value of the enzyme activity [82].

3.2.4 Enzyme immobilization and quantification

Enzyme immobilization (attachment of enzymes to electrode surface) is an important step in order to fabricate the biosensor so that enzyme should not denature and leach out of the support matrix. Physical adsorption method was employed to immobilize GOx onto the electrode in which enzyme binds to the electrode via electrostatic force. The GOx stock solution (10 mg/ml) was prepared in 0.1 M PBS for the immobilization of GOx. After fabrication of PNN electrodes, 10 µL aliquot from GOx stock solution was dropped onto it and kept overnight in an incubator at 4 °C. Subsequently, the electrodes were washed with 0.1 M PBS to remove loosely adhered GOx molecules and this solution was utilized for the enzyme loading quantification. The as-prepared bio-electrodes were kept in an incubator at 4 °C, when not in use. GOx molecules show optical characteristics which have been used for the quantification of enzymes. Each GOx molecule has an aromatic residue called tryptophan, which results in intrinsic fluorescence in it. Thus, when the solution containing GOx molecule has been excited at 280 nm, the fluorescence emission was obtained at 330 nm. The intensity of fluorescence emission at 330 nm was observed to be directly proportional to GOx concentration in the solution which has been directly used for enzyme quantification [55].

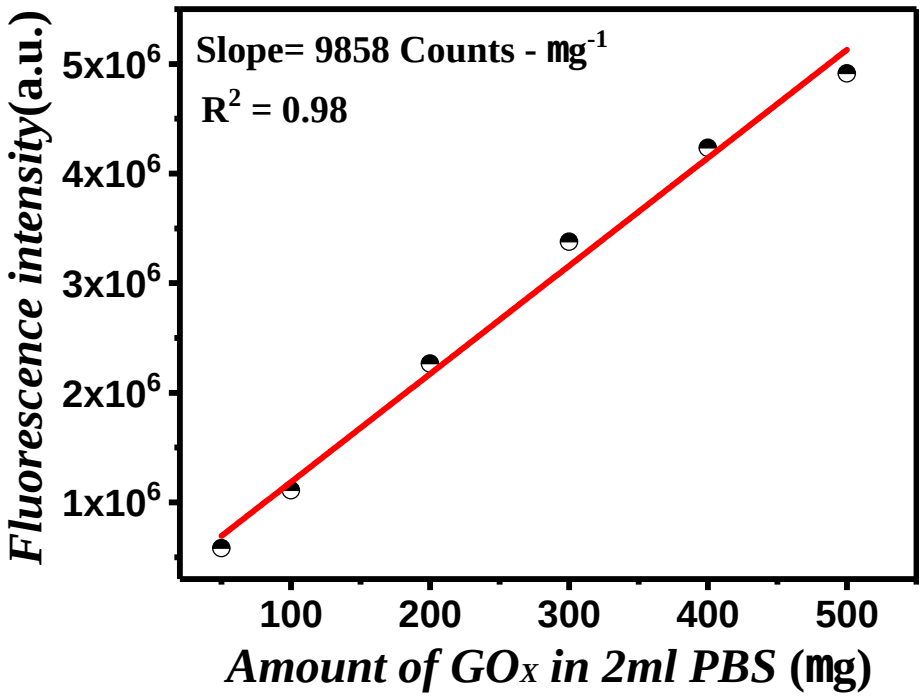

Fig. 3.4: **The linear calibration curve of fluorescence emission intensity obtained for known amount of GOx in PBS.**

A linear calibration curve as shown in Fig. 3.4 was obtained by measuring the fluorescence intensity corresponding to the known amount of GOx in 0.1 M PBS. Further, fluorescence was taken for PBS containing unadhered GOx molecules. Using the fluorescence intensity corresponding to unadhered GOx molecules and the calibration curve, amount of unadhered GOx was estimated. A known amount of enzyme (100 µg) has been immobilized over each electrode. Finally, the amount of enzyme immobilized over each electrode was determined by taking the difference of known and the calculated amount of unadhered enzymes.

3.3 Results and Discussion

3.3.1 Surface morphology and conductivity studies

To investigate the influence of different dopants *viz.* DBSA, MeSA, p-TSA, and $LiClO_4$ on the morphology of PPy electrodes, FESEM characterization was performed. As observed in FESEM images shown in Fig. 3.5, only granular morphology of PPy was obtained with the addition of DBSA. Additionally, with the incorporation of MeSA and p-TSA as the dopant, only granular surface morphology was observed. The obtained morphologies corresponding to DBSA, MeSA, and p-TSA were attributed to the low pH value (acidic nature of the dopants) of the electrolyte solution (pH-$\sim$2.5-3) which may have hindered the nanostructured growth. Further, the addition of $LiClO_4$ has shown a significant variation on the PPy morphology. As can be observed in FESEM images, high-density Polypyrrole nanofibers network (PNN) was obtained for PPy-$LiClO_4$ electrode which was realized to be favourable support matrix for the immobilization of GOx. Thus, $LiClO_4$ was chosen as a dopant for further study and its concentration was varied from 1-70 mM during the electropolymerization of PPy. To investigate the influence of $LiClO_4$ concentration on PNNs morphology and conductivity, chronoamperometric response recorded during electrodeposition has been analyzed. Figure 3.6 shows the chronoamperometric response of as-fabricated PNNs representing three regions of growth kinetics. The inset of Fig. 3.6 shows the current response of PNN-1 during polymerization defining three regions of the growth process. Initially, the abrupt decrease in current (Region 1) shows bulk film formation, followed by an increase in current (Region 2) due to oxidation of Pyrrole into radical cations

demonstrating the enhancement in surface area (nanostructure growth) and finally the stabilized current (Region 3) represents constant growth rate [83]. It is clearly visible from Fig. 3.6, that the anodic charge during PNN growth was dependent on $LiClO_4$ concentration and was found to increase with the increment in $LiClO_4$ concentration. The enhanced anodic current is directly related to the polymerization rate of Pyrrole which favors the longer fibrous growth [34] thereby resulting in the improved surface to volume ratio [83]. This indicates towards the correlation between $LiClO_4$ concentration and aspect ratio.

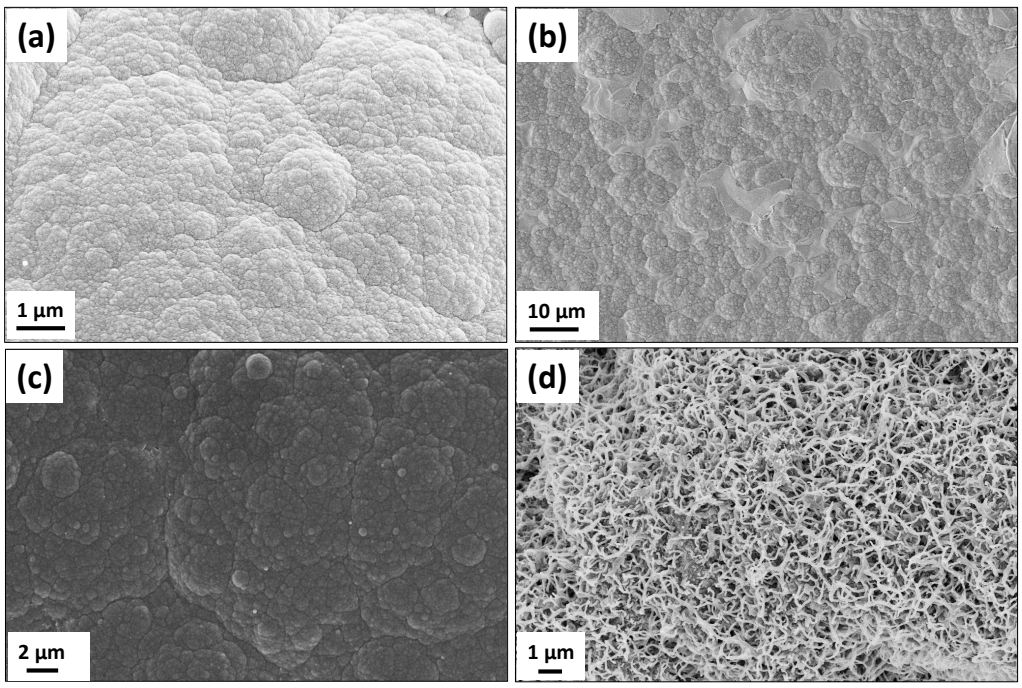

Fig. 3.5: **FESEM images of PPy doped with 70 mM concentration of (a) DBSA (b) MeSA (c) p-TSA (d) $LiClO_4$.**

Furthermore, to study the surface morphologies of fabricated PNNs, FESEM characterization was performed. Figure 3.7 (a-d) shows top view FESEM images of potentiostatically grown PPy films corresponding to PNN-1, PNN-10, PNN-50, and PNN-70 respectively. It is clear from FESEM images that nanostructured PPy films had interconnected nanofibrous growth for all concentrations of $LiClO_4$.

Figure 3.8 (a-d) displays cross-sectional view of PNNs which shows that initially bulk Polypyrrole film has been grown followed by nanofibrous network formation which is in agreement with the chronoamperometric response during growth (Fig. 3.6). The nanofibers length for PNN-1 was observed to be variable across the surface as evident from Fig. 3.7 (a). Thereafter, on increasing the concen-

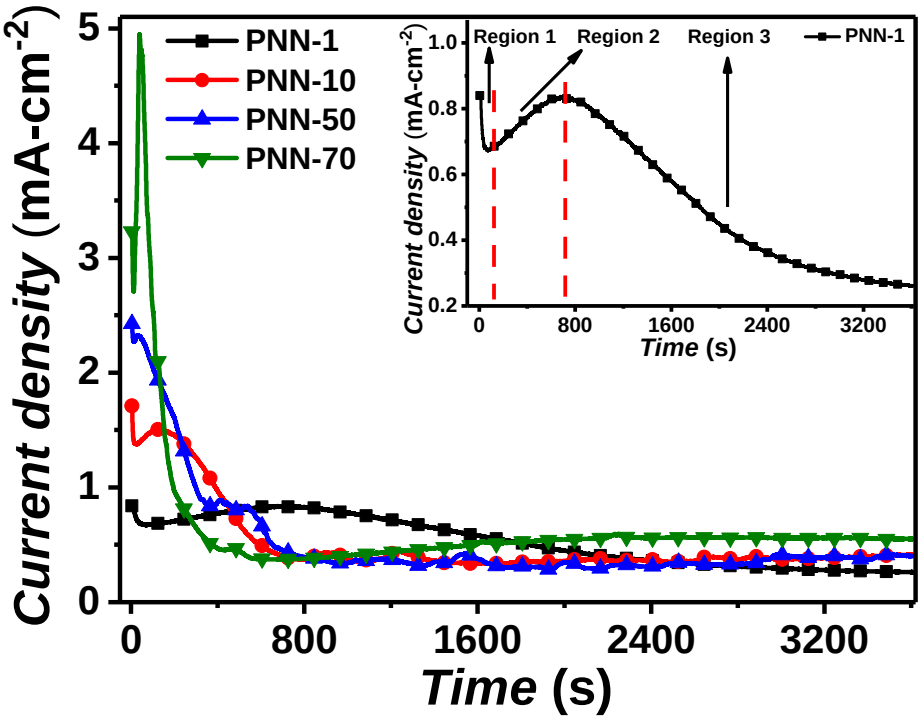

Fig. 3.6: **Chronoamperometric response of PNNs during electropolymerization of Polypyrrole synthesized at 0.85 V for 3600 s in aqueous solution of 0.1 M Py monomer, 0.1 M PBS (pH-6.8) and 1 mM (PNN-1), 10 mM (PNN-10), 50 mM (PNN-50), and 70 mM (PNN-70) concentration of $LiClO_4$. Inset shows three regions of growth kinetics (PNN-1).**

tration of $LiClO_4$ in PNN-10 and PNN-50, nanofibers growth along with patches of PPy bulk at some places has been observed. For highest concentration of $LiClO_4$ i.e. in PNN-70 homogeneous distribution of high-density nanofibers was obtained as clear from Fig. 3.7 (d). The nanofibrous growth with the improved surface to volume ratio ensures less hindered charge transport, high specific surface area, and enzyme loading. It was observed that the diameter and length of nanofibers have been increased from PNN-1 to PNN-70.

The diameter distribution of randomly selected 50 nanofibers from FESEM images was calculated using image processing toolbox of MATLAB. Histogram plot of the statistical variation in the diameter has been shown in Fig. 3.9, which clearly revealed that average diameter of nanofiber increases upon addition of $LiClO_4$ in the electrolyte solution. It was observed that with an increase in $LiClO_4$ concentration from 1 mM to 70 mM, the average diameter of nanofibers varied from 95 nm to 175 nm and was found to be maximum for 70 mM $LiClO_4$ concentration which is in accordance with the FESEM images. High-density long nanofibers were obtained for PNN-70 which is prerequisite for higher enzyme loading. Another important

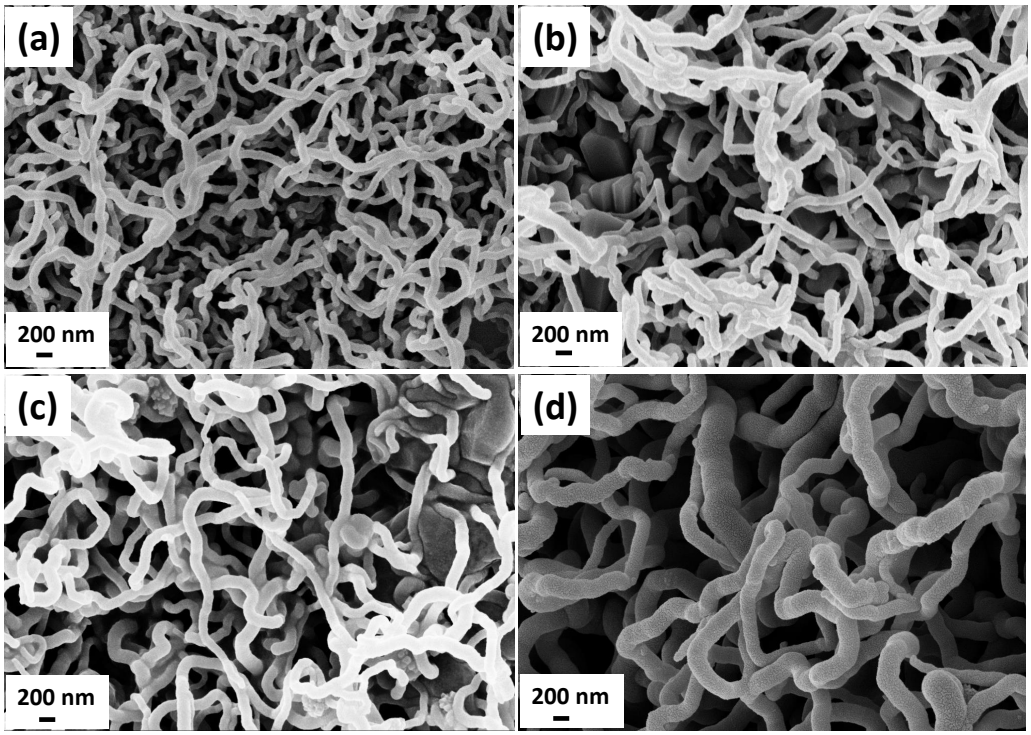

Fig. 3.7: **FESEM images showing top view of (a) PNN-1 (b) PNN-10 (c) PNN-50 (d) PNN-70.**

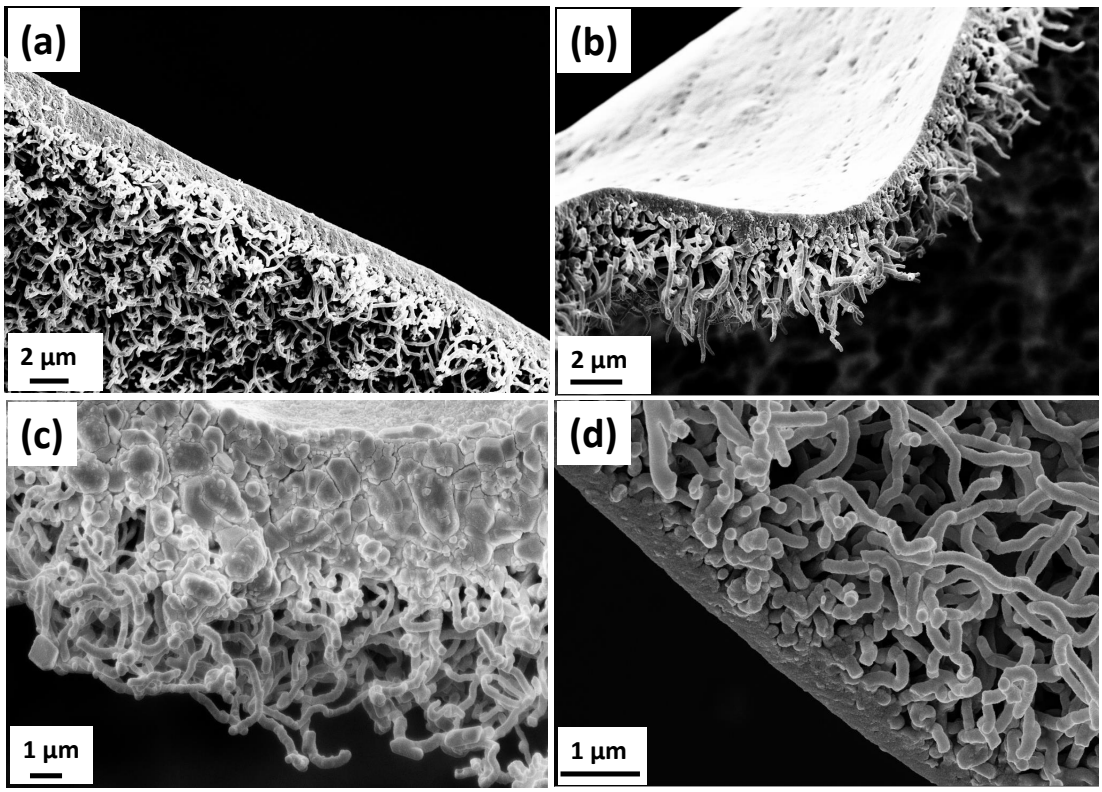

Fig. 3.8: **FESEM images showing cross sectional view of (a) PNN-1 (b) PNN-10 (c) PNN-50 (d) PNN-70.**

aspect of increasing $LiClO_4$ concentration was to improve the PNNs conductivity which is evident from the chronoamperometric response (Fig. 3.6) during elec-

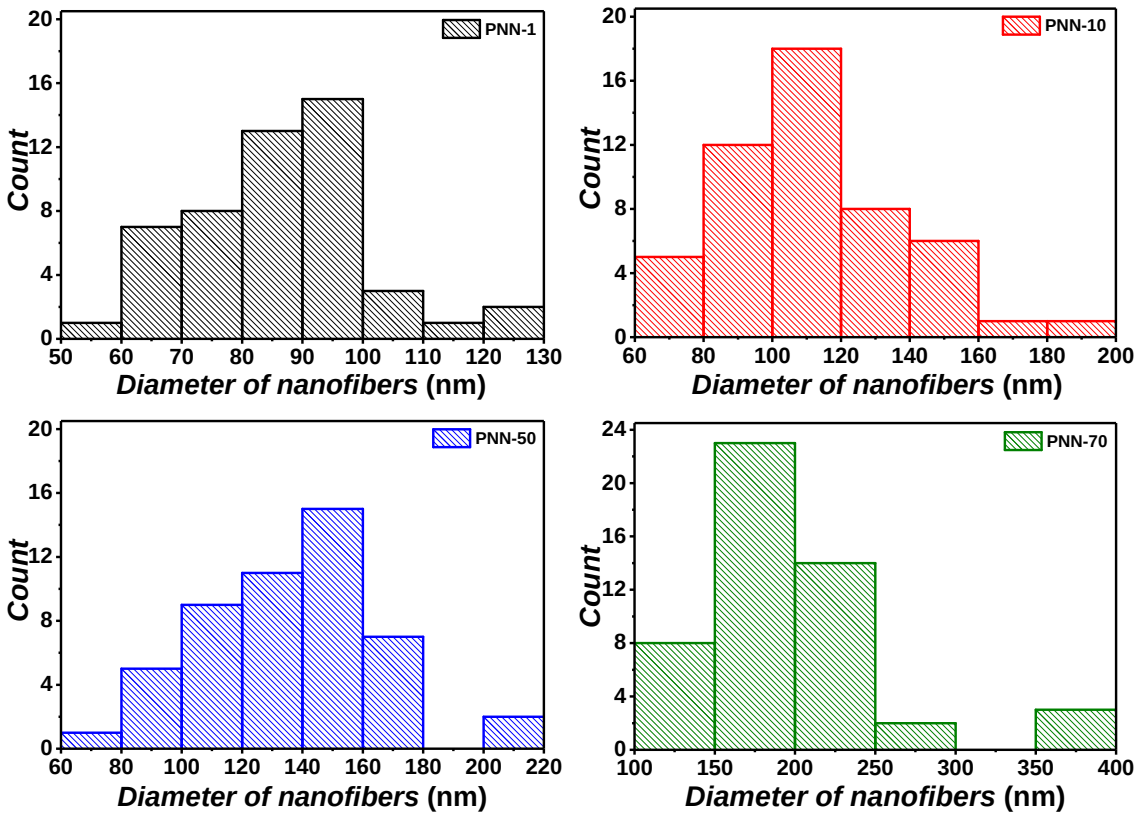

Fig. 3.9: **Histogram plot showing diameter distribution of PNN-1, PNN-10, PNN-50, and PNN-70.**

trosynthesis of Polypyrrole. With the increase in $LiClO_4$ concentration, the higher anodic charge was observed. This indicated towards higher conductivity of PNNs with increment in $LiClO_4$ concentration, which was further confirmed by cyclic voltammetry and electrochemical impedance spectroscopy studies.

3.3.2 Electrochemical characterization

Cyclic voltammetry

Furthermore, to investigate the surface area and conductivity of as prepared PNNs with increasing dopant concentration, cyclic voltammetry has been performed in a solution of 5 mM $K_3Fe(CN)_6$, $K_4Fe(CN)_6$ as redox couple containing 0.1 M KCl in 0.1 M PBS. All, as prepared electrodes were scanned at a scan rate of 10 mV/s and the potential of the working electrode was swept from -0.2 V to 0.7 V. Figure 3.10 shows cyclic voltammogram of all the PNNs in the presence of redox couple. The well-defined redox peaks obtained in each case can be attributed to the electroactivity of the PNNs. The increment in redox peak current was observed from PNN-1

to PNN-70 in the increasing order of the respective $LiClO_4$ concentrations. This enhancement in the redox peak currents further verifies the observed improvement in the surface area of the electrodes [58, 79, 84] as clear from FESEM images and chronoamperometric responses of PNN electrodes. For PNN-70 current was significantly improved as compared to other electrodes owing to its highest surface area [58, 79, 83, 84].

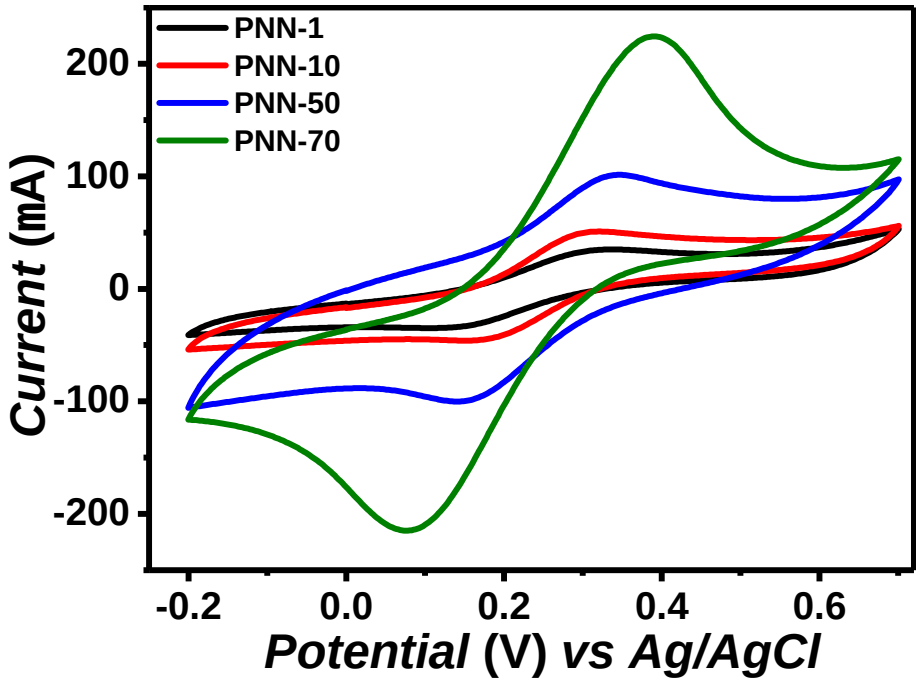

Fig. 3.10: **Cyclic voltammograms of PNNs (PNN-1 to PNN-70) recorded in 5 mM $K_3Fe(CN)_6$, $K_4Fe(CN)_6$ redox couple containing 0.1 M KCl in 0.1 M PBS (pH-6.8) at a scan rate of 10mV/s.**

Further, to calculate the electroactive surface area of each PNN (PNN-1 to PNN-70), CVs of all the electrodes were recorded in 5 mM $[Fe(CN)_6]^{3-/4-}$ containing 0.1 M KCl in 0.1 M PBS (pH 6.8) at different scan rates varying from 10 to 150 mV/s (shown in Fig. 3.11 (a-d)). The anodic peak currents (I_{pa}) were obtained from cyclic voltammograms (CVs) at different scan rates. The I_{pa} of as prepared PNNs has been shown in the inset of Fig. 3.11 (a-d) and were observed to be linearly proportional to the square root of scan rate ($\sqrt{v}$) (R^2=0.99) for each configuration. The I_{pa} vs $\sqrt{v}$ obtained from CV was used to determine the effective surface area of the electrodes using Randles-Sevcik equation (equation 3.2) in redox processes [58].

$$I_{Pa} = 2.69 * 10^5 * n^{3/2} * A_{eff} * \sqrt{D} * \sqrt{v} * C_0 \tag{3.2}$$

where D is diffusion coefficient (7.26×10^{-6} cm^2 s^{-1}) of 5 mM $K_3Fe(CN)_6$ in 0.1 M KCl, n refers to number of electron (n=1) involved in half reaction, A_{eff} is effective surface area of the electrode, v is the scan rate at which the potential was swept, and C_0 refers to the concentration of $K_3Fe(CN)_6$ and $K_4Fe(CN)_6$ in solution [58].

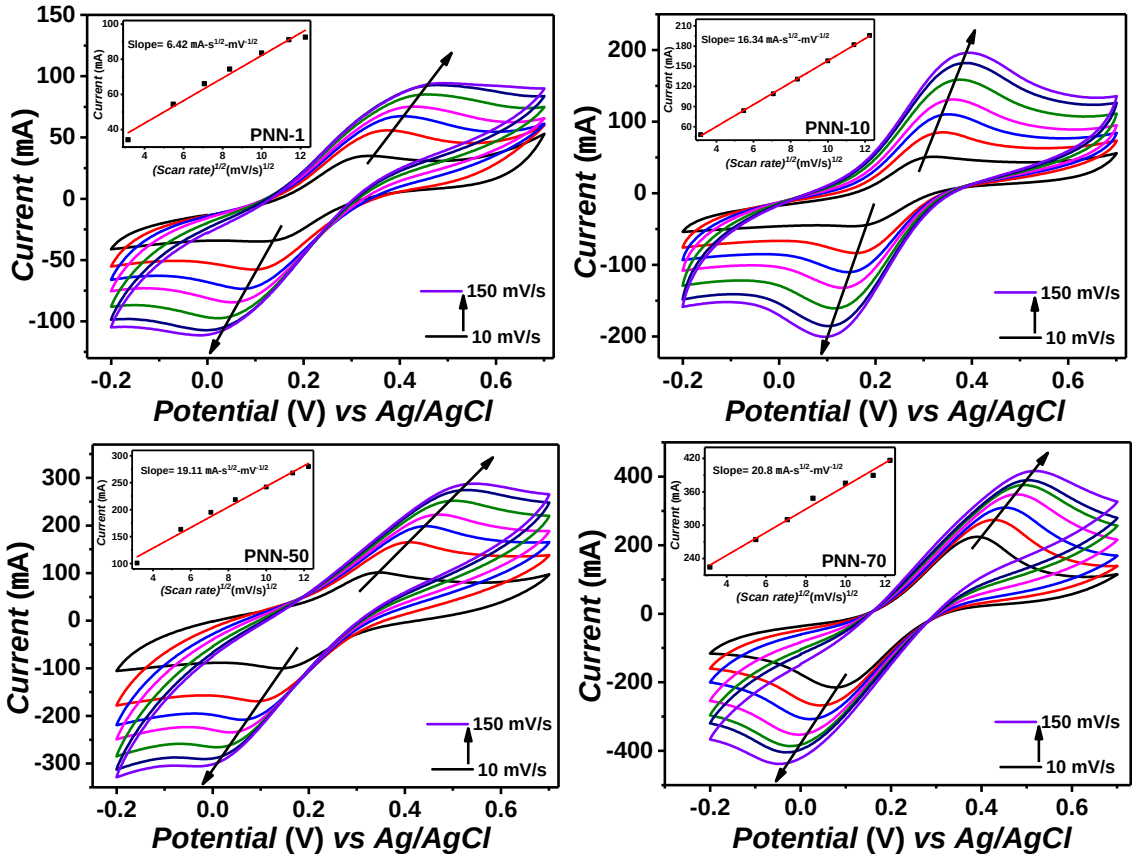

Fig. 3.11: **Cyclic voltammograms of PNNs recorded in 5 mM $K_3Fe(CN)_6$, $K_4Fe(CN)_6$ containing 0.1 M KCl in 0.1 M PBS (pH-6.8) at various scan rates (10-150 mV/s). Inset of Fig. 3.11 correspond to linear relation curves of I_{pa} (µA) vs $\sqrt{v}$ (mV/s) for PNN-1, PNN-10, PN-50, and PNN-70 respectively.**

The estimated values of the effective surface area for PNN-1, PNN-10, PNN-50, and PNN-70 were found to be 0.056, 0.14, 0.166, and 0.18 cm^2 respectively. The effective electroactive surface area calculated by Randles Sevcik equation was highest for PNN-70 and it was ~3.2 times higher as compared to PNN-1. Additionally, the increment in oxidation current with increased $LiClO_4$ concentration indicates towards highest conductivity for PNN-70 electrode which was further confirmed by EIS study.

Electrochemical impedance spectroscopy (EIS)

EIS was employed to investigate the interfacial behavior of electrode and electrolyte such as solution resistance (R_S), double layer capacitance (C_{dl}), charge transfer resistance (R_{ct}), and diffusion resistance (Warburg impedance) [85, 86]. EIS of Polypyrrole films (PNNs) was performed in 0.1 M PBS containing 5 mM $K_3Fe(CN)_6$ and $K_4Fe(CN)_6$ at an open circuit potential of 0.24 V. Prior to EIS measurements, open circuit voltage of 0.24 V was applied for 15 min to reach the equilibrium condition between electrode and electrolyte solution [87]. After equilibrium condition, the small input signal of 10 mV amplitude was applied to PNNs and impedance spectra (Nyquist plot) were recorded for a frequency range from 100 kHz to 0.1 Hz.

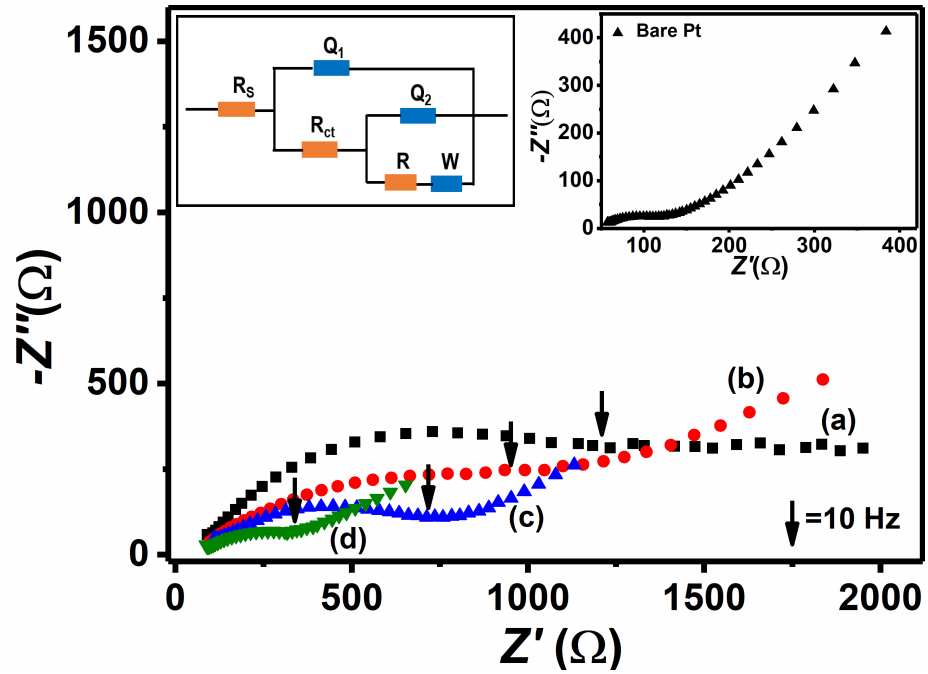

Fig. 3.12: **Nyquist plot of PNNs recorded in 5 mM $K_3Fe(CN)_6$, $K_4Fe(CN)_6$ redox couple into 0.1 M PBS with pH 6.8. Inset show Nyquist plot of bare Pt and equivalent electrical circuit used to fit Nyquist plot.**

The Nyquist plot of PNN-1 to PNN-70 has been shown in Fig. 3.12 and its inset shows the same for bare Pt electrode. Nyquist plot comprises of a semicircle part at higher frequencies and a linear part at lower frequencies representing electron transfer rate and diffusion controlled process, respectively. The diameter of semicircle part represents R_{ct} which relates to the conductivity of the film [88–90] and depressed semicircle in the high-frequency region has been corroborated to the increased roughness of the electrode surfaces [91]. For all PNNs, the obtained Nyquist plot was fitted to an equivalent electrical circuit using ZSimpWin 3.2. Each

Nyquist plot fits well to equivalent electrical circuit model of $R_S(Q_1(Q_2(RW)))$ (inset of Fig. 3.12). Table 3.1 shows the extracted equivalent circuit parameter values for bare Pt and as prepared PNNs.

The R_S value for all the electrodes was observed in the range from 40-55 Ω as shown in Table 3.1. The other circuit elements i.e. Q_1 and Q_2 have been defined as constant phase element (CPE) which corresponds to non-ideal double layer capacitance at the interface. The deviation from ideal capacitor behavior was represented by the value of n (=1). Among all the PNNs, both Q_1 and Q_2 corresponding to double layer capacitance at the interface were observed to be maximum for PNN-70. The enhancement in Q from PNN-1 to PNN-70 was attributed to decrease in the thickness of electronic double charge layer at the interface [86]. Moreover, for PNN-1 the value of R_{ct} was found to be 1341 Ω. Further with the increase in $LiClO_4$ concentration, R_{ct} value has been found to decrease with a minimum value of 385.1 Ω for PNN-70. This significant reduction in R_{ct} value from PNN-1 to PNN-70 represents a radical electron transfer process for PNN-70 which has been attributed to the highest conductivity of PNN-70. Additionally, suppression in a semi-circle from PNN-1 to PNN-70 represents the increment in the surface area of PNN-70.

3.3.3 Enzyme immobilization and quantification

To confirm the electroactivity of immobilized enzyme over the prepared electrode with the highest surface area (PNN-70), cyclic voltammetry was performed in 0.1 M PBS at a scan rate of 10 mV/s. Figure 3.13 shows the cyclic voltammetry of PNN-70 (without GOx) and the immobilized GOx over PNN-70 (PNN-70/GOx).

Table 3.1: **EIS parameters achieved by equivalent circuit of bare Pt electrode, PNN-1, PNN-10, PNN-50, and PNN-70 in 0.1 M PBS solution containing 5 mM $[Fe(CN)_6]^{3-/4-}$ (1:1).**

Electrode	R_S (Ω)	$Q_1(CPE_1)$ (S-sec^n)	n_1	R_{ct} (Ω)	W (S-sec^5)	$Q_2(CPE_2)$ (S-sec^n)	n_2
PNN-1	55.87	7.096E-6	0.5964	1341	0.000288	0.0007955	3.619E-6
PNN-10	51.33	5.535E-5	0.4425	1171	246.9	0.001004	0.4165
PNN-50	40.2	0.0001063	0.3126	430.7	0.002883	0.001134	0.8195
PNN-70	57.15	0.0001768	0.3906	385.1	4.378E19	0.002396	0.5632
Bare Pt	42.32	0.0002921	0.4788	123.2	0.003545	0.002141	0.657

As observed in CV, no peak was present for PNN-70 whereas PNN-70/GOx exhibited redox peaks at -0.52 V and -0.48 V. The redox peaks at -0.52 V and -0.48 V correspond to GOx(FAD) and GOx($FADH_2$) respectively, confirming the successful immobilization of GOx over PNN-70 [92]. The formal potential (E_0) of GOx was calculated by averaging the redox peak potentials and was found to be -0.50 V. The peak to peak separation voltage was 0.40 V attributing to quasi-reversible electrochemical reaction [93]. Thus the corresponding redox peaks shown in CV (Fig. 3.13) suggest the retained activity of GOx after immobilization onto PNN-70.

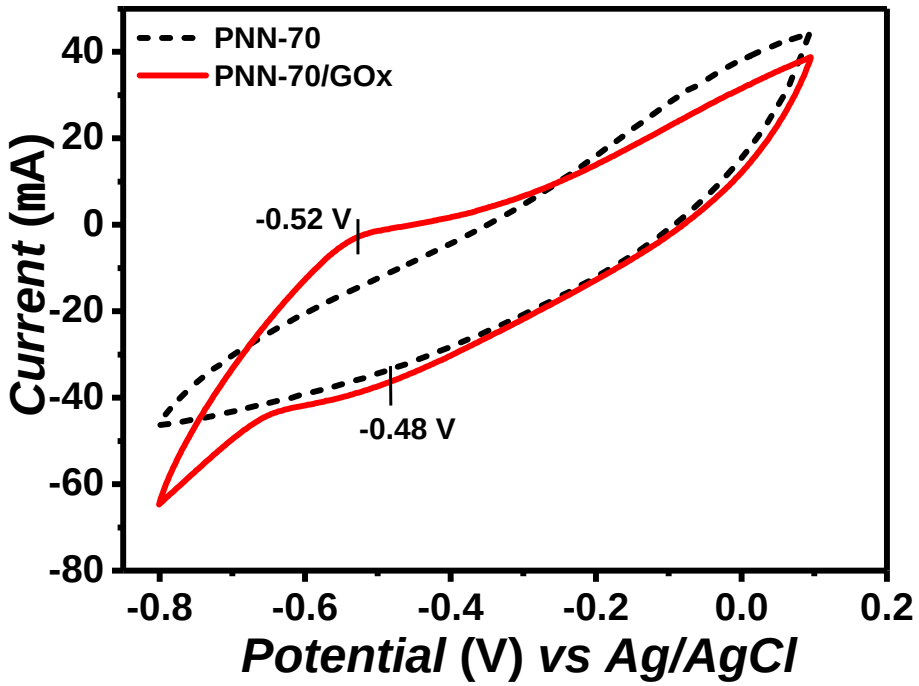

Fig. 3.13: **Cyclic voltammogram of PNN-70 (dotted lines) and PNN-70/GOx (solid lines) recorded in 0.1 M PBS (pH-6.8) at a scan rate of 10 mV/s.**

Moreover, the amount of enzyme loaded over the prepared electrode has been determined using fluorescence. Enzyme loading variation from PNN-1 to PNN-70 has been shown in Fig. 3.14 and it was observed to increase approximately by three times with increasing $LiClO_4$ concentration from 1 to 70 mM. As evident from FESEM images (Fig. 3.7) and CV characteristics (Fig. 3.10), the surface area was found to enhance with the increase in $LiClO_4$ concentration and one to one correspondence was observed between enzyme loading and surface area. For PNN-1 and PNN-10 surface area available for enzyme loading was approximately same therefore there is less improvement in enzyme loading for PNN-10 as compared to PNN-1. The highest surface area was obtained for PNN-70 which has provided

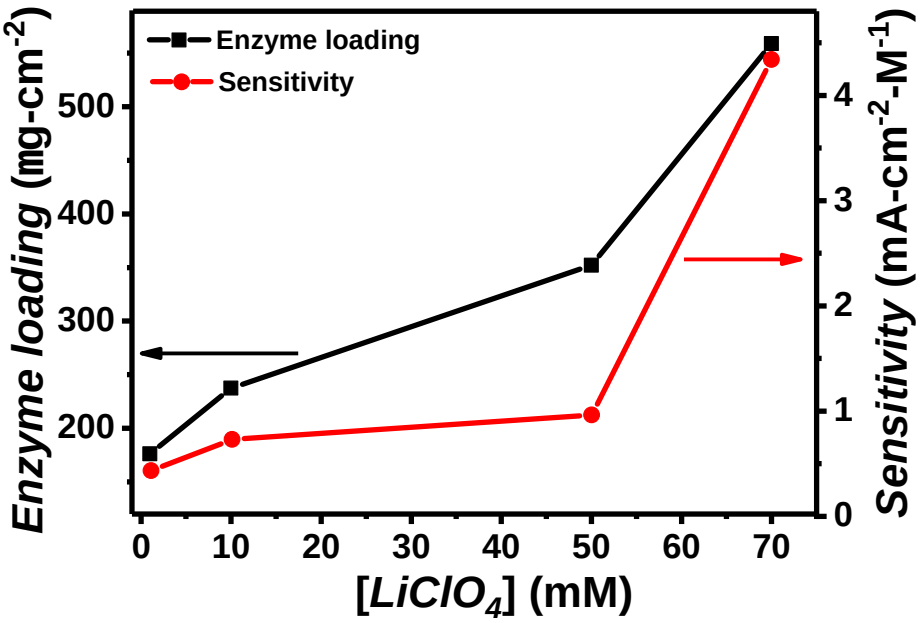

Fig. 3.14: **Enzyme loading and sensitivity variation of PNNs with $LiClO_4$ concentration.**

maximum enzyme loading (559 µg-cm^{-2}) for the same as clear from Fig. 3.14.

3.3.4 Biosensor characterization

Amperometric detection of glucose

The amperometric detection of glucose was performed in the three electrode electrochemical cell using Glass/Cr-Pt/PNN/GOx as working electrode. All the measurements were performed in 0.1 M PBS with pH 6.8 which was continuously stirred at 200 rpm using a mechanical stirrer. A constant potential of 0.7 V was applied to the working electrode and after reaching steady-state current, glucose aliquots were injected into the electrolyte solution for detection. For successive addition of glucose current response was recorded for all the as prepared electrodes. The steady state current density values corresponding to each glucose concentration were recorded to obtain calibration curve. Further, all the figure of merits of biosensor *viz.* sensitivity, response time, linear range and Km value were calculated from the calibration curve. Amperometric detection of glucose for as prepared electrodes *viz.* PNN-1 to PNN-70 has been shown in Fig. 3.15 (a-d). For each electrode, the current has been increased on successive addition of glucose. The current rise was observed upon injection of glucose into the electrolyte solution resulting in step like response. Calibration curves were obtained from these responses for all

the electrodes which have two regions: linear and steady-state region finally leading to a step-like response. At lower concentration of glucose instantaneous rise in current has been observed because initially, all the active sites of enzymes are available for detection. With the increase in glucose concentration, when all the active sites were occupied by glucose molecules, very small increment in current has been observed which leads to saturation region. The calibration curves follow typical enzyme kinetics which confirms proper immobilization with retained activity and strong enzyme affinity towards analyte.

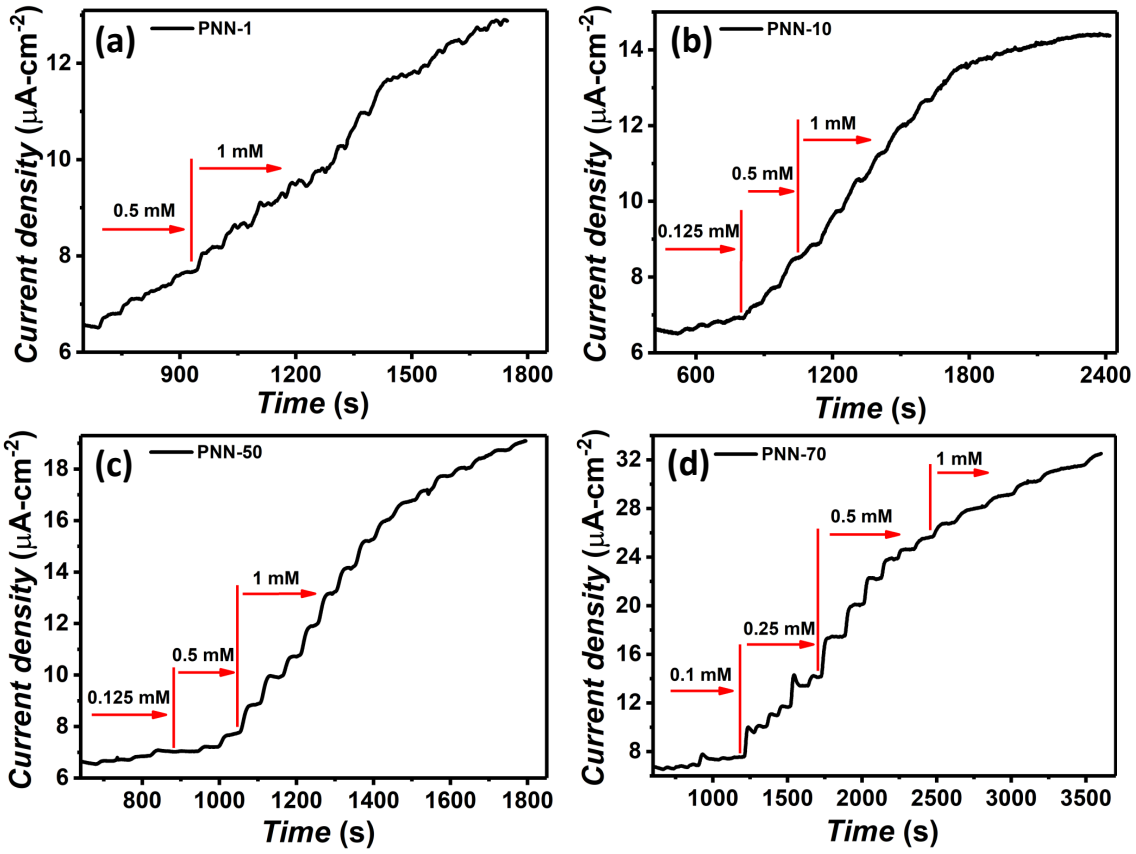

Fig. 3.15: **Amperometric detection of glucose for (a) PNN-1 (b) PNN-10 (c) PNN-50 (d) PNN-70.**

Figure 3.15 (a) shows the amperometric response for PNN-1 corresponding to electrode synthesized using 0.1 M Py and 1 mM $LiClO_4$ into PBS. Initially, 0.5 mM glucose has been injected into PBS, followed by 1 mM glucose injection with a time interval of 70 s. It was clearly visible from Fig. 3.15 (a) that step like response for PNN-1 was very noisy at higher glucose concentrations, which indicates towards poor performance of the as-fabricated biosensor. Further, the amperometric responses were improved with the increase in $LiClO_4$ concentration. The sensitiv-

ity of all fabricated biosensors was calculated with the help of calibration curve as shown in Fig. 3.16.

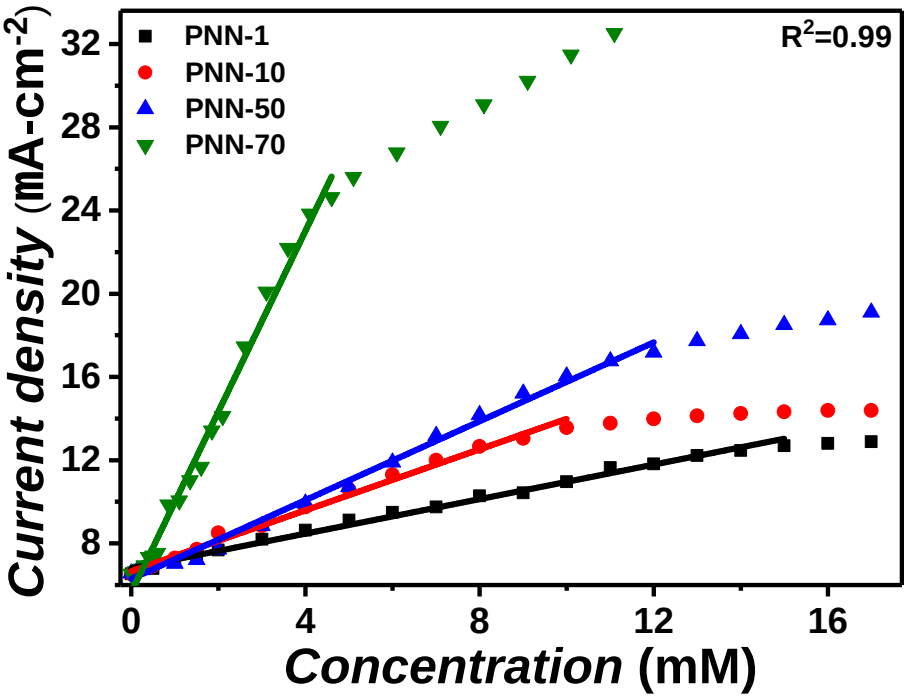

Fig. 3.16: **Calibration curves showing comparison of PNN-1, PNN-10, PNN-50, and PNN-70.**

Comparing the performance of all biosensors, appreciable improvement in sensitivity has been found for increased concentration of $LiClO_4$ in electrolyte solution during growth. Approximately ten times enhancement in the sensitivity has been observed from PNN-1 to PNN-70. Highest sensitivity of 4.34 mA-cm^{-2}-M^{-1} over a linear range of 0.1 - 4.6 mM was obtained for PNN-70/GOx. The sensitivity of fabricated biosensor (PNN-70/GOx) was found to be largely dependent on two parameters *viz.* the amount of enzyme loaded and improved charge transport to the electrode. The improved surface area for PNN-70 (confirmed by FESEM and

Table 3.2: **Comparison of PNN-1, PNN-10, PNN-50, and PNN-70 based glucose biosensor performance.**

Electrode	Sensitivity (mA-cm^{-2}-M^{-1})	Linear Range (mM)	Response Time (s)
PNN-1	0.414	0.5-15	~45
PNN-10	0.732	0.125-10	~45
PNN-50	1.00	0.125-12	~45
PNN-70	4.34	0.1-4.6	~45

CV) has been responsible for the enhanced enzyme loading resulting in the highest sensitivity for the same as evident from Fig. 3.14. In addition to higher enzyme loading, the reduced charge transfer resistance of PNN-70 (confirmed by EIS) has also played an important role in improving the sensitivity of PNN-70/GOx biosensor. Response time was calculated as the time taken to reach 90% of the steady-state value of current density from the glucose injection time. The calculated value of response time for each electrode was around 45 s. A comparison of all the figure of merits of the fabricated biosensors has been summarized in Table 3.2. It was observed that although the sensitivity and lower limit of detection have been found to improve from PNN-1 to PNN-70, the linear range of the device has decreased from 0.5 – 15 mM to 0.1 - 4.6 mM.

Michaelis Menten constant

The graphical method has been used for the estimation of K_m value of the fabricated PNN based electrodes [27]. Each observation obtained from amperometric response was represented by a straight line in K_m-V_{max} space. Median of all intersection points of these straight lines was determined to calculate the K_m value. The direct linear plot for PNN-70/GOx has been shown in Fig. 3.17. The obtained

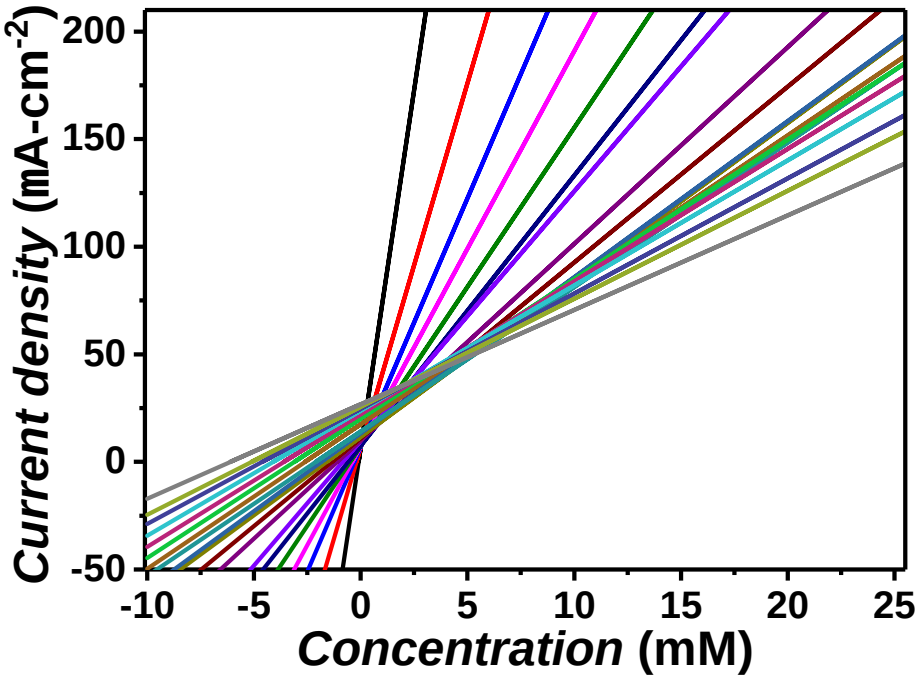

Fig. 3.17: **Direct linear plot of PNN-70 based glucose biosensor for estimation of K_m.**

values of K_m were found to vary between 1-3 mM for all the different types of electrodes and it was calculated as 1.3 mM for PNN-70 based biosensor, which indicates a strong affinity between enzyme and substrate molecules. The estimated K_m value (1.3 mM) was very less as compared to previously reported values [52, 94, 95]. Thus, the increase in $LiClO_4$ concentration has played a critical role in improving the properties of PNN electrodes (PNN-1 to PNN-70) which has led to improved performance of the biosensor.

Reproducibility, interference effect, and shelf life measurement

The reproducibility of the as-fabricated biosensor PNN-70/GOx was determined by comparing the amperometric response of four similarly prepared biosensor electrodes. The relative standard deviation (RSD) was found to be 14.1% for the same. Further, the influence of easily oxidizable electroactive interferents: ascorbic acid (0.1 mM) and uric acid (0.4 mM) was studied on the biosensing response of PNN-70 since these species are present in blood and may interfere in biosensor performance. Figure 3.18 shows the interference effect on sensing response of PNN-70. To study the effect of interferents' first 5 mM glucose was introduced into the cell and allowed to reach steady state. Subsequently, 0.1 mM ascorbic acid and 0.4 mM uric acid was introduced into the electrolyte solution which resulted in an increase of 0.27% and 2.6% in current density respectively.

GOx has been used as a model enzyme on the surface of PNN for the selective determination of glucose. It is one of the most widely explored enzyme due to its high catalytic activity, selectivity, and stability. For selective determination of glucose, Nafion has been widely accepted as a semipermeable membrane over GOx which also prevents the leaching of the enzymes from support matrix [96]. Moreover, use of various doped conducting polymers such as PPy in the form of bilayer has been proven to be attractive alternative for rejection of interferences [96–98]. Here, GOx was immobilized over PNN without using any anti-interference layer and the biosensor has shown very less interference effect. This anti-interference capability of the as-fabricated biosensor was attributed to the specificity and selectivity of GOx towards glucose. Additionally, to study the lifetime or storage stability of biosensor, amperometric response of PNN-70 has been recorded after 7 days. The device was observed to respond in a similar manner and the step-like re-

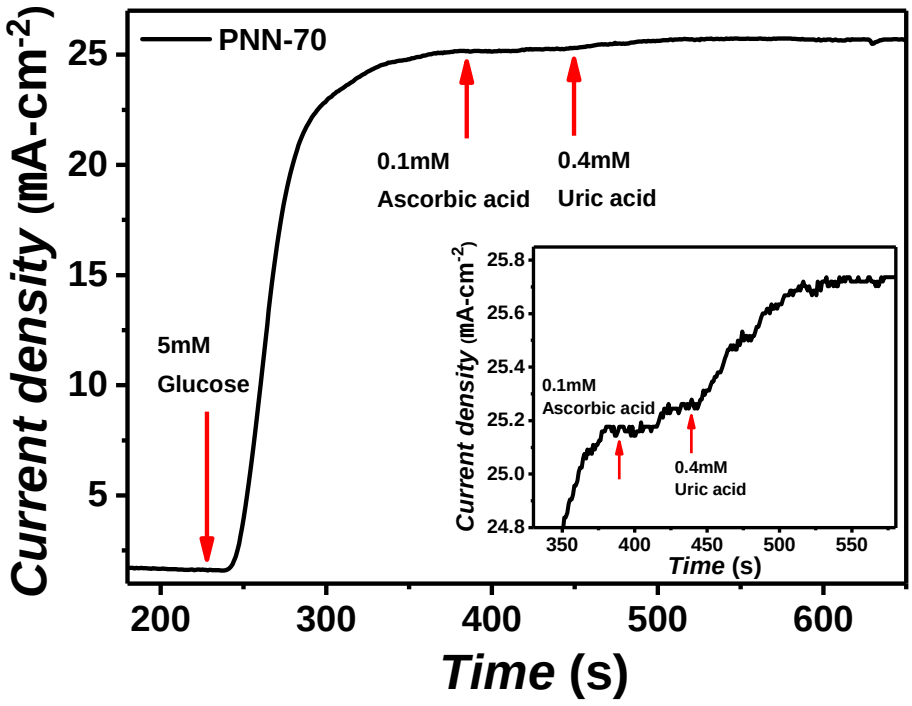

Fig. 3.18: **Interference effect of ascorbic acid and uric acid on biosensing response of PNN-70.**

sponse was obtained with a negligible change in sensitivity (3.99 mA-cm^{-2}-M^{-1}). Furthermore, it was found that biosensor has retained 92% of initial sensitivity which has shown a good stability because of biological compatibility of PNN and electrostatic binding provided between GOx and polycationic PNN. The polycationic nanofibers structure has provided the steady immobilization of GOx which in turn has helped in improving the stability of the physically adsorbed GOx along with the same conformation as of native GOx. Although, it was realized that sensitivity diminished on increasing the storage time due to leaching and denaturation of enzymes on PNN in long run. Thus, PNN has provided a stable and biocompatible environment for immobilization of GOx.

3.3.5 Enhancement of linear range of PNN based glucose biosensor

As observed in the previous section that the linear range of as-fabricated highest sensitivity glucose biosensor (PNN-70/GOx) is 0.1-4.6 mM. Further, to increase the linear range of the PNN-70 based glucose biosensor, a two-step immobilization technique was utilized. In this method, two immobilization techniques i.e. co-entrapment and physical adsorption immobilization has been used together and

two-step GOx immobilization was performed for the biosensor fabrication [99]. In the first step, taking the advantage of polymer matrix, co-entrapment method was used to incorporate the GOx molecules with the PPy followed by the physical adsorption of GOx onto the polymerized PPy electrode surface. Co-entrapment of GOx was carried out by mixing GOx (10 mg/ml) solution with the Py monomer solution during electrodeposition. The GOx was attached with the PPy during polymerization via electrostatic interaction between polycationic PPy and negatively charged GOx. Further, the physical adsorption of GOx was performed by adsorption of 10 µl GOx from 10 mg/ml GOx over polymerized PPy electrode surface. Finally, the as-fabricated biosensor was analysed by the amperometric detection method.

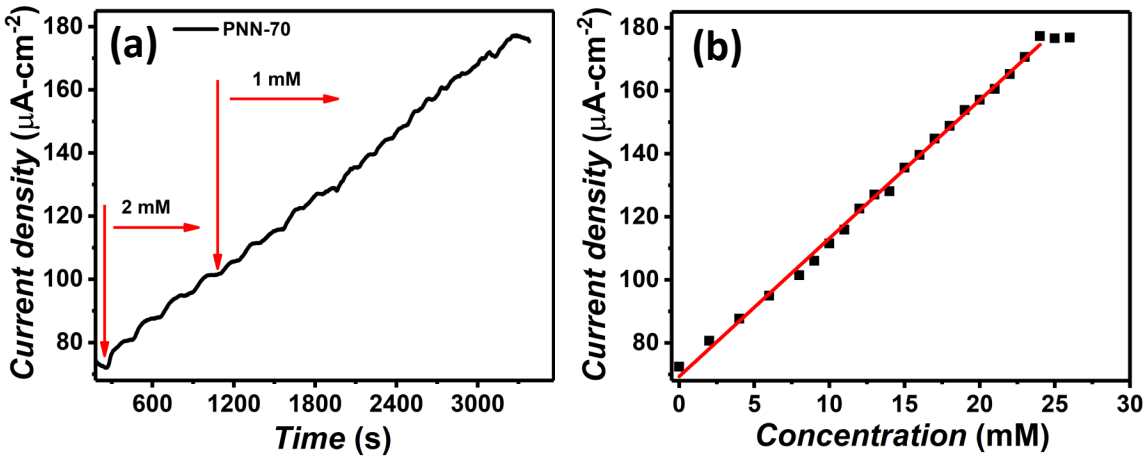

Fig. 3.19: **(a) Amperometric response (b) Calibration plot for PNN-70 based biosensor where two-step immobilization of GOx was carried out by co-entrapment and physical adsorption method.**

Figure 3.19 (a) shows the amperometric response of the PPy nanofibers based biosensor where the GOx was immobilized via a two-step method of co-entrapment and physical adsorption. Initially, 2 mM glucose concentration was injected into the electrolyte solution and a step like response was observed. After 8 mM glucose concentration, 1 mM concentration of glucose was injected and current rise was obtained. Corresponding to each glucose concentration, the current density was taken and plotted the calibration curve as shown in Fig. 3.19 (b). The slope of the calibration curve was calculated to determine the sensitivity of the biosensor. The sensitivity of the biosensor was 4.38 mA-cm^{-2}-M^{-1} with a linear range of 2-24 mM and a response time of 100 s. Thus, the linear range of the

biosensor was increased upto 24 mM with the two-step immobilization method. Although, the response time has been increased drastically for the same.

3.4 Conclusions

In summary, a PPy based enzymatic glucose biosensor has been fabricated by utilizing a simple one-step template free electrochemical approach. The improvement in surface area and conductivity of grown PNNs has played a significant role in the performance of glucose biosensor. The variation in $LiClO_4$ concentration was found to be responsible for the change in the conductivity and surface area of PNNs. With the increase in $LiClO_4$ concentration both: surface area and conductivity of PNNs has increased as evident from the study of chronoamperometric response during growth, FESEM, EIS, and CV. The higher surface area was an essential requirement for enhancement in enzyme loading which was found to be maximum i.e. 559 µg-cm^{-2} for PNN-70. The immobilization and activity of GOx onto PNN-70 was confirmed by FTIR and CV respectively. Furthermore, reduction in charge transfer resistance indicates towards the improved conductivity for PNN-70 as evident from R_{ct} value i.e. 358.1 Ω. Approximately three folds reduction in R_{ct} and increment in enzyme loading has been found for PNN-70 as compared to PNN-1, resulting in ten times increment in the sensitivity of PNN-70/GOx biosensor. Thus, the increased concentration of $LiClO_4$ was responsible for improved conductivity and higher surface area for PNN-70 which has led to a maximum sensitivity of 4.34 mA-cm^{-2}-M^{-1} with the response time approximately around 45 s over a linear range of 0.1 - 4.6 mM. The as-prepared biosensor has shown very good anti-interference capability for ascorbic acid (0.27%) and uric acid (2.6%), exhibiting high selectivity for glucose. Additionally, the linear range of the highest sensitivity biosensor was observed to increase upto 24 mM.

Chapter 4

Investigation of Dopant Effect on the Electrochemical Performance of 1-D Polypyrrole Nanofibers Based Glucose Biosensor

In the previous study, the surface area and electrochemical properties of PPy electrodes were tuned to improve the biosensor figure of merits. It was observed that the higher surface area facilitating the higher enzyme loading and improved electrochemical properties were responsible for improved biosensor performance. The dopant concentration variation was observed to have a significant effect on the PPy morphology and thereby influenced both surface area and electrochemical properties of PPy electrodes. Thus, for further investigation, the other dopant p-TSA concentration was also varied to probe into the morphological variations. In this chapter, we demonstrate a systematic study of the effect of two different dopants *viz.* Lithium perchlorate ($LiClO_4$) and para-Toluenesulfonic acid (p-TSA) on the performance of Polypyrrole (PPy) based enzymatic glucose biosensor. Both the dopants ($LiClO_4$ and p-TSA) were utilized with the aim of increasing the electrical conductivity of PPy films. The PPy nanofibers were synthesized over a Platinum coated glass substrate by electrochemical method. The morphological and electrochemical properties of PPy nanofibers utilizing template-free method have been tailored by dopant variation ($LiClO_4$ and pTSA) during electropolymerization. The as-

prepared PPy nanofibers (both PPy-$LiClO_4$ and PPy-pTSA) were utilized as a support matrix for enzyme attachment. The prepared enzymatic biosensors were later examined for the catalytic activity towards glucose oxidation using CV and amperometric method for detection of glucose. Both the morphological and electrochemical properties of PPy electrode have been observed to improve with PPy-pTSA, as compared to PPy-$LiClO_4$ electrode. The as-fabricated PPy-pTSA/GOx based glucose biosensor has demonstrated the highest sensitivity of 6.12 mA-cm^{-2}-M^{-1} with a linear range of 0.1-7.5 mM, which is better as compared to PPy-$LiClO_4$/GOx biosensor. Additionally, the as-prepared PPy-pTSA/GOx biosensor has presented good stability, selectivity, and reproducibility that validates the importance of the dopant effect in electrosynthesized PPy based biosensing applications.

4.1 Introduction

The template-free electro-synthesis method of PPy morphology has gained extensive interest due to its simplicity, large scale fabrication. The most important advantage of this method is the exclusion of the template, which has reduced the cost of fabrication and made the process easier as well. A wide variety of PPy nanostructures *viz.* nanofibers, nanorods, nanotubes, etc. have been reported to be easily synthesized by the electrochemical method which facilitates the growth of PPy nanostructures directly onto the electrode surface. The PPy morphology can be easily modified by varying the polymerization potential and time, monomer concentration, dopant size, and their concentration during the electropolymerization process [32, 36, 52]. The oxidized PPy has been reported to exhibit high electron affinity which is a prerequisite for the immobilization of negatively charged GOx over it via electrostatic interaction. The PPy nanostructures improve GOx immobilization by providing a high electroactive surface area which in turn enhances the performance of enzymatic electrochemical glucose biosensor. Thus the morphology and conductivity of PPy nanostructures were observed to be the major factors to influence the performance of biosensor [100]. The incorporation of different size anions during polymerization influences both the morphology and conductivity of PPy nanostructures. As reported, the modulation in the properties of PPy nanostructures can be obtained by various dopants *viz.* sodium dodecyl sulfate (SDS),

lithium perchlorate ($LiClO_4$), potassium nitrate (KNO_3), para-Toluene sulfonic acid (p-TSA), etc. [101]. In this regard, U. Paramo-Garcia et. al. [102] have discussed the thickness modulation of PPy films by different anionic dopants. G. Ozyilmaz et. al. [103] have presented the influence of p-Toluenesulfonic acid and Sodium p-Toluenesulfonate on PPy morphological properties. P. A. Palod et al. [52] reported the $LiClO_4$ doped PPy nanofibers for glucose detection. In this chapter, we have demonstrated the effect of two different size dopants *viz.* $LiClO_4$ and pTSA (where $LiClO_4$ is smaller size anion) on the morphology and electrochemical activity of the prepared PPy nanostructures. Here, we have prepared high electroactive bio-compatible PPy nanofibers with enhanced aspect ratio and improved electrochemical properties. The concentration of each dopant was varied and the best performing electrode corresponding to pTSA was compared to the same concentration of $LiClO_4$. Further, the PPy modified electrodes in case of both the dopants were immobilized with GOx and the electrocatalytic activities of both the as-prepared biosensors were compared towards glucose oxidation.

4.2 Experimental Details

4.2.1 Preparation of $LiClO_4$ and p-TSA doped PPy nanofibers electrode

The Pt (50 nm thickness) was deposited over the pre-cleaned glass substrates with an intermediate layer of 5 nm Chromium (Cr) (to improve the adhesion of Pt on glass) [104, 105] using DC magnetron sputtering. Further, PPy was deposited over the Pt-coated glass substrate using electropolymerization method. The Pyrrole (Py) monomer was distilled at 130°C before the electropolymerization process.

The electrolyte solution of 0.1 M Py and one of the investigated dopants *viz.* $LiClO_4$ and p-TSA in 0.1 M PBS (pH 6.8) were prepared. The concentration of both the dopants was varied from 1-70 mM for electrolyte solution preparation. The electrochemical deposition of PPy was executed using electrochemical workstation Autolab PGSTAT302N having three-electrode cell configuration as shown in Fig. 1. The cell consisted of an electrolyte solution where platinum coated glass substrate, platinum foil, and Ag/AgCl electrode have been utilized as working, counter, and reference electrode respectively. A constant potential of 0.85 V was applied to the

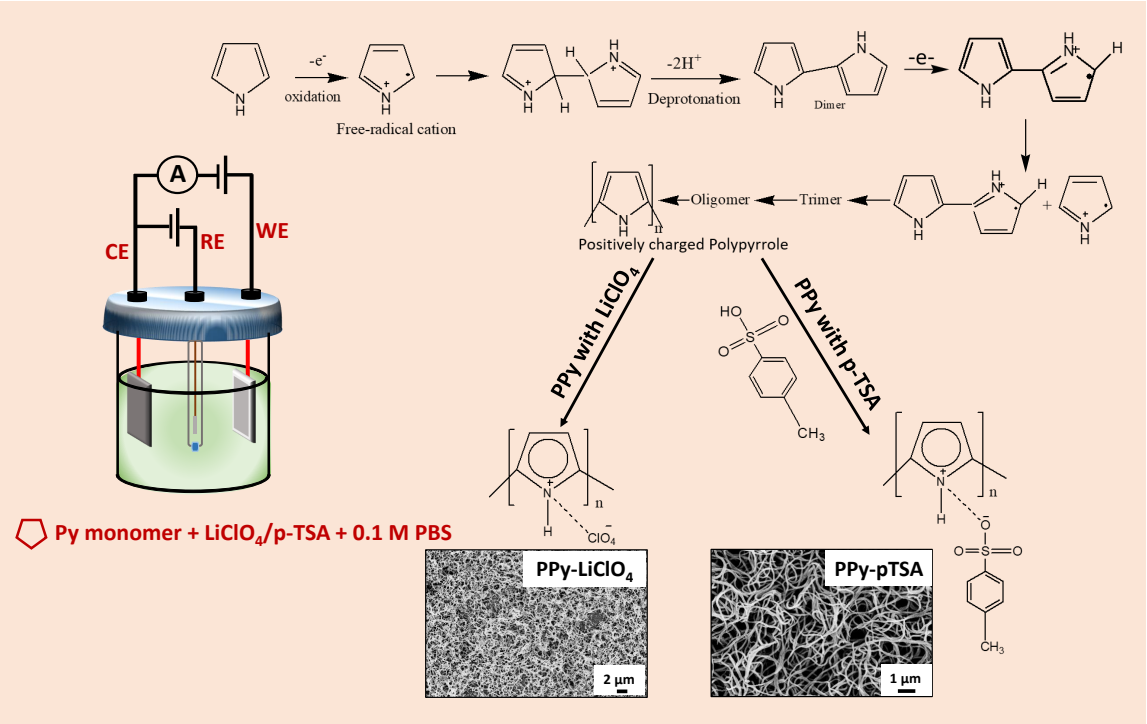

Fig. 4.1: **Schematic illustration of the electrochemical setup for Polypyrrole nanofibers growth process showing the mechanism of PPy formation with the incorporation of different dopants to PPy and surface morphology of formed PPy with $LiClO_4$ and p-TSA.**

working electrode for 3600 s to obtain PPy over a Pt-coated glass substrate. The morphology of electrosynthesized PPy was determined using Field Emission Scanning Electron Microscopy. The best performing electrode corresponding to 10 mM concentration of p-TSA was compared with the 10 mM concentration of $LiClO_4$ doped PPy electrode. The electrodes which have been prepared using $LiClO_4$ and p-TSA as dopants were named as PPy-$LiClO_4$ and PPy-pTSA respectively. Further, (GOx) was immobilized over the fabricated Glass/Pt/PPy electrode using physical adsorption immobilization method.

4.2.2 Enzyme immobilization and quantification

The attachment of GOx onto the fabricated electrodes PPy-$LiClO_4$ and PPy-pTSA was performed using a simple physical adsorption immobilization technique. This is the simplest process of enzyme immobilization in which enzyme binds to the electrode surface via electrostatic interaction between the positive charge on PPy and negatively charged GOx. In physical adsorption scheme, 10 μL GOx aliquot from a stock solution of 10 mg/mL prepared in 0.1 M PBS (pH 6.8) was dropped

onto PPy-$LiClO_4$ and PPy-pTSA electrodes and were kept in an incubator at 4 °C temperature. Both the types of electrodes were washed into PBS to collect loosely adhered GOx molecules. Further, this PBS solution was utilized for the estimation of GOx molecules attached to both the electrode surfaces. The optical characteristic of the GOx molecule was utilized to estimate the amount of enzyme loaded over the PPy-$LiClO_4$ and PPy-pTSA electrodes. A linear calibration curve corresponding to the known amount of GOx in 0.1 M PBS and its fluorescence intensity was obtained. Further, fluorescence intensity was measured for PBS containing unadhered GOx molecules for both the electrodes. Finally, the amount of unadhered GOx was estimated by using the calibration curve and the fluorescence intensity corresponding to unadhered GOx molecules. Thus the amount of enzyme immobilized over each electrode was estimated by taking the difference of the known amount of enzyme immobilized (100 μg) and the calculated unadhered enzymes.

4.3 Results and Discussion

The schematic illustration of PPy formation mechanism with the incorporation of dopants *viz.* $LiClO_4$ and pTSA has been presented in Fig. 4.1 which shows that when a potential is applied to the working electrode (dipped into the electrolyte solution of Py monomer and counter ion), the monomer units get oxidized and form radical cations. These radical cations eventually join with the other monomer unit or radical cation and form the oligomer units of PPy which in turn joins with the other radical cation and finally forms a positively charged PPy chain. The negatively charged dopants present in the solution gets attached to the positively charged PPy via electrostatic interaction and thus the anion incorporates within the PPy chain. Thus, the nature and size of the dopant ions incorporated during the polymerization process lead to the change in the morphology and electrical properties of the prepared PPy nanostructure [36] which were studied by FESEM and electrochemical characterizations respectively.

4.3.1 Surface characterization

To explore the effect of dopant concentration and the nature of dopant on the electropolymerized PPy morphology, FESEM images were taken. Figure 4.2 shows the

morphological variations for different concentrations of p-TSA. Uniform and high-density nanofibers have been observed for 10 mM concentration of p-TSA (Fig. 4.2 (b)) as evident from FESEM images. It was found that on further increasing the concentration of p-TSA i.e. 50 mM and 70 mM (pH of electrolyte solution-$\sim$3), only granular structures have been formed on the electrode surface as shown in Fig. 4.2 (c, d).

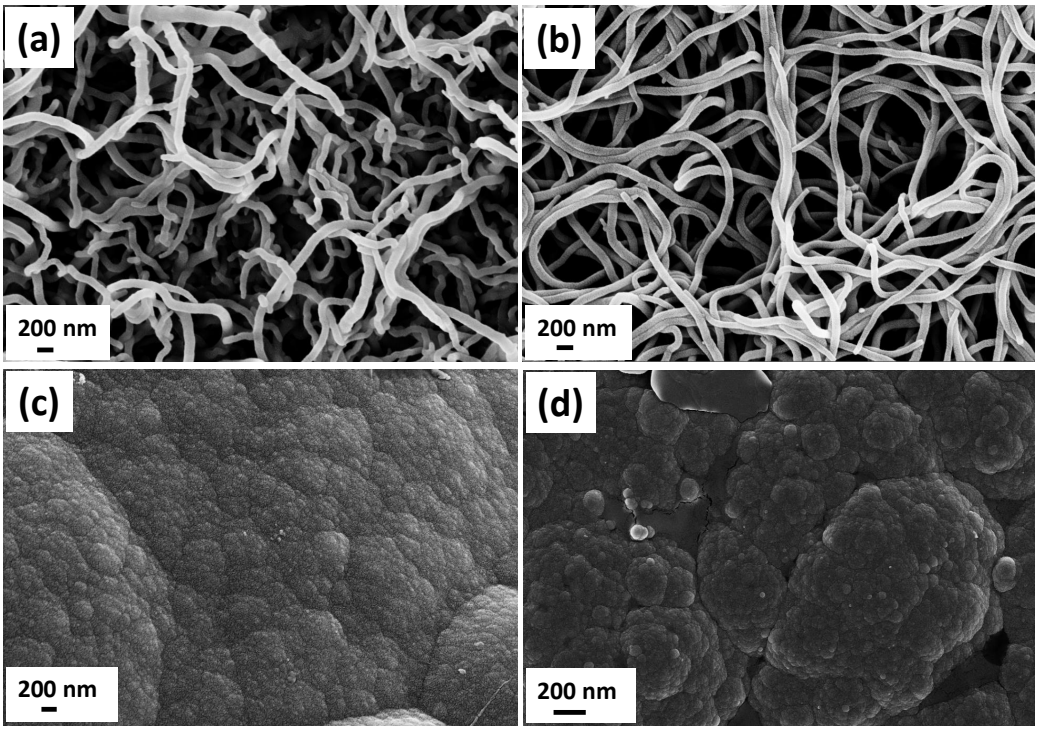

Fig. 4.2: **FESEM images of doped PPy nanofibers corresponding to (a) 1 mM (b) 10 mM (c) 50 mM, and (d) 70 mM concentration of p-TSA**

Figure 4.3 has shown the top view FESEM image of 50 mM p-TSA doped PPy morphology. A poor quality film having cracks were observed for 50 mM p-TSA concentration which has indicated that PPy morphology with higher p-TSA concentrations was not favourable for the enzyme immobilization. The PPy nanofibers formation has been observed in the presence of phosphate buffer solution (PBS) with a high pH value of the electrolyte solution [32, 34]. The presence of PBS facilitates hydrogen bonding between phosphate and pyrrole oligomers which favors the nanofibers formation [32]. The pH of the electrolyte solution was maintained at 6.8 without addition of any dopant. However, with the addition of pTSA as a dopant, the pH value was observed to reduce due to the acidic nature of pTSA. At the lower concentration of pTSA i.e. for 1 mM and 10 mM, the pH value of the electrolyte solution was found to decrease to 6 and 5.5 respectively and it was dras-

tically reduced to 4-2.5 at higher concentration of pTSA (for 50 mM and 70 mM). The reduced pH value at higher concentration of pTSA has hindered the growth of PPy nanofibers and was found to be responsible for the granular structure (2D structure) of PPy. The nanofibrous growth of PPy was obtained only at the lower concentration of pTSA. Furthermore, to probe into the effect of type of dopant, the morphology of PPy nanostructures synthesized using 10 mM concentration of $LiClO_4$ (same as of pTSA concentration) was investigated by FESEM characterization. Figure 4.4 (a, b) shows the top view FESEM images of PPy-$LiClO_4$ and

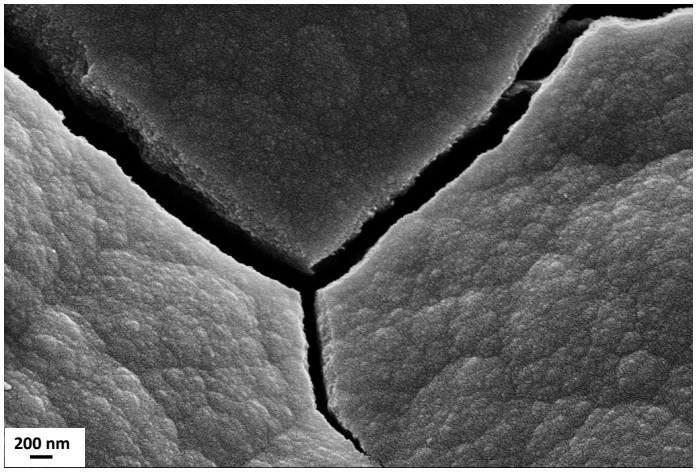

Fig. 4.3: **FESEM image showing top view of 50 mM doped PPy morphology.**

PPy-pTSA electrodes corresponding to 10 mM concentration of each dopant. As evident from the FESEM results, more uniform and high-density nanofibers have been grown for PPy-pTSA electrode as compared to PPy-$LiClO_4$ electrode which was further confirmed by the cross-sectional view of the same.

Figure 4.4 (c, d) have shown the cross-sectional view of PPy-$LiClO_4$ and PPy-pTSA electrodes respectively. The cross-sectional view of PPy-$LiClO_4$ and PPy-pTSA electrodes clearly demonstrates lesser density and shorter nanofibers for the Ppy-$LiClO_4$ electrode. However, for PPy-pTSA very long and high-density nanofibers have been obtained which can be attributed to the larger size of pTSA as compared to $LiClO_4$ [36, 102]. The obtained FESEM results have shown the significant effect of anion size on the morphology and density of PPy nanostructures.

The diameters of the fabricated nanofibers have been calculated by imtool of MATLAB. Figure 4.5 (a, b) have shown the histogram plot for diameter distribution of nanofibers for PPy-$LiClO_4$ and PPy-pTSA electrodes respectively. The distribution of nanofibers for both the electrodes was obtained by randomly selecting

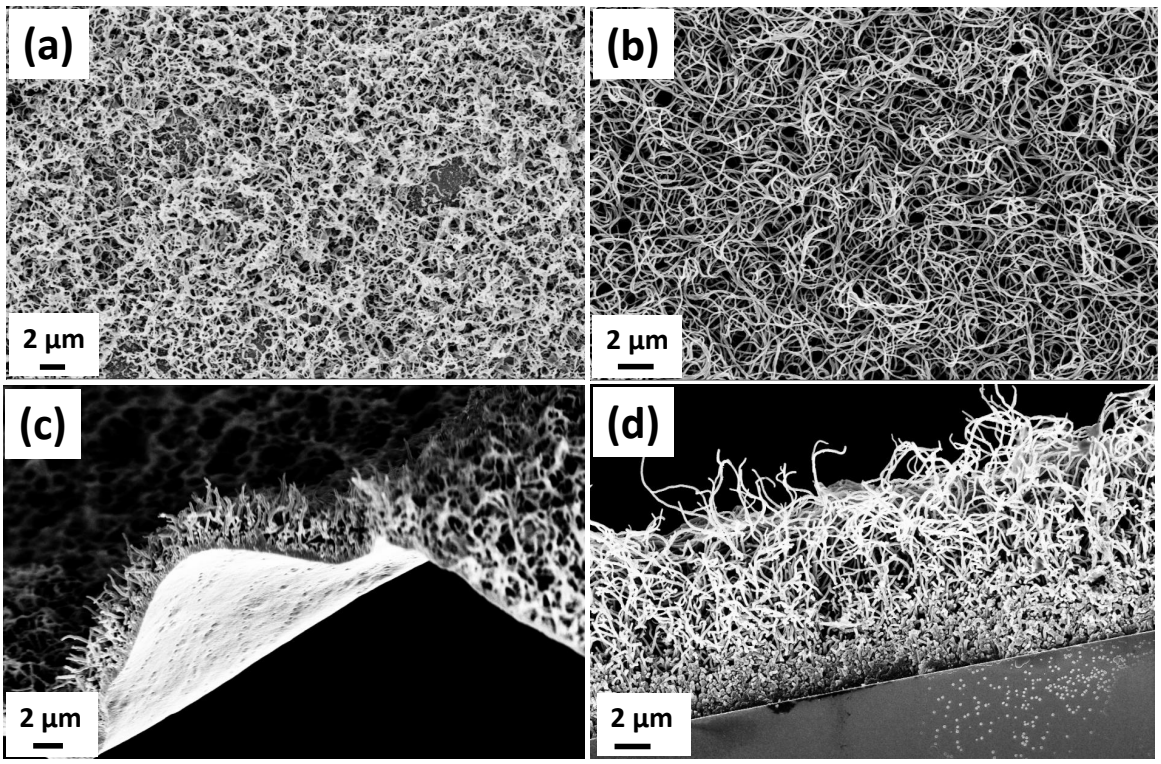

Fig. 4.4: **FESEM images showing top view of (a) PPy-$LiClO_4$ (b) PPy-pTSA and cross-sectional view of (c) PPy-$LiClO_4$ (d) PPy-pTSA nanofibers.**

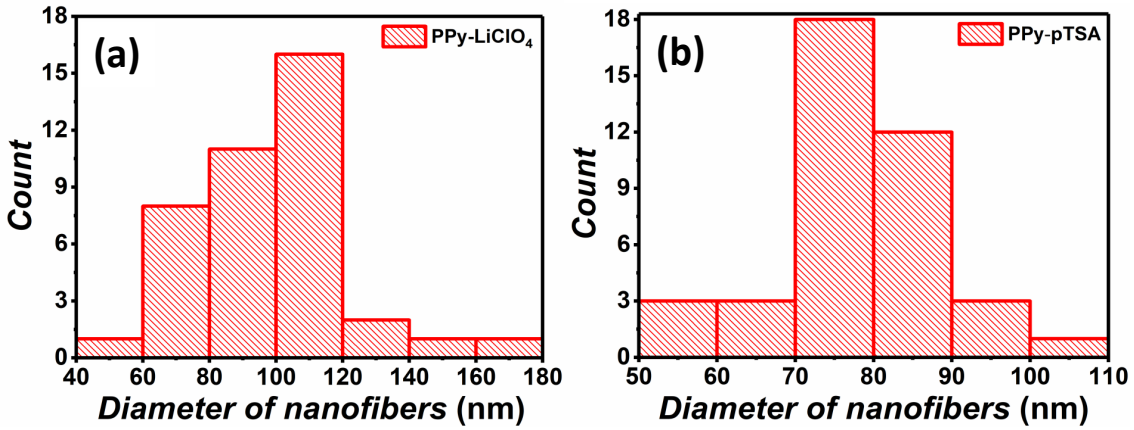

Fig. 4.5: **Histogram plot for diameter distribution of (a) PPy-$LiClO_4$ (b) PPy-pTSA nanofibers.**

approximately 50 nanofibers from the FESEM images. The diameter of PPy-$LiClO_4$ electrode was found to be in the range of 100-120 nm, while PPy-pTSA based electrode's diameter was in the range of 70-80 nm. Thus the observed results reveal that keeping the same concentration of both the dopants (rest other growth parameters were kept same) PPy-pTSA based electrode have facilitated nanofibers with very high aspect ratio, which in turn provide a higher electroactive surface area thereby improving biosensor performance.

4.3.2 Electrochemical impedance spectroscopy (EIS)

EIS is an effective technique to characterize the interfacial behavior of electrode and electrolyte solution. EIS was utilized to study the charge transfer capability of both PPy-$LiClO_4$ and PPy-pTSA based electrodes. In EIS, the solution resistance R_S, charge transfer resistance R_{ct}, Warburg impedance W and double layer capacitance C_{dl} defines the interface behavior of the electrode with the electrolyte solution [106]. To compare the behavior of both the electrodes, EIS of Ppy-$LiClO_4$ and PPy-pTSA was performed in an electrolyte solution of 5 mM $K_3Fe(CN)_6$ and $K_4Fe(CN)_6$ in 0.1 M PBS (pH-6.8). Initially, to reach the equilibrium state, open circuit potential of 0.24 V was applied to the electrode for 15 min. The EIS was performed at an open circuit potential of 0.24 V and a small ac input signal of 10 mV amplitude was applied to the electrode. The frequency of the input signal was varied from 100 kHz to 0.1 kHz. The recorded Nyquist plot of both Ppy-$LiClO_4$ and PPy-pTSA based electrodes has been shown in Fig. 4.6. Inset of Fig. 4.6 represents the Nyquist plot of bare Pt electrode. The Nyquist plot represents a semicircle at high frequency and a linear slope at lower frequencies. The semicircle with a diameter equivalent to R_{ct} defines the charge transport behavior at the electrode and electrolyte interface, while the linear region relates to the diffusion-controlled process which has been defined as Warburg impedance [91]. The intercept at x-axis gives the value of R_S. As evident from Fig. 4.6, the diameter of semicircle has been reduced significantly for PPy-pTSA electrode.

To calculate the R_{ct} value, obtained Nyquist plot was fitted to an equivalent electrical circuit using ZSimp Win 3.2 software. For both PPy-$LiClO_4$ and PPy-pTSA based electrode, the Nyquist plot was fitted to the electrical circuit of $R_S(Q_1(Q_2(RW)))$. All the electrical circuit parameter values of both the electrodes were extracted from the fitted equivalent circuit as tabulated in Table 4.1.

The R_S value for both the electrodes was observed to be in the range of 51-63 Ω as shown in Table 4.1. The other circuit elements i.e. Q_1 and Q_2 have been defined as constant phase element (CPE) which corresponds to non-ideal double layer capacitance at the interface. The deviation from ideal capacitor behavior was represented by the value of n (=1) [87]. Amidst both the electrodes, double layer capacitance Q_1 and Q_2 at the interface were observed to be less for PPy-pTSA. In addition to

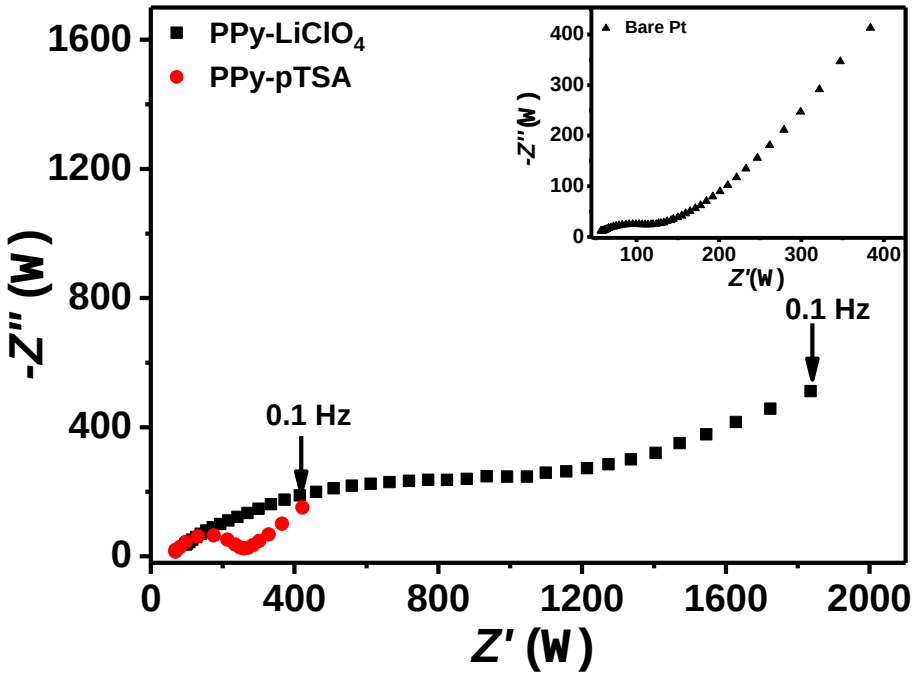

Fig. 4.6: **Nyquist plot of PPy-$LiClO_4$ and PPy-pTSA electrodes. The inset shows the same for bare Pt.**

Table 4.1: **EIS parameters values extracted from equivalent circuit of bare Pt electrode, PPy-$LiClO_4$ and PPy-pTSA in 0.1 M PBS solution containing 5 mM $[Fe(CN)_6]^{3-/4-}$ (1 : 1).**

Electrode	R_S (Ω)	$Q_1(CPE_1)$ (S-sec^n)	n_1	R_{ct} (Ω)	W (S-sec^5)	$Q_2(CPE_2)$ (S-sec^n)	n_2
PPy-$LiClO_4$	51.33	5.535E-5	0.4425	1171	246.9	0.001004	0.4165
PPy-pTSA	62.4	1.27E-05	0.7031	205.4	0.00526	0.000622	1
Bare Pt	42.32	0.0002921	0.4788	123.2	0.003545	0.002141	0.657

that, the value of R_{ct} was found to decrease drastically by five times from 1171 Ω to 205.4 Ω for PPy-pTSA as compared to PPy-$LiClO_4$ electrode. This significant reduction in R_{ct} value from PPy-$LiClO_4$ to PPy-pTSA represents a radical electron transfer process for PPy-pTSA which has been attributed to the higher conductivity of PPy-pTSA electrode. The observed reduction in charge transfer resistance of PPy-pTSA electrode indicated that the film conductivity improved has increased with the incorporation of larger size dopant [36, 107]. Additionally, the suppressed semi-circle for PPy-pTSA as compared to PPy-$LiClO_4$ represents the increment in the surface area of PPy-pTSA electrode [91] which further confirms the findings obtained from FESEM results.

4.3.3 Electroactive surface area

Furthermore, to find the electroactive surface area of both the electrodes cyclic voltammetry was executed in 5 mM $K_3Fe(CN)_6$, $K_4Fe(CN)_6$ containing 0.1 M KCl as supporting electrolyte into 0.1 M PBS. Both the as-prepared electrodes were scanned over a narrow potential window of -0.2 to 0.7 V at a scan rate of 10 mV/s. The recorded cyclic voltammogram of both PPy-$LiClO_4$ and PPy-pTSA has been shown in Fig. 4.7. For both the as-prepared electrodes well-defined peaks have been observed which demonstrate the electro-activity of both the electrodes. The peak current value corresponding to PPy-pTSA electrode was observed to be significantly higher as compared to PPy-$LiClO_4$ electrode indicating towards the increased surface area of PPy-pTSA electrode [58] which was also evident from FE-SEM images. Further, to determine the electroactive surface area of each electrode the working electrode was scanned in a potential range from -0.2 to 0.7 V at various scan rate ranging from 10 to 150 mV/s.

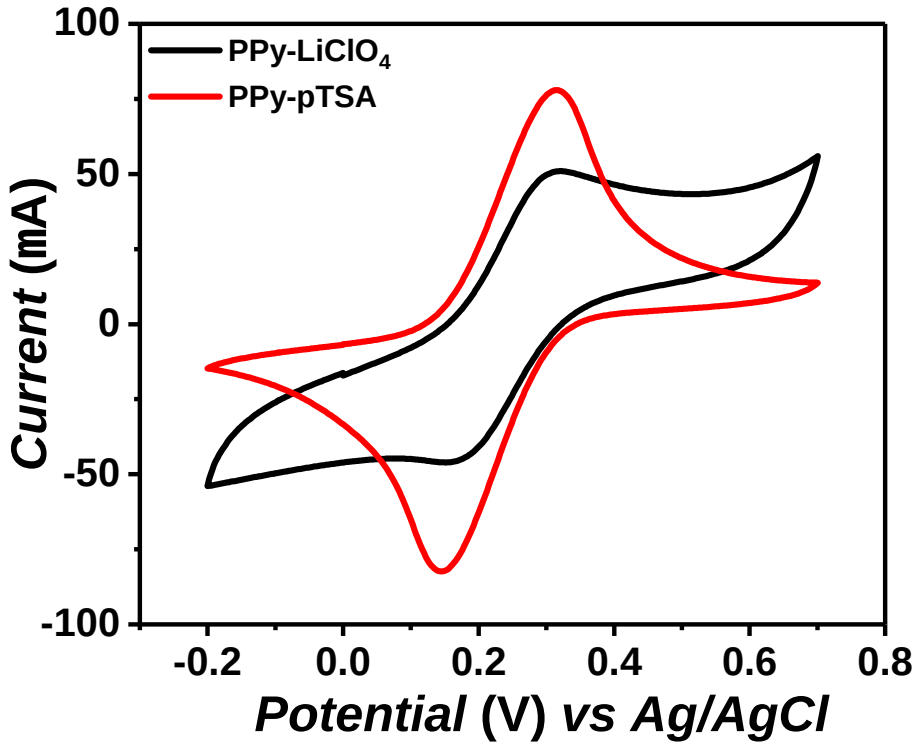

Fig. 4.7: **Cyclic voltammogram of PPy-$LiClO_4$ and PPy-pTSA based electrode performed in 5 mM $K_3Fe(CN)_6$, $K_4Fe(CN)_6$ containing 0.1 M KCl in 0.1 M PBS (pH-6.8) at a scan rate of 10 mV/s.**

The CVs of both PPy-$LiClO_4$ and PPy-pTSA electrode has been shown in Fig. 4.8 (a, b). The inset shows the linearly proportional curve of anodic peak current

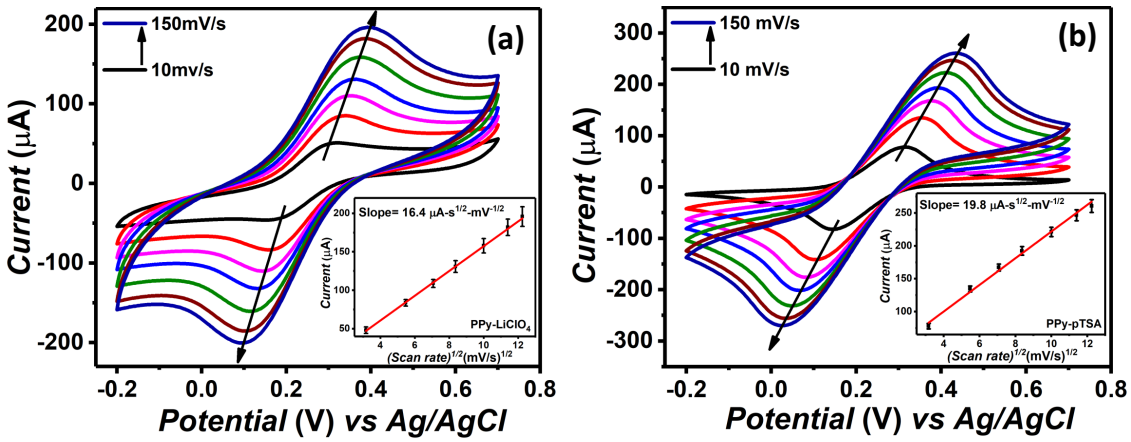

Fig. 4.8: **Cyclic voltammograms of (a) PPy-$LiClO_4$ (b) PPy-pTSA electrode recorded in 5 mM $K_3Fe(CN)_6$, $K_4Fe(CN)_6$ containing 0.1 M KCl in 0.1 M PBS (pH-6.8) at different scan rates. Inset shows the linear proportional curve of anodic peak current values *vs* square root of scan rate.**

values (I_{pa}) *vs* square root of applied scan rates ($\sqrt{v}$) (R^2=0.99). The slope obtained from a linear calibration plot of I_{pa} *vs* $\sqrt{v}$ was utilized to estimate the electroactive surface area of both PPy-$LiClO_4$ and PPy-pTSA electrodes using the Randles-Sevcik equation (equation 4.1) [58].

$$I_{Pa} = 2.69 * 10^5 * n^{3/2} * A_{eff} * \sqrt{D} * \sqrt{v} * C_0 \tag{4.1}$$

where D, diffusion coefficient of 5 mM $K_3Fe(CN)_6$ in 0.1 M KCl (7.26×10^{-6} cm^2 s^{-1}), v is the scan rate at which the potential was swept, C_0 is the concentration of $K_3Fe(CN)_6$ and $K_4Fe(CN)_6$ in solution, n denotes the number of electron (n=1) involved in half reaction, and A_{eff} is the effective surface area of the electrode [58]. The effective surface area of both PPy-$LiClO_4$ and PPy-pTSA electrode calculated by the Randles-Sevcik equation was estimated to be approximately 0.14 and 0.17 cm^2 respectively. The effective electroactive surface area by CV confirms the higher electrode surface area for PPy-pTSA electrode which was ~1.2 times of PPy-$LiClO_4$ electrode. In addition to this, the increased oxidation current (Fig. 4.7) for pTSA designates higher conductivity for PPy-pTSA electrode which has been also observed during EIS study.

4.3.4 Enzyme loading quantification

As the surface area of PPy-pTSA electrode was observed to be enhanced as compared to PPy-$LiClO_4$ electrode, the enzyme loading for PPy-pTSA electrode was likely to be increased. The amount of GOx loaded onto both PPy-$LiClO_4$ and PPy-pTSA electrodes was estimated by fluorescence. For both the electrodes, the amount of GOx loading has been presented in Fig. 4.9 which has shown the higher amount of GOx loaded over PPy-pTSA electrode as compared to PPy-$LiClO_4$. The amount of GOx loading for PPy-$LiClO_4$ and PPy-pTSA electrode was estimated to be 237 μg-cm^{-2} and 434 μg-cm^{-2} respectively which was approximately 1.8 times of PPy-$LiClO_4$ electrode. The increased GOx loading for PPy-pTSA was attributed to the increased surface area of PPy-pTSA electrode which has been confirmed by FESEM images and CV.

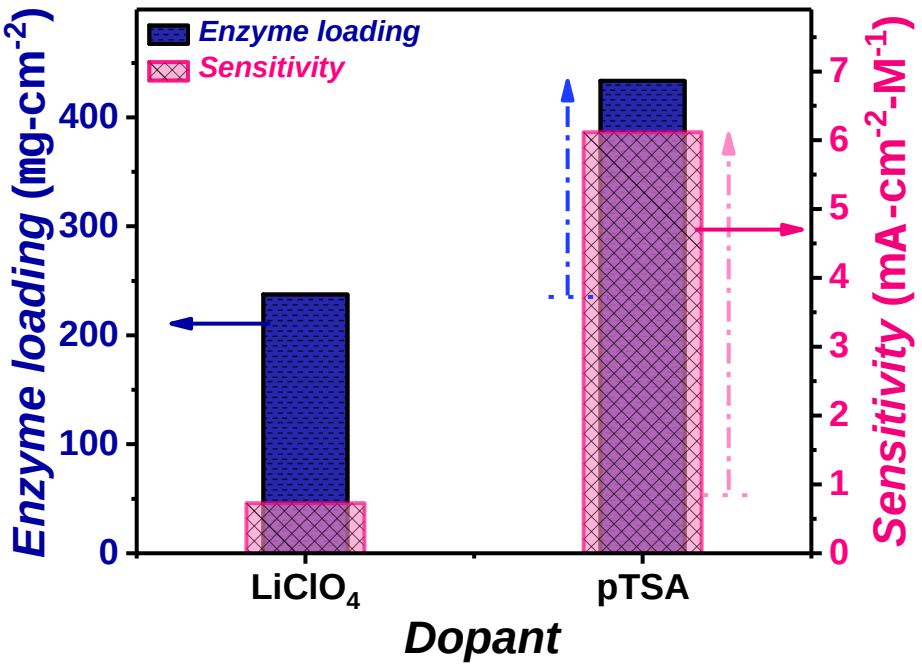

Fig. 4.9: **Enzyme loading variation and corresponding sensitivity of PPy-$LiClO_4$ and PPy-pTSA based electrode.**

4.3.5 Biosensor response towards glucose detection

The electrocatalytic activity of the fabricated biosensors towards glucose was determined using amperometric transduction method. For amperometric response, known concentrations of glucose were injected into the cell consisting of 0.1 M PBS

(pH = 6.8) as an electrolyte solution. The amperometric responses recorded for both the biosensors have been shown in Fig. 4.10.

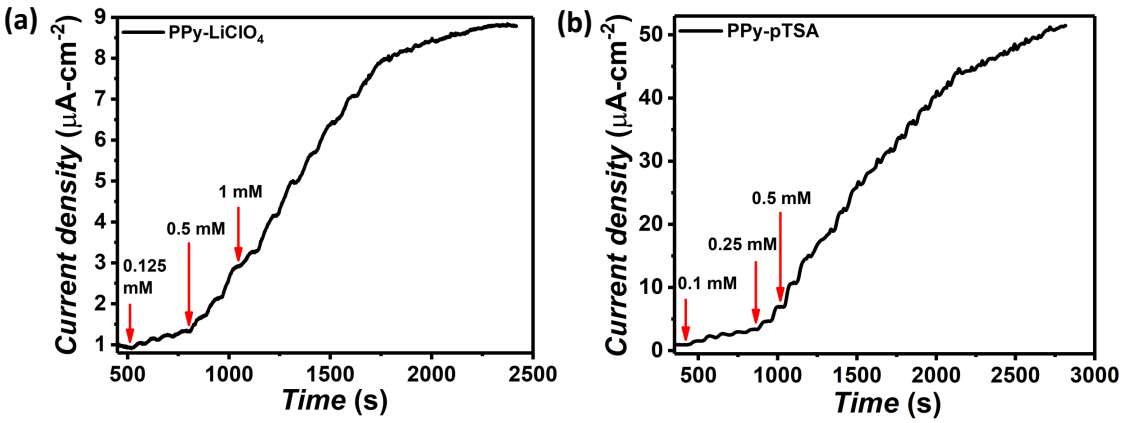

Fig. 4.10: **Amperometric response of (a) PPy-$LiClO_4$ (b) PPy-pTSA based biosensor.**

The observed current increment upon injection of glucose into the electrolyte solution has shown a step-like response. Initially, for PPy-$LiClO_4$ based biosensor, 0.125 mM glucose followed by 0.5 mM and 1 mM glucose was injected into the electrolyte solution as presented in Fig. 4.10 (a). The initial behavior of the electrode has shown the equal increment in the current with the addition of glucose corresponding to the linear range of the fabricated biosensor. Similarly, PPy-pTSA based biosensor has also exhibited step-like response with the successive addition of glucose. The steady state values of the current corresponding to glucose concentration has been taken for the calibration curve and shown in Fig. 4.11.

All the figure of merits of both the biosensors *viz.* sensitivity and linear range of operation were calculated using the calibration curve while response time has been evaluated from the amperometric response. As evident from Fig. 4.11, PPy-pTSA/GOx based biosensor has shown a higher sensitivity as compared to PPy-$LiClO_4$/GOx based biosensor. However, the linear range of operation of PPy-pTSA/GOx biosensor was observed to be reduced compared to PPy-$LiClO_4$/GOx. The response time was defined as the time taken to reach 90% of the steady state current value after the injection of glucose. The response time for both the biosensors has been observed to be the same. The sensitivity was found to increase by approximately 8 times, i.e. an appreciable enhancement has been observed with the addition of larger size dopant i.e. p-TSA during the synthesis of Polypyrrole

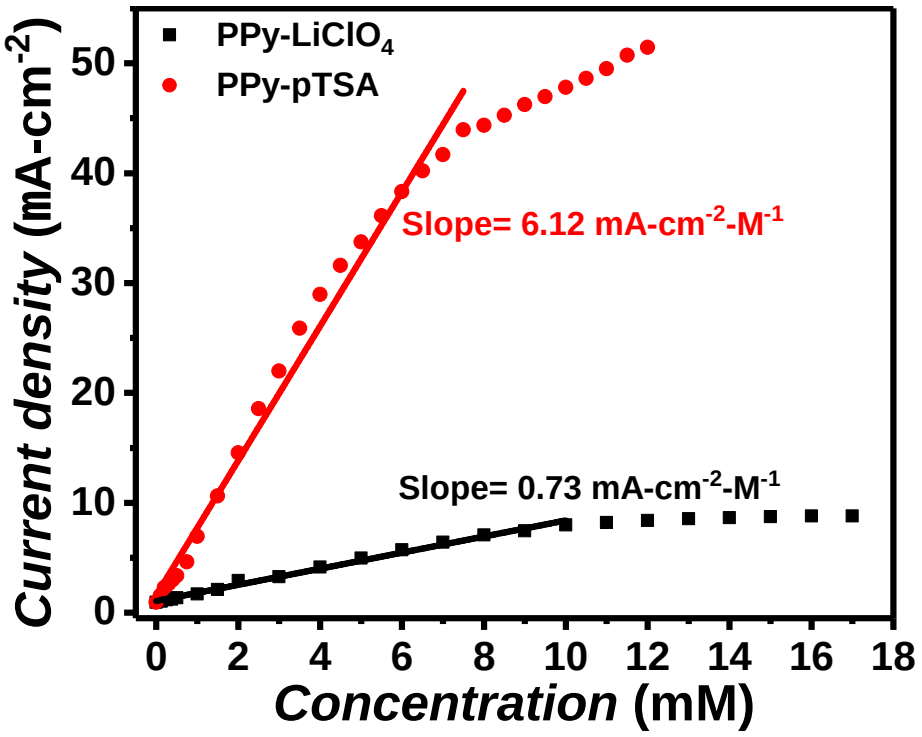

Fig. 4.11: **Calibration plot of PPy-$LiClO_4$ and PPy-pTSA based biosensor.**

nanofibers. The addition of p-TSA has facilitated a higher electroactive surface area and reduced charge transfer resistance of synthesized PPy nanofibers as compared to $LiClO_4$ which was confirmed by FESEM, CV, and EIS results. The obtained improvement in surface area and charge transfer resistance was found to be responsible for the 8 fold increment in the sensitivity of PPy-pTSA/GOx biosensor. The comparison table of both the glucose biosensors, fabricated via a simple template-free method has been tabulated in Table 4.2.

Table 4.2: **Comparison of PPy-$LiClO_4$ and PPy-pTSA based glucose biosensor performance.**

Electrode	Sensitivity ($mA\text{-}cm^{-2}\text{-}M^{-1}$)	Linear Range (mM)	Response Time (s)
PPy-$LiClO_4$	0.73	0.125-10	~45
PPy-pTSA	6.12	0.1-7.5	~45

Further to confirm the GOx mediated glucose oxidation as observed in the amperometric detection of glucose, cyclic voltammetry analysis of PPy-pTSA based electrode was carried out in unstirred 0.1 M PBS (pH-6.8). The potential applied to the working electrode was swept from 0 to 0.7 V. The recorded CV of Glass/Cr: Pt/PPy-pTSA/GOx electrode with and without glucose has been shown in Fig.

4.12.

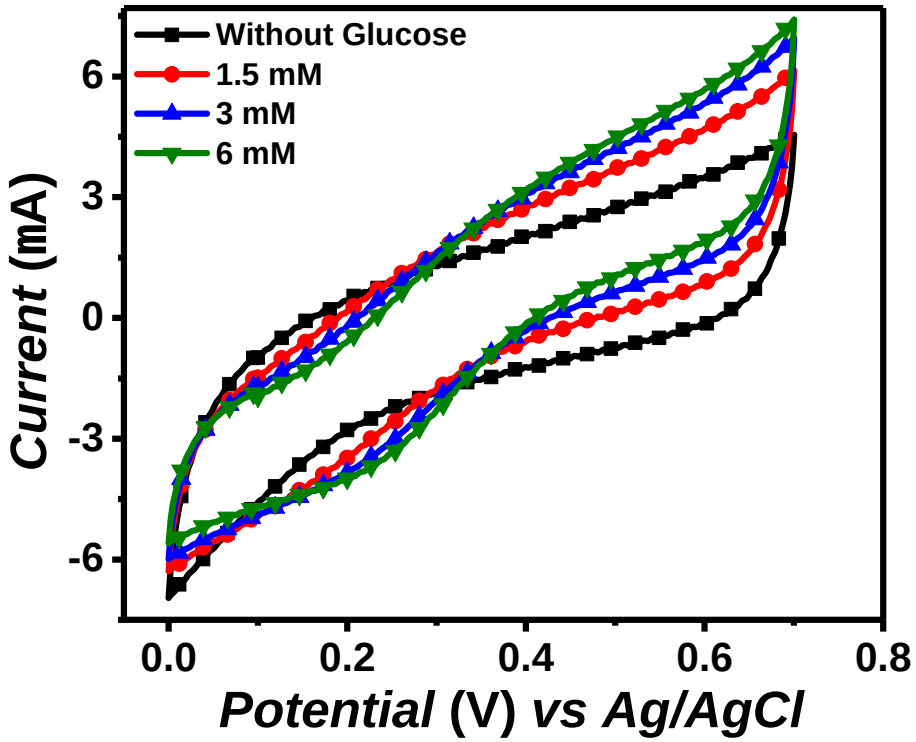

Fig. 4.12: **CV sensing of PPy-pTSA/GOx biosensor without and with glucose addition.**

A sharp increase in the anodic current was observed upon addition of glucose as compared to the background current obtained without glucose, validating the activity of GOx immobilized onto PPy-pTSA electrode [56]. The observed current increment suggests the proper immobilization of GOx over PPy-pTSA electrode and facile glucose oxidation catalyzed by GOx.

4.3.6 Reproducibility, shelf life measurement, and interference effect

The reproducibility of as-prepared biosensor was determined by analyzing the amperometric response of three similarly prepared biosensors. The relative standard deviation (RSD) of three biosensors' responses was found to be 5.87% which has presented good reproducibility of the PPy-pTSA/GOx biosensor. Moreover, to find out the stability of the as-prepared biosensor, it was stored in an incubator at 4°C for 14 days. and the amperometric responses were recorded on 10^{th} and 14^{th} day which has shown the similar behaviour of the biosensor electrode.

The amperometric response of the PPy-pTSA/GOx biosensor after 14 days storage

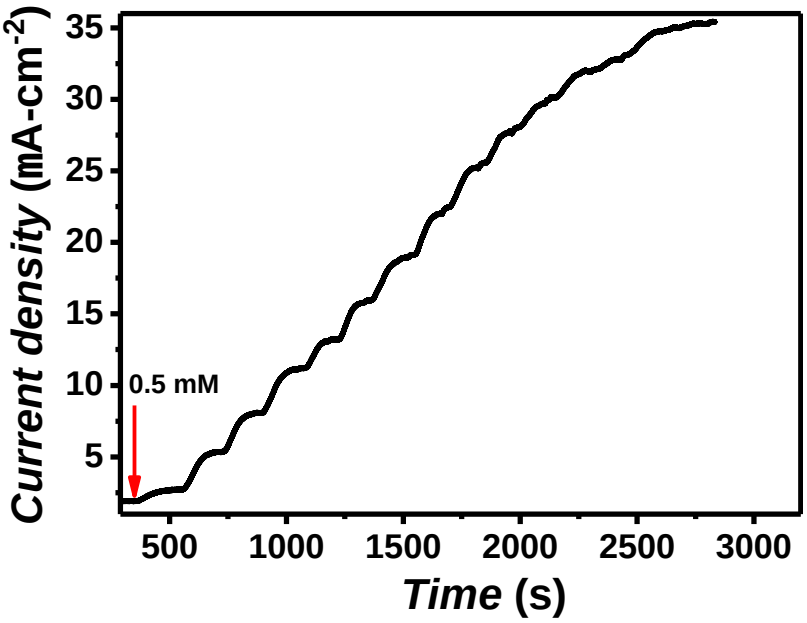

Fig. 4.13: **Amperometric response of PPy-pTSA based biosensor after 14 days.**

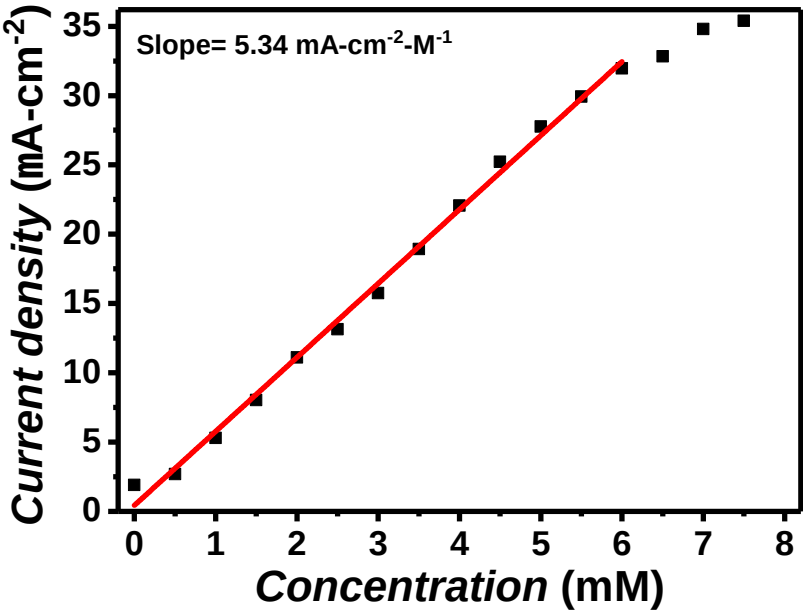

Fig. 4.14: **Calibration plot of PPy-pTSA based biosensor after 14 days.**

has been shown in Fig. 4.13. The corresponding calibration plot has been shown in Fig. 4.14. The sensitivity of the PPy-pTSA/GOx biosensor on 10^{th} and 14^{th} day has been presented in histogram plot shown in Fig. 4.15 showing the stability of the biosensor. After 14 days the proposed biosensor has shown the sensitivity of 90% of its initial sensitivity which has exhibited a very good stability of PP-pTSA/GOx glucose biosensor. The obtained biosensor stability can be the reason of proper immobilization of GOx over PPy-pTSA nanofibers which has provided a high surface area for the enzymes immobilization. Further, the interference ef-

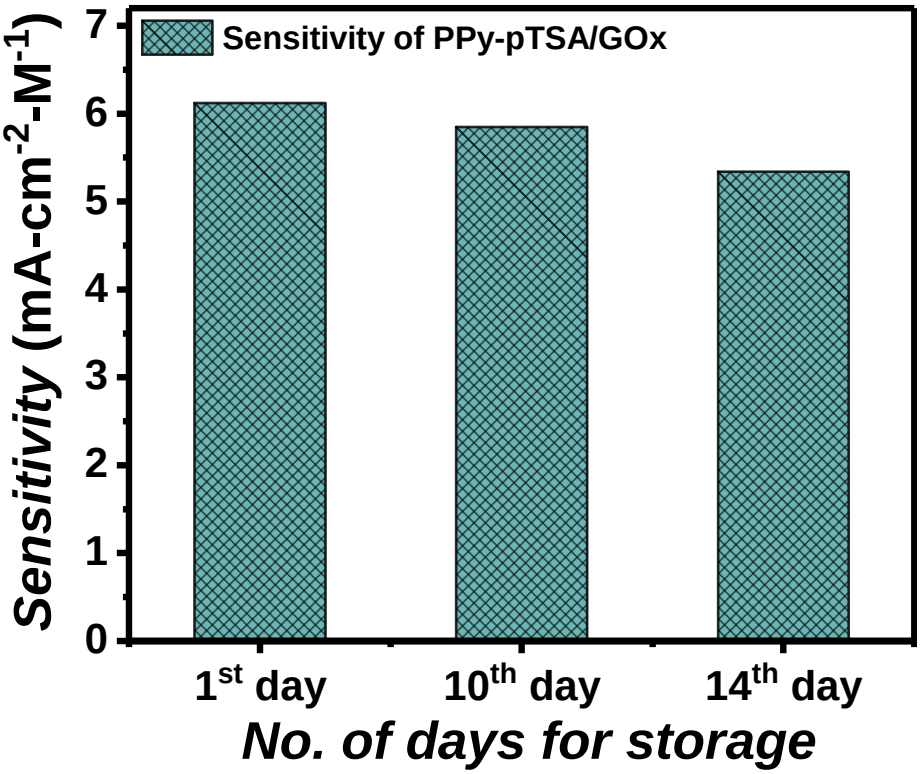

Fig. 4.15: **Histogram plot showing the storgae life of PPy-pTSA based biosensor.**

fect of the proposed biosensor was determined. To fabricate a practical glucose biosensor it is necessary to check the anti-interferent capability of the biosensor due to the presence of some other electroactive species *viz.* ascorbic acid and uric acid etc in human blood and serum [108]. These electroactive species oxidize easily at a potential of 0.7 V which has been applied for the glucose detection in this study. Thus, there is a possibility of inaccurate measurement of glucose concentration. Hence to check the anti-interfering capability of best performing electrode i.e. PPy-pTSA/GOx glucose biosensor, current response measurements were performed in 0.1 M PBS (pH-6.8) as shown in Fig. 4.16. Initially, 1.5 mM glucose was injected into the electrolyte solution and the current increment has been observed corresponding to glucose concentration.

Furthermore, after the steady state value of current corresponding to glucose, 0.1 mM ascorbic acid and 0.4 mM uric acid were injected and the effect of these anti-interferents' on the performance of glucose biosensor was examined. The addition of 0.1 mM ascorbic acid and 0.4 mM uric acid has shown 4.05% and 2.82% rise in the current respectively which is very less, indicating the good anti-interfering capability of PPy-pTSA/GOx glucose biosensor. The selectivity and anti-interference

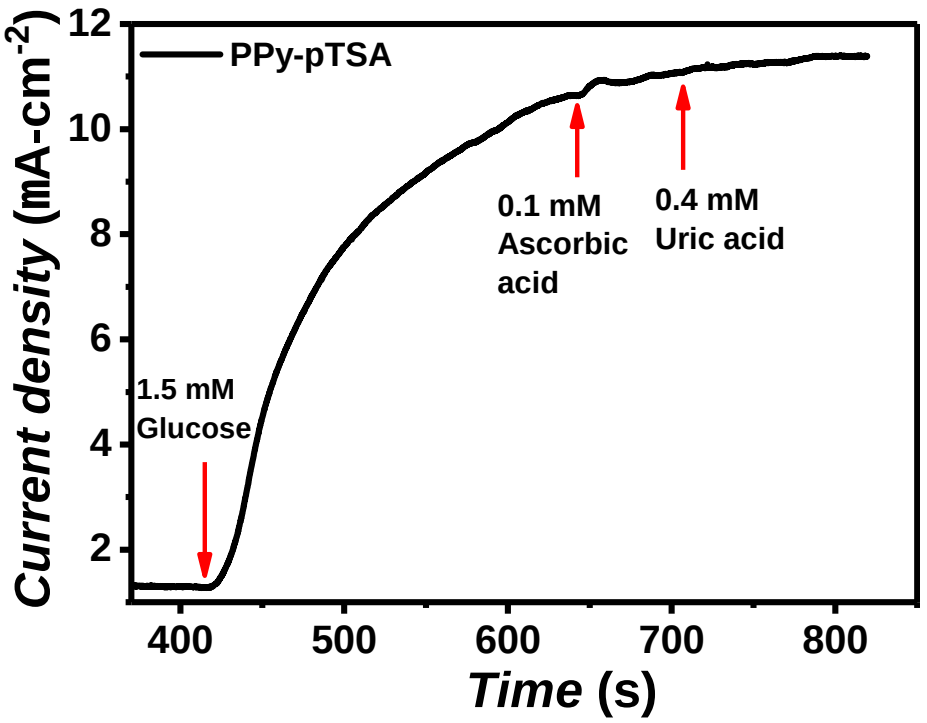

Fig. 4.16: **Interference effect of ascorbic acid and uric acid on PPy-pTSA based biosensor.**

capability of the as-prepared biosensor can be attributed to enzymes which are highly specific towards its substrate and well immobilized over the support matrix.

4.4 Conclusions

In summary, an enzymatic glucose biosensor utilizing electrosynthesized PPy nanofibers as a support matrix for enzyme immobilization has been demonstrated successfully. The effect of two different dopants *viz.* $LiClO_4$ and pTSA on the morphology and charge transfer resistance of PPy nanofibers have been studied systematically. The nature of the anion (dopant) has been observed to significantly influence several properties of as-prepared PPy nanofibers. With the use of pTSA as a dopant during PPy growth, the synthesized PPy nanofibers have provided much longer and thinner nanofibers (higher aspect ratio) as compared to PPy-$LiClO_4$. The higher aspect ratio obtained for PPy-pTSA (1.2 times of PPy-$LiClO_4$) electrode has provided higher enzyme loading (1.8 times higher of PPy-$LiClO_4$) which is one of the major factors for obtaining a higher sensitivity of the biosensor. In addition to the higher surface area, the charge transfer resistance has reduced drastically

5 folds for PPy-pTSA electrode which has been confirmed by FESEM and EIS respectively. The cumulative effect of the higher surface area (causing higher enzyme loading) and reduced charge transfer resistance have facilitated the development of higher sensitivity of PPy-pTSA/GOx biosensor.

Chapter 5

Effect of Crosslinking Immobilization on Polypyrrole Nanofibers-based Glucose Biosensor

In the previous studies, it was observed that higher enzyme loading has improved biosensor performance. Thus to enhance the enzyme loading, cross-linking immobilization of GOx over PPy nanofibers network (PNN) was investigated to improve biosensor performance. The PNN was electropolymerized over a Pt-coated glass substrate by potentiostatic deposition method. Further, the enzyme (GOx) was immobilized over the as-prepared PNN electrode utilizing physical adsorption and crosslinking immobilization method and the fabricated biosensors were analyzed using amperometric transduction method. The performance of both the types of the biosensor was compared and further investigations demonstrated the improvement in sensitivity of the fabricated glucose biosensor utilizing crosslinked GOx. The observed results have shown the significant effect of the enzyme immobilization technique on the performance of electrochemical enzymatic glucose biosensor.

5.1 Introduction

The immobilization i.e. attachment of enzymes to the support matrix is one of the vital steps for fabrication of an enzymatic biosensor. The support matrix having a high surface to volume ratio which provides a microenvironment to enzymes

should ensure the stability of enzymes after immobilization and enable electron transfer between enzyme and electrode surface [109–111]. The immobilization of these enzymes onto the support matrix can be performed via various well-known techniques such as physical adsorption, crosslinking, covalent binding, and co-entrapment. The choice of mode of immobilization plays a key role in the performance of biosensors as it directly affects enzyme loading which is responsible for the improvement in biosensor's performance [29]. In this chapter, we have demonstrated Polypyrrole nanofibers (electrochemically synthesized via template-free method) as a support matrix to immobilize GOx via crosslinker Glutaraldehyde. The GOx was utilized using physical adsorption and crosslinking immobilization method and a comparative study of enzyme immobilization techniques on the performance of glucose biosensor has been demonstrated. A stable and biocompatible support matrix of PPy nanofibers for GOx immobilization (microenvironment for enzyme immobilization) has been fabricated by electrochemical deposition method. The enzyme (GOx) immobilization over the PPy nanofibers was performed utilizing physical adsorption and crosslinking immobilization method with the aim of achieving better biosensor performance. The immobilization via crosslinking has been optimized to load BSA, glutaraldehyde, and subsequently GOx onto the support matrix. Further, the two types of fabricated biosensors were analyzed using amperometric detection method.

5.2 Experimental Section

5.2.1 Fabrication of PNN electrode

Primarily, the glass substrates (1cm x 1cm) were cleaned by ultrasonication in acetone, isopropanol for 10 min followed by DI water for 5 min. Further, Pt (50 nm) with an intermediate layer of chromium (5 nm) (to improve the adhesion of Pt on glass) was deposited over the cleaned glass substrates using DC magnetron sputtering at a base pressure of $1x10^{-6}$ mbar and a working pressure of 3 mTorr. The continuous flow of Ar gas was maintained at 10 sccm during Pt deposition. Furthermore, Polypyrrole was deposited over the Pt-coated glass substrate using electropolymerization method. For electropolymerization, Pyrrole (Py) was distilled at 130 °C and the electrolyte solution of 0.1 M Py, 70 mM $LiClO_4$ with 0.1 M PBS (pH

6.8) was prepared as discussed earlier. According to the optimized growth conditions, the best performing electrode corresponding to 70 mM $LiClO_4$ concentration named as PNN-70 has been taken for further improvement in the biosensor performance. The schematic illustration of biosensor fabrication has been represented in Fig. 5.1.

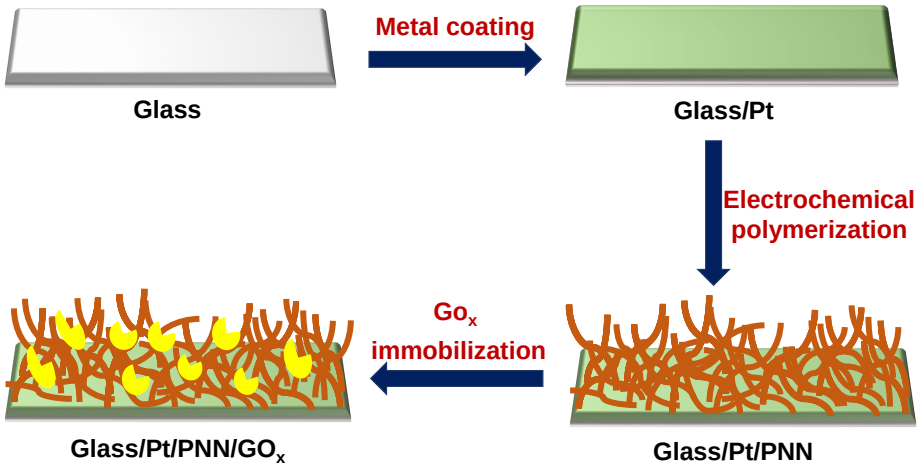

Fig. 5.1: **Schematic illustration of fabrication steps of PNN based biosesnor.**

Briefly, the electrochemical deposition of Polypyrrole was carried out using electrochemical workstation Autolab PGSTAT302N having three-electrode cell configuration. The cell consisted of electrolyte solution where platinum coated glass substrate, Ag/AgCl electrode, and platinum foil has been utilized as working, reference, and counter electrode respectively. A constant potential (0.85 V) was applied to the working electrode for 3600 s to obtain PNN over a Pt-coated glass substrate. The morphology of electrosynthesized Polypyrrole was determined using Field Emission Scanning Electron Microscopy (FESEM, Carl Zeiss SUPRA55). Further, Glucose oxidase (GOx) was immobilized over the fabricated Glass/Cr-Pt/PNN electrode using physical adsorption and crosslinking immobilization technique.

5.2.2 Modification of PNN electrode with GOx and its quantification

The immobilization of GOx onto the fabricated electrode was performed using physical adsorption and crosslinking immobilization techniques. Firstly, GOx was

physically adsorbed onto the prepared electrode. This is the simplest method of enzyme immobilization in which enzyme binds to the electrode surface via electrostatic interaction utilizing the positive charge on PPy. In physical adsorption process, GOx aliquot (10 µL) from a stock solution of 10 mg/mL prepared in 0.1 M PBS was dropped onto the fabricated PNN-70 electrode and was kept in an incubator at 4 °C temperature. However, for crosslinking immobilization method, GOx was crosslinked over the PNN-70 electrode surface via glutaraldehyde, which has been used as a crosslinker. The immobilization via crosslinking has been optimized to load Bovine serum albumin (BSA), glutaraldehyde, and subsequently GOx onto the support matrix. A mixture of 10 mg/mL bovine serum albumin (BSA) and 20 µL glutaraldehyde was prepared in 1 mL PBS and 10 μL aliquot of this mixture solution was drop cast over the as-prepared electrode. After drying the electrode at room temperature, 10 μL aliquots of GOx was immobilized over it and kept in an incubator at 4°C temperature. The electrodes immobilized with GOx using physical adsorption and cross-linking methods were named as PNN-70/PA-GOx and PNN-70/CL-GOx respectively. Both the types of electrodes were washed into PBS to remove loosely adhered GOx molecules. Further, this PBS solution was utilized for the estimation of GOx molecules attached to both electrode surfaces. The schematic illustration of Physical adsorption and cross-linked immobilization has been shown in Fig. 5.2 which has demonstrated a monolayer of enzyme has been loaded in case of physical adsorption. With the cross-linking immobilization multi-layers of enzyme have been loaded.

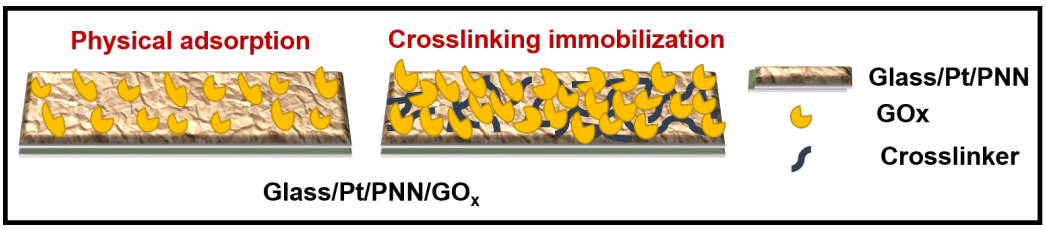

***Fig. 5.2:* Schematic illustration of physical adsorption and cross-linking immobilization of GOx.**

Further, the amount of enzyme loaded over the PNN support matrix was determined by using the optical characteristic of the GOx molecule. A linear calibration curve corresponding to the known amount of GOx in 0.1 M PBS and its fluorescence intensity was obtained. Further, fluorescence intensity was measured for PBS containing unadhered GOx molecules for both the electrodes. Finally, the amount

of unadhered GOx was estimated by using the calibration curve and the fluorescence intensity corresponding to unadhered GOx molecules. Thus the amount of enzyme immobilized over each electrode was determined by taking the difference of the known amount of enzyme immobilized (100 μg) and the calculated unadhered enzymes.

5.3 Results and Discussion

5.3.1 Morphological characterization

The morphology of as-prepared PNN electrode synthesized at a potential of 0.85 V in an electrolyte solution of 0.1 M Py, 70 mM $LiClO_4$, and 0.1 M PBS was determined using FESEM. Figure 5.3 (a, b) shows the top view FESEM image of PNN electrode and the magnified view of the grown nanofibers has been presented in Fig. 5.3 (b).

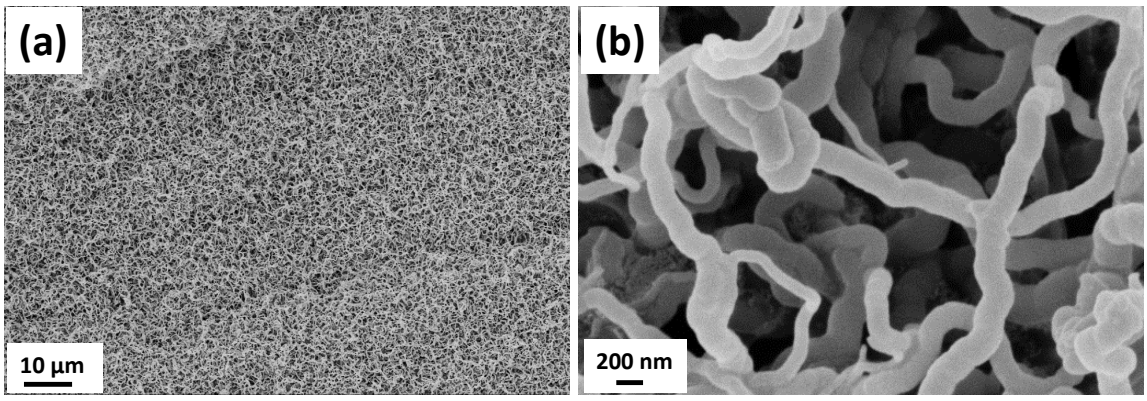

Fig. 5.3: **FESEM image showing top view of (a) PNN electrode (b) magnified view of the same.**

As evident from the FESEM images that high-density uniform nanofibers growth have been observed over a large area for the optimized growth conditions. The synthesized nanofibers were longer as compared to the diameter which shows higher aspect ratio of the obtained nanofibers, as clear from Fig. 5.3. The nanofibrous growth with improved aspect ratio ensures less hindered charge transport, high specific surface area and thus higher enzyme loading which directly influences the biosensor figure of merits. Figure 5.4 shows the histogram plot of the diameter distribution of grown nanofibers.

The diameter distribution of nanofibers was obtained from FESEM images by

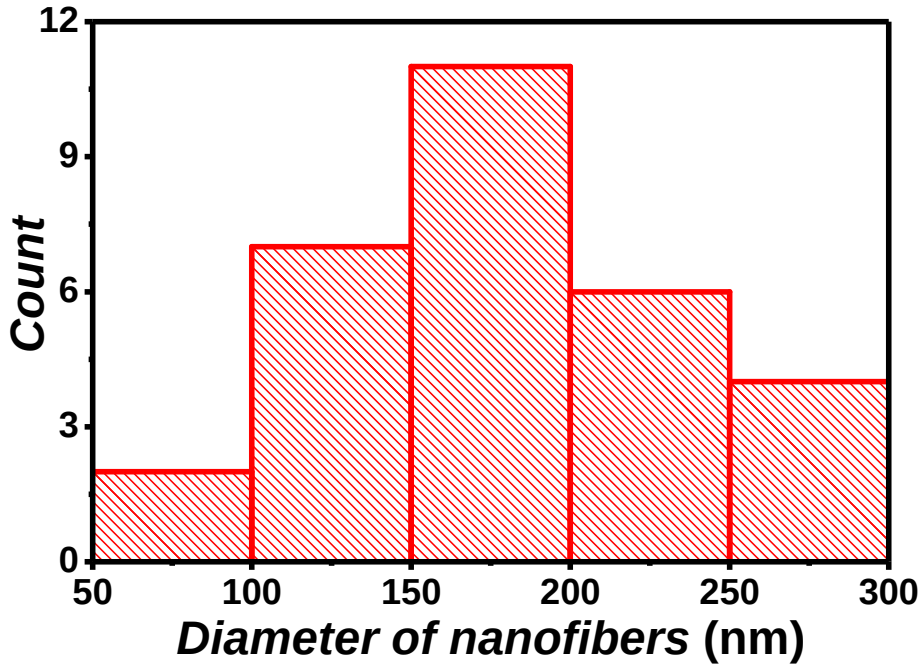

Fig. 5.4: **Diameter distribution of randomly selected nanofibers from FESEM image of PNN electrode.**

randomly selecting 30 nanofibers using "imtool" of MATLAB and it was estimated to be in a range of 150-200 nm. The FESEM image clearly shows the porous and homogeneously distributed nanofibers morphology having a high surface area which is beneficial for higher enzyme loading.

5.3.2 Enzyme immobilization, structural analysis, and quantification

Enzyme (GOx) is a protein which comprises of a number of amino acids. These amino acids have been reported to be arranged into helices, turns, and sheets which account for the complex structures and activity of enzymes. The immobilization of GOx was confirmed by the FESEM image as shown in Fig. 5.5.

The structure and activity of GOx are very much sensitive to the microenvironment of the GOx. Thus, the structural analysis of GOx was performed using FTIR spectroscopy after the immobilization of GOx. FTIR (FTIR in Attenuated Total Reflectance (ATR) mode) study has been utilized to analyze the effect of immobilization methods on the conformational changes in the structure of GOx. To confirm the immobilization of GOx, FTIR of PNN-70, native GOx, and immobilized GOx was performed. The changes in the structure of GOx after immobilization onto

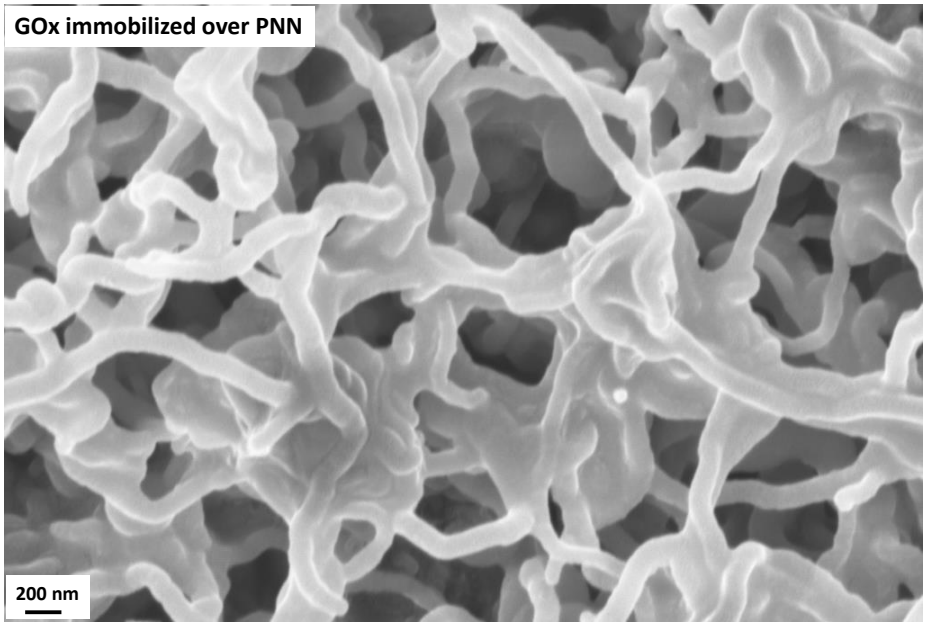

Fig. 5.5: **The FESEM image of GOx immobilized over PNN electrode.**

PNN electrode was studied with respect to FTIR of native GOx. In FTIR spectra of protein, the amide group, amide I (1700-1600 cm^{-1}) and amide II (1600-1500 cm^{-1}) have been observed to be very much sensitive to protein conformation [112]. Fig-

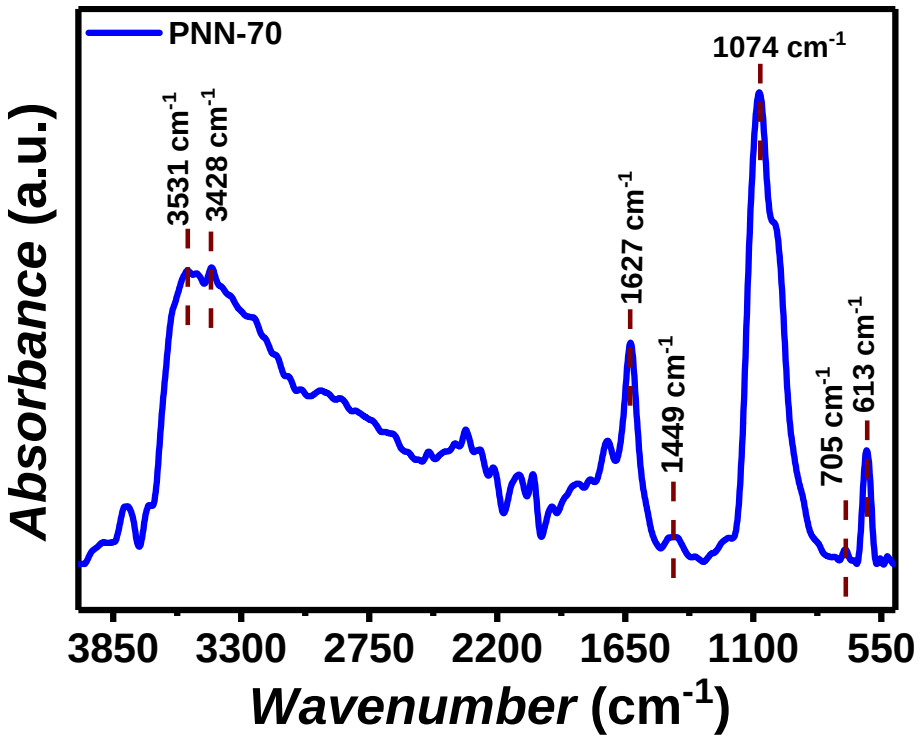

Fig. 5.6: **FTIR spectra of PNN electrode.**

ure 5.6 shows the FTIR spectra of as-prepared PNN-70. The spectra of PNN-70 showed the significant peaks at 3571 cm^{-1} and 3428 cm^{-1} which can be attributed

to amine N-H stretching, peaks at 1627 cm^{-1} and 1449 cm^{-1} indicates C=C and C-C stretching respectively. In addition, peak at 1074 cm^{-1} assigned to N-H and C-H aromatic in-plane bending. Furthermore, peaks at 705 cm^{-1} and 613 cm^{-1} correspond to C-H and C-C out of plane deformation in heterocyclic aromatic rings of polymeric conjugation in PPy which was in good agreement with the literature [7, 58]. The FTIR spectra of native GOx and immobilized GOx via physical adsorption and cross-linking has been shown in Fig. 5.7. The FTIR spectra for

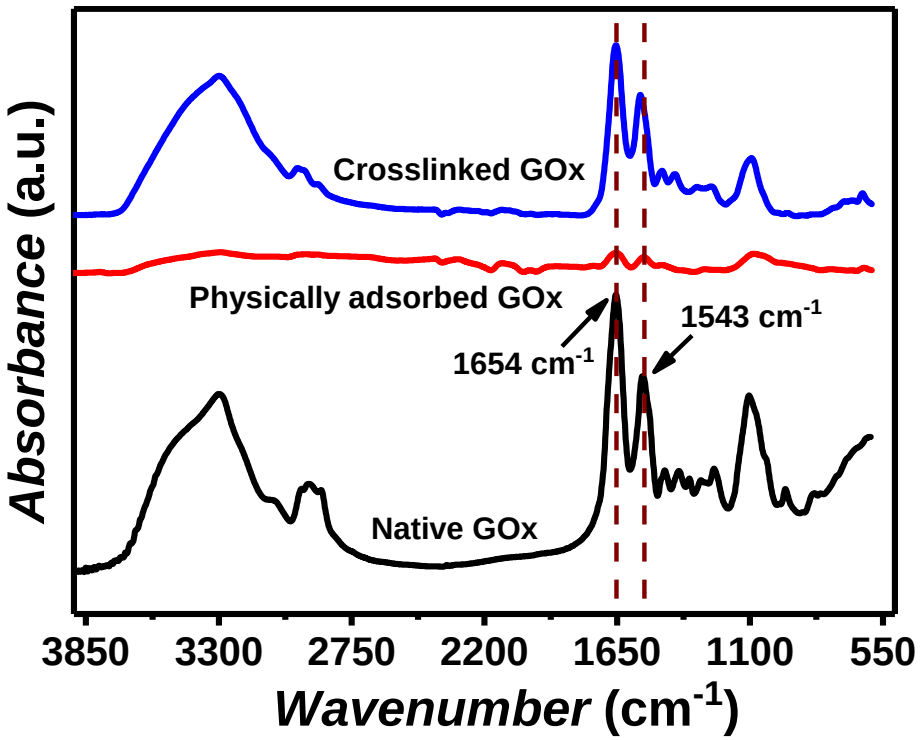

Fig. 5.7: **FTIR spectra of Native GOx, Physically adsorbed and Crosslinked GOx.**

native GOx has shown two characteristics amide bands: amide I and amide II centered at around 1645 cm^{-1} and 1543 cm^{-1} respectively. The amide I band at 1654 cm^{-1} corresponds to -C=O stretching vibration while amide II at 1543 cm^{-1} relates to N-H in-plane bending [7]. Figure 5.7 shows that for both the type of immobilization methods the absorption bands (amide I and amide II) have been found at the same peaks as that of native GOx which confirm the proper immobilization of GOx with its retained activity. Additionally, the cross-linking immobilization has shown higher intensity in FTIR spectra as compared to physical adsorption which has demonstrated higher enzyme loading for crosslinked GOx. Further to obtain quantitative information of secondary structure elements of the GOx, amide I peak was analyzed. Deconvolution of amide I band ranging from 1600-1700 cm^{-1} was

performed using Voigt function. The peak positions in spectra were determined using minima of second derivative spectra of amide I region. Deconvoluted peaks in amide I spectra of native, physically adsorbed, and crosslinked GOx were fitted to a cumulative peak obtained same as original spectra for all. The deconvoluted spectra of native, physically adsorbed and crosslinked GOx has been shown in Fig. 5.8 (a-c). The bands at 1650-1660 cm^{-1}, 1620-1640 cm^{-1}, and 1660-1685 cm^{-1} have been designated to α-helix, β-sheets, and β-turns respectively. Moreover, the bands at 1610-1620 cm^{-1} and 1685-1695 cm^{-1} have been assigned to antiparallel β-sheets and bands at 1640-1650 cm^{-1} were referred to random coils present in GOx structure [113]. The percent of individual secondary element was determined by dividing the area of each band to the total area of amide I. The reckoned secondary structure elements of GOx in different microenvironments have been presented in Fig 5.9.

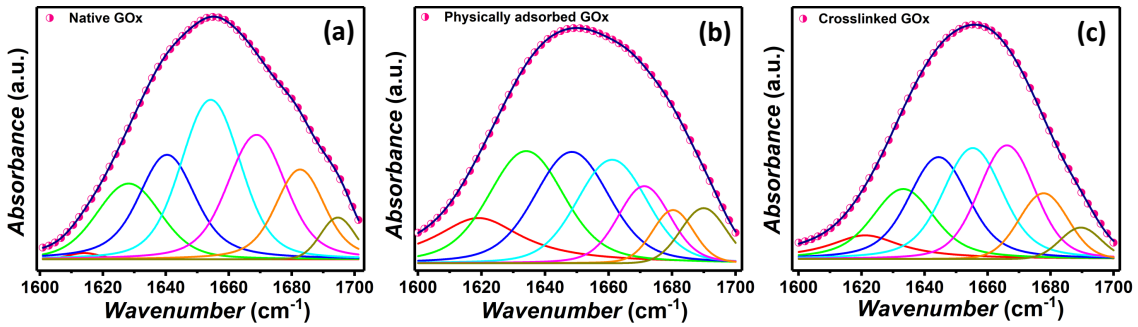

Fig. 5.8: **Deconvolution of amide I spectra of (a) Native (b) Physically adsorbed, and (c) Crosslinked GOx.**

The secondary structure conformation of native GOx has shown ∼28% α-helix, ∼33% β-sheets, ∼35% β-turns, and ∼4% antiparallel β-sheets. However, after physical adsorption of GOx, α-helix and β-sheets were reduced to ∼24% and ∼23% respectively. There was no significant change in β-turns (∼34%). Additionally, the antiparallel β-sheets were found to increase up to ∼19% for physically adsorbed GOx. The crosslinking immobilization of GOx has revealed ∼23% α-helix, ∼23% β-sheets, ∼30% β-turns, ∼4% antiparallel β-sheets, and ∼20% random coils. The obtained percent changes in the secondary structure elements α-helix and β-sheet were related to the GOx's activity. With physical adsorption and crosslinking immobilization of GOx, conformational changes in the secondary structure of GOx has been found to vary as compared to native GOx. Regardless of the changes in

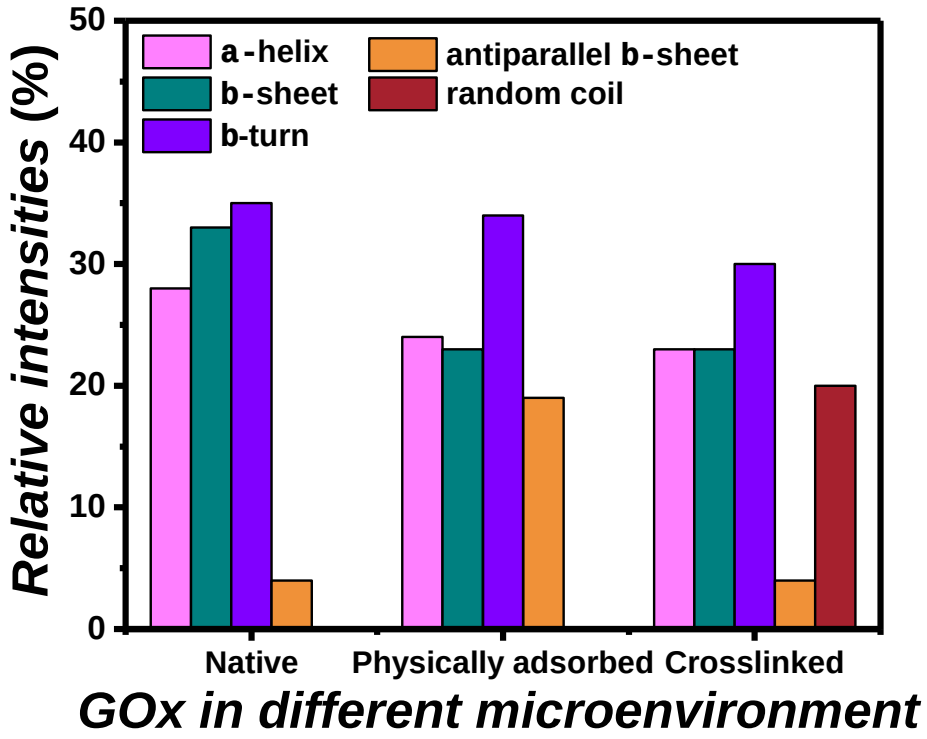

Fig. 5.9: **Relative amount of secondary structure elements of GOx for all different microenvironments (Native, Physically adsorbed, and Crosslinked GOx) calculated from deconvolution of amide I spectra.**

the percentage of secondary structure elements after immobilization of GOx, the presence of α-helix and β-sheets define the retained activity of GOx.
Further, the immobilization of GOx was confirmed by EIS which was related to the impedance changes on surface modification of PNN with GOx. EIS was performed in 0.1 M PBS with pH-6.8 consisting of 5 mM redox couple, i.e. $K_3Fe(CN)_6$ and $K_4Fe(CN)_6$. A small ac input signal of 10 mV amplitude with frequency varying from 100 kHz to 0.1 Hz was applied to the electrode for recording impedance spectra. The obtained impedance spectra of modified electrodes have been shown in Fig. 5.10.

The impedance spectra presented in Nyquist plot consist of a semicircle part at the higher frequency and a linear part in the lower frequency region. The observed Nyquist plots for all the electrodes were related to the interfacial behavior of each electrode. The semicircle region and the linear region correspond to the electron transfer limited processes and diffusion limiting processes respectively. The semicircle diameter represents the electron transfer resistance experienced by redox couple at the electrode and electrolyte interface which relates to the conductivity of the modified electrode [58] The obtained impedance spectra for each mod-

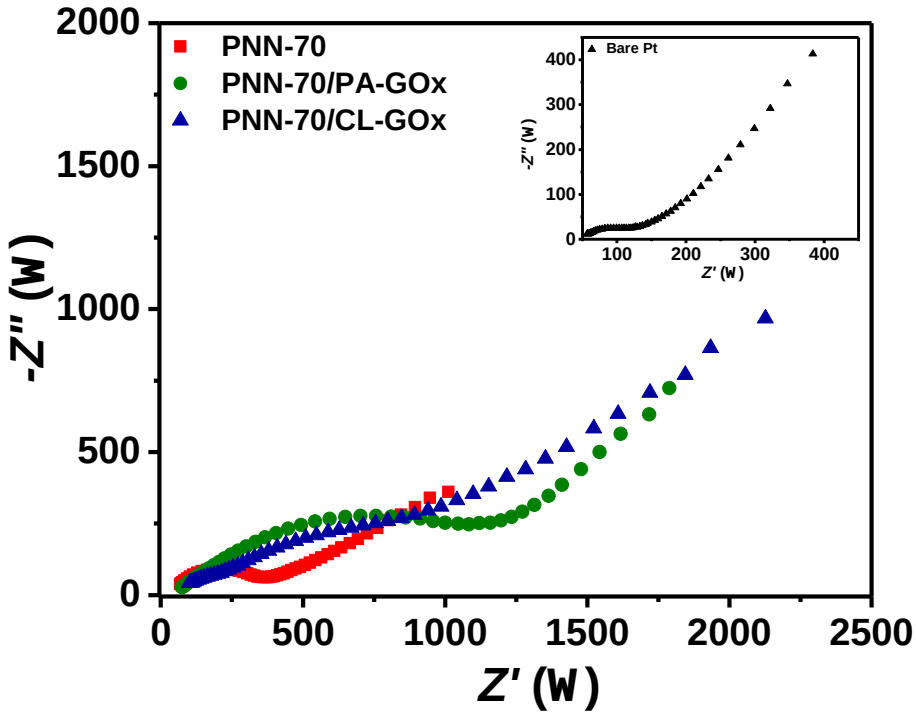

Fig. 5.10: **Nyquist plot of Bare Pt, PNN-70, Physically adsorbed and Crosslinked GOx over PNN-70.**

ified electrode was fitted to an equivalent electrical circuit of R(Q(R$_s$(Q(R$_{ct}$W)))) using ZSimpWin 3.2 impedance software. Where R$_{ct}$ defines the charge transfer resistance value. As shown in Fig. 5.10 upon immobilization of GOx, the semi-circle diameter has been found to increase for both the immobilization processes as compared to PNN-70 electrode. The increment in the R$_{ct}$ value from 350 Ω to 1201 Ω and 1918 Ω was obtained for PNN-70/PA-GOx and PNN-70/CL-GOx biosensor respectively. The decrease in the conductivity of physically adsorbed and crosslinked GOx electrode as compared to PNN after immobilization of GOx was due to the non-conductive behavior of GOx [114]. The observed increment in charge transfer resistance after the immobilization of GOx onto PNN-70 electrode confirms the immobilization of GOx for both the type of immobilization methods [115]. Furthermore, for both the type of immobilization, the amount of enzyme loaded over PNN-70 electrode was calculated by Fluorescence utilizing the optical property of Tryptophan present in GOx [56]. In case of physical adsorption, the GOx binds to PPy via electrostatic interaction between polycationic PPy and GOx while in crosslinking method GOx binds to the surface of PPy via a covalent bond between an amino group of enzyme and PNN via the crosslinker glutaraldehyde. When GOx is immobilized onto functionalized PPy support matrix, one aldehyde

group of glutaraldehyde reacts with the primary amino group of GOx and the other aldehyde group of crosslinker binds with the amino group of BSA and PPy support matrix [116, 117] The as-fabricated PNN-70 electrode has high-density nanofibers having a higher surface area which can provide higher enzyme loading. The loading mainly depends on the surface area and the method of enzyme immobilization. The amount of GOx loaded over PNN-70 was found ~559 μg-cm^{-2} and ~642 μg-cm^{-2} for physical adsorption and crosslinking immobilization respectively which depicts that the crosslinking immobilization has facilitated higher enzyme loading which was in good agreement with the observations of FTIR spectra. The higher enzyme loading is a prerequisite for improved sensitivity of the biosensor.

5.3.3 Biosensor response

Cyclic voltammetry analysis

To study the catalytic activity of GOx towards glucose oxidation, cyclic voltammetry of both the as-prepared biosensors was performed in 0.1 M PBS (pH-6.8) without stirring where the potential applied to the working electrode was swept from 0 to 0.7 V at a scan rate of 100 mV/s. Figure 5.11 represents a comparison be-

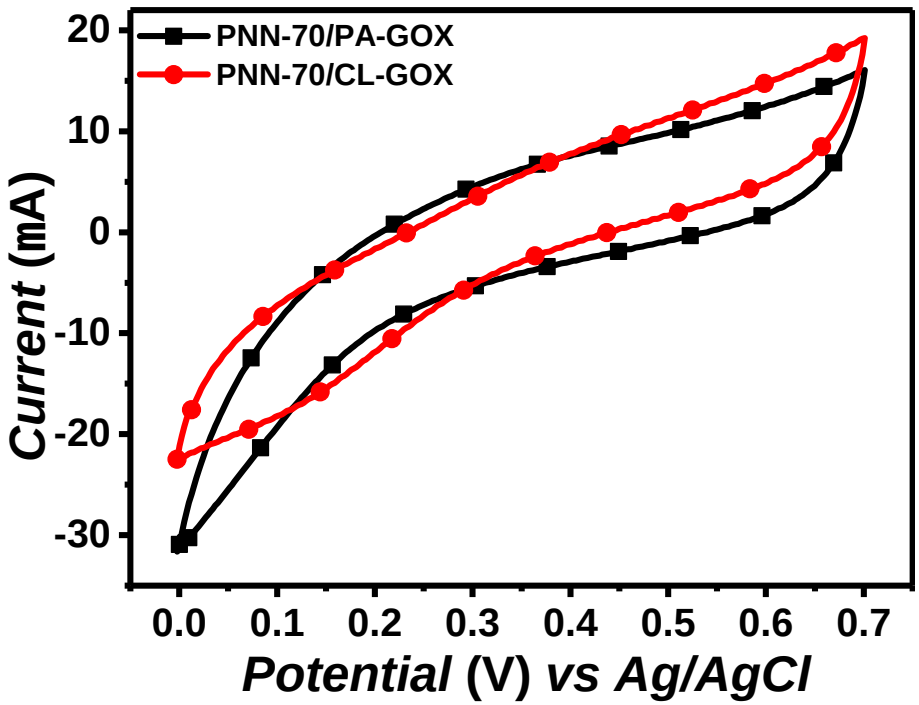

Fig. 5.11: **Comparison of physically adsorbed GOx and crosslinked GOx over PNN-70 with the injection of 3 mM glucose.**

tween CV responses of physical adsorption and crosslinked GOx based electrodes with the addition of 3 mM glucose concentration. As evident from Fig. 5.11 the oxidation current values has been significantly enhanced for crosslinked GOx as compared to physically adsorbed GOx. The CV response for physically adsorbed glucose biosensor with and without glucose has been shown in Fig. 5.12. The inset shows the magnified view of the anodic peak currents.

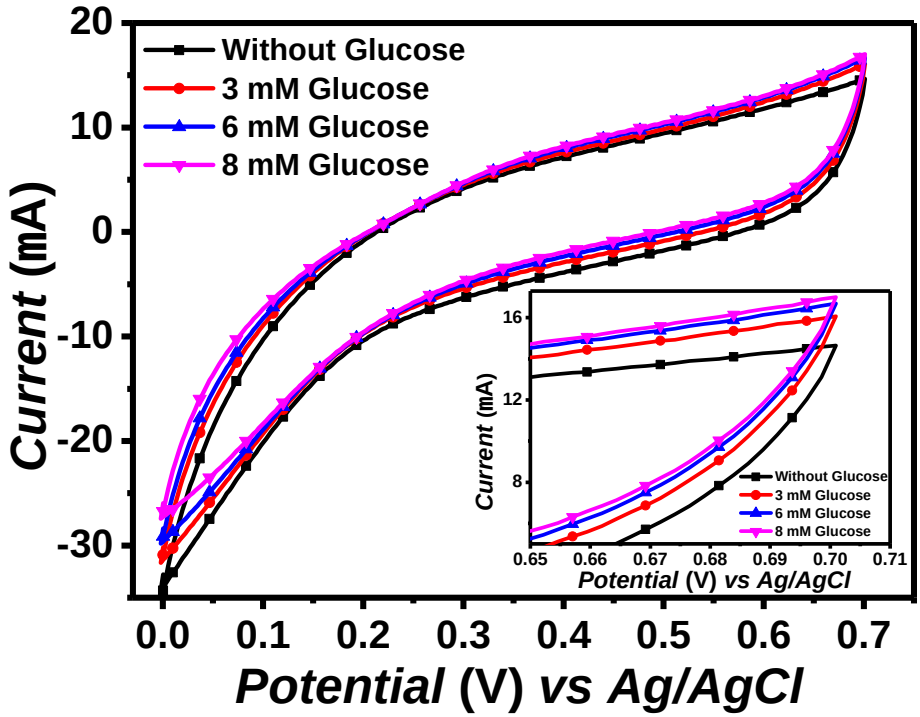

***Fig. 5.12:* CV sensing response of physically adsorbed GOx based biosensor with successive addition of glucose. The inset shows the magnified view of anodic peak currents.**

Figure 5.13 shows the cyclic voltammogram of the crosslinked electrode, The CV shows the electrode behavior without glucose and with the subsequent addition of glucose. With the injection of glucose to the electrolyte solution, a sharp increase in the anodic current was observed as compared to the current obtained without glucose, validating the activity of GOx immobilized onto PNN-70 for both the immobilization processes. The crosslinked PNN-70 i.e. PNN-70/CL-GOx biosensor has shown the current increment up to 3 mM glucose concentration. The observed current rise suggests the glucose oxidation catalyzed by GOx. The obtained current increment for crosslinked GOx based electrode was correlated with higher enzyme loading in case of crosslinking immobilization as compared to physical adsorption which was evident from enzyme loading estimation. Further

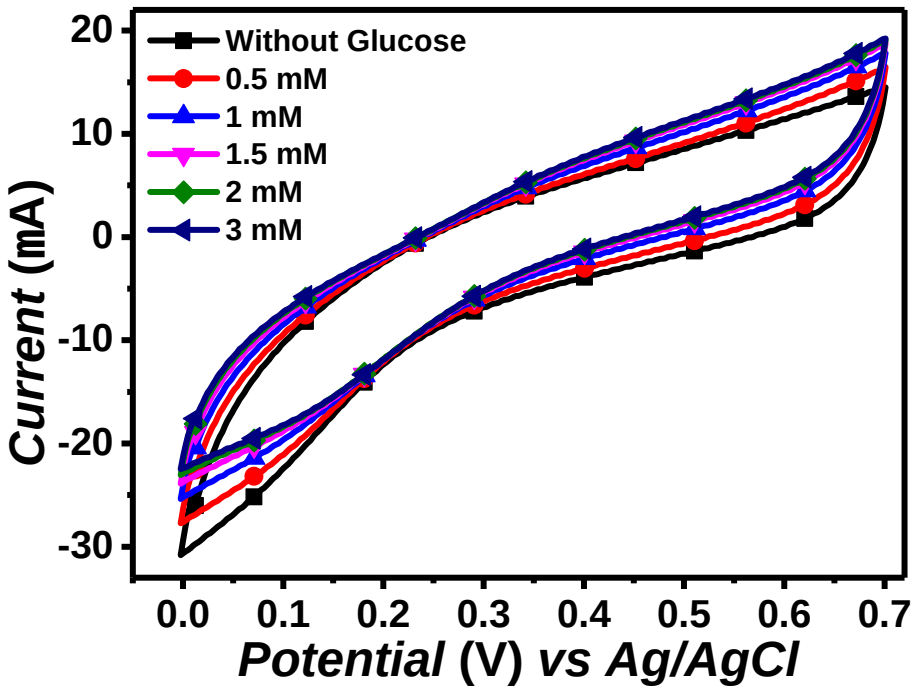

Fig. 5.13: **CV sensing response of cross-linked GOx based biosensor with successive addition of glucose.**

to confirm the observed results amperometric detection of glucose was carried out for both the types of electrodes.

Amperometric detection of glucose

The as-fabricated two types of biosensors were analyzed using amperometric detection method. Amperometric detection of glucose was carried out in a three electrode electrochemical cell using both the types of electrodes as the working electrode. All the current measurements were performed at a constant potential of 0.7 V applied to the working electrode immersed in continuously stirred 0.1 M PBS (pH 6.8). Successively glucose aliquots were injected into the electrolyte solution after steady state current value was reached.

Amperometric response of both the biosensors prepared by using physical adsorption and crosslinking immobilization methods have been presented in Fig. 5.14. The current response of the fabricated biosensors showed an instantaneous increment in the current upon injection of glucose representing the rate of oxidation of glucose. The immediate rise in the current indicates toward the retained catalytic activity of the enzyme, after immobilization on PNN-70 electrode as also visible from CV. In case of physical adsorption firstly 0.1 mM glucose was injected

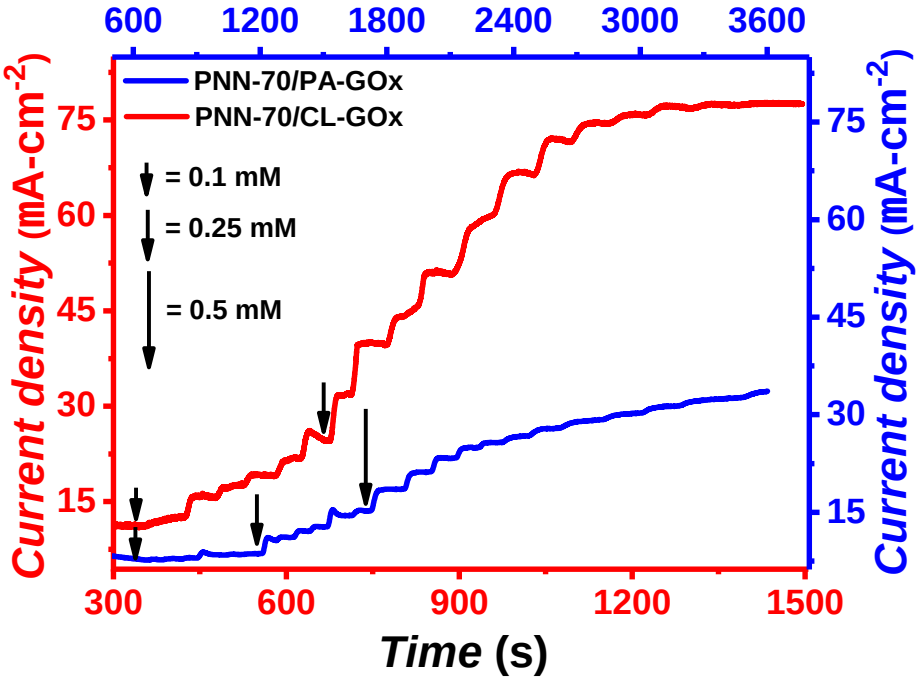

Fig. 5.14: **Amperometric responses of biosensors fabricated utilizing physical adsorption and crosslinking immobilization of GOx.**

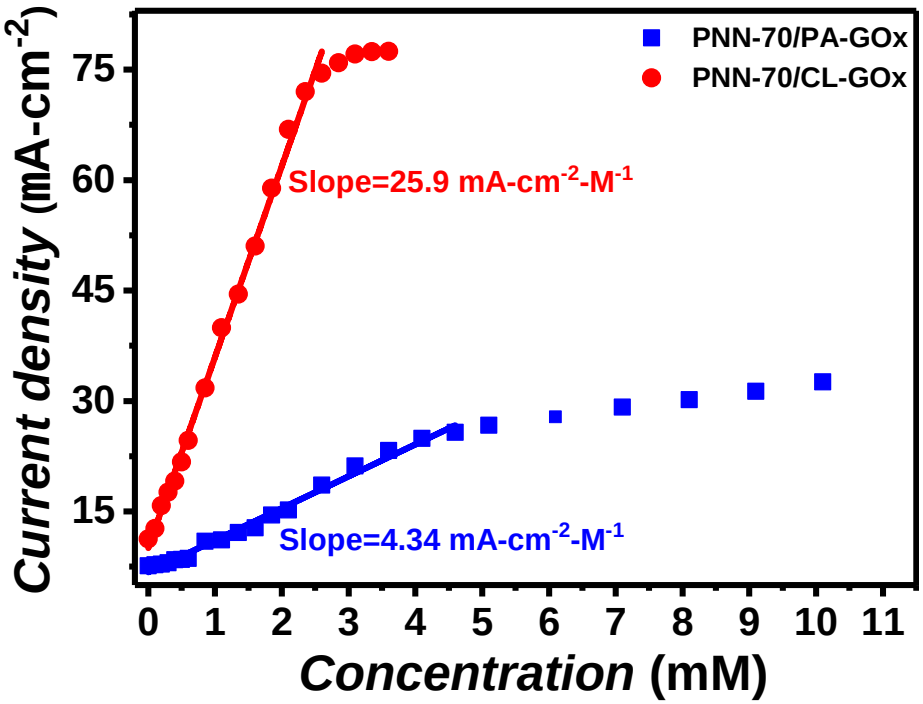

Fig. 5.15: **Calibration curves of physically adsorbed and crosslinked GOx based biosensors obtained from amperometric response.**

with the successive addition of 0.25 mM, 0.5 mM, and 1 mM glucose at every 70 s showing the corresponding rise in the current density and a step-like response has been obtained as evident from Fig. 5.14. Additionally, the amperometric response of crosslinked GOx over PNN-70 has also shown the step-like response with the

successive addition of 0.1 mM glucose followed by 0.25 mM glucose at every 50 s. The calibration plots of both the biosensors were obtained from the corresponding amperometric responses, and the performance of both the biosensors was compared as shown in Fig. 5.15. The calibration curves of both the biosensors follow the enzyme kinetics. For physical adsorption, initially at the lower concentrations of glucose up to 4.6 mM, the current density has increased linearly. Further increase in glucose concentration has led to saturation in the current density. The linear range corresponds to the fact that active sites of the enzyme are still available for the redox reaction. However, the saturation region observed at the higher concentration of glucose represents that all the active sites of the enzymes have been occupied by the glucose molecules. After the saturation region, no further increment in the current was observed with the addition of glucose. The sensitivity of the obtained biosensors was defined as the slope of the calibration curve for linear range, and the calculated value of sensitivity was observed as 4.34 mA-cm^{-2}-M^{-1} with a linear range of 0.1-4.6 mM for physically adsorbed GOx based biosensor. However, the improved sensitivity of 25.9 mA-cm^{-2}-M^{-1} was obtained by incorporating the crosslinked GOx as noticeable from Fig 15. The linear range of detection for crosslinked GOx based electrode was estimated to be 0.1 – 2.6 mM. In addition to sensitivity and linear range of detection, the response time for each biosensor was defined as the time taken to reach 90% of the steady state current value which was calculated to be approximately 45 s and 30 s for the biosensors prepared by physical adsorption and crosslinking immobilization techniques respectively. The observed improvement in the performance of crosslinked GOx based biosensor was ascribed to increased enzyme loading due to cross-linking immobilization of GOx. Cross-linking technique incorporates the higher amount of enzyme over the support matrix due to the covalent bond formation with a cross-linker. Thus, the observed results have shown a significant improvement in the sensitivity of biosensor with the cross-linking immobilization as compared to physical adsorption method (depicted in Fig. 16).

Further, a similar study has been performed for the other type of PPy nanofibrous electrode i.e. PPy-pTSA based electrode which was fabricated with pTSA as the dopant as discussed in chapter 4. The enzyme was immobilized over the PPy-pTSA electrode by cross-linking and the electrode was named PPy-pTSA/CL-GOx.

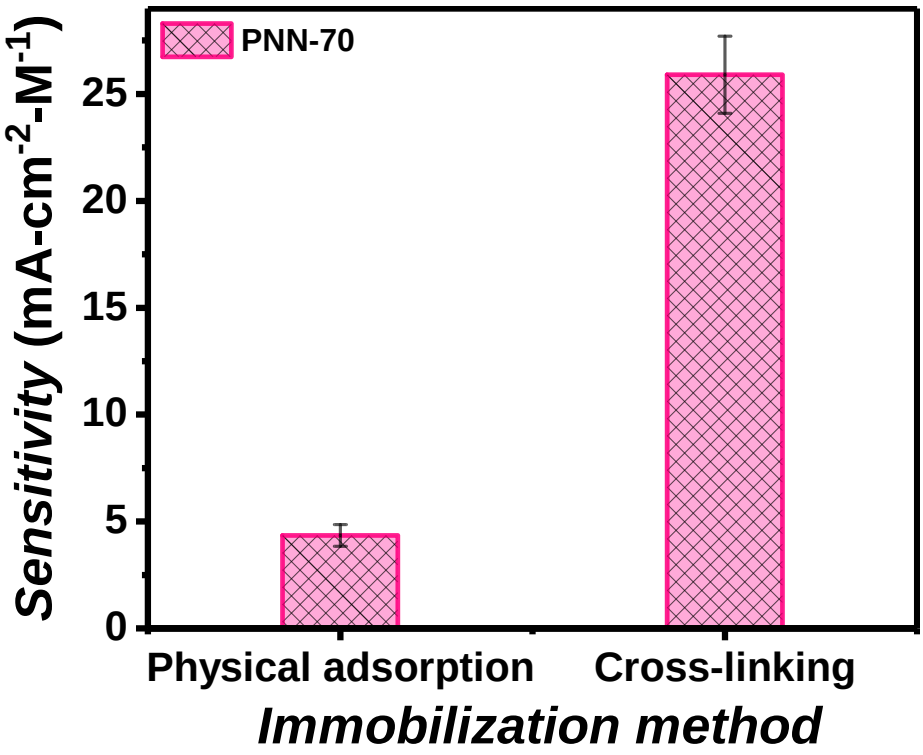

Fig. 5.16: **Sensitivity variation of physically adsorbed and cross-linked GOx over PNN-70 based biosensor.**

Corresponding to physical adsorption, the electrode was named as PPy-pTSA/PA-GOx. The amperometric response of the as-fabricated PPy-pTSA/CL-GOx biosensor has been shown in Fig. 5.17. Initially, 0.1 mM glucose was injected in the electrolyte solution followed by 0.25 mM glucose. The current was observed to rise instantaneously which confirms the retained activity of GOx on cross-linking. The corresponding calibration curves were obtained from the amperometric responses. The sensitivity was increased to 29.17 mA-cm^{-2}-M^{-1} in linear range of operation of 0.1-2.5 mM for PPy-pTSA/CL-GOx electrode as shown in Fig. 5.18. The response time was estimated to be 30 s for the biosensor. Fig. 5.18 has indicated that with the cross-linking the sensitivity of the biosensor was improved as also depicted in Fig. 5.16.

A comparison of all figure of merits of the prepared biosensors has been illustrated in Table 5.1 which has shown that PPy-pTSA/CL-GOx type biosensor has shown the highest sensitivity among the other electrodes. The immobilization methods have shown significant influence on the sensitivity and linear range of operation of the glucose biosensor. With the crosslinked GOx the sensitivity of the glucose biosensor was improved drastically. Although, the linear range of the pre-

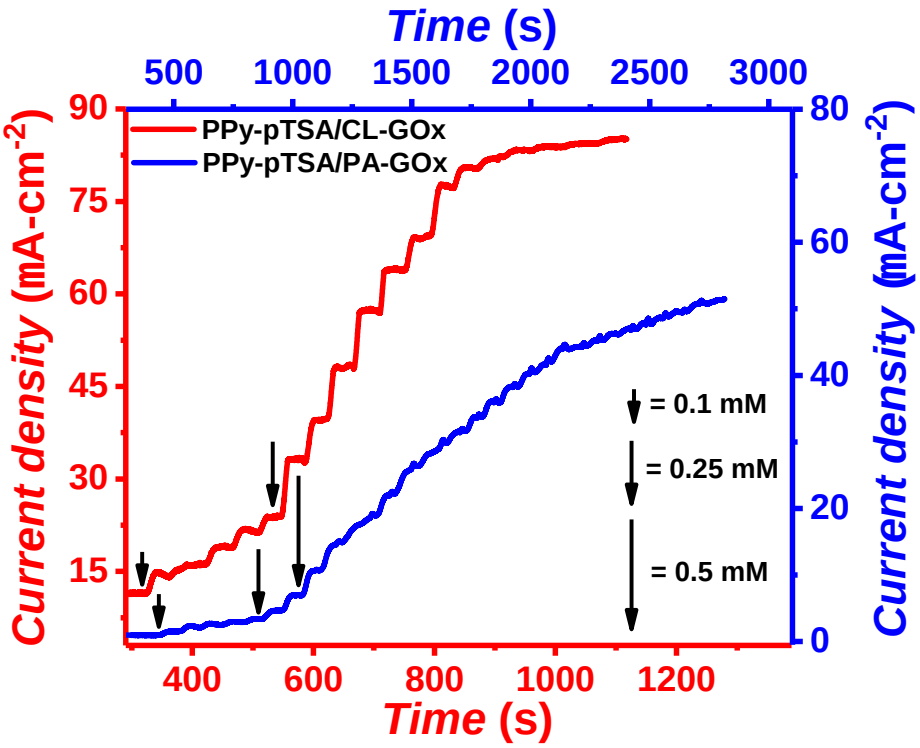

Fig. 5.17: **Amperometric responses of PPy-pTSA/PA-GOx and PPy-pTSA/CL-GOx biosensors.**

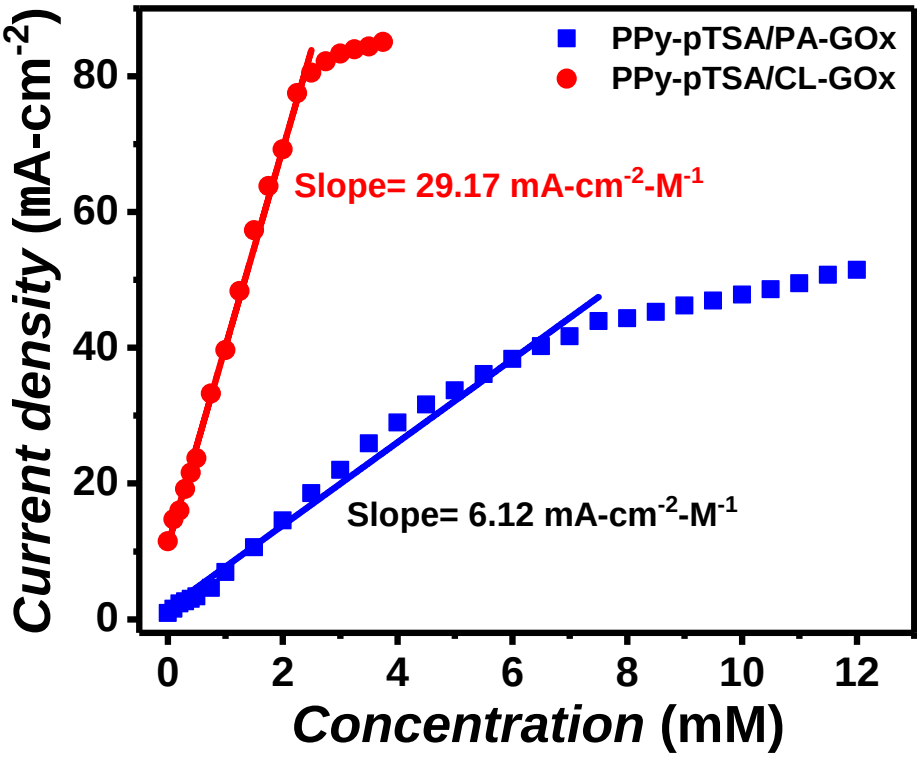

Fig. 5.18: **Calibration curves of PPy-pTSA/PA-GOx and PPy-pTSA/CL-GOx biosensors.**

sented glucose biosensor with crosslinking was observed to be narrower. Thus, the measurement of glucose in the human blood sample using the proposed biosensor

can be performed by the dilution of the blood sample. Moreover, the crosslinked GOx based glucose biosensor with the linear range of 0.1-2.5 mM can find application for noninvasive glucose detection in human body fluids such as sweat and saliva [16, 118].

Table 5.1: **Comparison of prepared electrodes using physical adsorption and crosslinking immobilization of GOx.**

Electrode	Sensitivity ($mA\text{-}cm^{-2}\text{-}M^{-1}$)	Linear Range (mM)	Response Time (s)
PNN-70/PA-GOx	4.34	0.1-4.6	∼45
PNN-70/CL-GOx	25.9	0.1-2.6	∼30
PPy-pTSA/PA-GOx	6.12	0.1-7.5	∼45
PPy-pTSA/CL-GOx	29.17	0.1-2.5	∼30

Michaelis Menten constant

The Michaelis Menten constant (K_m) value of the PPy-pTSA/CL-GOx based glucose biosensor was estimated by the graphical method [27]. Each observation obtained from amperometric response was represented by a straight line in K_m-V_{max} space. Median of all intersection points of these straight lines was determined to

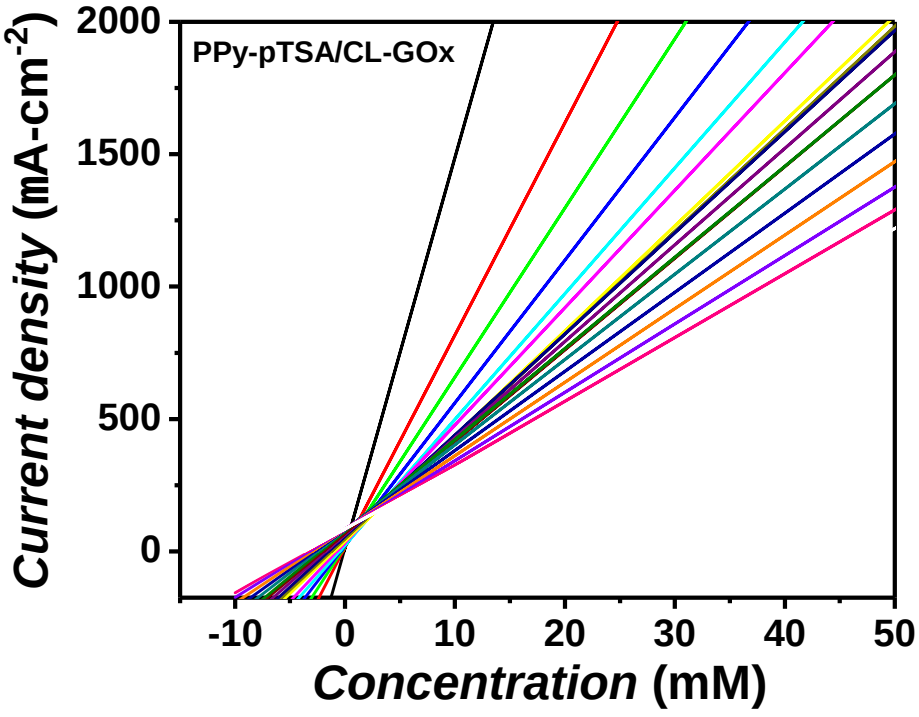

Fig. 5.19: **Direct linear plot of cross-linked based biosensor for K_m estimation.**

calculate the K_m value. The direct linear plot for cross-linked GOx based biosensor has been shown in Fig. 5.19. The calculated value of K_m was found to be 1.79 mM for the same, which indicates a strong affinity between enzyme and substrate molecules.

Interference effect study, reproducibility, and real blood sample analysis

In addition to glucose, human blood and serum contain several other electroactive species viz. uric acid, ascorbic acid, etc. which also gets easily oxidized at 0.7 V potential. Thus these electroactive species may also interfere with the biosensor response during glucose detection. Hence, it is required to define the anti-interference capability of the biosensor for obtaining a practical glucose biosensor. Here, the effect of interfering species; ascorbic acid (0.1 mM) and uric acid (0.4 mM) was examined on the performance of PNN-70/CL-GOx glucose biosensor. To study the influence of interferents' initially 0.25 mM glucose was introduced into the cell and allowed to reach a steady state. Afterward sequentially 0.1 mM ascorbic acid and 0.4 mM uric acid was injected into the electrolyte solution. Figure 5.20 shows the interference effect on sensing response of crosslinked immobilized GOx onto PNN-70 electrode.

The current response shows the similar behaviour of biosensor, and an increase of 0.36% and 3.7% in the current density corresponding to ascorbic acid and uric acid respectively was observed. The current response presents that, the biosensor has shown a very less current rise as compared to glucose which specifies the anti-interference capability of biosensor owing to the high specificity and selectivity of enzymes towards glucose.

Moreover, the reproducibility of the as-fabricated crosslinked GOx based biosensor was determined. The amperometric responses of three similarly prepared biosensors were compared, and a relative standard deviation of 6.6% was obtained which was found to be in an acceptable range. Furthermore, to check the reliability of as-fabricated biosensor for practical application real whole blood sample was taken. The freshly taken whole blood sample was injected into the electrochemical cell consisting of PBS, and the current rise was observed relating to the glucose concentration which was compared with the glucose concentration measured by standard GOD-POD colorimetric assay and was observed to be 5.5 mM. The estimated value

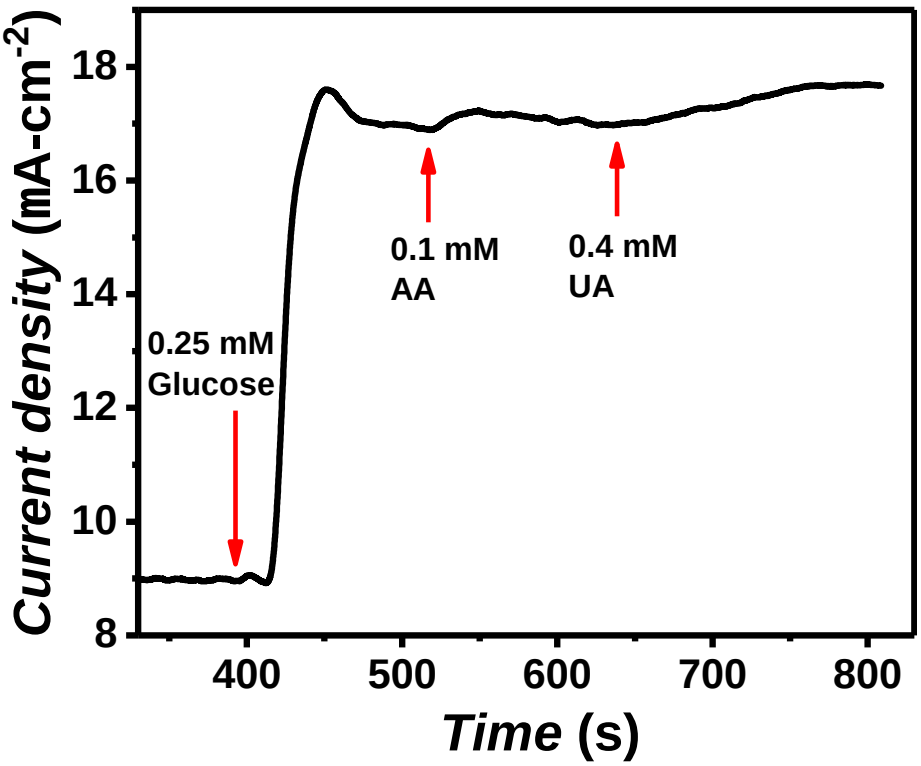

Fig. 5.20: **Interference effect of ascorbic acid and uric acid on the performance of crosslinked GOx biosensor.**

of glucose concentration by as-fabricated biosensor was 5.1 mM with a deviation of 7.2% which was in good agreement with the glucose concentration measured by standard glucose assay.

5.3.4 Comparison of the as-fabricated biosensor with recently reported glucose biosensors

The performance of developed biosensor was compared with the recently reported work. Table 5.2 shows the comparison of all figure of merits of the best performing biosensor with some previously reported work where different PPy nanostructures have been employed as a support matrix for GOx immobilization. The as-fabricated PNN based biosensor has demonstrated fairly good sensitivity and reasonable response time.

5.4 Conclusions

In summary, an enzymatic glucose biosensor based on PPy nanofibers has been fabricated successfully. The PNN electrode has been employed as a support matrix

Table 5.2: **Comparison of different figure of merits of fabricated biosensor with some previously reported work.**

Electrode	Sensitivity ($mA\text{-}cm^{-2}\text{-}M^{-1}$)	Linear Range (mM)	Response Time (s)	K_m (mM)	Reference
Glass/Cr-Pt/PPy-pTSA/CL-GOx	29.17	0.1-2.5	30	1.79	This work
Glass/Cr-Pt/PNN-70/CL-GOx	25.9	0.1-2.6	30	1.9	This work
Pt/PPy-PVS/GOx	-	0.05-1	200	-	[119]
Pt/PPy/GOx	0.22	0-10	15	37.6	[94]
Glass/Au/PPy/GOx	1.9	0.125-11.25	30-35	15.9	[52]
SWCNTs[a]-$PhSO_3^-$-/PPy-GOx	6	0.02-6	-	-	[59]
AAO/Pt/PPy/GOx	7.4	0.5-13	3	7.01	[95]
AAO/Pt/PPy/GOx	18.6	0.25-25	10	-	[55]

[a]Single walled carbon nanotube.

for GOx immobilization. The two types of electrodes *viz.* PNN-70 and PPy-pTSA utilized as support matrix has provided a biocompatible environment to GOx. The immobilization of GOx has been performed via physical adsorption, and crosslinking method and the performance of both types of biosensor has been evaluated and compared. The incorporation of crosslinked GOx via glutaraldehyde (crosslinker) has resulted in approximately five times enhancement in the sensitivity along with improved response time. The biosensor has shown the sensitivity of 4.34 $mA\text{-}cm^{-2}\text{-}M^{-1}$ and 6.12 $mA\text{-}cm^{-2}\text{-}M^{-1}$ with response time of 45 s for physically adsorbed GOx while 25.9 $mA\text{-}cm^{-2}\text{-}M^{-1}$ and 29.17 $mA\text{-}cm^{-2}\text{-}M^{-1}$ with response time of $\sim$30 s respectively for crosslinked GOx. The biosensor fabricated with the crosslinked GOx has shown the increased enzyme loading as compared to physically adsorbed GOx leading to an enhanced sensitivity of the prepared biosensor. The observed results have shown that the selection of immobilization technique plays a significant role in the performance of biosensors as it directly affects the enzyme loading which is one of the vital aspects that is responsible for the improvement in biosensors performance.

Chapter 6

Investigation Towards the Electrochemical Performance of PPy/ZnO Nanocomposite Electrode

In this chapter, a nanocomposite electrode of electrodeposited Polypyrrole (PPy) over vertically aligned 1-D ZnO nanorods (ZNR) has been investigated towards the biosensor fabrication. The ZNRs over Pt-coated glass substrate were synthesized by hydrothermal method and the as-fabricated ZNRs were utilized as the template for the electrodeposition of PPy to form a composite. The PPy was electropolymerized over ZNR using the cyclic voltammetry (CV) deposition method. The thickness of PPy over ZNRs was optimized by using a different number of cycles in CV deposition. The modification of ZNR with PPy was confirmed by FESEM, TEM, XRD, and Raman. With the modification of PPy, charge transfer resistance of the electrode was reduced approximately 300 times and the electroactive surface area was improved $\sim$9 folds as compared to ZNR electrode. Additionally, the Photoluminescence study has presented the suppressed visible emission with the PPy deposition. Thereby the PPy modified electrode has demonstrated a high specific surface area, high electro-activity, and suppressed visible emission as compared to bare ZNR electrode.

6.1 Introduction

Recently, the nanocomposite structures of organic and inorganic material have received great attention due to the improved performance of these materials. They offer new functional hybrid materials having synergetic properties of both organic and inorganic materials, which have found widespread applications in optoelectronics, biosensors, gas sensors, energy storage, supercapacitors, antistatic coatings, etc [120–123]. Nanostructured metal oxide semiconductors such as ZnO, SnO_2, V_2O_5, TiO_2 etc. are some of the encouraging materials in electronics and optoelectronics [124, 125]. Among all, ZnO nanostructures have attracted wide attention from the last few decades owing to its extraordinary electrical and optical properties [85]. ZnO has been reported to be a direct bandgap semiconductor material with wide band gap (3.3 eV at 300 K), high excitonic binding energy (60 meV at 300 K), and good electron mobility of 205 $cm^2V^{-1}s^{-1}$ which makes it a suitable candidate for extensive range of applications in biomedical such as detection of urea, glucose, cholesterol, etc. [126] and also in optoelectronics applications such as UV lasers [127], UV detectors [128] transistors [129], gas sensors [130], piezoelectric devices [131]. Variety of ZnO nanostructures *viz.* nanotubes, nanobelts, nanorods, nanospheres, etc. have been reported which can be grown by different physical (pulsed laser deposition, molecular beam epitaxy, chemical vapor deposition, etc.) and solution based (electrochemical, hydrothermal, sol-gel, etc.) methods [132]. Amidst these methods, the physical methods of ZnO synthesis are expensive and require complex processing steps. Though, the as-grown ZnO films synthesized by physical methods have a good quality of thin films. While solution-based methods are economical. However, ZnO synthesized by solution methods generally shows visible luminescence at different emission wavelengths along with the UV exciton emission peak. The visible emission peak in ZnO at different wavelength has been reported to be present due to a variety of defects incorporated during solution-based growth [133]. In this regard, surface modification of inorganic nanostructures has fascinated a great deal of attention because it provides excellent integration and an improved interface between nanostructures and conducting polymer (CP) matrices [134]. CPs *viz.* Poly(3,4-ethylene dioxythiophene), Polyaniline, Polythiophene, Polypyrrole, etc. have been widely explored.

Among different CPs, PPy has been accepted as one of the most widely used material due to its facile synthesis, high electrical conductivity, environment stability and biocompatibility which enables its potential applications in biosensors, energy storage, actuators, anti-corrosives, electrochromic displays, anti-static materials, electromechanical devices, fuel cells, etc. [135, 136]. The PPy in its oxidized state has demonstrated high electron affinity which is crucial for the improved performance of the device. Various PPy nanostructures *viz.* nanotubes, nanowires, nanofibers, nanoparticles, etc. can be synthesized via chemical, Physical and electrochemical method [52]. Among all, the electrochemical deposition method has been realized as a simple and direct approach which facilitate the deposition of PPy directly on the electrode surface. Combining the high flexibility and solution processability of PPy with the structural, chemical, and high functional stability of ZnO has opened up new possibilities in high performance flexible electronic devices. B. Yan et al. [137] have fabricated the flexible ZnO microrods/PPy composite electrode and discussed it's application towards the photocatalysis. J. Huang et. al. [138] have synthesized ZnO/PPy composite by ultrasound assisted chemical polymerization and presented the superior capacity stability of the composite material. In this work, 1-D ZNR/Ppy nanocomposite electrodes were fabricated by a two-step approach. The ZnO nanorods (ZNRs) were modified with the PPy to improve both electrical and optical properties of ZnO for a wide variety of applications. The ZNRs were synthesized by a simple, economical and scalable method. The prepared ZNR were utilized as the templates for the electropolymerization of PPy. The as-prepared ZNR/PPy nanocomposite material was characterized by FESEM, TEM, Raman, and structural characterization was performed by XRD. The deposition of PPy over ZNR has drastically improved the electrical properties of ZNR which can be a promising nanocomposite electrode for the fabrication of biosensor.

6.2 Experimental Details

6.2.1 Chemicals

All chemicals of analytical grade were purchased from Sigma Aldrich and used without further purification. Anhydrous zinc acetate, 2-Methoxy ethanol, Ethanolamine, Zinc nitrate hexahydrate ($Zn(NO_3)_2{\cdot}6H_2O$), Hexamethylenete-

tramine (HMTA) ($C_6H_{12}N_4$), Sodium phosphate dibasic (Na_2HPO_4, Sodium phosphate monobasic (NaH_2PO_4), Pyrrole (Py) monomer, Lithium perchlorate ($LiClO_4$), Potassium ferricyanide/ferrocyanide $[Fe(CN)_6]^{3-/4-}$ were used for the experiments. Phosphate buffer solution (0.1 M, pH 6.8) was prepared by using NaH_2PO_4 and Na_2HPO_4.

6.2.2 Synthesis of ZnO nanorods and ZnO nanorods/PPy electrode

At first, the glass substrates (1 cm x 1 cm) were cleaned by ultrasonication in acetone, isopropanol and finally in DI. The cleaned substrates were treated with the RCA clean-1 process to make the hydrophilic surface. Further, a Platinum layer (50 nm) with a buffer layer (5 nm) of Chromium (Cr) was sputtered over glass substrate at a base pressure of $1x10^{-6}$ mbar and a working pressure of 3 mTorr. Additionally, the substrates were rotated at 10 rpm to obtain uniform Pt deposition. Furthermore, the ZnO nanorods were hydrothermally grown on Pt (50 nm) coated glass substrate with an intermediate layer of Chromium (5 nm). The schematic illustration of the fabrication steps of the ZnO nanorods/PPy nanocomposite electrode has been shown in Fig. 6.1.

Briefly, a thin seed layer of ZnO was deposited over the Pt-coated glass substrate using a spin coating technique. To deposit the seed layer, firstly, an equimolar (2 M) seed solution of zinc acetate and ethanolamine was prepared in 2-methoxy ethanol and spin-coated on a Pt-coated glass substrate. The spin-coated sample was annealed at a temperature of 235 °C in an oven for 5 min to obtain the ZnO seed layer. Further, the seed layer coated samples were placed vertically in an equimolar (50 mM) nutrient solution of Zinc nitrate and HMTA [108]. The hydrothermal growth of ZnO was carried out at a temperature of 95 °C for 10 hrs. Finally, ZnO grown samples were washed thoroughly in DI water to remove any residual/precipitated salts and dried at room temperature. After synthesis of ZnO nanorods, PPy was electropolymerized over ZnO nanorods using cyclic voltammetry method of deposition. The as-synthesized Pt/ZNR electrode was utilized as the working electrode and dipped into an electrolyte solution of 0.1 M distilled Py monomer and 50 mM $LiClO_4$. The potential of the working electrode was swept

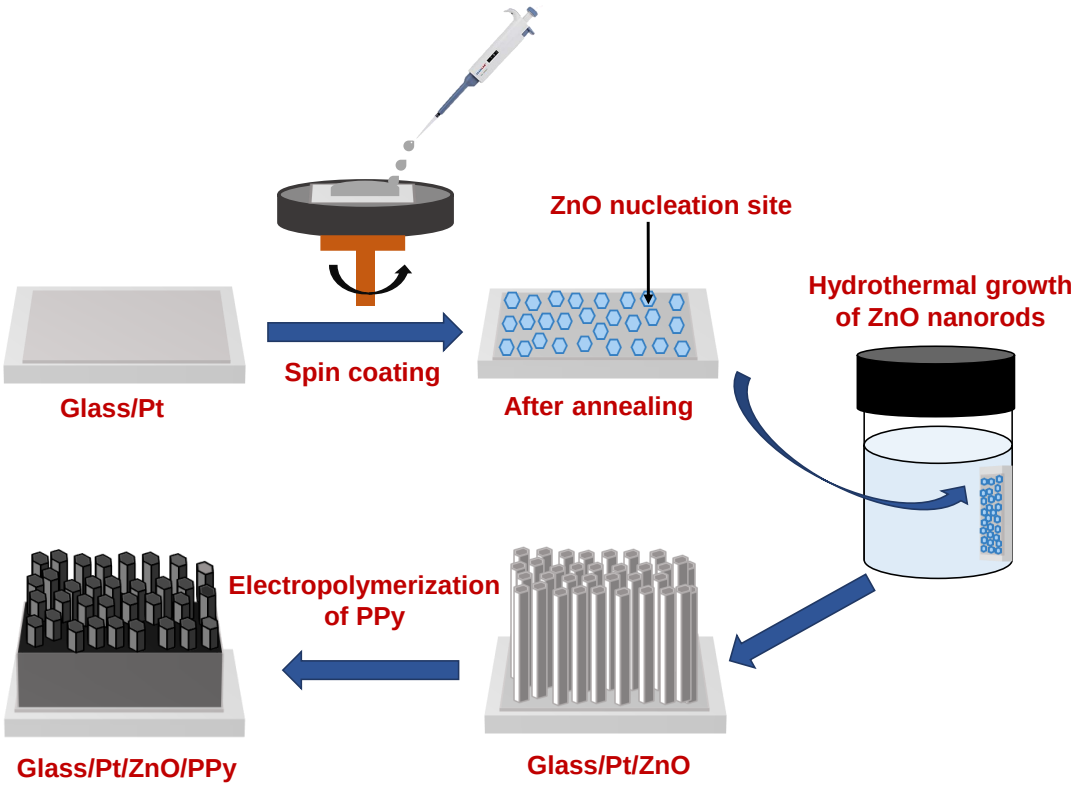

Fig. 6.1: **Schematic illustration of fabrication steps of ZNR/PPy composite electrode.**

from -0.5 to 1.5 V at a scan rate of 50 mV/s. Thus accordingly a core-shell structure of ZnO/PPy was obtained. The thickness of PPy over ZnO nanorods was varied by using a different number of cycles (5, 20, and 30 cycles) of deposition in the CV method. For the discussion, the corresponding electrodes for 5, 20, and 30 number of cycles for deposition were named ZNR/PPy-5, ZNR/PPy-20, and ZNR/PPy-30 respectively.

6.3 Results and Discussion

6.3.1 Morphological characterization

In order to study the surface morphology and to confirm the deposition of PPy onto ZnO nanorods, FESEM characterization was carried out for hydrothermally grown ZnO nanorods and electrodeposited PPy over ZnO nanorods. Figure 6.2(a, b) shows the top view and cross-sectional view FESEM micrographs of hydrothermally synthesized ZNR structure.

The surface morphology of ZNRs has presented the nanorods with a clear

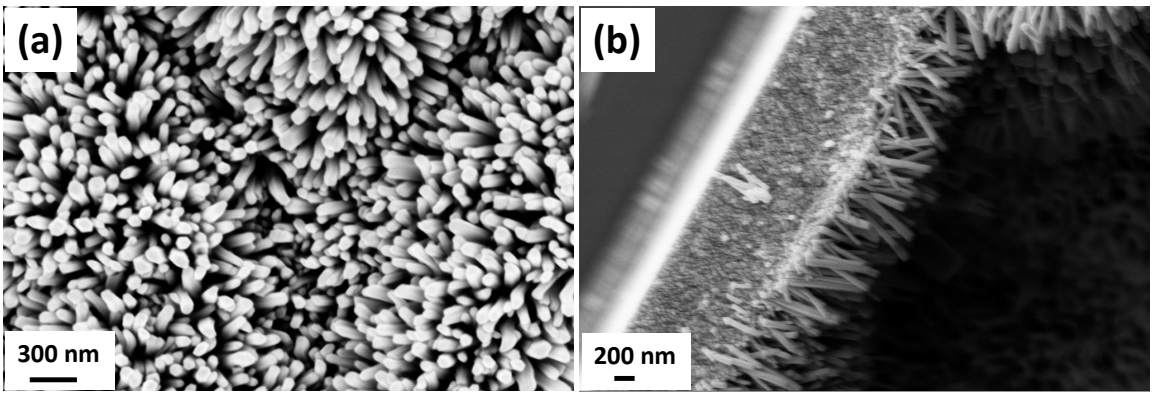

Fig. 6.2: **FESEM images showing (a) Top view (b) cross-sectional view of ZnO nanorods.**

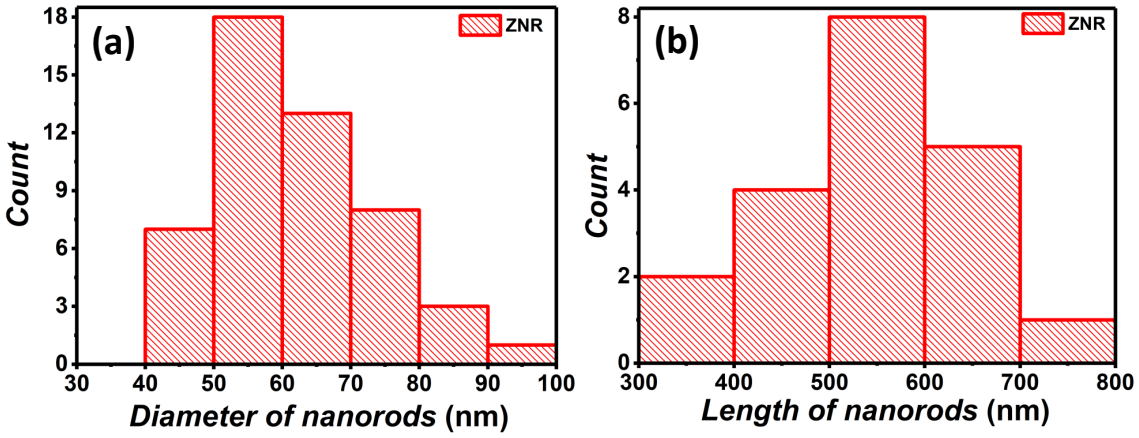

Fig. 6.3: **Diameter and length distribution of ZnO nanorods.**

hexagonal facet. Figure 6.3 (a, b) demonstrates the histogram plot for diameter and length distribution of ZNRs respectively. The diameter and length distribution of ZNRs have been calculated by imtool in MATLAB by randomly selecting approximately 50 nanorods from FESEM images. The histogram plot for ZNRs has shown an average diameter of ∼60 nm and length of ∼600 nm which has demonstrated an aspect ratio of ∼10 for the same. The FESEM images of electrodeposited PPy with variable thickness over ZnO nanorods have been shown in Fig. 6.4 (a-c). The FESEM images have demonstrated that the PPy thickness over the grown ZNR has been increased as the number of cycles for the deposition were increased. This clearly signified that as the electropolymerization progresses, the PPy layer formation starts at the Pt surface and a thin PPy layer starts forming interconnects among the ZnO nanorods.

Further, as the number of cycles was increased for the deposition of PPy, the thickness of PPy increased filling up the gaps between the ZnO nanorods as also

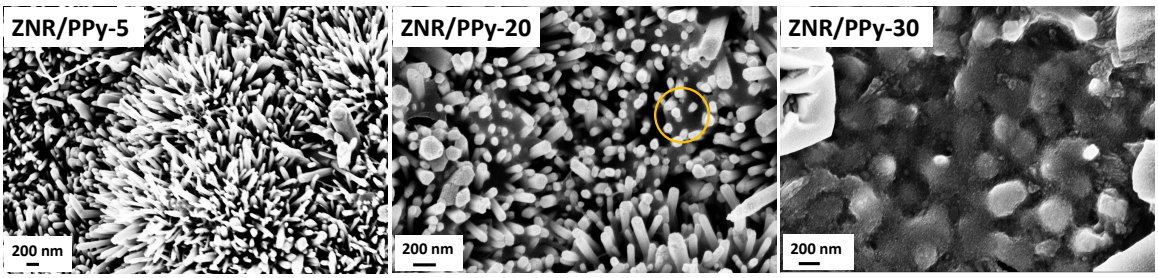

Fig. 6.4: **FESEM images of PPy deposited ZnO nanorods for (a) 5 cycles (b) 20 cycles (c) 30 cycles.**

evident from FESEM images. Further, the ZNRs were completely covered by PPy for 30 number of cycles as shown in Fig. 6.4 (c). The diameter of electrodeposited PPy over ZnO nanorods was measured to be ∼180 nm after the full coverage of ZnO nanorod. The optimum thickness of PPy was observed for ZNR/PPy-20 electrode. Thus, for further study, we have taken ZNR/PPy-20 electrode and referred to as ZNR/PPy.

6.3.2 TEM analysis

Further, to confirm the deposition of PPy over 1-D ZnO nanorods, the as-prepared ZNR/PPy-20 electrode was characterized by HR-TEM.

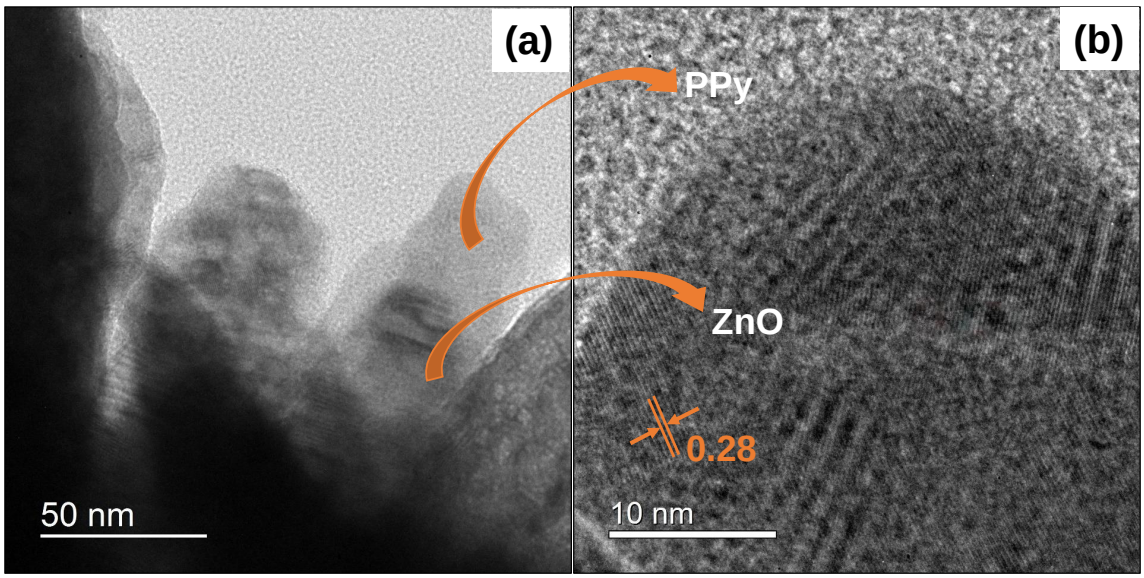

Fig. 6.5: **(a) TEM image (b) HR-TEM image of ZNR/PPy electrode.**

Figure 6.5 (a, b) have shown the TEM and HR-TEM images of electrodeposited PPy over 1-D ZnO nanorods which have represented the core-shell structure of ZNR/PPy electrode. The coating around ZnO was expected to be PPy as presented

in the TEM image. The as-grown ZNR was confirmed with the lattice spacing of 0.28 nm which attributes to the (100) crystal plane of ZnO crystals [139, 140] and the coating of PPy was found to be amorphous in nature [120].

6.3.3 XRD study

To observe the structural difference between ZNR and ZNR/PPy electrodes, the XRD pattern of both the electrodes were recorded. Figure 6.6 has shown the XRD pattern of ZNR and ZNR/PPy electrodes. The bare ZNR electrode has exhibited sharp peaks at 2θ= 31.7°, 34.4°, 36.2°, 39.6°, 47.5°, 56.6°, 62.8°, and 68° corresponding to (100), (002), (101), (102), (110), (103), and (112) phases. All the peaks were in good agreement with the standard JCPDS (space group P63mc, JCPDS – 36 – 1451) of hexagonal wurtzite structure of ZnO. Additionally, the peak at 2θ=40° was ascribed to Pt deposited glass substrate [85]. The XRD pattern of ZNR/PPy has shown all the peaks corresponding to ZnO and a broad peak at 2θ=22.4° which was attributed to PPy [141]. The observed broad peak has demonstrated the amorphous structure of PPy [135, 142]. The diffraction pattern of ZNR/PPy electrode has shown the peaks of ZnO along with the broad peak at 22.4° which demonstrate the interaction of PPy with ZnO nanorods [139]. The crystallite size of ZNR and ZNR/PPy was estimated by Scherrer's formula (equation 6.1).

$$D = \frac{k \times \lambda}{\beta \times cos\theta} \tag{6.1}$$

where D refers to the crystallite size, k denotes the constant value (0.94), λ is the wavelength of Cu Kα (1.54Å), θ represents the corresponding angle of each plane, and β defines the full width of θ at half of the maximum value [135].

The average value of the crystallite size of ZNR was found to be 33 nm. However, with the deposition of PPy, the crystallite size was increased to 36 nm which confirm the PPy coating. Additionally, the decrease in the intensity of the XRD peaks corresponding to each phase was observed with the PPy deposition which was attributed to the interaction between ZnO nanorods and PPy.

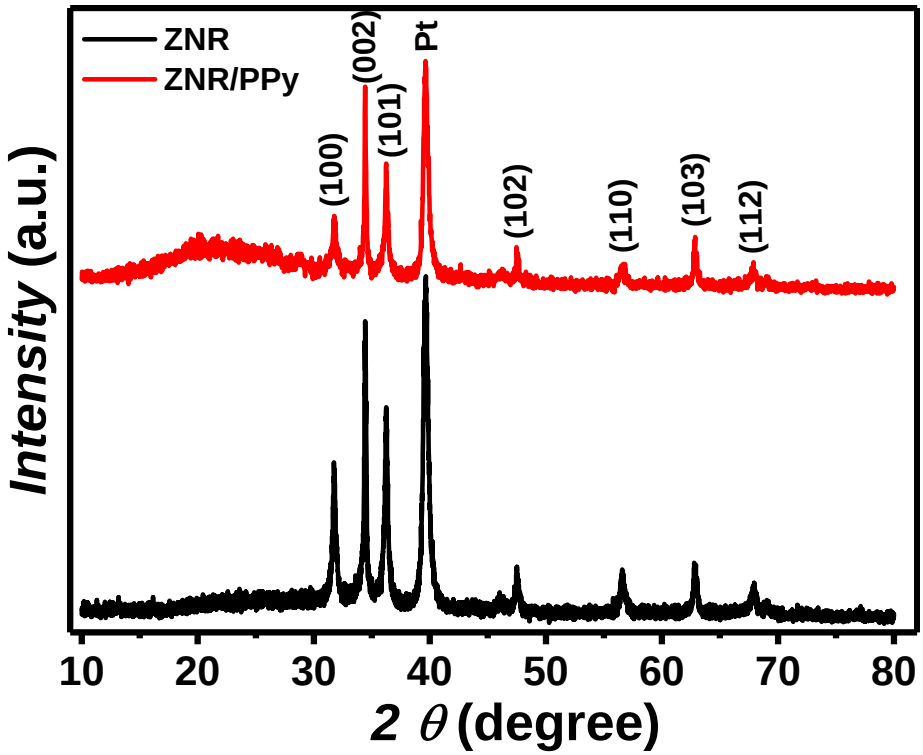

Fig. 6.6: **XRD pattern of ZNR and ZNR/PPy electrodes.**

6.3.4 Raman characterization of ZNR and ZNR/PPy nanocomposite

The Raman spectra of as-synthesized ZNR and ZNR/PPy electrode with 488 nm laser light source have been shown in Figure 6.7. The Raman spectra of ZNR electrode has shown the intense peak at 438 cm^{-1} referred to E_2 (high) mode in ZnO which indicate the vibrations of O atoms in the sub-lattice. The strong E_2 (high) mode peak shows the characteristics of a wurtzite structure and good crystallinity. In addition to E_2 (high) peak, other peaks were also observed at 200, 333, and 382 cm^{-1} which were in good agreement with the literature [143, 144]. Moreover, with the surface functionalization of ZnO by PPy (ZNR/PPy), the intensity of peak corresponding to E_2 (high) mode was observed to be suppressed. Additionally, the peaks at 936, 987, 1052, 1369, and 1579 cm^{-1} were observed with the PPy deposition which has been attributed to the confirmation of PPy deposition. The peak at 1369 and 1579 cm^{-1} were related to the aromatic ring stretching and C=C stretching [137]. The peak at 936 and 1052 cm^{-1} correspond to the bipolaron deformation and in-plane vibrations of C-H bond [134]. The presence of all the peaks corresponding to PPy with ZnO has clearly indicated the deposition of PPy over ZNRs.

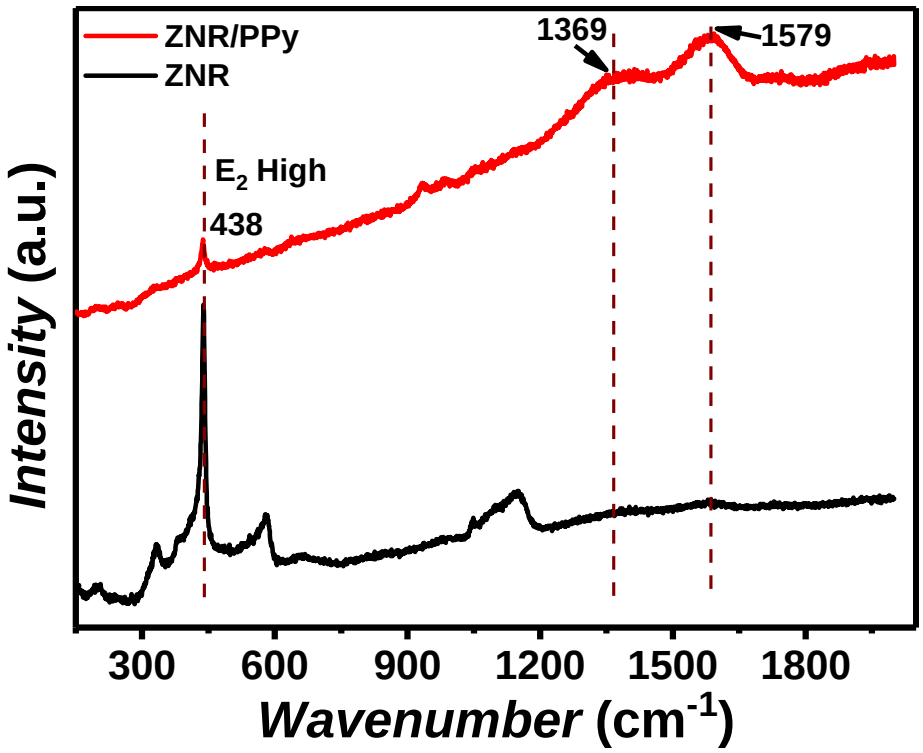

Fig. 6.7: **Raman shift of ZNR and ZNR/PPy electrode.**

6.3.5 Optical characterization of PPy coated ZnO nanorods

Photoluminescence study

To study the optical characteristics of as-prepared ZNRs and ZNR/PPy electrodes, room temperature Photoluminescence (PL) was performed. The observed PL spectra of ZNR and electrodeposited PPy over ZNR have been shown in Fig. 6.8. The PL spectra of ZnO has shown two main characteristic peaks corresponding to near band edge emission (NBE) and deep level emission (DLE). A sharp peak at 382 nm in the near UV region and a wide band in visible region ranging from 450 to 740 nm centered at 582 nm was obtained. The sharp peak of NBE in UV region signifies the development of highly crystalline ZNRs and the broad peak in a visible region corresponding to DLE shows a different type of defects present in ZNRs as reported previously [145]. The PL spectra of ZNR/PPy has shown that with the deposition of PPy over ZNR the emission in the visible region was quenched significantly. The NBE to DLE ratio was estimated to relate the structural and optical properties of ZNR and ZNR/PPy electrode which was increased approximately 4 times for ZNR/PPy. This increase in the NBE/DLE ratio has shown the suppression in the defect levels of ZNRs with PPy modification which has indicated towards

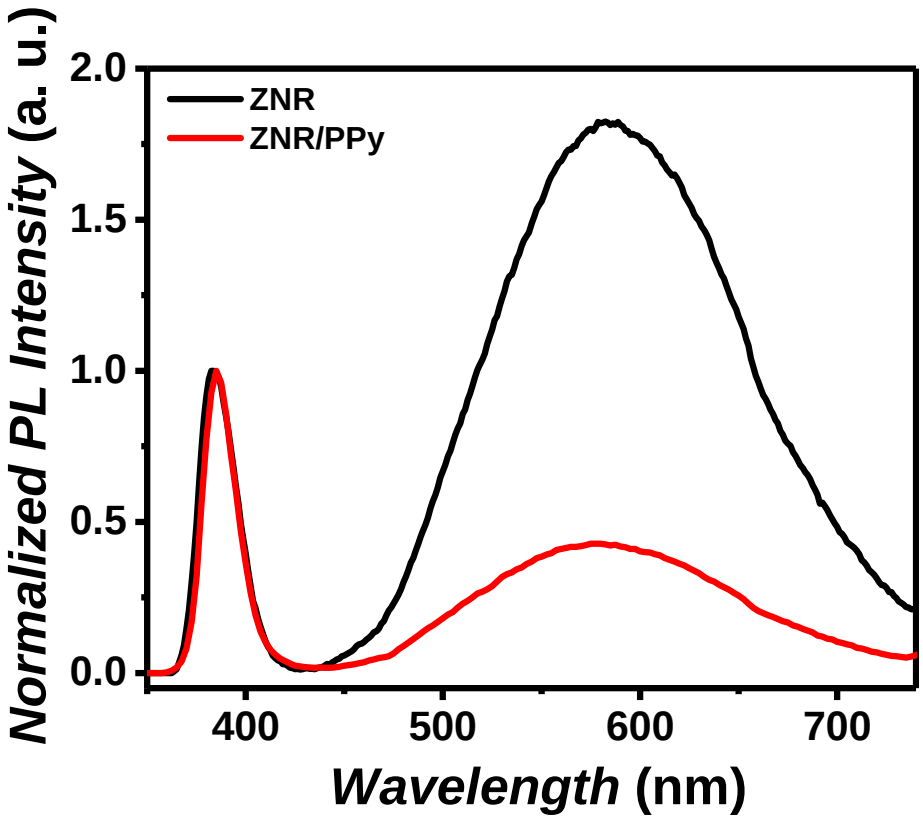

Fig. 6.8: **Normalized PL spectra of as-synthesized ZNR and ZNR/PPy.**

the improved charge transfer properties of ZNR/PPy electrode [146]. Further, the electrochemical properties of ZNR and ZNR/PPy electrodes were investigated to confirm the improved charge transfer characteristics.

6.3.6 Electroactive surface area

To study the influence of PPy deposition on ZNR, the electrochemical properties of both ZNR and ZNR/PPy were studied by cyclic voltammetry (CV). The CVs of ZNR and ZNR/PPy electrodes were carried out in 5 mM $K_3Fe(CN)_6$, $K_4Fe(CN)_6$ in 0.1 M PBS with 0.1 M KCl in a potential range of -0.2 to 0.7 V at a scan rate of 10 mV/s. The recorded CVs of ZNR and ZNR/PPy have been shown in Fig. 6.9. Both the electrodes were found to exhibit well-defined redox peaks which have demonstrated the electro-activity of the as-prepared electrodes.

The ZNR has exhibited a peak to peak separation potential of 358 mV. However, for ZNR/PPy significantly reduced the peak to peak separation potential of 78 mV was observed indicating the quasi-reversible electrochemical behavior of the electrodes [93]. A significant enhancement in the redox current values was obtained for ZNR/PPy electrode as evident in Fig. 6.9. The sharp increase in the anodic

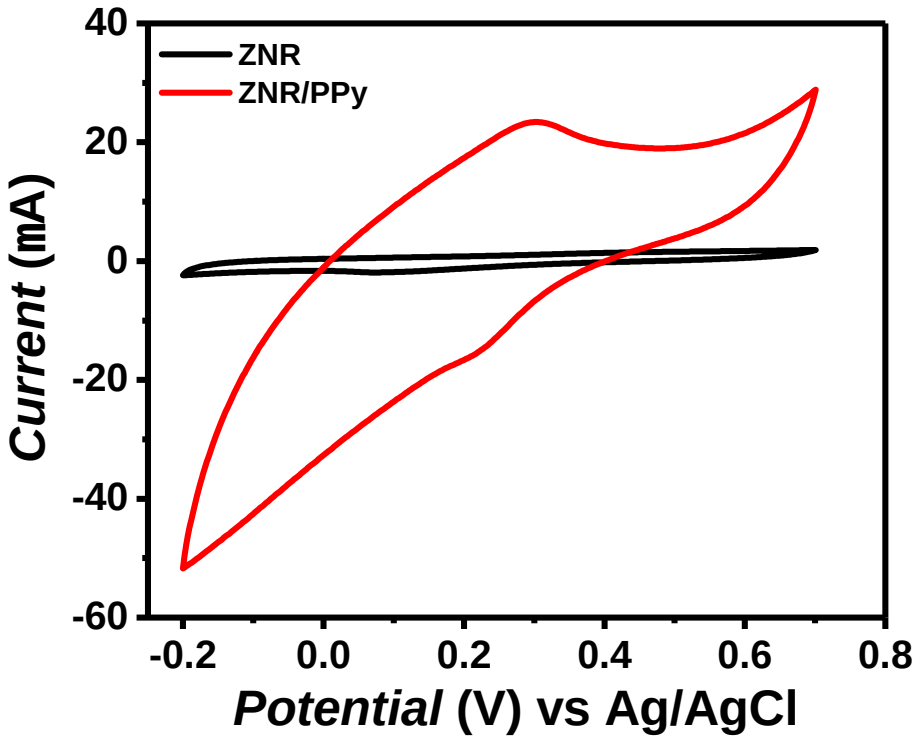

Fig. 6.9: **Cyclic voltammogram of ZNR and ZNR/PPy electrode recorded in 5 mM $[Fe(CN)_6]^{3-/4-}$ redox couple containing 0.1 M KCl in 0.1 M PBS at a scan rate of 10 mV/s.**

current of ZNR/PPy electrode has demonstrated a high electrocatalytic activity of ZNR/PPy as compared to ZNR electrode [58]. In addition to the high electroactivity, the increased anodic current values correspond to the high surface area of ZNR/PPy electrode [79, 84]. The CVs of both the electrodes recorded at different scan rates varying from 10-100 mV/s have been shown in Fig. 6.10 (a, b). The electroactive surface area of both the as-prepared electrodes was determined by using the linear plot of anodic current (I_{pa}) vs square root of different scan rates ($\sqrt{v}$) in CV. The slopes corresponding to both the electrodes were estimated and the electroactive surface area of each electrode was calculated by using the Randles-Sevcik equation (equation 6.2).

$$I_{Pa} = 2.69 * 10^5 * n^{3/2} * A_{eff} * \sqrt{D} * \sqrt{v} * C_0 \tag{6.2}$$

where I_{pa} denotes the anodic peak current value, v refers to the scan rate, A_{eff} is the effective surface area of the electrode, D defines the diffusion coefficient (7.26×10^{-6}cm^2 s^{-1}) of 5 mM $K_3Fe(CN)_6$ in 0.1 M KCl, C_0 is the concentration of $K_3Fe(CN)_6$ and $K_4Fe(CN)_6$ in solution, and n defines the number of electron (n=1)

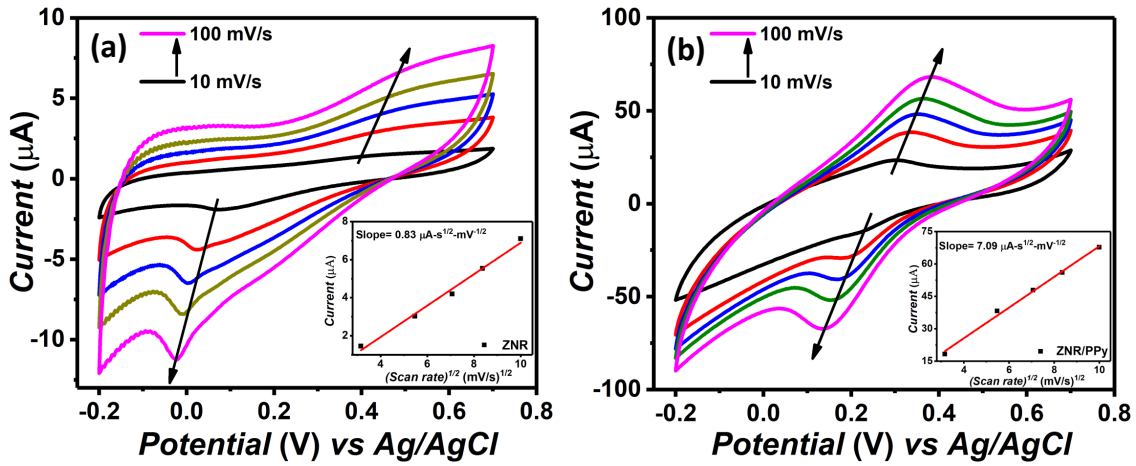

Fig. 6.10: **Cyclic voltammogram of (a) ZNR (b) ZNR/PPy electrode recorded in 5 mM $[Fe(CN)_6]^{3-/4-}$ redox couple containing 0.1 M KCl in 0.1 M PBS at different scan rates from 10-100 mV/s. The inset shows the linear calibration curve of I_{pa} vs $\sqrt{v}$.**

involved in half reaction [34]. The effective surface area of ZNR and ZNR/PPy electrode were estimated to be 0.007 and 0.062 cm^2 respectively which has shown $\sim$9 times higher surface area for ZNR/PPy as compared to ZNR electrode.

6.3.7 Electrochemical impedance spectroscopy (EIS)

To investigate the influence of PPy deposition over ZNR, EIS of both the electrodes was performed in 5 mM $Fe(CN)_6]^{3-/4-}$ redox couple in 0.1 M PBS. A small ac signal of 10 mV amplitude with frequency varying from 100 kHz to 0.1 Hz was applied to the working electrode for EIS spectra. The as-recorded Nyquist plot of ZNR and ZNR/PPy electrodes have been shown in Fig. 6.11 which consist of a semicircle region at a higher frequency and a linear region at low frequency. The diameter of the semicircle defines the charge transfer resistance (R_{ct}) and correspond to the charge transport kinetics at the electrode-electrolyte interface. However, the linear region refers to the diffusion controlled process at the electrode [58, 147]. As observed in Fig. 6.11 the diameter of semicircle for ZNR/PPy electrode has drastically reduced as compared to ZNR electrode.

Further, the obtained Nyquist plot for both the electrodes was fitted to an equivalent electrical circuit using ZSimp Win 3.2 software and all the electrical parameter values were extracted for both the electrodes. The charge transfer resistance (Rct) value of ZNR electrode was calculated to be 121 kΩ which was further significantly

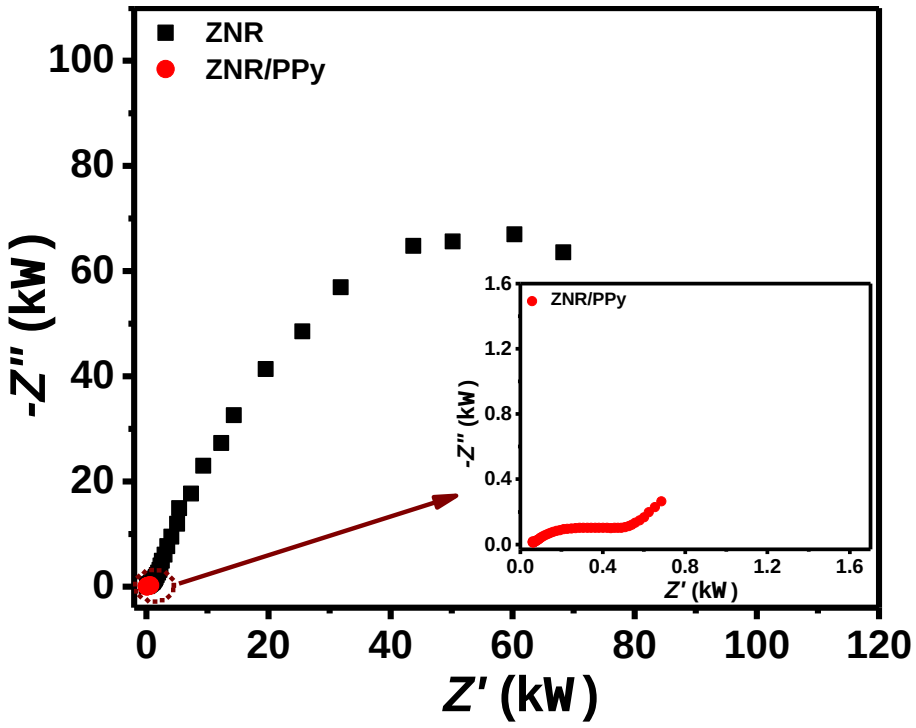

Fig. 6.11: **Nyquist plot of ZNR and ZNR/PPy electrode.**

reduced to 404 Ω for ZNR/PPy electrode. This significant reduction in Rct value was attributed to the facile charge transfer to the electrode with the deposition of PPy. In addition to the improved charge transfer at the interface, the depressed semicircle represents the enhanced surface area of the electrode with PPy deposition [121] as also confirmed by CV.

6.4 Conclusions

In summary, a nanocomposite electrode of electrodeposited Polypyrrole (PPy) over vertically aligned 1-D ZnO nanorods (ZNR) has been successfully fabricated. The ZNRs over Pt-coated glass substrate were synthesized by hydrothermal method and the as-fabricated ZNRs were found to have a high aspect ratio of nearly 10. The hydrothermally grown ZNRs were utilized as the template for the electrodeposition of PPy to form a composite. The PPy was electropolymerized over ZNRs using the cyclic voltammetry deposition method. Corresponding to the optimum thickness of PPy the composite electrode ZNR/PPy-20 performance was compared with the bare ZNR electrode. The modification of ZNR with PPy was confirmed by FESEM, TEM, FTIR, Raman, and XRD. With the modification of PPy, both the electrical and optical properties of ZNR were found to be significantly improved.

The charge transfer resistance of the ZNR/PPy-20 electrode was reduced approximately 300 times and the electroactive surface area was improved $\sim$9 folds as compared to ZNR electrode. Thereby the modified electrode with the PPy has demonstrated a high specific surface area, high electro-activity, and suppressed visible emission as compared to bare ZnO electrode.

Chapter 7

Conclusions and Scope for Future Work

7.1 Conclusions

In this work, an amperometric enzymatic glucose biosensor based on PPy nanostructures have been fabricated by using a simple, scalable template-free method. The electro-synthesized PPy nanostructures were utilized as the support matrix. The objectives defined in this work towards the high sensitivity biosensor by the template-free approach were achieved by improving the enzyme loading over the support matrix which was optimized mainly by fabricating the high surface area nanofibers and improving the electrochemical properties of the nanofibers. The PPy nanofibers based biosensor performance was improved by varying the types of dopants, their concentration, and enzyme loading techniques. Based on the results of the experimental work carried out for this dissertation and the conceptual understanding acquired in the course of this study, the major conclusions of the present work have been listed below:

1. Different PPy nanostructures have been synthesized over Pt-coated glass substrate utilizing electrochemical deposition method. The electro-synthesis parameters were optimized for the growth of PPy nanostructures and the effect of different dopants *viz.* DBSA, MeSA, p-TSA, and $LiClO_4$ on PPy morphology has been investigated. The observed results showed that the pH of the electrolyte solution has a significant influence on the growth of PPy nanos-

tructures where $LiClO_4$ has favored the PPy nanofibers growth.

2. The Polypyrrole nanofibers network (PNNs) were synthesized by varying $LiClO_4$ concentration from 1- 70 mM. The optimized growth conditions for sufficiently thick, high electroactive, and high-density PPy nanofibers with controlled diameter were obtained for 70 mM $LiClO_4$ concentration. The high electro-active surface area ($\sim$3 times) leading to higher enzyme loading and reduced charge transfer resistance ($\sim$3 times) of PNNs with $LiClO_4$ concentration from 1-70 mM were found to play a significant role in the improved sensitivity of the biosensor. The sensitivity of the as-fabricated PNN-70 type biosensor was observed to 4.34 mA-cm^{-2}-M^{-1} which was increased approximately 10 times as compared to PNN-1 type biosensor due to the higher enzyme loading and reduced charge transfer resistance.

3. Further, the performance of glucose biosensor was significantly influenced by incorporating p-TSA as the dopant with electro-polymerized PPy nanofibers. The two different types of electrodes viz. PPy-$LiClO_4$ and PPy-pTSA were fabricated which has shown a significant increment in the electroactive surface area and reduction in charge transfer resistance for PPy-pTSA electrode. The PPy-pTSA based biosensor has shown the sensitivity of 6.12 mA-cm^{-2}-M^{-1} in a linear range of 0.1-7.5 mM and a response time of $\sim$45 s.

4. Different types of immobilization technique *viz.* physical adsorption and crosslinking were employed for biosensor fabrication. The crosslinking immobilization of GOx onto PNN was found to exhibit higher enzyme loading thereby the biosensor with cross-linking has shown 6 folds increment in the sensitivity as compared to physically adsorbed GOx based glucose biosensor. The enhanced sensitivity of 25-30 mA-cm^{-2}-M^{-1} in a linear range of 0.1-2.5 mM with the response time of 30 s was obtained for cross-linked based biosensor.

5. Further to utilize the synergetic effect of organic and inorganic materials, the nanocomposite of PPy with ZnO was fabricated using electrochemical deposition of PPy over ZNR. The charge transfer resistance of the ZNR/PPy-20 electrode (404 Ω) was reduced approximately 300 times and the electroactive

surface area was improved ∼9 folds as compared to ZNR electrode. Thereby the modified electrode with the PPy has demonstrated a high specific surface area and high electro-activity as compared to bare ZnO electrode. Thus the improved electrochemical properties of the composite electrode can be utilized for biosensor fabrication.

7.2 Future Scope of the Work

The research work carried out during this dissertation has highlighted the importance of electrochemical properties of PPy nanostructures as support matrix utilized for enzyme immobilization and different immobilization techniques for the fabrication of biosensor. In addition to the presented research work, further improvement in the PPy properties can be performed to improve the biosensor performance.

This section deals with further studies that can be performed to extend the present research work findings:

1. The improved electrochemical properties i.e. higher electro-active surface area and reduced charge transfer resistance of PPy-ZnO composite electrode can be utilized for the fabrication of glucose biosensor or other biosensing device application.

2. The growth of PPy nanostructures can be optimized to improve the biosensor figure of merits. The other electrosynthesis parameters *viz.* deposition method (CV, amperometric, pulsed deposition, etc.), polymerization time, etc. can be utilized for different type of PPy nanostructures and their density so that active site of enzymes could be exposed out from the protein shell.

3. The obtained PPy nanofibers can be incorporated with metal nanoparticles which can improve the catalytic activity of the electrode for improving the biosensor response.

4. The other immobilization techniques such as co-entrapment (feasible for polymeric matrices), covalent binding can be utilized to enhance the enzyme loading and thus the biosensor performance can be improved.

5. Further, the stability of the PPy nanofibers based glucose biosensor can be enhanced by using other polymer membranes such as nafion, polyethyleneimine (PEI), cellulose etc. [148–151]. Nafion, a semi-permeable membrane is reported to have good biocompatibility, mechanical and thermal stability and most importantly it facilitates a protective layer to improve the biosensor stability. Additionally, the cellulose matrix can be used for the entrapment of enzymes which has also been reported to promote the stability of the enzyme. These semi-permeable membranes act as preventive layer and are beneficial to attract more GOx and also minimize the leaching out of GOx from the PPy nanostructures which can provide long-term stability to the biosensor [151].

6. Further improvement in the biosensor performance can be achieved by fabricating the nanocomposites of PPy with carbon nanotubes, graphene oxide, etc. Especially the response time of the presented biosensors can be minimized by the composites of these materials. It would be of particular interest to perform a systematic study to probe into the influence of composite materials on the response time of the biosensor.

7. PPy nanofibers based biosensors with optimized growth conditions can also be used for the detection of other analyte molecules such as cholesterol, urea, etc.

8. The fabricated PPy nanofibers can be utilized for the integrated biosensor device application.

9. The obtained PPy nanofibers can be utilized in other applications such as batteries, supercapacitors, antistatic coatings, gas sensing, mechanical actuators, etc.

REFERENCES

[1] S Vigneshvar et al. "Recent advances in biosensor technology for potential applications–an overview". In: *Frontiers in bioengineering and biotechnology* 4 (2016), pp. 11–20.

[2] Masashige Taguchi et al. "Nanomaterial-mediated biosensors for monitoring glucose". In: *Journal of diabetes science and technology* 8.2 (2014), pp. 403–411.

[3] Hyeonseok Yoon. "Current trends in sensors based on conducting polymer nanomaterials". In: *Nanomaterials* 3.3 (2013), pp. 524–549.

[4] Eun-Hyung Yoo and Soo-Youn Lee. "Glucose biosensors: an overview of use in clinical practice". In: *Sensors* 10.5 (2010), pp. 4558–4576.

[5] Lee Fung Ang, Lip Yee Por, and Mun Fei Yam. "Development of an amperometric-based glucose biosensor to measure the glucose content of fruit". In: *PloS one* 10.3 (2015), e0111859.

[6] Chao Chen et al. "Recent advances in electrochemical glucose biosensors: a review". In: *Rsc Advances* 3.14 (2013), pp. 4473–4491.

[7] Yibing Xie and Ye Zhao. "Electrochemical biosensing based on polypyrrole/titania nanotube hybrid". In: *Materials Science and Engineering: C* 33.8 (2013), pp. 5028–5035.

[8] Leila Syedmoradi et al. "Point of care testing: The impact of nanotechnology". In: *Biosensors and Bioelectronics* 87 (2017), pp. 373–387.

[9] Suprava Patel et al. "Biosensors in health care: the milestones achieved in their development towards lab-on-chip-analysis". In: *Biochemistry research international* 2016 (2016).

[10] Chandran Karunakaran, Raju Rajkumar, and Kalpana Bhargava. "Introduction to biosensors". In: *Biosensors and bioelectronics*. Elsevier, 2015, pp. 1–68.

[11] Celine IL Justino, Teresa A Rocha-Santos, and Armando C Duarte. "Review of analytical figures of merit of sensors and biosensors in clinical applications". In: *TrAC Trends in Analytical Chemistry* 29.10 (2010), pp. 1172–1183.

[12] AL Galant, RC Kaufman, and JD Wilson. "Glucose: Detection and analysis". In: *Food Chemistry* 188 (2015), pp. 149–160.

[13] Gregor Ocvirk, Harvey Buck, and Stacy Hunt DuVall. "Electrochemical glucose biosensors for diabetes care". In: *Trends in Bioelectroanalysis*. Springer, 2016, pp. 1–101.

[14] Joseph Wang. "Glucose biosensors: 40 years of advances and challenges". In: *Electroanalysis: An International Journal Devoted to Fundamental and Practical Aspects of Electroanalysis* 13.12 (2001), pp. 983–988.

[15] *IDF Diabetes Atlas (2017), Technical report*. 2017.

[16] Danielle Bruen et al. "Glucose sensing for diabetes monitoring: recent developments". In: *Sensors* 17.8 (2017), p. 1866.

[17] Yusuke Kemmochi et al. "Metabolic disorders and diabetic complications in spontaneously diabetic Torii Leprfa rat: a new obese type 2 diabetic model". In: *Journal of diabetes research* 2013 (2013).

[18] *Diabetes: A Public Health Concern*. URL: `https://medium.com/@AmericanMilU/diabetes-a-public-health-concern-a742cbff3fee`.

[19] Tim DH Bugg. *Introduction to enzyme and coenzyme chemistry*. John Wiley & Sons, 2012.

[20] Chun Ming Wong, Kwun Hei Wong, and Xiao Dong Chen. "Glucose oxidase: natural occurrence, function, properties and industrial applications". In: *Applied microbiology and biotechnology* 78.6 (2008), pp. 927–938.

[21] Greg T Hermanson. *Bioconjugate techniques*. Academic press, 2013.

[22] SMY Shija, Y Hong, and FMM Chale. "Trends of Avicennia marina Productivity as Influenced by Climatic Seasons: A Case Study of Mbweni Mangrove Forest Ecosystem". In: *Huria: Journal of the Open University of Tanzania* 19.1 (2015), pp. 15–28.

[23] R Gupta et al. "In Silico Structure Modeling and Characterization of Hypothetical Protein YP_004590319. 1 Present in Enterobacter aerogens". In: *J Proteomics Bioinform* 10 (2017), pp. 152–170.

[24] Athel Cornish-Bowden. *Principles of enzyme kinetics*. Elsevier, 2014.

[25] OpenStax College. *Anatomy and physiology*. Rice University, 2013.

[26] Keith Dalziel. "Physical significance of Michaelis constants". In: *Nature* 196.4860 (1962), p. 1203.

[27] Robert Eisenthal and Athel Cornish-Bowden. "The direct linear plot. A new graphical procedure for estimating enzyme kinetic parameters". In: *Biochemical Journal* 139.3 (1974), pp. 715–720.

[28] Sercan Karav et al. “Recent advances in immobilization strategies for glycosidases”. In: *Biotechnology progress* 33.1 (2017), pp. 104–112.

[29] Audrey Sassolas, Loic J Blum, and Beatrice D Leca-Bouvier. “Immobilization strategies to develop enzymatic biosensors”. In: *Biotechnology advances* 30.3 (2012), pp. 489–511.

[30] Abdirahman Yussuf et al. “Synthesis and Characterization of Conductive Polypyrrole: The Influence of the Oxidants and Monomer on the Electrical, Thermal, and Morphological Properties”. In: *International Journal of Polymer Science* 2018 (2018).

[31] Nihan Aydemir, Jenny Malmstrom, and Jadranka Travas-Sejdic. “Conducting polymer based electrochemical biosensors”. In: *Physical Chemistry Chemical Physics* 18.12 (2016), pp. 8264–8277.

[32] Jianfeng Zang et al. “Template-free electrochemical synthesis of superhydrophilic polypyrrole nanofiber network”. In: *Macromolecules* 41.19 (2008), pp. 7053–7057.

[33] Jiayue Wen et al. “Synthesis of polypyrrole nanoparticles and their applications in electrically conductive adhesives for improving conductivity”. In: *RSC Advances* 7.84 (2017), pp. 53219–53225.

[34] Ahmed Fakhry, Francoise Pillier, and Catherine Debiemme-Chouvy. “Templateless electrogeneration of polypyrrole nanostructures: impact of the anionic composition and pH of the monomer solution”. In: *Journal of Materials Chemistry A* 2.25 (2014), pp. 9859–9865.

[35] Robert C Weast, Melvin J Astle, William H Beyer, et al. *CRC handbook of chemistry and physics*. Vol. 69. CRC press Boca Raton, FL, 1988.

[36] Pooria Moozarm Nia, Woi Pei Meng, and Y Alias. “One-step electrodeposition of polypyrrole-copper nano particles for H2O2 detection”. In: *Journal of The Electrochemical Society* 163.3 (2016), B8–B14.

[37] Matthew A Cooper. “Optical biosensors in drug discovery”. In: *Nature reviews Drug discovery* 1.7 (2002), p. 515.

[38] Ashok Kumar et al. “Biosensors based on piezoelectric crystal detectors: theory and application”. In: *JOM-e* 52.10 (2000), pp. 1–6.

[39] J. Cooper, A. Cass, and T. Cass. *Biosensors*. Practical Approach Series No 268. OUP Oxford, 2004. ISBN: 9780199638451.

[40] Joseph Wang. “Electrochemical glucose biosensors”. In: *Chemical reviews* 108.2 (2008), pp. 814–825.

[41] Ning An et al. “Immobilization of enzymes on clay minerals for biocatalysts and biosensors”. In: *Applied Clay Science* 114 (2015), pp. 283–296.

[42] Tugba Ceren Gokoglan et al. “Paper based glucose biosensor using graphene modified with a conducting polymer and gold nanoparticles”. In: *Journal of The Electrochemical Society* 164.6 (2017), G59–G64.

[43] A Malinauskas, J Malinauskiene, and A Ramanavicius. “Conducting polymer-based nanostructurized materials: electrochemical aspects”. In: *Nanotechnology* 16.10 (2005), R51.

[44] Chul Park, Changsoo Lee, and Oh Kwon. “Conducting polymer based nanobiosensors”. In: *Polymers* 8.7 (2016), p. 249.

[45] Guangqing Xu et al. “Modification of polypyrrole nanowires array with platinum nanoparticles and glucose oxidase for fabrication of a novel glucose biosensor”. In: *Analytica chimica acta* 755 (2012), pp. 100–107.

[46] Chunxiao Feng et al. “Glucose biosensors based on Ag nanoparticles modified TiO 2 nanotube arrays”. In: *Journal of Solid State Electrochemistry* 18.1 (2014), pp. 163–171.

[47] Joseph G Ayenimo and Samuel B Adeloju. “Improved potentiometric glucose detection with ultra-thin polypyrrole-glucose oxidase films”. In: *Analytical Methods* 6.22 (2014), pp. 8996–9006.

[48] Jingwen Liao et al. “Nanostructured PPy coating on titanium fabricated via template-free electrochemical polymerization in PBS”. In: *Surface and Coatings Technology* 228 (2013), S41–S43.

[49] Laith Al-Mashat et al. “Electropolymerized polypyrrole nanowires for hydrogen gas sensing”. In: *The Journal of Physical Chemistry C* 116.24 (2012), pp. 13388–13394.

[50] Zhangxun Xia et al. “Controllable synthesis of vertically aligned polypyrrole nanowires as advanced electrode support for fuel cells”. In: *Journal of Power Sources* 256 (2014), pp. 125–132.

[51] Charles R Martin. “Template synthesis of electronically conductive polymer nanostructures”. In: *Accounts of chemical research* 28.2 (1995), pp. 61–68.

[52] Pragya Agar Palod and Vipul Singh. “Facile synthesis of high density polypyrrole nanofiber network with controllable diameters by one step template free electropolymerization for biosensing applications”. In: *Sensors and Actuators B: Chemical* 209 (2015), pp. 85–93.

[53] Rui Xiao et al. “Controlled electrochemical synthesis of conductive polymer nanotube structures”. In: *Journal of the American Chemical Society* 129.14 (2007), pp. 4483–4489.

[54] EMI Mala Ekanayake, Daluwathu MG Preethichandra, and Keiichi Kaneto. "Effect of glucose oxidase immobilizing techniques on performances of nano scale polypyrrole glucose biosensors". In: *Japanese Journal of Applied Physics* 47.2S (2008), p. 1321.

[55] Pragya Agar Palod et al. "Template-assisted electrochemical growth of polypyrrole nanotubes for development of high sensitivity glucose biosensor". In: *Applied biochemistry and biotechnology* 174.3 (2014), pp. 1059–1072.

[56] Pragya Agar Palod and Vipul Singh. "Improvement in glucose biosensing response of electrochemically grown polypyrrole nanotubes by incorporating crosslinked glucose oxidase". In: *Materials Science and Engineering: C* 55 (2015), pp. 420–430.

[57] GQ Xu et al. "Polypyrrole (PPy) nanowire arrays entrapped with glucose oxidase biosensor for glucose detection". In: *2012 7th IEEE International Conference on Nano/Micro Engineered and Molecular Systems (NEMS)*. IEEE. 2012, pp. 511–514.

[58] Bishnu Kumar Shrestha et al. "Globular Shaped Polypyrrole Doped Well-Dispersed Functionalized Multiwall Carbon Nanotubes/Nafion Composite for Enzymatic Glucose Biosensor Application". In: *Scientific reports* 7.1 (2017), p. 16191.

[59] Matei Raicopol et al. "Functionalized single-walled carbon nanotubes/polypyrrole composites for amperometric glucose biosensors". In: *Nanoscale research letters* 8.1 (2013), p. 316.

[60] Merih Zeynep Cetin and Pinar Camurlu. "Utilization of Polypyrrole Nanofibers in Glucose Detection". In: *Journal of The Electrochemical Society* 164.12 (2017), B585–B590.

[61] Navid Yasrebi et al. "Optimization of Sputtering Parameters for the Deposition of Low Resistivity Indium Tin Oxide Thin Films". In: *Acta Metallurgica Sinica (English Letters)* 27.2 (2014), pp. 324–330.

[62] Baoli Wu et al. "Biosensors for determination of glucose with glucose oxidase immobilized on an eggshell membrane". In: *Talanta* 64.2 (2004), pp. 546–553.

[63] Gerhard Hübschen et al. *Materials characterization using Nondestructive Evaluation (NDE) methods*. Woodhead Publishing, 2016.

[64] Ludovica Sartini et al. "Nuclear instruments and methods in physics research section A: Accelerators, spectrometers, detectors and associated equipment". In: *Nuclear Instruments and Methods in Physics Research A* (2010).

[65] B.D. Cullity and S.R. Stock. *Elements of X-ray Diffraction, Third Edition*. English (US). Prentice-Hall, 2001.

[66] Peter J Brown et al. "Effect of interchain interactions on the absorption and emission of poly (3-hexylthiophene)". In: *Physical Review B* 67.6 (2003), p. 064203.

[67] Dieter K Schroder. *Semiconductor material and device characterization*. John Wiley & Sons, 2006.

[68] Peter EJ Flewitt and Robert K Wild. *Physical methods for materials characterisation*. CRC Press, 2017.

[69] Andrzej Lasia. "Electrochemical impedance spectroscopy and its applications". In: *Modern aspects of electrochemistry*. Springer, 2002, pp. 143–248.

[70] Adriano Sacco. "Electrochemical impedance spectroscopy: Fundamentals and application in dye-sensitized solar cells". In: *Renewable and Sustainable Energy Reviews* 79 (2017), pp. 814–829.

[71] Noemie Elgrishi et al. "A practical beginner's guide to cyclic voltammetry". In: *Journal of Chemical Education* 95.2 (2017), pp. 197–206.

[72] Peter T Kissinger and William R Heineman. "Cyclic voltammetry". In: *Journal of Chemical Education* 60.9 (1983), p. 702.

[73] Chung-Che Tsai and Gou-Jen Wang. "A Glucose Biosensor Based on a 3D Nanostructured Gold Electrode". In: *Journal of The Electrochemical Society* 160.1 (2013), B1–B5.

[74] Thanh-Hai Le, Yukyung Kim, and Hyeonseok Yoon. "Electrical and electrochemical properties of conducting polymers". In: *Polymers* 9.4 (2017), p. 150.

[75] Ravindra Kumar, Satyendra Singh, and BC Yadav. "Conducting polymers: synthesis, properties and applications". In: *International Advanced Research Journal in Science, Engineering and Technology* 2.11 (2015), pp. 110–124.

[76] Yang Tan and Khashayar Ghandi. "Kinetics and mechanism of pyrrole chemical polymerization". In: *Synthetic Metals* 175 (2013), pp. 183–191.

[77] Ioannis S Chronakis, Sven Grapenson, and Alexandra Jakob. "Conductive polypyrrole nanofibers via electrospinning: electrical and morphological properties". In: *Polymer* 47.5 (2006), pp. 1597–1603.

[78] Said Sadki et al. "The mechanisms of pyrrole electropolymerization". In: *Chemical Society Reviews* 29.5 (2000), pp. 283–293.

[79] Deepak P Dubal et al. "Porous polypyrrole clusters prepared by electropolymerization for a high performance supercapacitor". In: *Journal of Materials Chemistry* 22.7 (2012), pp. 3044–3052.

[80] Catherine Debiemme-Chouvy. "Template-free one-step electrochemical formation of polypyrrole nanowire array". In: *Electrochemistry communications* 11.2 (2009), pp. 298–301.

[81] Keith Wilson and John Walker. *Principles and techniques of biochemistry and molecular biology*. Cambridge university press, 2010.

[82] J Todd Holland et al. "Rational redesign of glucose oxidase for improved catalytic function and stability". In: *PloS one* 7.6 (2012), e37924.

[83] Romulo AO Castro et al. "Electrosynthesis and characterization of polypyrrole/cashew gum composite grown on gold surface in aqueous medium". In: *International Journal of Electrochemical Science* 12.1 (2017), pp. 50–61.

[84] E Rouya et al. "Electrochemical characterization of the surface area of nanoporous gold films". In: *Journal of The Electrochemical Society* 159.4 (2012), K97–K102.

[85] Mayoorika Shukla et al. "Influence of aspect ratio and surface defect density on hydrothermally grown ZnO nanorods towards amperometric glucose biosensing applications". In: *Applied Surface Science* 422 (2017), pp. 798–808.

[86] FZ Engin Sagirli, ES Kayali, and AS Sarac. "Electrochemical Impedance Spectroscopic Study on Polypyrrole/Barium Titanate/Poly (acrylonitrile-co-methylacrylate) Nanoparticles". In: *Journal of The Electrochemical Society* 163.3 (2016), H205–H212.

[87] A Ramanavicius et al. "Electrochemical impedance spectroscopy of polypyrrole based electrochemical immunosensor". In: *Bioelectrochemistry* 79.1 (2010), pp. 11–16.

[88] LFQP Marchesi et al. "Investigation of polypyrrole degradation using electrochemical impedance spectroscopy". In: *The Journal of Physical Chemistry B* 115.31 (2011), pp. 9570–9575.

[89] Nesrine Harfouche, Belkacem Nessark, and Francois Xavier Perrin. "Electrochemical and surface characterization of composite material: Polyaniline/LiMn2O4". In: *Journal of Electroanalytical Chemistry* 756 (2015), pp. 179–185.

[90] Murat Ates et al. "Electrolyte type and concentration effects on poly (3-(2-aminoethyl thiophene) electro-coated on glassy carbon electrode via impedimetric study". In: *Iranian Polymer Journal* 22.3 (2013), pp. 199–208.

[91] Lin Niu et al. "Electrochemical impedance and morphological characterization of platinum-modified polyaniline film electrodes and their electrocatalytic activity for methanol oxidation". In: *Journal of Electroanalytical Chemistry* 544 (2003), pp. 121–128.

[92] Carolina Gonzalez-Gaitan et al. “Effects of the surface chemistry and structure of carbon nanotubes on the coating of glucose oxidase and electrochemical biosensors performance”. In: *RSC Advances* 7.43 (2017), pp. 26867–26878.

[93] Zepeng Kang et al. “Direct electrochemistry and bioelectrocatalysis of glucose oxidase in CS/CNC film and its application in glucose biosensing and biofuel cells”. In: *RSC Advances* 7.8 (2017), pp. 4572–4579.

[94] Yuh-Ming Uang and Tse-Chuan Chou. “Fabrication of glucose oxidase/polypyrrole biosensor by galvanostatic method in various pH aqueous solutions”. In: *Biosensors and Bioelectronics* 19.3 (2003), pp. 141–147.

[95] EMI Mala Ekanayake, Daluwathu MG Preethichandra, and Keiichi Kaneto. “Polypyrrole nanotube array sensor for enhanced adsorption of glucose oxidase in glucose biosensors”. In: *Biosensors and Bioelectronics* 23.1 (2007), pp. 107–113.

[96] Margalida Artigues, Jordi Abellà, and Sergi Colominas. “Analytical Parameters of an Amperometric Glucose Biosensor for Fast Analysis in Food Samples”. In: *Sensors* 17.11 (2017), p. 2620.

[97] Joseph G Ayenimo and Samuel B Adeloju. “Amperometric detection of glucose in fruit juices with polypyrrole-based biosensor with an integrated permselective layer for exclusion of interferences”. In: *Food chemistry* 229 (2017), pp. 127–135.

[98] Cheng Chen, Yan Jiang, and Jinqing Kan. “A noninterference polypyrrole glucose biosensor”. In: *Biosensors and Bioelectronics* 22.5 (2006), pp. 639–643.

[99] Daluwathu Mulla Gamage Preethichandra and Mitsuyoshi Onoda. “Functional Design of Electrochemical Biosensors Using Polypyrrole”. In: *Electronics and Communications in Japan* 99.7 (2016), pp. 55–63.

[100] Pramila Jakhar, Mayoorika Shukla, and Vipul Singh. “Influence of LiClO4 Concentration on 1-D Polypyrrole Nanofibers for Enhanced Performance of Glucose Biosensor”. In: *Journal of The Electrochemical Society* 165.7 (2018), G80–G89.

[101] N Su et al. “Synthesis and characterization of polypyrrole doped with anionic spherical polyelectrolyte brushes.” In: *Express Polymer Letters* 6.9 (2012).

[102] U Páramo-García, JG Ibanez, and N Batina. “Electrochemical modulation of the thickness of polypyrrole films by using different anionic dopants”. In: *Int J Electrochem Sci* 6 (2011), pp. 5172–88.

[103] G Ozyilmaz, AT Ozyilmaz, and F Can. "Glucose oxidase-polypyrrole electrodes synthesized in p-toluenesulfonic acid and sodium p-toluenesulfonate". In: *Applied biochemistry and microbiology* 47.2 (2011), pp. 196–205.

[104] Vittorio Guarnieri et al. "Platinum metallization for MEMS application: Focus on coating adhesion for biomedical applications". In: *Biomatter* 4.1 (2014), e28822.

[105] Robert G Johnson et al. "Adhesion layer for platinum based sensors". Pat. US Patent 4,952,904.

[106] Yong Chen et al. "Effects of transition metal ions on the electrochemical performance of polypyrrole electrode". In: *Journal of Materials Science: Materials in Electronics* 29 (2018), pp. 11020–11029.

[107] Shubhra Goel, Nasreen A Mazumdar, and Alka Gupta. "Synthesis and characterization of polypyrrole nanofibers with different dopants". In: *Polymers for Advanced Technologies* 21.3 (2010), pp. 205–210.

[108] Mayoorika Shukla et al. "Facile hydrothermal synthesis of mn doped ZnO nanopencils for development of amperometric glucose biosensors". In: *Materials Research Express* 5.5 (2018), p. 055031.

[109] Mohammed ElKaoutit et al. "Bio-functionalization of electro-synthesized polypyrrole surface by heme enzyme using a mixture of Nafion and glutaraldehyde as synergetic immobilization matrix: Conformational characterization and electrocatalytic studies". In: *Applied Surface Science* 257.24 (2011), pp. 10926–10935.

[110] Mehmet Senel, Muamer Dervisevic, and Emre Cevik. "A novel amperometric glucose biosensor based on reconstitution of glucose oxidase on thiophene-3-boronic acid polymer layer". In: *Current Applied Physics* 13.7 (2013), pp. 1199–1204.

[111] PD Gaikwad et al. "Immobilization of GOD on electrochemically synthesized PANI film by cross-linking via glutaraldehyde for determination of glucose". In: *International Journal of Electrochemical Science* 1.8 (2006), pp. 425–434.

[112] Barbara Kowalewska and Katarzyna Jakubow. "The impact of immobilization process on the electrochemical performance, bioactivity and conformation of glucose oxidase enzyme". In: *Sensors and Actuators B: Chemical* 238 (2017), pp. 852–861.

[113] Xiaoqing Xu et al. “Effects of guanidinium ions on the conformational structure of glucose oxidase studied by electrochemistry, spectroscopy, and theoretical calculations: towards developing a chemical-induced protein conformation assay”. In: *Physical Chemistry Chemical Physics* 14.16 (2012), pp. 5824–5836.

[114] Wenwei Tang et al. “Glucose biosensor based on a glassy carbon electrode modified with polythionine and multiwalled carbon nanotubes”. In: *PloS one* 9.5 (2014), e95030.

[115] Mei Yan et al. “A disposable electrochemical immunosensor based on carbon screen-printed electrodes for the detection of prostate specific antigen”. In: *Biosensors and Bioelectronics* 38.1 (2012), pp. 355–361.

[116] Wei Wang et al. “Glucose biosensor based on glucose oxidase immobilized on unhybridized titanium dioxide nanotube arrays”. In: *Microchimica Acta* 181.3-4 (2014), pp. 381–387.

[117] Fernando López-Gallego et al. “Enzyme stabilization by glutaraldehyde crosslinking of adsorbed proteins on aminated supports”. In: *Journal of Biotechnology* 119.1 (2005), pp. 70–75.

[118] Kash Anderson et al. “A highly sensitive nonenzymatic glucose biosensor based on the regulatory effect of glucose on electrochemical behaviors of colloidal silver nanoparticles on MoS2”. In: *Sensors* 17.8 (2017), p. 1807.

[119] Ozlem Colak et al. “Glucose biosensor based on the immobilization of glucose oxidase on electrochemically synthesized polypyrrole-poly (vinyl sulphonate) composite film by cross-linking with glutaraldehyde”. In: *Artificial Cells, Blood Substitutes, and Biotechnology* 40.5 (2012), pp. 354–361.

[120] Yuya Oaki, Takahiro Oki, and Hiroaki Imai. “Enhanced photoconductive properties of a simple composite coaxial nanostructure of zinc oxide and polypyrrole”. In: *Journal of Materials Chemistry* 22.39 (2012), pp. 21195–21200.

[121] Fang Wang et al. “A scalable route to prepare core–shell structured ZnO@ PEDOT nanowires and PEDOT nanotubes and their properties as electrode materials”. In: *Applied Surface Science* 370 (2016), pp. 102–110.

[122] Shilpa Jain et al. “Ammonia detection of 1-D ZnO/polypyrrole nanocomposite: Effect of CSA doping and their structural, chemical, thermal and gas sensing behavior”. In: *Applied Surface Science* 396 (2017), pp. 1317–1325.

[123] Falong Wang et al. “Preparation of polypyrrole/poly (N-methylpyrrole)/nano-ZnO composite and its anticorrosive performance”. In: *International Journal of Electrochemical Science* 10 (2015), pp. 6721–6731.

[124] Yang Huang et al. “High performance UV light photodetectors based on Sn-nanodot-embedded SnO 2 nanobelts”. In: *Journal of Materials Chemistry C* 3.20 (2015), pp. 5253–5258.

[125] Yanru Xie et al. “A self-powered UV photodetector based on TiO 2 nanorod arrays”. In: *Nanoscale research letters* 8.1 (2013), p. 188.

[126] Yin Zhang et al. “Biomedical applications of zinc oxide nanomaterials”. In: *Current molecular medicine* 13.10 (2013), pp. 1633–1645.

[127] Michael H Huang et al. “Room-temperature ultraviolet nanowire nanolasers”. In: *science* 292.5523 (2001), pp. 1897–1899.

[128] Anubha Bilgaiyan et al. “Improved photo response of hybrid ZnO/P3HT bilayered photo diode”. In: *2015 IEEE SENSORS*. IEEE. 2015, pp. 1–4.

[129] Kavindra Kandpal and Navneet Gupta. “Zinc Oxide Thin Film Transistors: Advances, Challenges and Future Trends”. In: *Bulletin of Electrical Engineering and Informatics* 5.2 (2016), pp. 205–212.

[130] Ling Zhu and Wen Zeng. “Room-temperature gas sensing of ZnO-based gas sensor: A review”. In: *Sensors and Actuators A: Physical* 267 (2017), pp. 242–261.

[131] P Rajagopalan, Vipul Singh, and IA Palani. “Enhancement of ZnO-based flexible nano generators via a sol–gel technique for sensing and energy harvesting applications”. In: *Nanotechnology* 29.10 (2018), p. 105406.

[132] Zhong Lin Wang. “Zinc oxide nanostructures: growth, properties and applications”. In: *Journal of physics: condensed matter* 16.25 (2004), R829.

[133] Gaige Zheng et al. “Ultraviolet emission enhancement in ZnO thin films modified by nanocrystalline TiO2”. In: *Optical Materials* 67 (2017), pp. 139–144.

[134] Saeideh Ebrahimiasl et al. “Novel conductive polypyrrole/zinc oxide/chitosan bionanocomposite: synthesis, characterization, antioxidant, and antibacterial activities”. In: *International journal of nanomedicine* 10 (2015), p. 217.

[135] Rajinder Singh, Ram Bilash Choudhary, and Rohit Kandulna. “Delocalization of π electrons and trapping action of ZnO nanoparticles in PPY matrix for hybrid solar cell application”. In: *Journal of Molecular Structure* 1156 (2018), pp. 633–644.

[136] MA Chougule et al. “Polypyrrole–ZnO nanohybrids: effect of CSA doping on structure, morphology and optoelectronic properties”. In: *Applied Nanoscience* 3.5 (2013), pp. 423–429.

[137] Bingxi Yan et al. “Flexible photocatalytic composite film of ZnO-microrods/polypyrrole”. In: *ACS applied materials & interfaces* 9.34 (2017), pp. 29113–29119.

[138] Jianhang Huang et al. “Ultrasound assisted polymerization for synthesis of ZnO/Polypyrrole composites for zinc/nickel rechargeable battery”. In: *Journal of Power Sources* 271 (2014), pp. 143–151.

[139] Nguyen Viet Tuyen, Nguyen Ngoc Long, and Ta Dinh Canh. “Synthesis and characteristics of single-crystal Ni-doped ZnO nanorods prepared by a microwave irradiation method”. In: *e-Journal of Surface Science and Nanotechnology* 9 (2011), pp. 472–476.

[140] XL Xu et al. “Excellent acetone sensor of La-doped ZnO nanofibers with unique bead-like structures”. In: *Sensors and Actuators B: Chemical* 213 (2015), pp. 222–233.

[141] Kh Ghanbari and N Hajheidari. “ZnO–CuxO/polypyrrole nanocomposite modified electrode for simultaneous determination of ascorbic acid, dopamine, and uric acid”. In: *Analytical biochemistry* 473 (2015), pp. 53–62.

[142] Pritam Patil et al. “Synthesis of 1-D ZnO nanorods and polypyrrole/1-D ZnO nanocomposites for photocatalysis and gas sensor applications”. In: *Bulletin of Materials Science* 39.3 (2016), pp. 655–665.

[143] Satyaprakash Sahoo, GL Sharma, and Ram S Katiyar. “Raman spectroscopy to probe residual stress in ZnO nanowire”. In: *Journal of Raman Spectroscopy* 43.1 (2012), pp. 72–75.

[144] C Bundesmann et al. “Raman scattering in ZnO thin films doped with Fe, Sb, Al, Ga, and Li”. In: *Applied Physics Letters* 83.10 (2003), pp. 1974–1976.

[145] Jitesh Agrawal et al. “Zinc Interstitial Rich ZnO Honeycomb Nanostructures for Deep UV Photodetection”. In: *physica status solidi (RRL)–Rapid Research Letters* 12.10 (2018), p. 1800241.

[146] Mayoorika Shukla, IA Palani, Vipul Singh, et al. “A Comparative Analysis of ZnO Nanorods and Nanopencils Towards Amperometric Biosensing Applications”. In: *Journal of nanoscience and nanotechnology* 19.7 (2019), pp. 3816–3824.

[147] Xueping Zhang et al. “Direct electrochemistry of glucose oxidase on novel free-standing nitrogen-doped carbon nanospheres carbon nanofibers composite film”. In: *Scientific reports* 5 (2015), p. 9885.

[148] Jose I Reyes-De-Corcuera, Hanna E Olstad, and Rosalia Garcia-Torres. "Stability and stabilization of enzyme biosensors: the key to successful application and commercialization". In: *Annual review of food science and technology* 9 (2018), pp. 293–322.

[149] Soichi Yabuki, Miho Iwamoto, and Yoshiki Hirata. "Long-term stability of a cellulose-based glucose oxidase membrane". In: *Materials* 7.2 (2014), pp. 899–905.

[150] Apurva Sonawane, Pandiaraj Manickam, and Shekhar Bhansali. "Stability of enzymatic biosensors for wearable applications". In: *IEEE reviews in biomedical engineering* 10 (2017), pp. 174–186.

[151] Marcelinus Christwardana and Domenico Frattini. "Electrochemical Study of Enzymatic Glucose Sensors Biocatalyst: Thermal Degradation after Long-Term Storage". In: *Chemosensors* 6.4 (2018), pp. 53–65.